Summer 7-22-2013

Design of Novel Protein-based MRI Contrast Agernets with High Relaxivity and Stability for Biomedical Imaging

Shenghui Xue
Department of Biology

DESIGN OF NOVEL PROTEIN-BASED MRI CONTRAST AGERNETS WITH HIGH RELAXIVITY AND STABILTY FOR BIOMEDICAL IMAGING

by

SHENGHUI XUE

Under the Direction of Drs. Jenny J. Yang and Zhi-Ren Liu

ABSTRACT

Magnetic resonance imaging (MRI) is the leading imaging technique for disease diagnostics. MRI contrast agents facilitate MRI technique to obtain tissue-specific image with improved sensitivity and signal-to-noise ratio. However, the applications of current MRI contrast agents are hampered by their uncontrolled blood circulation time, low relaxivity, and low specificity. To address such need, I have developed a series of analitical methods to determine and evaluate the strong metal binding affinity and metal selectivity of developed protein-based contrast agents (ProCAs). In addition, we have successed designed contrast agents ProCA3 series based on key determinats for metal binding sites and relaxivity. We have dementrated that one of the ProCA3 variants, ProCA32, has a high Gd^{3+} affinity less than 10^{-21} M and high metal selectivity

with relxivity of more than 30 $mM^{-1}s^{-1}$ per Gd and 60 $mM^{-1}s^{-1}$ per particle. Moreover, we have demonstrated that ProCA3 variants have proper blood circulation time, high relaxivity, high metal selectivity and low toxicity, which facilitate MR imaging of multiple organs, such as liver, kidney, and blood vessels, as well as tumors. ProCA32 is also able to image liver metastases a tumor size less than 0.25 mm, which is more than fourty times more sensitive than that of clinical diagnostics of liver metastases using MRI and our developed methodology. We have further created ProCA3 variants with targeting peptide moieties such as ProCA3.bomb or ProCA3.affi to against cancer biomarkers such as GRPR and HER2 with capability to imaging tumor biomarker expressions *in vivo* at molecular level. We have shown that ProCA3 has an excellent safety profile and pharmacokinetics for MRI in animals. With our additional effect in protein expression, modification, and scale up production of these developed protein contrast agents, ProCA3 is expected to be a promising MRI contrast for the diagnostics for disease, such as metastatic tumor and blood vessel abnormalities, and tumor biomarkers.

INDEX WORDS: MRI contrast agent, Gadolinium, Melanoma, Tumor diagnostics, Liver metastasis, Relaxivities

DESIGN OF NOVEL PROTEIN-BASED MRI CONTRAST AGERNETS WITH HIGH RELAXIVITY AND STABILTY FOR BIOMEDICAL IMAGING

by

SHENGHUI XUE

A Dissertation Submitted in Partial Fulfillment of the Requirements for the Degree of

Doctor of Philosophy

in the College of Arts and Sciences

Georgia State University

2013

DESIGN OF NOVEL PROTEIN-BASED MRI CONTRAST AGERNETS WITH HIGH RELAXIVITY AND STABILTY FOR BIOMEDICAL IMAGING

by

SHENGHUI XUE

Committee Chairs: Drs. Jenny Jie Yang and Zhi-Ren Liu

Committee: Dr. Phang C. Tai

Dr. Ritu Aneja

Electronic Version Approved:

Office of Graduate Studies

College of Arts and Sciences

Georgia State University

August 2013

DEDICATION

This page is optional. The heading is also optional. You may write whatever you would like on this page. It should be double-spaced. This is not included in the table of contents.

ACKNOWLEDGEMENTS

I would like to deeply thank Dr. Jenny Jie Yang for her guidance and support in the past six years. She always ready to help me not only in my sicientific research but also my life. I deeply appreciate the scientific training from her. From these training, I not only learned how to be a good researcher with sharp mind and fine hand, but also learned colabration, team work and communication with others. I would like to thank Dr. Zhi-Ren Liu for his mentoring in my research. Dr. Liu give a me a lot of good guildance on my project. Without his patient mentoring, all this work could't be done. I would like deeply thank Dr. Phang-Cheng Tai for his great help. Dr. Tai recruited me from China. He is also one of my committee members. Starting from Jan-05- 2007, the date for my interview to GSU in Beijing, he gives me a lot of guildance and help in the past six years. I would like to thank Dr. Ritu Aneja for her great help and suggestions in my research. I would like to deeply thank Dr. Yuan Liu and Dr. Ke Zen for their great help for setting up my life in U.S. and for their patient teaching on science and technique.

I would like to deelply thank Dr. Hans Grossniklus and Dr. Hua Yang for their help on tumor model and training on HE, IHC stainging, Dr. Khan Heckmatayar for trainging me how to use MRI, Dr. Hui Mao, Dr. Lily Yang, Dr. Robert Long, Dr. Qun Zhao, Dr. Hyunki Kim, Dr. Guihua Zhai and Dr. Jason Langley for their help on MRI data collection and analysis, Dr. Chirs Rorden, Dr. Thomas Yankeelov, Dr. Kitajima Hiroumi, Dr. Dinggang Shen and Joonsang Lee for their suggestion on MRI data analysis, Dr. Chalet Tan for the great suggestion on the pharmacokinetics study of ProCA, Dr. George Perice, Dr. Sidny Crow, Dr. Fengkun Du, Trudy, Jennifer Hooder, Yaoyao Liu for large-scale expression and purification of ProCA, Dr. Xiaoping Hu, Dr. William

Thomas Dixon, Dr. Michael Kirberger, Katheryn Lee Meenach, Natalie White and Mattew Cameron for their critical reviews for my manuscripts, Dr. Amy Lee for kindly providing us the plasmid of wild type parvalbumin (PV), Dr. Malty Pagel for his help on exploring CEST effects of ProCA and his great suggestions on my research, Dr. Flask for kindly providing us Eovist, Dr. Micheal Henzl forproviding us protocol of EDTA-agarose preparation and Gwen Spratt for patent.

I would like to thank all of the labmembers from Dr. Yang and Dr. Liu's group for their help. Especially, I deeply thank Dr. Yubin Zhou, Dr. Yun Huang, Dr. Ning Chen, Dr. Jin Zou, Ling Wei, and Dr. Yanyi Chen for their patient trainings and suggestions when I just came to this lab. I would lie to show my deep appriation to our MRI group members Dr. Jingjuan Qiao, Fan Pu, Dr. Jie Jiang, Dr. Lixia Wei, Dr. Shunyi Li, Kendra Hubbard and Rose. We closely work together and help each other to fight for our dream. I would like to thank Dr. Michael Kirberger, Andrina, Dr. Xue Wang, Dr. Shen Tang, Dr. Yusheng Jiang, Wangda Zhou, Chen Zhang, You Zhuo, Jie Feng, Liangwei Li, Juan Zou, Fluorence Reddish, Li Zhang, Anvi Patel, Demesheka Goosby, Bing Xu, Yingwei Zhang, Xiaowei Liu and Ravi Chakra for the help in the past five and half years. My friend Guoxin Fu, Jiang Wu, Hongmei Zhang, Xiaowei Liu and Han Zhang for their great help in my life especially when I was just come the US.

Especially, I would like to thank my deeply loved girl friend Fan Pu, parents Xianglan Hu and Ziwan Xue, my grand parents Yueying Wang and Naishun Xue for their understanding and supports.

TABLE OF CONTENTS

LIST OF TABLES

LIST OF FIGURES

LIST OF ABBREVIATIONS

3D: three-dimensional

3DGE: 3D gradient echo

AIF: arterial input function

ALP: alkaline phosphatase

ALT: alanine transaminase

AST: aspartate transaminase

BSA: bovine serum albumin

CCMV: cowpea chlorotic mottle virus

CD2: cluster of differentiation

CNR: contrast-to-noise ratio

CNS: central nervous system

CT: computed tomography

CV: column volume

Cys: cystein

DD: dipole-dipole

DEC-MRI: dynamic contrast enhanced-MRI

DTPA: diethylene-triamine-pentaacetic acid

EDTA: ethylenediaminetetraacetic acid

EGFR: epidermal growth factor receptor

EGTA: ethylene glycol tetraacetic acid

EnDOR: Electron-nuclear double resonance spectroscopy

FAK: focal adhesion kinase

FDA: U S Food and Drug Administration

fov: field of view

FPLC: fast protein liquid chromatography

FSE: fast spin echo

FSEMS: fast spin echo multi-slices

Gd^{3+}: Gadolinium

Gd-DTPA: gadolinium-diethylene-triamine-pentaacetic acid

GMP: good manufacturing practice

GRF: glomerular filtration rate

GRP: gastrin-releasing peptide

GRPR: gastric-releasing peptide receptor

HER2 or HER2/Neu: human epidermal growth factor receptor 2

ICP-OES: inductively coupled plasma atomic emission spectroscopy

IHC: immunohistochemistry

IPTG: isopropyl β-D-1-thiogalactopyranoside

K_d: dissociation constant

LD_{50}: median lethal dose

LDH: lactate dehydrogenase

LRET: luminescence resounance energy transfer

MEMS: multi-echo-multi-slices

Mn-DPDP: manganese dipyridoxal diphosphate

MRI: magnetic resonance imaging

MVD: mean vascular density

NHS: N-hydroxysuccinimide

NIR: near infared

NMRD: Nuclear Magnetic Relaxation Dispersion

NSF: nephrogenic systemic fibrosis

NTA: nitrilotriacetic acid

OD: optical density

PCR: polymerase chain reaction

PEG: polyethylene glycol

PET: positron emission tomography

PMSF: phenylmethylsulfonyl fluoride

ProCA: protein-based MRI contrast agent

ProCA1.affi: ProCA1 linked with the HER-2 targeting moiety, affibody

ProCA1.GRP 52: ProCA1 with GRP peptide grafted between residues 52 and 53 of ProCA1

ProCA3.bomb or ProCA3.bombesin: ProCA3 linked with bombsin peptide

PV: parvalbumin

R_1: longitudinal relaxation rate

r_1: longitudinal relaxivity

R_2: transverse relaxation rate

r_2: transverse relaxivity

RGD: Arg-Gly-Asp

SBM: Solomon-Bloembergen-Morgan

SC: scalar or contact

SDS-PAGE: sodium dodecyl sulfate polyacrylamide gel electrophoresis

SE: spin echo

SPECT: single-photon emission computed tomography

T_1: longitudinal relaxation time

T_2: transverse relaxation time

TBST: Tris-buffered saline with Tween 20

TE: echo time

TR: repetition time

V_c: initial volume distribution

V_{dss}: steady state phase

VEGF: vascular endothelial growth factor

WT: wild type

ZFS: zero field splitting

ΔK_{obs}: the difference of the decay rates of Tb^{3+} in the presence of H_2O and D_2O

τ: life time

Γ: the radiative decay

1 INTRODUCTION

1.1 MRI and MRI contrast agents

1.1.1 Magnetic resonance imaging

Magnetic resonance imaging (MRI) is a promising imaging technique, which provides three dimensional images of living subjects by exploiting the magnetic properties of water hydrogens and their interactions with an external magnetic field. In addition, MRI is a non-invasive technique and does not require the use of radioactive probes, which significantly reduces the potential of side-effects due to radioactive exposure. In addition to its superior soft tissue contrast, MRI also has high resolution, especially compared to positron emission tomography (PET) and to single-photon emission computed tomography (SPECT). The resolution of preclinical scanner can reach 10 μM or even less. Owing to these advantages, MRI has become one of the most prevalent imaging modalities in clinical and preclinical tests.[1-3] It has wide applicability in diagnosing and following the treatment of different types of cancers and other human diseases including various cardiovascular diseases and disorders of the central nervous system.[4-8]

1.1.2 MRI contrast agents

Compared to PET and SPECT, however, MRI has relatively low sensitivity. To enhance the contrast and sensitivity of imaging, 35% of clinical MRI scans requires the injection of MRI contrast agents.[9] Current MRI contrast agents are based on paramagnetic, ferromagnetic or su-per paramagnetic metal ions. All MRI contrast agents can decrease both longitudinal (T_1) and

transverse (T_2) relaxation times of water protons. MRI contrast agents that can decrease the same level of T_1 and T_2 relaxation times of water protons are called T_1-weighted MRI contrast agents. Contrast agents that cause much shorter T_2 than T_1 are called T_2-weighted contrast agents.[10] T_1-weighted contrast agents are preferred due to their capability of generating brighter contrast. Gadolinium (Gd^{3+}), a lanthanide metal with seven unpaired electrons, long electron spin relaxation time, and high magnetic moment, is one of the most widely used ions in T_1-weighted MRI contrast agents.[11]

1.1.3 Clinical MRI contrast agents

MRI contrast agents increase the difference in contrast between tissues by changing the tissue relaxation time. Since the first MRI contrast agent, gadopentetate dimeglumine, approved in 1987, MRI contrast agents have been successfully applied in the MR imaging of different type of tissue. They have also been successfully applied in diagnostics and characterization of tumors and other diseased tissue where the permeability of the blood vessel is changed, such as infrared, strock, liver fibrosis, neoruon degenerative diseases and so on. These clinical contrast agents are applied to probe abnormal function organs such as liver, kidney, and gall bladder.

In general, currently clinically approved Gd^{3+}-based MRI contrast agents are all formed by one Gd^{3+} encapsulated by organic chelators, such as DTPA or DOTA (Table 1-1). Total 8 nitrogen and oxygen from chelator function as Gd^{3+} binding ligands. In addition, Gd^{3+} in clinical MRI contrast agent has one coordination water molecule, and water molecules robustly interact with Gd^{3+} through the Gd-O interactions. Based on the charge and structures of chelators, current clinically approved Gd^{3+} MRI contrast agents can be divided into four groups: ionic linear

contrast agents (Magnevist, Multihance, Abalavar and Eovist), non-ionic linear contrast agents (Ominiscan and Optimark), ionic cyclic contrast agents (ProHance and Gadovist) and non-ionic cyclic contrast agents (Dotarem). Except Multihance and Eovist, most of the clinical MRI contrast agents function as extracellular contrast agents, are excreted from kidney. These are applied to image the whole body, blood vesculature and central nervous system with great success. Eovist and multihance can be uptaken by the hepatocyte with 50 % and 5 % billiary excretion, respecitvely. These two contrast agents are widely applied for the imaging of liver and billiary diseases, such as hepatocellular carcinoma, PEComa, liver metastases, and liver fibrosis.[12, 13]

With the application of MRI contrast agents, contrast enhanced MRI became one of the best imaging technique for the disease diagnosis. Take the diagnosis of liver metastases as an example. The diagnosis of the liver metastases mainly relies on imaging techinques, such as MRI, CT, untrasound and PET. MRI is the best diagnostic approach for the liver metastases. With the administration of the contrast agents, MRI can detect all of the liver metastases with a size of 2 cm or larger and most of those are 1 -2 cm in size. Although intraceaoprative ultrasound may detect leisions down to 2 mm, such technique requires surgery and can only detect tumors on the surface of the liver.[14] Besides disease diagnosis, clinical MRI contrast agents play critical roles in MRI guilded biopsy and MRI guilded intervention therapy for many types of dieseases, such as prostate cancer and liver cancer.[15]

While having many advantages, current clinical contrast agents have a short half-life time (half-life of approximately 0.5 - 3 minutes in the blood vessels of mice and elimination half life of about 1.5 hours in patients[16, 17]) because of their small molecular mass. If the properties

of MRI contrast agents are optimized, this would lengthen the time window for MRI data collection and eliminate repeated dose injections. Moreover, the number of potential biological targets for molecular imaging could be significantly increased if the detection limits of the contrast agents were improved (~30 μM in mouse skeletal muscle for the contrast agent [Gd(HP-DO3A)(H2O)][18]). All of these factors have driven the need to develop contrast agents with significantly improved relaxivity, optimal retention time, and increased potential targeting capabilities. In my Ph. D. reasearch, we developed a new class of the protein-based MRI contrast agents (ProCAs). I will introduce my research regarding the improvement of relaxivity, blood retention, and molecular imaging with biomarker targeted ProCAs in Chapters 4, 7 and 8.

The toxicity and pharmacokinetics of clinical MRI contrast agents have been well characterized since 1980. A high safety profile has been found in all of these studies. They were also proven to be safer than iodinated contrast agents for CT and x-ray radiography. However, clinical MRI contrast agents require an injection dosage of 0.1 - 0.3 mmol/kg and a local concentration of 100 μM of contrast agent to clearly see contrast differences in tissues. The injection dosage and concentration could be theoretically lower if the longitudinal relaxivity (r_1) of the contrast agents were optimal. Concerns have been raised in renal toxicity caused by release of free Gd^{3+} from the most commonly used contrast agent, gadolinium-diethylene-triamine-pentaacetic acid (Gd-DTPA), with increased reports of nephrogenic systemic fibrosis (NSF), a complication found in patients with end stage renal failure (GRF < 30 ml min^{-1}). [19, 20,21-24]

Table 1-1. Clinical Gd^{3+}-based MRI contrast agent. [25-29]

chemical name	generic name	brand name	r_1^{20} [a]	K_{eq}	Aproval	dosage for body image (mmol/kg)	dosage for CNS image (mmol/kg)	dosage for MR angiography (mmol/kg)	Structure
$[Gd(DTPA)(H_2O)]^{2-}$	gadopentetate dimeglumine	Magnevist	3.8	22.1	USA, EU, Japan	0.1	0.1-0.2	0.1-0.3	
$[Gd(DOTA)(H_2O)]^{-}$	Gadoterate meglumine	Dotarem	3.5	25.8	EU	0.1	0.1-0.3	0.2	
[Gd(DTPA-BMA)(H_2O)]	gadodiamide	Omniscan	3.8	16.9	USA, EU, Japan	0.1-0.3	0.1-0.3	0.1-0.3	
[Gd(HP-DO3A)(H_2O)]	gadoteridol	ProHance	3.7	23.8	USA, EU, Japan	0.1-0.3	0.1-0.3	not approved	
[Gd(DO3A-butrol)(H_2O)]	gadobutrol	Gadovist	3.7	21.8	EU, Canada	not approved	0.1-0.3	0.1-0.3	
[Gd(DTPA-BMEA)(H_2O)]	Gadoversetamide	OpiMARK	4.1	16.6	USA	0.1	0.1	not approved	
$[Gd(BOPTA)(H_2O)]^{2-}$	Gadobenate dimeglumine	MultiHance	4.8	22.6	USA, EU	0.05 (liver)	0.1	not approved	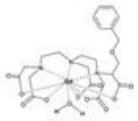
$[Gd(EOB-DTPA)(H_2O]^{2-}$	Gadoxetic acid disodium	Eovist	5.5	23.4	USA, EU	0.025	not approved	not approved	
Diphenylcyclohexyl phosphodiester-Gd-DTPA	gadofosveset trisodium	Ablavar	20 - 45		USA, EU	not approved	not approved	0.003	

1.1.4 Criteria for the design of Gd^{3+} MRI contrast agents

Several factors must be considered for a ideal contrast agent. First, negligible or low toxicity is a prerequisite. The contrast agents should be thermodynamically and kinetically stable, with high binding affinity and metal selectivity to minimize the release of free Gd^{3+}. A high metal selectivity for paramagnetic metal ions against physiological metal ions such as Zn^{2+} and Ca^{2+} is required.[30, 31] Second, high relaxivity, especially for longitudinal relaxivity, is preferred in order to obtain images with high dose efficiency and high contrast-to-noise ratio (CNR). Third, an ideal contrast agent should have proper vascular retention time allowing for imaging of tissue enhancement, gauging tissue blood perfusion, and evaluating changes in capillary integrity. Different strategies have been applied to increase the contrast capability of small chelator based MRI contrast agents. For example, the non-covalent binding of small chelators to plasma proteins, such as albumin (MS-325), greatly increases the relaxivity and blood retention time. On the other hand, the applications of those contrast agents are currently limited to magnetic resonance angiography.[32, 33] A contrast agent with proper excretion time from the body is desired for optimal imaging and reduced toxicity. Molecules that are greater than 7 nm (~ 60 kDa) in diameter are able to pass through the glomeruli. The circulation half-life of the aforementioned molecules, compared to molecules with a hydrodynamic diameter of less than 5 nm, dramatically increases to over 78 minutes in mice, as the molecular weight is larger than 60 kDa.[34-37] Finally, targeting specific molecular entities is greatly desired for increasing the specificity of MRI contrast agents as powerful diagnostic and prognostic tools with the advantage of high spatial resolution. Due to limited expression of biomarkers in the disease region, developing contrast agents with high dose efficiency, low toxicity, optimal

pharmacokinetics, and capability of targeting and permeability are required for robust molecular imaging. A thorough understanding of the relaxivity theory will be beneficial for the development of MRI contrast agents with optimized relaxivity.

1.1.5 Relaxivity theory

Proton relaxivity r_i (in units of $mM^{-1}s^{-1}$) represents the efficiency of a paramagnetic contrast agent to enhance the relaxation rate of water protons. The relaxivity can be defined in Equation (1-1),

$$r_i = \left(\frac{1}{T_{is}} - \frac{1}{T_{ib}}\right) / [Gd^{3+}] \quad i = 1, 2 \tag{1-1}$$

where r_i is the relaxivity, T_{is} is the relaxation time of water protons in the presence of contrast agent with a certain concentration, T_{ib} is the relaxation time of water protons without contrast agent, and $[Gd^{3+}]$ is the concentration of Gd^{3+}. The r_i is composed of the contributions from inner sphere r_i^{IS}, second coordination sphere r_i^{2nd}, and outer sphere r_i^{OS} (Equation 1-2). The r_1^{IS} and r_1^{2nd} can each be defined by varying parameters q, T_{1m}, and τ_m in Equation (1-3),

$$r_i = r_i^{IS} + r_i^{2nd} + r_i^{OS} \quad i = 1, 2 \tag{1-2}$$

$$\frac{1}{T_1} = \frac{P_M q}{T_{1m} + \tau_m} \tag{1-3}$$

where P_M is the mole fraction of metal ion per solvent molecule, q is the number of water molecules bound per metal, T_{1m} is the relaxation time of bound water, and τ_m is the residence time of the bound water (the reciprocal of the water exchange rate, k_{ex}) (Fig. 1-1).

The factors which influence T_{1m} are described by the Solomon-Bloembergen Equation[38-40] (Equations 1-4 to 1-7).

$$\frac{1}{T1m} = \frac{1}{T_1^{DD}} + \frac{1}{T_1^{SC}} \tag{1-4}$$

$$\frac{1}{T_1^{DD}} = \frac{2}{15}\frac{\gamma_I^2 g^2 \mu_B^2}{r_{GdH}^6} S(S+1)(\frac{\mu_0}{4\pi})^2(\frac{7\tau_{c2}}{1+\omega_s^2\tau_{c2}^2} + \frac{3\tau_{c1}}{1+\omega_I^2\tau_{c1}^2}) \tag{1-5}$$

$$\frac{1}{T_1^{SC}} = \frac{2S(S+1)}{3}(\frac{A}{\hbar})^2(\frac{\tau_{e2}}{1+\omega_s^2\tau_{e2}^2}) \tag{1-6}$$

where T_1^{DD} is the relaxation time of bonded water generated by dipole-dipole (DD) mechanism, T_1^{SC} is the relaxation time of bonded water generated by scalar or contact (SC) mechanism, γ_I is the nuclear gyromagnetic ratio, g is the electron g-factor, μ_B is Bohr magneton, μ_0 is permeability of vacuum, S is the spin quantum number of the metal ion, r_{GdH} is the distance between Gd^{3+} and a proton, τ_c is the correlation time, A/ħ is the electron-nuclear hyperfine coupling constant, ω_I is the proton nuclear spin, and ω_s is the electron spin resonance frequency (rad s^{-1}), which is 658-fold of ω_I. Since the contribution of T_1^{DD} is much more pronounced than T_1^{SC} in Gd^{3+}-based MRI contrast agents, the effects of scalar or contact mechanism can be neglected.[41]

To optimize T_{1m} for the design of novel contrast agents, τ_c should be carefully considered. τ_c is a time constant that refers to local magnetic fluctuations. These local magnetic fluctuations are characterized by electronic relaxation time of metal ion (T_{ie}), rotational correlation time of metal water complex (τ_R), and residence time of the bound water (τ_m).

$$\frac{1}{\tau_{ci}} = \frac{1}{\tau_R} + \frac{1}{\tau_m} + \frac{1}{T_{ie}} \quad i=1,2 \tag{1-7}$$

For metal ions with S >1/2, the collision between ions and solvent molecules induces the zero field splitting (ZFS) of the electron spin level. T_{ie} is related to ZFS, which is characterized by the modulation of zero-field-splitting interaction (τ_v) and the mean-square zero-field-splitting energy (Δ^2). As described by Bloembergen, Morgan[42] and McLachlan[43] in Equations (1-8) -(1-10), T_{ie} is governed by the magnetic field, the spin quantum number, τ_v, and Δ^2.

$$\frac{1}{T1e} = 2C\left(\frac{1}{1+\omega_s^2\tau_v^2} + \frac{4}{1+4\omega_s^2\tau_v^2}\right) \quad (1\text{-}8)$$

$$\frac{1}{T2e} = C\left(\frac{5}{1+\omega_s^2\tau_v^2} + \frac{2}{1+4\omega_s^2\tau_v^2} + 3\right) \quad (1\text{-}9)$$

$$C = \frac{1}{50}\Delta^2\tau_v[4S(S+1)-3] \quad (1\text{-}10)$$

T_{ie} is largely determined by the environment of metal ion, which is largely determined by τ_v, and Δ^2. The T_{ie} value in low field (B < 0.1T) is small, and dominates τ_c. For gadolinium based contrast agents, as field strength increases, the electron spin relaxation time increases. τ_R becomes the dominant factor. T_{1e} (electronic longitudinal relaxation time) is about 10 ns and T_{2e} (electronic transverse relaxation time) is 1 ns at 50 MHz in water.[17] Based on our simulation by Equations (1-8)-(1-10) using τ_v=10 ps and $\Delta^2 = 5 \times 10^{19}\ s^{-2}$, the strong magnetic moment of Gd^{3+} gives a T_{1e} value of about 0.5, 2.8, 10.5, 64, and 114 ns at 20, 60, 120, 200, 300, and 400 MHz, respectively.

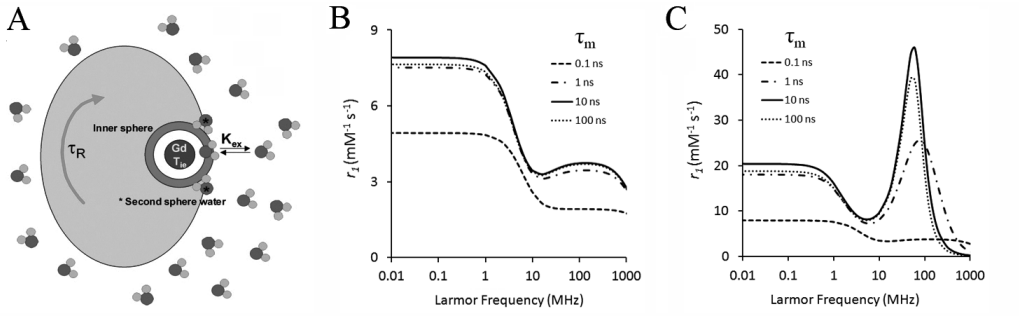

Figure 1-1. Relaxivity theory of Gd^{3+}-based MRI contrast agents.

A. Schematic representation of a Gd^{3+} chelate surrounded by bulk water with one inner sphere and two second sphere water molecules; τ_R refers to the rotational correlation time of the molecule and k_{ex} to the water/proton exchange rate or the reciprocal of residence lifetime of the coordinated water τ_m. Modified after Toth *et al.*[38] B. Simulated magnetic field-dependent relaxivity r_1 of clinical MRI contrast agents based on the given τ_R, τ_m, τ_v, and Δ^2 and Equations (1-3 to 1-10) using combinations of τ_R (100 ps), τ_m (0.1, 1, 10, and 100 ns), τ_v (10 ps), and Δ^2 (5×10^{19} s^{-2}) under a magnetic field strength from 0.01 MHz to 1000 MHz. Clinical MRI contrast agents such as DPTA and other small molecules have τ_R at 100 ps level. Their relaxivity values are shown at the level of 5 mM^{-1} s^{-1}. C. Simulated magnetic field-dependent relaxivity r_1 of macromolecular MRI contrast agents based on the given τ_R, τ_m, τ_v, and Δ^2 and Equations (1-3 to 1-10) using combinations of τ_R (10 ns), τ_m (0.1, 1, 10, and 100 ns), τ_v (10 ps), and Δ^2 (5×10^{19} s^{-2}) under a magnetic field strength from 0.01 MHz to 1000 MHz. Our protein-based MRI contrast agents have a τ_R at 10 ns level, and their relaxivities can be increased to be more than 10- to 20- fold greater than that of clinical MRI contrast agents at the clinical field strengths. This simulation was performed using Solomon-Bloembergen-Morgan (SBM) Equations (Equations 1-3 to 1-10) based on different τ_R (100 ps, and 10 ns), τ_m (0.1, 1, 10, and 100 ns), τ_v (10 ps), and Δ^2 (5×10^{19} s^{-2}).[38-40, 42, 44]

Figs. 1-1B and C show our simulations of the relaxivity as a function of resonance frequency changes based on equations (1-3) through (1-10). Here, we only consider the contribution from the dipole-dipole mechanism. For Gd^{3+}-based MRI contrast agents, the contribution from the scalar or contact mechanism is too small to be considered.[41] For small molecules (Fig. 1-1B), a short τ_R is the major reason for the low relaxivity seen in these contrast agents. Contrast agents based on small chelators such as DTPA have a τ_R of approximately 54 ps at 37 ˚C.[28] This value is much smaller than T_{ie} (T_{1e} is about 2.8 ns at 60 MHz based on simulation) and τ_m (143 ns).[28, 29] According to Equation (1-7), the reciprocal of correlation time, $1/\tau_c$, is described by the three time constants T_{ie}, τ_R, and τ_m. The smallest value of these time constants governs the value of τ_c.[10] Therefore, τ_R determines the value of τ_c, which subsequently determines T_{1m} and thus restricts the relaxivity to values less than 10 $mM^{-1}s^{-1}$, regardless of the adjustment of the other parameters. In order to generate an effective image, a contrast agent concentration of 0.1 mM is needed.[10, 45, 46]

Since τ_R is the limiting factor for r_1 at clinical magnetic field strengths, optimizing τ_R can effectively increase relaxivity. As shown in Figs. 1B and C, when τ_R increases from 100 ps to 10 ns, r_1 increases from 3.7 to 46.1 $mmol^{-1}$ s^{-1} at 60 MHz (τ_m = 10 ns). The theoretical calculation by the Solomon-Bloembergen-Morgan (SBM) Equation shows that the maximum relaxivity, r_1, can be achieved is up to 100 $mM^{-1}s^{-1}$ for Gd^{3+} contrast agents with q=1 and optimized τ_R (around 10 ns) and τ_m. Maximum relaxivity is calculated in a magnetic field strength ranging from 0.5 T to 1.5 T. Outside of this range, the relaxivity is dramatically reduced. With increased application of MRI in higher magnetic field, there is a strong need to develop MRI contrast agents with improved relaxivity in higher magnetic field. Caravan and colleagues[41] show that contrast

agents with τ_R values ranging from 0.5 to 4.6 ns exhibit excellent relaxivity at high magnetic field. Furthermore, according to Helm's[44] simulation, the optimized τ_R decreased to about 1 ns at 3 T and further decreased to less than 1 ns at 9.4 T. Accordingly, the optimized τ_m decreases from about 20 ns at 1.4 T to less than 10 ns at 9.4 T. Increasing the molecular weight of contrast agents by covalently or noncovalently linking Gd^{3+} chelates to large molecules can slow the overall τ_R of the molecule, but this approach does not necessarily increase the local τ_R of the $Gd^{3+-1}H$ vector, and the relaxivity of this class of contrast agents is usually much lower than the expected relaxivity due to internal flexibility and uncontrolled local motion.[10]

Relaxivity can also be enhanced by optimizing τ_m. When τ_m is too small, relaxivity decreases because the coordination water in the complex does not have enough time to be relaxed. On the other hand, if τ_m is too large, the relaxation effects will not be transferred to the solvent effectively.[10] τ_m influences the relaxivity in two ways. In addition to being a component of $1/T_1$ as described by Equation (1-3), τ_m also indirectly contributes to the relaxivity by changing τ_c as described by Equations (1-3 to 1-7). If τ_m is smaller than τ_R and T_{ie}, T_{1m} is governed by τ_m (Equation 1-7). τ_m can be measured by recording the transverse relaxation rate as a function of temperature using O^{17}-NMR or by fitting into the nuclear magnetic resonance dispersion (NMRD) profile.

For macromolecules with a τ_R of around 10 ns, modifying τ_m will significantly change the relaxivity. As shown in Fig. 1-1C at 20 MHz, relaxivity can be increased from < 5 mM^{-1} s^{-1} at a τ_m of 100 ps to ~ 25 mM^{-1} s^{-1} at τ_m of 1 ns, to a maximum of 46 mM^{-1} s^{-1} at τ_m of 10 ns, and then decreased to 39 mM^{-1} s^{-1} at τ_m of 100 ns. According to the simulation by Doble and coworkers, the optimal value of τ_m is 30 and 15 ns in 20 and 60 MHz, respectively.[47] Replacing the

oxygen/nitrogen donors of the aminocarboxylates by oxygen ligands from hydroxypyridinone complex increases the water exchange rate by decreasing the energy differences between eight- and nine- coordinate states, which in turn enhances the relaxivity of the MRI contrast agents.[47-49] The relaxivity of these classes of contrast agents is further increased upon binding to human serum albumin via benzyl derivatives or PEG.[47, 49] A pH responsive contrast agent (GdDOTA-4AmP^{5-}) was developed based on τ_m values that vary in response to pH changes, from a slower inner sphere water exchange (τ_m = 26 μs) at high pH to a faster exchange at low pH due to the protonation of four phosphate groups at the Gd^{3+} binding sites.[50]

The relaxivity enhancement is also associated with r_{GdH}. As shown in Equations (1-4) and (1-5), T_{1m} is also affected significantly by the distance between Gd^{3+} and its coordination water proton (r_{GdH}). $1/T_{1m}$ is a function of $1/r_{GdH}^6$. The reported distance between Gd^{3+} and water proton in the inner sphere of the contrast agent varies between 2.7 to 3.3 Å.[10] However, most of reported r_{GdH} are obtained by fitting NMRD profile in different magnetic fields.[10] Electron-nuclear double resonance (EnDOR) spectroscopy studies demonstrate that r_{GdH} is approximately 3.1 Å for 8- and 9-coordinated Gd^{3+} complex, and r_{GdH} is independent of the ligand type or the total charge.[33, 51, 52]

For small molecules, contributions from the second sphere to the overall relaxivity are usually not significant due to the lack of interface for interactions with water, fast water diffusion, fast molecular tumbling, and longer proton Gd^{3+}-proton distance. However, such contributions cannot be neglected when calculating a macromolecule complex with an optimized τ_c and large interface for water molecule interactions. The Equations to describe the second sphere relaxivity are the same as Equations (3) to (5); the only differences are replacing

water number, correlation time and Gd^{3+}-water distance (r_{GdH}^{2nd}) with values corresponding to the second sphere. According to the simulation at 20 and 60 MHz with r_{GdH}^{2nd} = 5 Å, τ_R = 10 ns, τ_m = 10 ns, and q = 4, the second sphere relaxivity in a protein metal complex could potentially increase to 3.3 and 8.8 mM^{-1} s^{-1}, respectively. A class of small molecules with q = 0 exhibit considerable relaxivity.[53] Such relaxivity can be further enhanced upon binding to albumin.[10, 33] In this case, the second and outer sphere water of this class of molecules were proposed to be influenced by Gd^{3+}.

Although the SBM Equation is widely used to characterize relaxation phenomena, the application of the SBM Equation is subject to several limitations. First, SBM is invalid in low magnetic fields. Electronic spin Hamiltonian is contributed by time dependent Zeeman energy and time independent ZFS energy. The perturbation theory assumption (redfield limit) to the SBM is valid at high field strength, where Zeeman energy is much larger than ZFS energy.[10,44,54, 55] Second, T_{ie} is field dependent and the Equations (1-8) and (1-9) are only valid as monoexponential processes occurring in a very narrow magnetic field range ($\omega_s^2\tau_v^2 << 1$). Outside of this extreme field condition, the electronic relaxation becomes multiexponential.[41, 54, 55] Third, to apply the SBM Equation to macromolecules such as dendrimers and nanoparticles, the overall τ_R can not be equal the τ_R of Gd^{3+}-^{1}H vector. This is because the rotation of Gd^{3+}-^{1}H vector is much more flexible than the macromolecule itself and the relaxivity increase is limited by uncontrolled local motion.[29] Fourth, the relaxivity of Gd^{3+} chelators conjugated to large molecules such as proteins could decrease, since donors present in proteins near the Gd^{3+} location interact with Gd^{3+} to decrease the water number.[56, 57]

As shown from Equation (1-2), the overall relaxivity of contrast agents is composed of

the inner sphere, 2nd sphere and outer sphere relaxivity. In the outer sphere, the interaction between Gd^{3+} and water is only governed by translational diffusion. In principle, macromolecules have a greater potential to tune outer sphere relaxivity because their environments have different solvent accessibility and hydration surface as opposed to small chelators. The contribution of the outer sphere relaxivity to the overall relaxivity is described by the diffusion coefficient of water and the distance to Gd^{3+} using the hard-sphere model (Equation 1-11 to 1-13).[58-60]

$$\frac{1}{T_1}=\left(\frac{32\pi}{405}\right)\gamma_I^2\gamma_S^2\hbar^2\left(\frac{\mu_0}{4\pi}\right)^2 S(S+1)\frac{N_A[M]}{aD}\left[3j(\omega_I)+7j(\omega_s)\right] \tag{1-11}$$

$$j(\omega)=\mathrm{Re}\left\{\frac{1+\frac{1}{4}\left(i\omega\tau_D+\frac{\tau_D}{T_{ie}}\right)^{1/2}}{1+\left(i\omega\tau_D+\frac{\tau_D}{T_{ie}}\right)^{1/2}+\frac{4}{9}\left(i\omega\tau_D+\frac{\tau_D}{T_{ie}}\right)+\frac{1}{9}\left(i\omega\tau_D+\frac{\tau_D}{T_{ie}}\right)^{3/2}}\right\} \quad i=1,\ 2 \tag{1-12}$$

$$\tau_D=\frac{a^2}{D} \tag{1-13}$$

Where N_A is Avogadro's number, ħ is the Dirac constant, [M] is the concentration of the metal ion, a is the distance of closet approach between water and Gd complex, D is the sum of the diffusion constant of solvent proton and Gd-complex. τ_D is the diffusion correlation time, j(ω) is the spectral density function, Re stands for "the real part of".

Due to the contribution of outer sphere relaxivity, some contrast agents with no inner-sphere water molecules also have high relaxivity. $Gd(C_{11}\text{-DOTP})^{5-}$ is a $Gd\text{-DOPT}^{5-}$ derivative with q = 0. $Gd(C_{11}\text{-DOTP})^{5-}$ has an overall r_1 relaxivity about 4.6 $mM^{-1}\ s^{-1}$ at 20 MHz at 25 ˚C, which

dramatically increase to 23 mM^{-1} s^{-1} when it binds to albumin. The NMRD of this contrast agent fits well with outer-sphere relaxivity theory for q = 0 complex with rapid outer sphere water exchange, indicating that the outer-sphere water plays a critical role on the relaxivity of Gd(C_{11}-DOTP)$^{5-}$ and albumin-Gd(C_{11}-DOTP)$^{5-}$ complex.[61]

1.2 Current progress in development of Gd^{3+} MRI contrast agents with improved relaxivity

1.2.1 Application of Gd^{3+} labeled protein as MRI contrast agents

The relaxivity of clinical contrast agents, such as Gd-DTPA, is not optimized, which requires high injection dosage. Gd^{3+} is labeled to proteins with improved imaging capabilities. Two strategies were used to label proteins with Gd^{3+}: (1) covalent or noncovalent conjugation of Gd^{3+}-chelates to proteins; (2) directly designing Gd^{3+} binding pockets on the protein (the protein itself serves as a chelator). The first strategy has been extensively studied to develop MRI contrast agents. Some Gd^{3+} chelates were designed to noncovalently interact with proteins, which dramatically changes the relaxivity and distribution of Gd^{3+} chelates.[32, 33] In addition, proteins, such as albumin, were directly reacted with DTPA-dianhydride and the DTPA-proterin complex and then loaded with Gd^{3+}.[62] Gd^{3+}-labeled albumin has been applied to many preclinical studies, such as evaluating tumor permeability and angiogenesis by dynamic contrast enhanced MR imaging of cancer tissue, and monitoring the changes of tumor vasculature.[63, 64] Dr. Meade and colleagues developed a class of biodegradable contrast agents based on conjugation of evenly distributed lysine residues on protein polymers to Gd-chelates. By optimizing the polymer length and lysine distribution, an r_1 of 14 mM^{-1} s^{-1} per Gd^{3+} and 461 mM^{-1} s^{-1} per particle (60 MHz and 37 ˚C) was achieved. Interestingly, these contrast agents can

be degraded by plasmin, which facilitates fast excretion *in vivo*.[65]

Since it is not an easy task to build a Gd^{3+} binding site on a protein with high Gd^{3+} binding affinity, only a few groups use strategy (2) to label Gd^{3+} to proteins. In this strategy, protein functions as chelater to interact Gd^{3+} and the key parameters that govern relaxivity can be optimized by protein design. The design and application of this class of contrast agents will be introduced in section 1.3 and 1.4.

1.2.2 Current progress to improve the relaxivity of the contrast agents

Since relaxivity is a key determinant for dose efficiency of MRI contrast agents, several strategies have been applied to improve the relaxivity. One of the most used strategies currently is to increase τ_R, since the τ_R of small contrast agents is on the order of 100 ps, which is the limiting factor to increasing the relaxivity (Fig. 1-1B and C). Meade and coworkers have conjugated three to seven DOTA-Gd-alkyne complexes to azide to form a triazole ring with constrained local rotation of the Gd^{3+} complex. They found that the relaxivity of DOTA-Gd-alkyne increases along with molecular size and restricted rotation of Gd(III) chelates. Gd-DOTA-alkyne derivative with one Gd^{3+} has a relaxivity of 3.2 $mmol^{-1} s^{-1}$ (at 60 MHz 37 ˚C). The per Gd^{3+} relaxivity with seven Gd-DOTA complex increases up to 12.2 $mM^{-1} s^{-1}$ at 60 MHz 37 ˚C.[66]

Since τ_R increases with expanding molecular weight, macromolecular-based contrast agents have been generated either by covalent binding of small monomeric agents or by non-covalent binding to macromolecules such as proteins (e.g. serum albumin) and polylysine with an observed increase in relaxivity (Table 1-2).[67-73] Nanosized candidates, such as dendrimers, micelles, liposomes, nanoparticle emulsion, lipid nanoparticles, viral capsid, and nanotubes (Table 1-2), have been conjugated with chelators such as DTPA or DOTA. Due to the increase in

molecular size, the per Gd^{3+} relaxivities of these contrast agents are increased several folds compared with current clinical contrast agents. Although the relaxivity values are much lower than the theoretical upper limit, the per particle relaxivity can be extremely high due to high amount of Gd^{3+} conjugation. For example, the per Gd^{3+} relaxivity of emulsion is 10.8 $mM^{-1} s^{-1}$ at 60 MHz, which is approximately three-fold higher than that of Gd-DTPA. Raymond's group conjugates gadolinium chelates to the interior and exterior surfaces of MS2 viral capsids which leads to a peak relaxivity of 41.6 $mM^{-1} s^{-1}$ at 30 MHz[74].

Unfortunately, it is not an easy task to optimize τ_R and τ_m for macromolecular-based contrast agents, as the macromolecular contrast agents face several limitations. First, the local motion of the $Gd^{3+-1}H$ vector is hard to optimize due to the flexible spacer between the carrier and the contrast agent. In addition, since r_1 decreases when $\omega^2\tau_c^2 > 1$ (Equations 1-3 to 1-7), macromolecular contrast agents, such as nanoparticles that have a large τ_R, may exhibit a sharp drop in relaxivity at high magnetic field. Moreover, as our simulation shows in Fig. 1-1C, when macromolecules have optimized τ_R value (in range of 10 ns) in clinical magnetic fields, τ_m often becomes the limiting factor to significantly increasing the relaxivity. Macromolecule contrast agents face an additional size limitation because increased size results in low permeability in *in vivo* applications. Furthermore, the size and charge differences in these high payload MRI contrast agents could influence blood distribution, which could potentially lower the efficient delivery of the contrast agents to the desired targeting site.

Tight noncovalent aggregation between small Gd^{3+} contrast agents with protein derivatives can yield significantly higher relaxivity due to decreased local motion and increased τ_R.[33] Binding to albumin, a 65 kDa protein in the serum, increases τ_R of MS-325, and consequently

increases the relaxivity of MS-325 from 6.9 to 42 mM^{-1} s^{-1} at 20 MHz 37 ˚C.[75] Binding to albumin also increases the blood circulation of MS-325. Recently, several responsive contrast agents have been developed based on τ_R values that vary with a change in relaxivity due to either metabolite[76] or zinc-triggered binding of small chelators to albumin.[77] Proton relaxivity can also be increased by decreasing the internal motion of the contrast agents through multilocus binding.[78] Caravan points out that targeting contrast agents to other proteins could potentially increase relaxivity by decreasing τ_R. For example, the relaxivity of EP-2104R, a fibrin-specific contrast agent with four Gd-DOTA molecules conjugated to a fibrin targeting peptide, increases from 10.1 mM^{-1} s^{1} at 60 MHz 37 ˚C in TBS buffer to 17.8 mM^{-1} s^{-1} in clotted plasma at 60 MHz 37˚C.[79] Similarly, collagen targeted contrast agent, EP-3533[80], exhibits a comparable r_1 increase in the presence of plasma.

According to Equation 1-3, increasing q should significantly shorten the relaxation time of water protons and result in a higher relaxivity. However, increasing q for small chelators may decrease the stability of the metal chelator complex because of the risk of free Gd^{3+} release. Tweedle suggests that Gd^{3+} deposit in bones is correlated with instability of gadolinium contrast agents.[21, 81, 82] In addition, when q increases from 1 to 2, Gd^{3+} has greater solvent accessibility and is able to interact with anions[56, 57] which decreases the relaxivity. Therefore, most of the clinically approved contrast agents, except for ProHance with q = 1.3,[81] have an inner sphere q value equal to 1.

Recently, Raymond's group designed a series of contrast agents using hydroxypyridinone class compounds with increased q values. When q is equal to 2, r_1 is increased to approximately 9 mM^{-1} s^{-1} at 20 MHz 25 ˚C.[45, 47-49, 83, 84] When q is equal to 3, the

relaxivity is further increased up to 13.1 mM^{-1} s^{-1} at 20 MHz 25 ˚C. Interestingly, their primary stability constant pGd value is 18.7, which is similar to the stability constant of clinical contrast agents.[85] However, the design of Gd^{3+} binding proteins with desired change of water coordination number is not reported. I will introduce my research on the optimization of relaxivity and metal stability of ProCA3 variants by manupulating of water number at the coordination shell (Chapter 4).

Table 1-2. The relaxivity of typical Gd3+- based MRI contrast agents. [61, 62, 72, 77, 78, 84-102]

CA class	Compounds	r_1 ($mM^{-1} s^{-1}$)	r_2 ($mM^{-1} s^{-1}$)	B_0 (T)
Designed proteins	CA1	117	129	1.5
Small compound	Gd-DTPA	5.4	8	1.5
	Pyridine-N-oxide Analogues	4.54		0.47
HOPO derivatives	Gd-TREN-1,2-HOPO	10.5		0.47
	Gd-TACN-3,2-HOPO	13.1		0.47
Cell-permeable CAs	Gd^{3+}-DTPA-Arg_8	7.8		1.5
Linear polymer	Gd4(H2O)	4.5		9.4
Dendrimers	Gadomer-17	13		1.5
Protein carriers	Albumin	11.5	12.4	0.25
	Poly-lysine	13	15	0.47
	protein polymer contrast agents	14		1.5
	High-density lipoprotein	41	55	0.47
Multimeric CAs		12.2		1.5
Targeting peptide conguated CAs	EP-2104	24.9		0.47
		17.8	27.7	1.5
	EP-3533	27.9		0.47
		15.6	32.5	1.5
	EP-1084	27.7		0.47
Liposome	ACPL	12	11	1.5
porous polymersomes	porous polymersomes	7.2		1.5
Nanoglobular MRI CAs	G3 nanoglobular MRI CA	10.0		3
Nanoparticle emulsion	Gd-perfluorocarbon nanoparticles	34	50	1.5
Ca^{2+}-protein	α-lactalbumin	4.2	5	3
Nanoassembled Capsules	NACs	24		0.54
Gold Nanoparticles	Au@DTDTPA-Gdx	4.1		7
	Y-DtNP	~60		0.7
Lipid Nanoparticles	GdDOTA(GAC12)2	40		0.47
Hydroxypyridonate Viral capsid conjugates	Gd-TREN-bis-HOPO-TAM-CO2H	41.6		0.7
Dendrimer Nanoclusters	dendrimer nanoclusters	12.3		1.5
Trimetallic Nitride Metallofullerene CA	$Gd_3N@C_{80}[DiPEG(OH)_x]$	79		2.4
Nanodiamond	Nanodiamond	58.82		1.5
Paramagnetic nanoparticles	$Gd@C_{82}(OH)_{22\pm2}$	61.1		4.7

1.3 DESIGN OF PROTEIN-BASED MRI CONTRAST AGENTS WITH HIGH RELAXIVITY

1.3.1 Choice of protein as a scaffold for designing MRI contrast agents

We have developed a class of novel MRI contrast agents with high relaxivity using proteins as a scaffold. Our design of protein-based contrast agents (ProCAs) is based on several considerations in addition to the above discussion about relaxivity theory. First, proteins are biocompatible materials that are advantageous for *in vivo* applications. There are many protein drugs such as insulin that have been successfully applied against human diseases.[86] Second, some well-folded proteins have a proper size which allows for good circulation time and tissue penetration. A well-packed globular protein with molecular weight of 10 - 14 kDa has a size of 2 - 3 nm that can be easily excreted from the kidneys. Third, through numerous efforts, we have developed computational and protein engineering strategies to design metal binding sites in proteins with high coordination and strong metal binding properties. Fourth, the structural and dynamic properties of some proteins have been well studied by various methods, especially high resolution NMR. These properties are essential for designing Gd^{3+}-MRI contrast agents with desired metal binding and relaxation properties. Fifth, once the high relaxivity and metal binding affinity have been achieved, it is relatively simple and straightforward to extend the applications to targeted contrast agents with the addition of targeting moieties for various disease biomarkers by protein modification. Sixth, current advances in biotechnology and pharmacology facilities make it feasible to produce a large number of protein agents for preclinical and clinic needs.

1.3.2 Design of MRI contrast agents using CD2 as a scaffold

Based on our hypothesis that an MRI contrast agent with high relaxivity, high dose efficiency and strong metal binding affinity can be achieved by designing Gd^{3+} binding sites into a scaffold protein with desired metal binding properties and relaxation parameters such as q, τ_m and τ_R, we have chosen domain 1 of the cell adhesion protein, CD2, as a scaffold protein to host Gd^{3+}-binding sites. Domain 1 of CD2 is a small (99 amino acid) well packed beta-sheet protein with a popular Ig fold. It has a rotational correlation time value of ~ 10 - 30 ns[87] which matches the optimal relaxivity for the current clinically allowed magnetic field strength. It has a size of about 2.5 nm with good circulation and tissue penetration.[88] In addition, we have successfully designed several calcium binding sites with similar coordination properties to Gd^{3+} using our developed computational methods and established structural parameters describing the common properties of Ca^{2+} and Ln^{3+} binding sites.[89-97] Further, we have determined the NMR structure of one of the CD2 variants and demonstrated that it has the desired metal binding geometric properties. These unique factors make CD2 one of the best candidates for the design of protein-based MRI contrast agents.

The design of Gd^{3+} binding sites is based on our analysis of metal binding sites in over 500 small chelators and metal proteins. Gd^{3+}, Tb^{3+} and Ln^{3+} have coordination similar to Ca^{2+} with a strong preference for oxygen ligands. Although small molecules such as DTPA use both oxygen and nitrogen as ligands, proteins almost always use oxygen as a ligand with an average number of 7.2 for Ln^{3+}.[98] For example, oxygen ligands from the side chain oxygens of Glu15, Glu56, Asp 58, Asp62 and Asp64 are used at different stretches of the protein sequence. One position of metal geometry is left open to allow fast water exchange between solvent and

metal (Fig. 1-2). We reasoned that an embedded metal binding site without internal flexibility is the key to achieving high relaxivity. As a comparison, we have also created a metal binding site with high flexibility by inserting a Gd^{3+} binding loop between positions 52 and 53 with flexible linkers between them, named CA9.CD2.

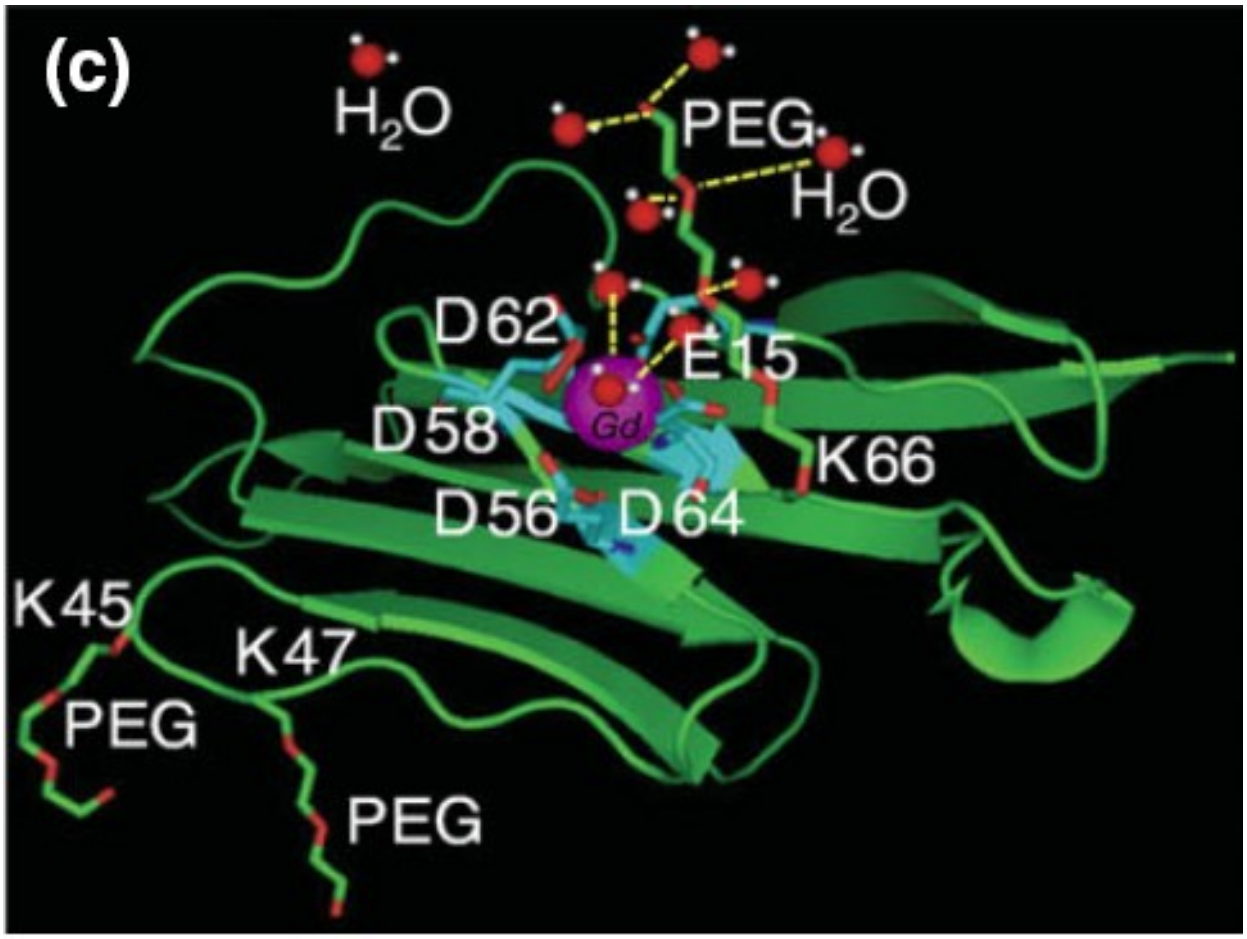

Figure 1-2. A carton demonstration of ProCA1 with PEG modifications.

Oxygen ligands from the side chain of Glu15, Glu56, Asp 58, Asp62 and Asp64 are used at different stretches of the protein sequence. One position of metal geometry is left open to allow fast water exchange between solvent and metal. Adapted with permission from referernce[99].

The relaxivity values of the designed contrast agents are determined at 1.5, 3 and 9.4 T. As shown in Table 1-2, the designed contrast agent ProCA1, previously named CD2.CA1, exhibits per Gd^{3+} r_1 relaxivity up to 117 mM^{-1} s^{-1} at 1.5 T 25 ˚C, a more than 20-fold increase compared to that of Gd-DTPA. This is very important since it allows a significantly lower local concentration of Gd^{3+} (~ 0.69 μM) for high resolution imaging.

1.3.3 Factors contributing to high relaxivity in ProCAs

Several factors such as correlation time and inner, second, and outer sphere water number contribute to the significantly increased relaxivity in ProCAs compared to small molecular-based contrast agents.

Optimized correlation time is one of the major reasons for the significantly increased relaxivity of ProCAs. As shown in Equations (3)-(10) and Fig. 1-1C, a protein contrast agent with τ_R of ~ 10 ns has near optimal relaxivity value at clinically relevant magnetic field strength (1.4 T). We have applied high resolution NMR to probe the dynamic properties of our designed protein contrast agents.[87, 100] Consistent with other proteins of similar size, the τ_c of protein MRI contrast agents is 9.08 ns in the presence of metal and 9.20 ns in the absence of metal. The dynamic NMR experiments suggest that the metal binding pocket of the protein contrast agents rotates along with the scaffold protein as a rigid complex. In contrast, the relaxivity of CA9.CD2 is much lower than ProCA1(r_1 = 3.5 mM^{-1} s^{-1} at 3 T 25 °C), in which the Gd^{3+} binding site is linked by flexible linkers and the estimated τ_c of the flexible metal binding site is 3.04 ns.

Water number is also optimized in the protein-based MRI contrast agents. As shown in Equation (3), the relaxivity of the contrast agents is directly related to q. The relaxivity of the

contrast agent can be increased when more water molecules can interact with Gd^{3+} at the same time. An enzyme responsive contrast agent, Egad, inhibits water access to Gd^{3+} (q = 0) by appending a galactopyranose moiety to a Gd-DO3A chelate. In response to galactosidase activation, galactopyranose sugar is cleaved from Gd^{3+}, and the Gd^{3+} is exposed to water proton. After enzyme cleavage, q increased from 0.7 to 1.2[101] and the r_1 increased from 0.903 mM^{-1} s^{-1} to 2.72 mM^{-1} s^{-1} accordingly.[102] Using the luminescence lifetime of Tb^{3+}, we have shown that the water number of protein contrast agent ProCA1 is 2.1.[103] An increase of the water number q will increase the relaxivity (Equation 3). In addition, proteins with large molecular surfaces may have additional contributions from 2nd sphere relaxivity that could reach 3.3 and 8.8 mM^{-1} s^{-1} at 20 and 60 MHz, respectively (τ_R = 10 ns, τ_m = 10 ns, q = 4, r_{GdH} = 5 Å). Taken together, it is likely that coordination water from the inner, second, and outer spheres of ProCA1 may all contribute to the dramatic increase of relaxivity of ProCA1.

The success in the design of the first generation ProCA, named ProCA1 opens a new avenue to significantly increase relaxivity. However, clinical application of contrast agents also requires strong metal binding stability and high payload if possible. In this dissertation, we will report our design of a new generation of the ProCAs, named ProCA3 variants. This new generation of the ProCAs has multiple Gd^{3+} binding sites in one scaffold protein with improved stablitity, solubility, and pharmacokinetics. The design of the ProCA3 variants will be discussed in Chapter 3.

1.4 *IN VITRO* AND *IN VIVO* PROPERTIES OF PROTEIN-BASED MRI CONTRAST AGENTS

1.4.1 Thermodynamic and conditional stability of MRI contrast agents

Long term toxicity of the contrast agents is caused mainly by the toxic systemic effects of Gd^{3+} and free chelators (the LD_{50} of Gd^{3+} is 0.2-0.3 mmol/kg and the LD_{50} of Na_3Ca-DTPA is 5 mmol/kg).[104] Gd^{3+} has an ionic radius of 0.99 Å, which is very similar to the ionic radius of Ca^{2+}. Therefore, free Gd^{3+} is likely to compete with Ca^{2+} in the biological system and cause further interference with the Ca^{2+} signaling pathway by interacting with calcium binding proteins such as calcium sensing receptor,[105] Ca-ATPase,[106] and voltage-gated calcium channels.[107]

The metal stability of contrast agents to Gd^{3+} often is characterized by the thermodynamic stability, the conditional stability, and the kinetic stability. Since Gd^{3+}-based contrast agents are used in medical diagnosis, it is extremely important that Gd^{3+} and chelators remain in complex *in vivo*, and that they exhibit high metal binding stability and selectivity. Thermodynamic stability can be described by Equations (1-14) and (1-15),

$$Gd + L \leftrightarrow GdL \tag{1-14}$$

$$K_{ML} = \frac{[GdL]}{[Gd] \times [L]} \tag{1-15}$$

where K_{ML} is thermodynamic stability constant, [GdL] is the concentration of metal ligand complex and [Gd] and [L] are the concentrations of free Gd^{3+} and ligand in the solvent. Clinical MRI contrast agents have thermodynamic stability constants ranging from 16.6-25.8 (log K_{ML}) (Table 1). ProCA3, a new generation of contrast agents with two Gd^{3+} binding sites, has a thermodynamic stability constant of 21.6, which is greater than Gd-DTPA-BMA (log K_{ML}= 16.6)

(Xue et al., unpublished data). The conditional stability constant characterizes the stability of the metal-chelator complex at physiological pH, which considers protonation of the chelator at pH 7.4.[81] To assess the metal binding affinity and selectivity of ProCAs, we have applied several spectroscopic methods such as dye competition and Tb^{3+}-sensitized energy transfer. ProCA1 has a metal selectivity for Gd^{3+} over physiological metal ions (log (K_{Gd}/K_{Ca}) > 9.84, log (K_{Gd}/K_{Mg}) > 10.06, log (K_{Gd}/K_{Zn}) = 5.34). Although the Gd^{3+} binding constant (log K_a) for ProCA1 is weaker than DTPA, the metal selectivities of ProCA1 for Gd^{3+} over Zn^{2+} and Mg^{2+} are 2.4 fold and 1.3 fold greater than Gd-DTPA (log (K_{Gd}/K_{Mg}) = 4.25, log (K_{Gd}/K_{Zn}) = 4.17). The ProCA1 metal selectivity values of Gd^{3+} over Ca^{2+} are comparable to Gd-DTPA (log (K_{Gd}/K_{Ca}) = 11.70).[103] We further assessed the stability of Gd^{3+} binding under conditions mimicking the extracellular environment and the effect of other biological metal ions on the relaxivities of ProCAs. The relaxivities (r_1 and r_2) of ProCAs were not significantly affected in the presence of up to 10 mM excess Ca^{2+}, supporting the strong stability and metal selectivity for the Gd^{3+}-protein complex.[103]

It is worth pointing out that achieving unprecedentedly strong metal stability and selectivity of our designed Gd^{3+}-protein, significantly greater than those of a few reported peptides or designed protein-based complexes, is not a trivial achievement because of *in vivo* applications. For example, a peptide fragment encompassing an EF-hand calcium binding loop and a DNA-HTH motif was designed with a thermodynamic stability constant of 5.2 and *r1* relaxivity of 21.2 mM^{-1} s^{-1} at 60 MHz 37 ˚C.[108] A thermodynamic stability constant of 7.1 was reported for metal binding to a genetically engineered subunit of cowpea chlorotic mottle virus (CCMV) capsid with r_1 relaxivity of up to 210 mM^{-1} s^{-1} per particle at 61 MHz 23˚C.[109] Clearly,

significant improvement of Gd^{3+} binding affinity is a prerequisite for *in vivo* application.

Due to the unique nature of proteins, traditional methods such as pH titration[110] can not be applied to determine metal stability of protein contrast agents. To address such need, I have developed a series of analitical methods to determine and evaluate the metal binding affinity and metal selectivity of developed protein contrast agents. In addition, we dementrate that one of the ProCA3 variants, ProCA32, has a high Gd^{3+} affinity less than 10^{-21} M and high metal selectivity. This part of work will be discussed in Chapter 4.

1.4.2 The kinetic stability and metal selectivity of MRI contrast agents

Metalloproteins plays essential roles in the biological system. Ca^{2+} binding proteins play varity roles on cell proliferation, migration, protein-protein interaction, protease activation, signal transduction, immunoresponses et al.,.[111-124] Metaloproteins such as Ca^{2+}- and Zn^{2+}-binding proteins could potentially interact with free Gd^{3+} released from contrast agents *in vivo*. Blood plasma and interstitial fluid contain multiple ions such as Ca^{2+} and Zn^{2+} that can potentially compete with Gd^{3+} in the contrast agent to release free Gd^{3+}. High concentrations of phosphate (0.6 M) and bicarbonate (0.36 M) in the biological system form a precipitant with free Gd^{3+}, which in turn further drives the disassociation of Gd^{3+} from the metal contrast agent complex. The rate of this dissociation process is determined by the kinetic stability properties of the contrast agents; contrast agents with high kinetic stability will release less Gd^{3+} per unit time.[125] To evaluate the kinetic stability, the dissociation rate of the Gd^{3+} from the complex is usually measured at pH=1, at which the dissociation rate of a contrast agent is significantly increased compared with physiological pH. Generally, linear contrast agents have higher dissociation rates or lower kinetic stability than cyclic contrast agents. Among these approved

contrast agents, Gd-DTPA-BMA has the lowest kinetic stability, while Gd-DOTA has highest kinetic stability. Wedeking et al.,[126] show that the dissociation rate of the Gd-chelator complex correlates well with the Gd^{3+} retention in mice 14 days after injection of these Gd^{3+} chelates.

1.4.3 Transmetallation studies of MRI contrast agents

The transmetallation of Gd^{3+} chelates by physiological ions such as Fe^{3+}, Cu^{2+}, and Zn^{2+} must also be considered in the development of the contrast agents. Laurent et al., applied the relaxometric protocols to compare the transmetallation of the approved contrast agents (2.5 mM) in the presence of 2.5 mM Zn^{2+} in the phosphate buffer. Highest kinetic stability was observed for Gd-DOTA.[127] Frenzel et al.,[128] further tested the kinetic profile of Gd^{3+} dissociation of Gd^{3+}-based MRI contrast agents in serum for up to 15 days using coupled HPLC-ICP-MS. Nonionic linear contrast agents, such as Gd-DTPA-BMA, show 10 times higher Gd^{3+} release than that of ionic linear contrast agents, such as Gd-DTPA. In contrast, no free Gd^{3+} release is detected from macrocyclic contrast agents, such as Gd-DOTA.[128] All this data indicates cyclic contrast agents have increased kinetic stability compared to linear contrast agents.

1.4.4 Acute and chronic toxicity study on MRI contrast agents

The physiological deposit sites of Gd^{3+} are in bone, lung, and liver. Gd^{3+} retention in bone correlates directly with the dissociation rate of the contrast agents. Tweedle et al., compared the Gd^{3+} retention in mice 14 days post injection of Gd^{3+} chelates with different dissociation rate. Mice injected with Gd-DTPA-BMA or Gd-NP-DO3A showed much higher Gd^{3+} accumulation in the whole body, especially in bone and liver, than that of the mice injected with Gd-DOTA or Gd-HP-DO3A.[126] Gibby et al., analyzed Gd^{3+} concentration in the bones of hip

replacement patients after injection of 0.1 mmol/kg Gd-HP-DO3A or 0.1 mmol/kg Gd-DTPA-BMA. Their findings indicated that Gd^{3+} retention was 1.77 μg Gd/g bone for Gd-DTPA-BMA and 0.447 μg Gd/g bone for Gd-HP-DO3A, revealed by ICP-AES.[82] The dissociation of the contrast agents, especially in patients with preexisting kidney conditions, is proposed to trigger NSF. Recent biopsies of NSF patients found insoluble Gd^{3+}-phosphate deposits in the skin.[129] The long term fate of internalized paramagnetic liposomes is well characterized by Kok et al., The distribution and relaxivity of the contrast agents were tracked for five days after internalization. Both r_1 and r_2 of the contrast agents were much lower than the starting r_1 and r_2, due to the gradual dissociation of Gd^{3+} from the contrast agents and interaction with intracellular anions such as phosphate and Zn^{2+} to form precipitates.[130]

The acute toxicity of contrast agents was studied in our laboratory with cytotoxicity and blood enzyme tests. The cytotoxicity of designed proteins was examined with cell lines SW620, SW480 and HEK293, using the MTT assay.[131, 132] A slight decrease in viability was observed in HEK293 cells treated with CD2 and ProCA1 protein. No cytotoxicity was observed in all tested cells treated with designed proteins and concentrations up to 50 μM. In addition, the acute toxicity, measured with liver enzymes (ALT, ALP, AST, LDH), urea nitrogen, bilirubin, and total protein from CD1 mice 48 hours post tail veil injection of 4 μmol/kg ProCA1, was found to be negligible compared to control subjects (CD-1 mice). [103]

Long term toxicity can also be caused by immunogenicity towards contrast agents. To test the immune response to ProCA1 and PEGylated ProCA1, they were injected into a rabbit and ProCA1 was found to illicit a weak antibody production shown with rabbit antiserum, magnified with the addition of adjuvant. Injection of PEGylated ProCA1 with adjuvant produced

an even weaker antibody production compared with ProCA1 without adjuvant, as shown by ELISA. No significant immuno-responses were observed without using adjuvant. The results suggest that the protein MRI contrast agents do not generate strong immune-responses in rabbits.[99]

The serum stability test is useful for screen unstable compounds *in vitro*. To test the resistance to enzymatic cleavage, we have analyzed the serum stability of designed proteins by incubating the designed proteins in complex with an equal concentration of $GdCl_3$ in human serum at 37 ˚C. The degradation of the protein was analyzed by both SDS-PAGE and MALDI mass spectrometry. The results showed that the protein remained intact for at least 48 hours in the absence of serum as well as in the presence of 70% human serum following the 48 hour incubation.[103] Although great achievement has been made in the design of protein based MRI contrast agents with good acute toxicity safety profile, the long term Gd^{3+} retention and pharmacokinetics of ProCAs have not been well studied in detail. In Chapter 7, I will introduce my researches on the biodistribution, pharmacokinetics and toxicity study of ProCAs variants.

1.5 *In vivo* MR image enhancement by the developed protein contrast agents

After tail vein injection of 2.4 μmol Gd^{3+}/kg ProCA1, which is about 40-fold lower than the dosage of Gd-DTPA used in diagnostic imaging, we observed the MRI contrast enhancement in several organs of CD^{-1} mice at 3 T, 4.7 T and 9.4 T. The T_1 contrast enhancement in the kidney cortex diminished substantially 18 h after the administration of Gd^{3+}-CA1.CD2.[103] To further increase the contrast capability, protein-based MRI contrast agents with four and two Gd^{3+} binding sites in a single protein, were engineered, expressed and characterized (denoted as

ProCA2 and ProCA3, respectively). Fig. 1-3 shows that tail vein injection of 0.02 mmol/kg ProCA3 (~10-fold lower dosage (0.02 mmol/kg) than that of Gd-DTPA (0.2 mmol/kg)) resulted in an enhancement of blood, liver and kidney 50 minutes post-injection at 4.7 T. The blood circulation time was much longer than small molecule contrast agents, which indicates that ProCA3 could be potentially used as a blood pool contrast agent. The enhancement of liver and kidney completely disappeared two days after injection.[103]

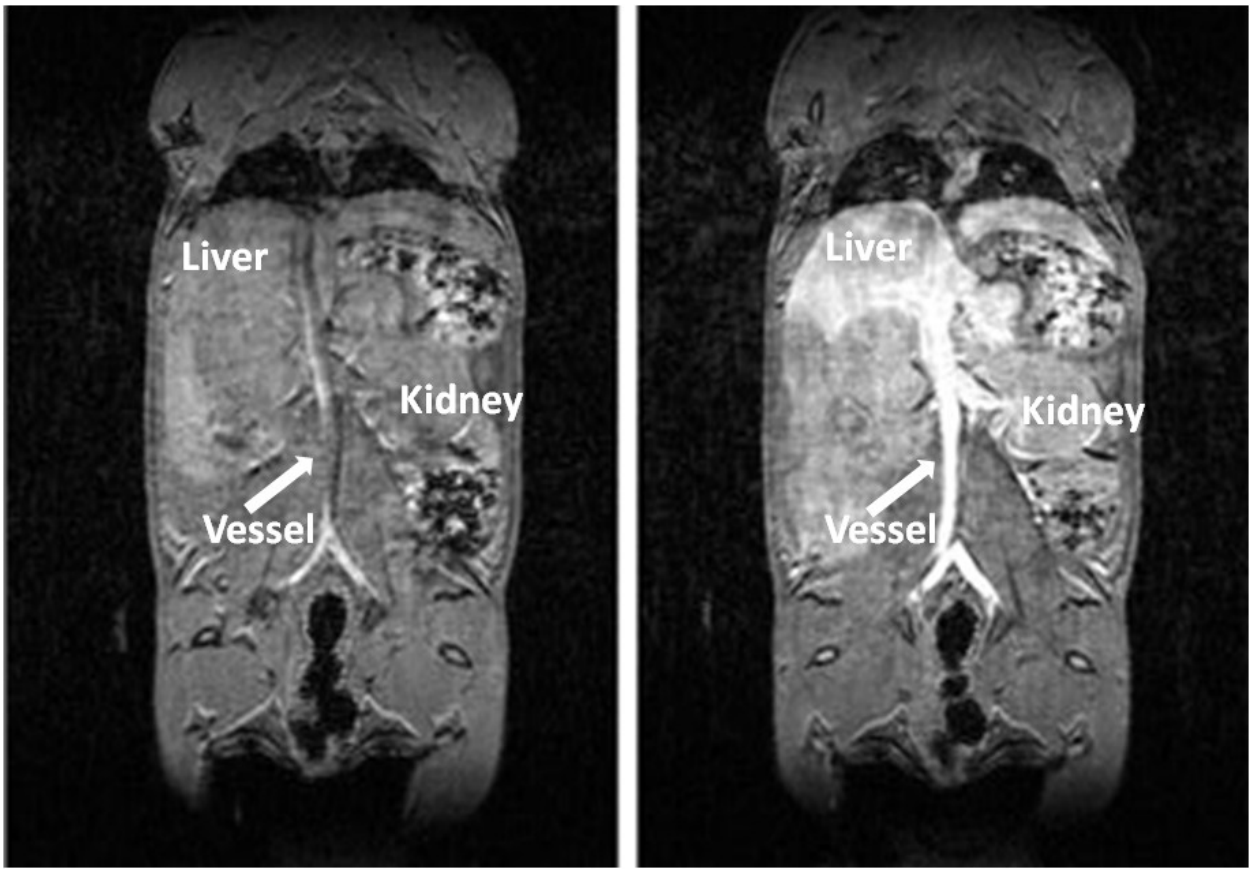

Figure 1-3. Mouse MR imaging before (left) and after injection of modified ProCA3 for 50 min (right).

0.02 mmol/kg of ProCA3 was injected into the anaesthetized CD1 mouse via tail vein. The mouse was scanned before injection (left) and 44 min post injection (right). MR imaging were generated under 4.7 T magnetic fields with TR =40 ms and TE=2.9 ms. After inject with ProCA3, the liver, blood vessel and kidney show high contrast enhancement.

Using inductively-coupled plasma mass spectrometry (ICP-MS), we analyzed the biodistribution of Gd-ProCA1 in different mice organs one hour after injection compared to Gd-DTPA and $GdCl_3$. Gd-ProCA1 was predominantly located in the kidney of injected mice. Almost no increasing signal was detected using Gd-DTPA and $GdCl_3$ was detected mainly in the liver.[133] These biodistribution results were further confirmed using immunohistochemical staining and ELISA assay by monitoring protein in different tissues.[103] In Chapter 7, I will further report our research of the biodistritbuion of ProCAs analyzed by various techniques.

1.6 MOLECULAR IMAGING BY MRI AND BY PROTEIN-BASED MRI CONTRAST AGENTS

1.6.1 Molecular imaging by MRI

Current assessments of disease biomarkers in patients using invasive methods such as biopsy coupled with immunostaining are prone to errors. For example, one out of five HER2/Neu clinical tests for breast cancer provides incorrect results, which severely affects the selection of appropriate patients for personalized treatment using targeted therapies.[134, 135] With its capability to provide repetitive and non-invasive assessment of biological/disease processes of the same organs at various time points, molecular imaging of disease biomarkers by MRI can potentially be an ideal method to enhance our understanding of the disease, to monitor disease progression and to monitor the effect of drug activity during preclinical and clinical drug treatment. Use of MRI for molecular imaging is likely to significantly reduce the cost and number of animals required for preclinical studies. However, the application of MRI to assess specific disease markers for diagnosis and drug effect monitoring has been severely hampered by the lack of contrast agents that combine high relaxivity, targeting capability, and tissue permeability.

In principle, molecular imaging of diseases via receptor-mediated recognition depends on several factors including the number of receptors on the cell surfaces, the binding affinity of the target peptide to the receptor, the diffusion capability, circulation time, and kinetic stability. The majority of receptors or biomarkers have an expression level of < 10^6 per cell. Unfortunately, about 5×10^6 Gd^{3+}/cell are required to obtain a clear contrast enhanced image using currently approved contrast agents based on small chelators (e.g. DTPA) because of the low relaxivity of 5 $mM^{-1}s^{-1}$.[136] Although endocytosis of contrast agents in tissue is considered a beneficial process for accumulation of a contrast agent in a local area, recent studies show that the relaxation enhancement is "quenched" and reaches a plateau when the local concentration of Gd is higher than 10^{10} Gd^{3+}/cell.[137-139] The decline of the relaxivity in this case is probably caused by insufficient water exchange across the plasma membrane.

To achieve molecular imaging by MRI, many studies have been devoted to developing targeted MRI contrast agents.[80, 140-155] Most reported molecules are targeted to biomarkers expressed on the surface of blood vessels and it is difficult to target the biomarkers outside of the blood vessels. In order to improve the dose efficiency, antibodies and peptide fragments with high affinity to receptors are extensively used in conjugation with high payload MRI contrast agents, or contrast agents with high dose efficiency. Demitri *et al.* developed two-component Gd^{3+}-based MRI contrast agents by the binding of avidin-Gd^{3+} complexes to tumor cells prelabeled with a biotinlyated antibody in two steps.[156, 157] Unfortunately, the practical application of these contrast agents to target tumors *in vivo* is limited by slow diffusion. We and others have shown that an antibody exhibits improper distribution and mainly clusters around the tumor blood vessel even 24 hours-post injection in mice.[155] Due to their relatively small size com-

pared to the antibodies, peptide fragments have excellent tissue penetration.[149, 158-160] However, molecular imaging by peptide targeting requires further improvement in targeting capability and resistance to protease cleavage. To date, very limited success has been reported in spite of significant research conducted to improve molecular imaging with MRI. Therefore, there is a critical need for the development of MRI contrast agents with significantly improved relaxivity and improved targeting capability to image the expression level and spatial distributions of biomarkers by MRI.

1.6.2 Molecular maging gastric-releasing peptide receptor by ProCA1.GRP

GRPR is a cancer biomarker with a high expression level in many cancer cells and a low expression level in normal cells.[161-164] Its natural ligand, gastrin-releasing peptide (GRP), can tightly bind to GRPR with a dissociation constant of about 2 nM.[165]

We have further developed protein-based MRI contrast agent with targeting capability for molecular imaging of cancer biomarkers such as gastric-releasing peptide receptor (GRPR). We hypothesize that insertion of GRP to ProCA1 (denoted as ProCA1.GRP) provides a strong targeting capability for the molecular imaging of prostate cancer using MRI via the specific interaction between GRPR and ProCA1.GRP. GRP is grafted between residues 52 and 53 of ProCA1 (denoted as ProCA1.GRP(52)) (Fig. 1-4) or linked to the C-terminal of ProCA1 (denoted as ProCA1.GRPC). The targeting capability of the developed GRP-targeting contrast agent has been examined using various binding assays. ProCA1.GRP(52) showed higher binding capability with GRPR positive cancer cells compared to ProCA1.GRPC.

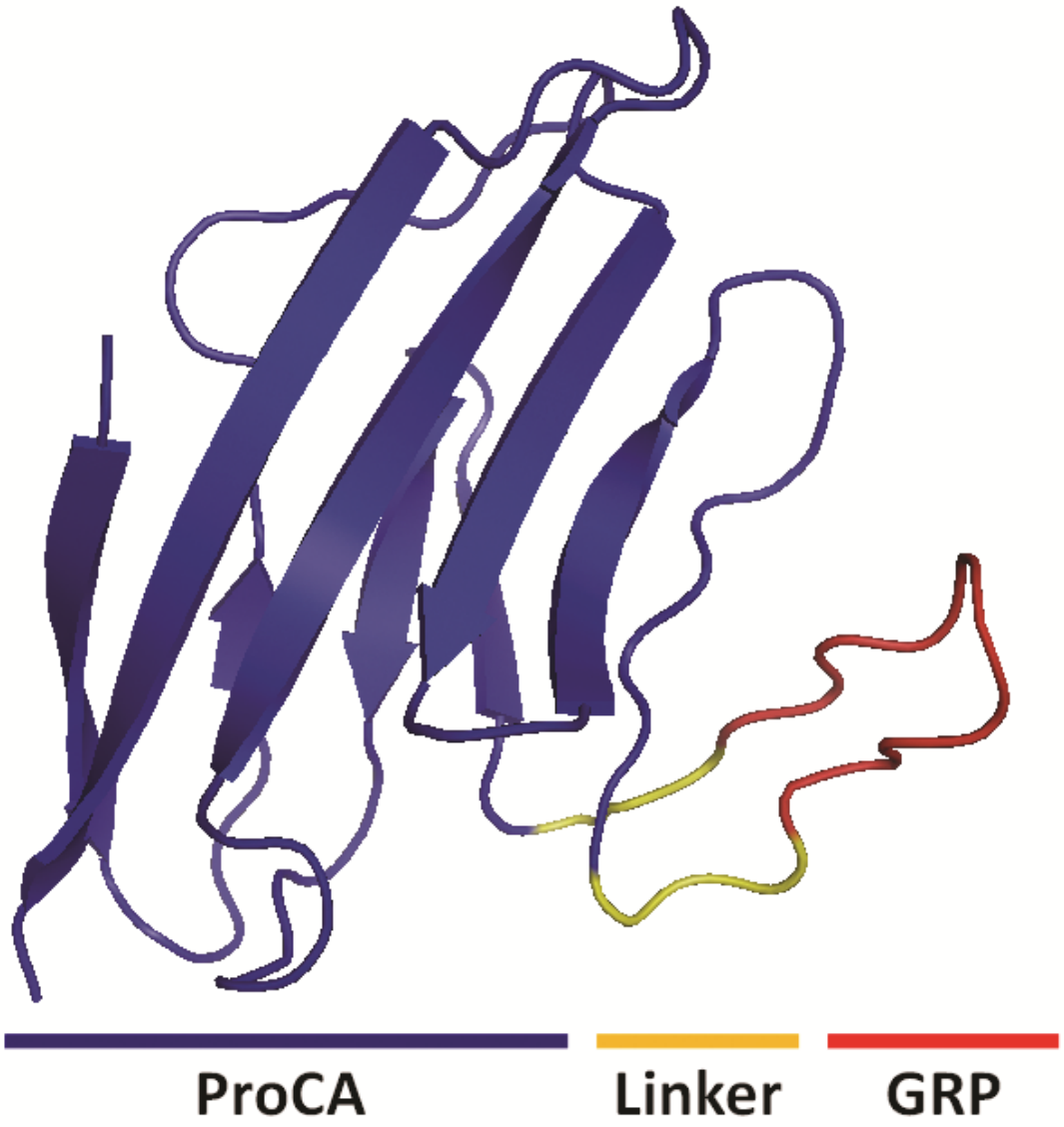

Figure 1-4. Model structure of ProCA1.GRP(52).

Model structure of ProCA1.GRP(52) predicted by I-TASSER.[166-168] The tumor targeting peptide, GRP, is grafted in ProCA1 with flexible linkers.

We then tested whether ProCA1.GRP can be applied to the targeted imaging by scanning the cancer cells using MRI. Cancer cells with different GRPR expression levels were incubated with ProCA1.GRP. The cells with high GRPR expression, PC3 and DU145, showed enhanced signals in the presence of our targeted MRI contrast agents as demonstrated by T_1-weighted imaging. In contrast, no changes were observed in H441 cells, which have a low expression level of GRPR. We also evaluated the targeting capabilities of ProCA.GRP in the living animals with a prostate tumor model. Fig. 1-5 shows that PC3 tumor in xenograft mice can be imaged by intratumoral injection of Gd-ProCA1.GRP(52),[164] which indicate that Gd-ProCA1.GRP(52) is promising for the MR imaging of expression level of GRPR.

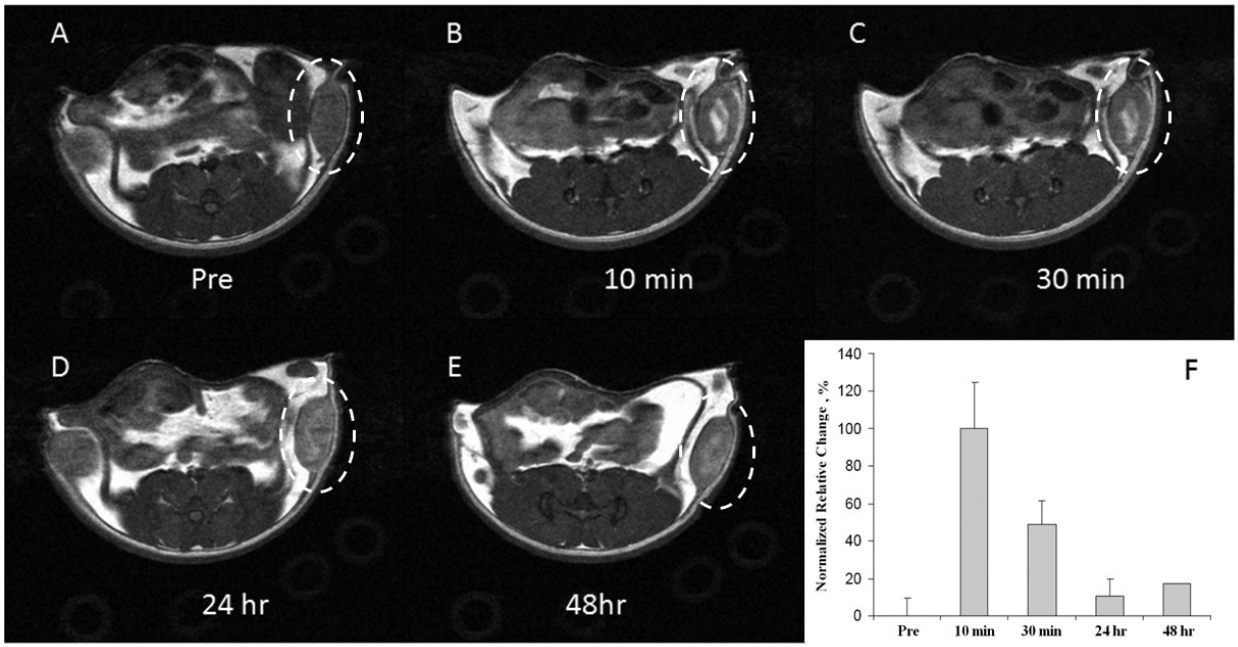

Figure 1-5. T_1-weighted MR imaging of PC3 (circled) xenograft mice pre and post intratumoral injection of Pro-CA1.GRP(52).

T_1-weighted MR imaging of PC3 (circled) xenograft mice pre and post intratumoral injection of ProCA1.GRP(52). A. Pre-injection; B. 10 min post injection; C. 30 min post injection; D. 24 h post injection; E. 48 h post injection. F. MRI signal intensity changes from PC3 tumor before and after injection of ProCA1.GRP(52). Modified after Wei et al.[164]

1.6.3 Molecular imaging of Her-2 expression by ProCA1.affi

Breast cancer is the second most common cancer in women. According to national cancer institute, it is estimated that 39,510 women will be diagnosed to have breast cancer and 39,510 women will die for this disease. HER-2 is a major prognosis biomarker expressed in 30% breast cancer and 60 - 70% of DCIS tissue. Monitoring the spatial and temporal changes of several molecular biomarkers such as HER2/EGFR sharing the same signaling pathway during cancer progression and treatment is the key for understanding the molecular basis of cancers, for early and accurate diagnosis, and for developing effective drugs with synergistic effects to treat this deadly disease. Biomarkers such as the epidermal growth factor receptors EGFR and HER2/Neu are highly expressed in various diseases such as breast and ovarian cancers and play important roles in disease progression and survival. They are also major drug targets for targeted therapy. Since the clinical application of targeted therapy is largely limited because current methods for assessment of these cancer biomarkers involve invasive methods, such as biopsy. The effectiveness of the target therapy largely depends on the pre-selection of patients over-expressing these biomarkers. To date, one of five HER2/Neu clinical tests, including biopsy and immunohistochemistry (IHC), provides incorrect results, leading to improper selection of appropriate patients for personalized treatment using biomarker targeted therapies.[134, 135] There is an urgent need to develop non-invasive and accurate methods for diagnosis and selection of patients and to monitor biomarker levels/distribution and their changes upon treatment by targeted drugs.

Due to the high relaxivity and tumor penetration, we use ProCA1.Affi to carry the molecular imaging of HER-2, instead of using HER-2 antibody for molecular imaging. We linked

HER-2 affibody at the C-terminal of ProCA1. The fusion protein, named ProCA1.affi, has a molecular weight of 15 kDa. HERE-2 affibody strongly and selectively binds to HER-2 with a K_d of 22 pM, which is comparable with the binding affinity of antibody.

Since ProCA1.affi has high relaxivity, high tumor penetration, and high binding affinity to HER-2, ProCA1.affi could be used as a prognosis tool to evaluate HER-2 expression level in tumor. We implant tumors in mouse. SKOV-3 has high HER-2 expression level (10^6 receptors/cell), whereas MDA-MB-231 tumor has low HER-2 expression level (10^4 receptors/cell). As show from Fig. 1-6, after tail vain injection of contrast agents, ProCA1.affi can specifically enhance MR images of SKOV-3 tumor which has high expression level of HER-2. These results indicate that ProCA1.affi can be used to evaluate the expression level of HER-2 biomarkers by the molecular imaging of MRI. It could be further applied to quantitatively evaluate tumor biomarker expression using MRI.

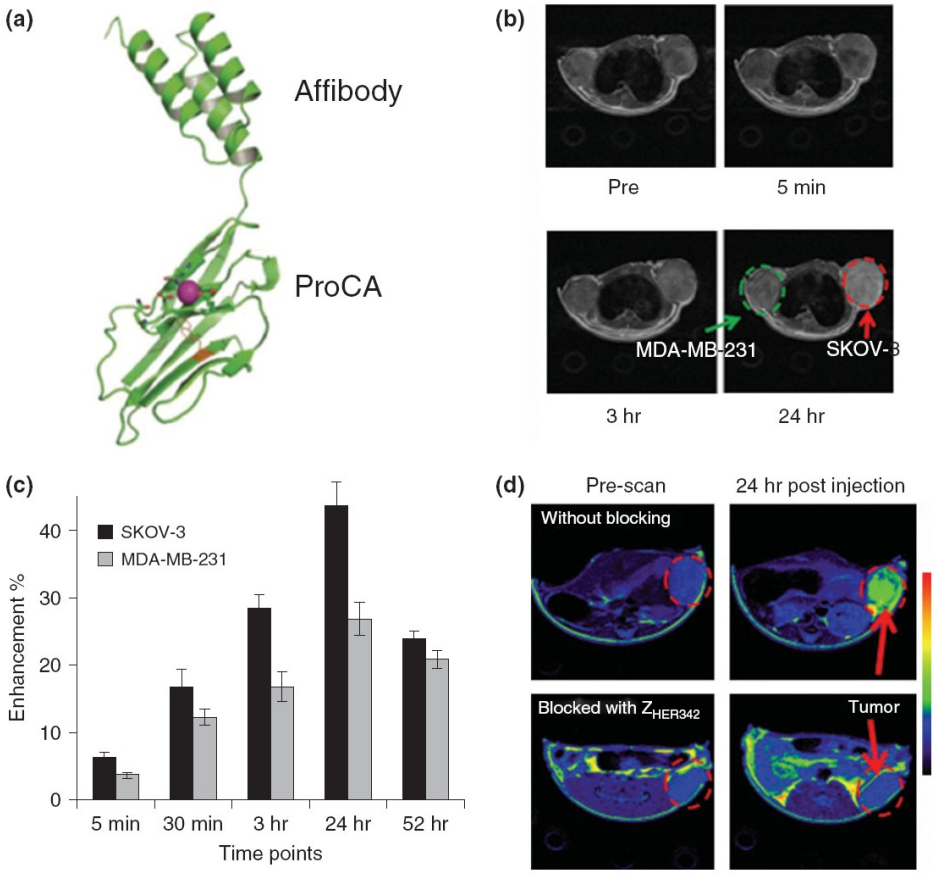

Figure 1-6. Molecular imaging of HER-2 by ProCA1.affi.

(a) Model structure of ProCA1.Affi. (b) Magnetic resonance imaging (MRI) of HER-2 xenograft tumor (SKOV-3 and MDA-MB-231) before and after injection of 0.02 mmol/kg ProCA1.affi. (c) Tumor intensity changes over time postinjection of ProCA1.affi. SKOV-3 has much higher HER-2 expression and SOKV-3 has more MRI signal enhancement than that of MDA-MB-231. The MRI signal intensities of SKOV-3 or MDA-MB-231 tumor regions from six adjacent slides were quantified by Image J software. The average signal intensities and the standard derivation were then calculated from these six adjacent slides. (d) MRI of the mouse SKOV3 tumor pre-blocked by affibody $ZHER2_{:342}$ (bottom) and without blocking (top). Adapted with permission from referernce.[155, 169]

Mainly due to the large size and low permeability, antibody is not an ideal targeting moiety for molecular imaging. To test the penetration of contrast agents to tumor, we linked the HER-2 targeting moiety, affibody, to ProCA (named ProCA1.affi) and then compared the tumor penetration of antibody (MW about 150 kDa) and ProCA. Affi (MW about 15 kDa) at different time point. We I. V. inject either HER-2 antibody or ProCA.affi into the SKOV-3 tumor bearing mice. ProCA.affibody can be stained in the tumor after 4 hours post injection. On the contrary, no antibody in tumor can be stained by IHC at the same time point. ProCA.affi are evenly distributed in tumor with high concentration 24 hours post injection, whereas the antibody only localized in the region near the blood vessel with much lower accumulation (Fig. 1-7). These results indicate that ProCA.affi has a proper size for tumor penetration and targeting.[99, 103, 155, 164, 169] In Chapter 7, I will report our studies to develop biomarker targeted contrast agents based on ProCA3 variants with signficantly imporved stability and shorter blood rentention time than ProCA1 vairants for molecular imaging of cancers.

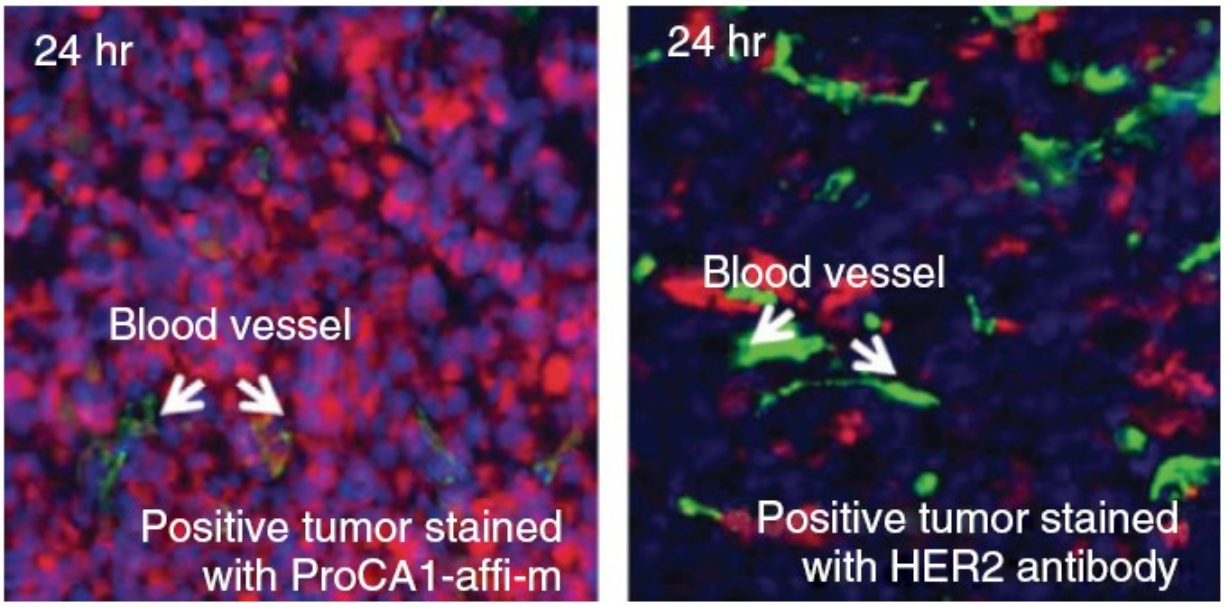

Figure 1-7. Immunofluoresence imaging of ProCA1.affi (left) or HER-2 antibody (right) in SKOV-3 xenograft tumors in mice after IV injection.

ProCA1.affi and HER-2 antibody are stained with red color. Blood vessel is stained with green color. ProCA1.affi is evenly distributed in tumor 24-h post injection, whereas HER-2 antibody only accumulated in near the blood vessel. Adapted with permission from references.[155]

1.7 Development of MRI contrast agents for both T_1-weighted and T_2-weighted MRI.

The relaxation decay of water can be characterized into two processes: spin-lettice relaxiation time (T_1) and spin-spin relaxiaition time (T_2). As show in Fig. 1-8, once put a proton into a constant magnetic field, the net magnetisation will be face z axis. After giving a RF pulse, the net magnetisation will be forced in to different directions. After this radio frequency is finished, the protons will return to the orgininal state. Such process can be characterized by observing the signal increase on the z-axis (T_1 relaxiation time) or the signal loss on the xy-plane (T_2 relaxiation time).

The signal differences of tissue in MRI are determines by the T_1 and T_2 relaxation time differences in these tissue and such differences can be visilized by MRI using different repetition time (TR) and echo time (TE). Based on the different TR and TE, the basic MRI scnascan be devided in devided three major groups: T_1-weighted MRI, T_2 (or T_2*)-weighted MRI, proton density MRI. T_1-weighted MRI usually have a short TR (at around 300 – 500 ms) and shor TE, T_2 (or T_2*)-weighted MRI have a long TR (usually more than 3 s) and long TE (at around 40 – 100 ms), while proton density imaging have long TR (more than 3 s) and shor TE (at around 10 ms). By utilizing different TR and TE parameters, MRI is able to show the differences of T_1 or T_2 (or T_2*) of the tissue, or both of them.[170]

Gadolinium-based MRI contrast agents are most frequently used as T_1 contrast agents due to its ability to short the T_1 time of the water and tissue, while the ion oxide nanoparticles are widely used as T_2 weighted MRI contrast agents because of their high efficiency or shortening T_2 of the tissue. Most of the MRI contrast agents can be used to either increase MRI signal in T_1 weighted sequence or decrease MRI signal in T_2 weighted MRI, but these contrast agents

cannot be applied to both T_1-weighted MRI and T_2-weighted MRI with the same contrast agents because of their intrinsic properties. In addition, clinical Gd^{3+}-based MRI contrast agents has very low relaxivity and sensitivity which further limits their application in T_1-weighted MRI.

In princle, if a MRI contrast agent has both high r_1 and r_2, such contrast agent can be used to increase signal in T_1-weighted MRI and to decrease the signal in T_2-weighted MRI. In addition, the MRI signals changes induced by these contrast agents can be further boosted by deviding the MRI signal from T_2-weighted MRI to T_1-weighted MRI. We name this approach as T_2/T_1 ratiometic imaing. As show from Fig. 1-8 and Equation 1-1 and 1-2, the T_2/T_1 ratiometric imaging can futher increase the signal to noise ratio and decrease unwanted signal generated by the proton density differences, inhomogenecity of magnetic field and motion artifacts. Xiaoyuan Chen and colleagues use iron oxide nanoparticles with T_2-weighted contrast agent mixed with Gd-DTPA, a T_1-weighted MRI contrast agents, with effert to improve the in vivo contrast capabilities.[171] However, the dramatically different PK/PD limits the effect of both T_1 and T_2 proterties. To data, such concept has not been widely reported in the literature due to the limited relaxivity of small contrst agents. This question will be addressed in Chapter 5.

1.8 Motivation of this dissertation and questions to be addressed

In the past three decades, Contrast- enhanced MRI has heen widely successfully applied the disgnosis of different type of disease, such as cancer and cardiovascular diseases. Althroguh great achievement has been made, the current application of the contrast agent in MRI still have some major limitations need to be improved, such as transmetalation, low relaxivity and unble to apply for molecular imaging. In the past 10 years, our lab developed a novel class of MRI contrast agents using protein as Gd^{3+} chelator. The protein-based MRI contrast agents

(ProCAs) have more than 10 times higher r_1 and r_2 relaxivity than that of clinical MRI contrast agents. Such high relaxivity improves the dose efficiency *in vivo*. In addition, because of the high relaxivity and longer blood rention time, the targeted ProCA1 variants can be applied for molecular imaging of biomarker using MRI for the cancer diagnosis. However, the metal stability, metal selectivity, protein production of first generation of ProCA needs to be improved. In addition, the application of ProCAs for the diagnosis has not been fully explored. To further extend the application of ProCAs in disease diagnosis, we ask the following questions:

1). Can we develp a new generation of MRI contrast agents with multiple Gd^{3+} binding sites? 2). Can we improve the metal stablity and metal selectivity of ProCA so that we can prevent the Gd^{3+} resease in vivo? 3). Can we tune the relaxivities of ProCAs by protein design? 4). Can we design MRI contrast agents for liver imaging? 5). How early the metastatic tumor can be detected by MRI? 6). What is the smallest size of tumors can be detected? 7). Can we improve accuracy and specificity of tumor detection by taking advantage of both r_1 and r_2 values of ProCAs?

1.9 Overview of this desertation

To address the pressing needs for better MRI contrast agents and questions discussed above, in this Ph.D. dissertation, I have developed a novel class of MRI contrast agents, ProCA3 series, by protein engineering in collaboration with collabrators and team members.

Chapter 2 details experimental methods and protocols that we are used for the dissertation.

Chapter 3 describes our rationales for design a novel class of protein contrast agents (ProCA3 series) and our hypotheses about increasing metal selectivity and relaxivity by protein

engineering. Our effort in cloning, bacterial expression, purification and conformational characterization of ProCA3 variants will be reported.

Chapter 4 reports the development of novel methods for determination of strong metal binding affinity and selectivity of metalloprotiens. The metal binding affinity and selectivity of ProCAs are detailed. Their relaxivity at different field strenghths are also carefully studied to verify our hypotheses proposed in Chapter 3.

Chapter 5 reports our characterization of in vitro detection limits and mouse detection dose required for the in vivo MRI application. In addition, a new method taking advantage of high R1 and R2 values of the unique properties of ProCAs has developed. The application of ProCA32 in vivo detection of liver metastasis and transplanted liver cancer will be reported.

Chapter 6 reports our intial studies about the application of ProCA3s to dynamic contrast enhanced MRI.

Chapter 7 reports the detailed studies for the safety profile and pharmacokinetics of this novel class of MRI contrast agents (ProCA3 variants) for *in vivo* MRI imaging.

Chapter 8 reports our attempt in extending the application of ProCA3 variants for the molecular imaging of tumor biomarkers

Chapter 9 reports our additional studies for protein modification by Pegylation, humanization of ProCAs variants, and our effort on overcoming the barrier of the large scale production of ProCA3 variants by establish a GMP-like protocol for the expression and purification of ProCA3 variants.

In Appendix, I will also include our other studies in prediction and identification of the Ca^{2+} and calmodulin binding sites in VP1 and VP7 of rotavirus, and neuron proteins such as dicer, clc7 and exportin 5.

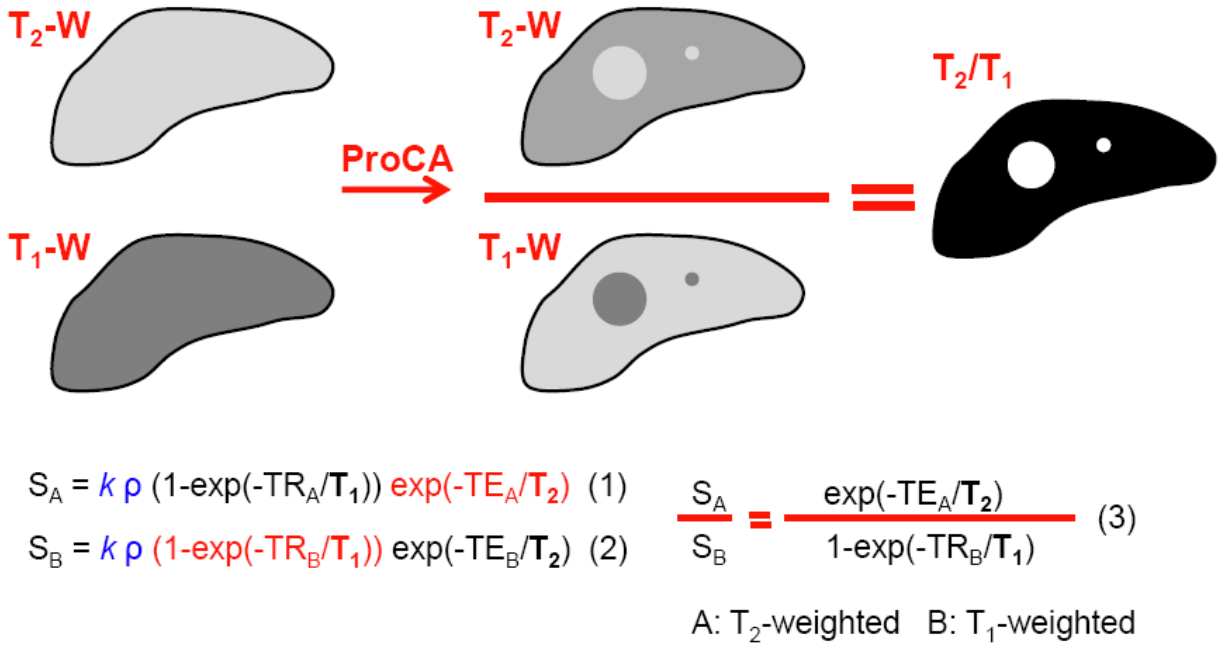

Figure 1-8. The basic principle of T2/T1 ratiometric MRI imaging for the detection of small tumors in the liver.

Without injection of the MRI contrast agents, the tumor and liver have the same MRI signal intensity in both T_1-weighted and T_2-weighted MRI because of the similar T_1 and T_2 relaxiation time between tumor and liver. After IV injection of the ProCA within 1 hour, ProCA will accumulate in the liver tissue rather than tumor. Because ProCA has both high r_1 and r_2, both T_1 and T_2 in liver tissue decreased and the T_1 and T_2 in tumor remain unchanged. As a results, liver shows hyper-intnsity in T_2-weighted MRI and tumor shows hypo-intensity in the T_1-weighted MRI. By the ratio of the MRI intensity of T_2-weighted MRI over T_1-weighted MRI, the signal differences between liver and tumor dramatically boosted. As shown in Equation 1-1 and 1-2, the MRI signal is in both T_1-weigthed and T_2-weighted MRI are determined by the instrumental setings (k), proton density (ρ), T_1 and T_2 of the tissue, and different setings of TR and TE. By the ratio of MRI

signal of T_2-weighted MRI over T_1-weighted MRI, some parameters such as k and ρ are canceled out, the signal intensity of the tissue of ratio metric imaging is mainly determined by the T_1 and T_2 of the tissue, TE values in T_2-weighted MRI and TR values in the T_1-weighted MRI.

Table 1-3. Summary list of the Protein-based MRI contrast agents

Name of ProCA	Discription
ProCA1	The first generation of ProCAs with one Gd^{3+} binding site in a scaffold protein.
ProCA2	The second generation of ProCAs with 2- 4 Gd^{3+} binding sites in a scaffold protein.
ProCA3	The third generation of ProCAs with two Gd^{3+} binding sites in a scaffold protein.
ProCA30	Wild type protein of ProCA3 with no mutations.
ProCA31	ProCA3 variants with F103W mutation to introduce fluorescence probe to ProCA3
ProCA32	ProCA3 variants with S56D and F103W mutations. This ProCA3 viriants has the highest stability and metal selectivity.
ProCA33	ProCA3 variants with E60D and F103W mutations.
ProCA34	ProCA3 variants with G99D and F103W mutations.
ProCA35	ProCA3 variants with S56D, E60D and F103W mutations.This ProCA3 variants has the highest r_1 and r_2 relaxivities among all the ProCA3 variants.
ProCA36	ProCA3 variants with S56D, E60D, G99D and F103W mutations.
ProCA32M	PEGlyated ProCA32 by PEG-40-NHS-ester.
ProCA32-P40	PEGlyated ProCA32 by PEG-40-NHS-ester, same as ProCA32M.
ProCA3.bomb	ProCA32 linked with GRPR targeting peptide in the C-terminal through GGG linker
ProCA3.Affi	ProCA32 linked with HER-2 affibody in the C-terminal through GGG linker.
ProCA3.RGD	ProCA32 linked with GRDGRDGRDGRD in the C-terminal by GGG linker.
ProCA32Cys	ProCA32 with additional cystein at the C-terminal. This cystein residue can be used for site specific PEGlytion and labling.
ProCA32.selectin	ProCA32 linked with selectin-targeting peptide in the C-terminal by GGG linker.
hProCA32	Humanlized ProCA32

2 EXPERIMENTal Methods

2.1 Simulation of the relaxivity over a broad magnetic field

The relaxivity of the clinical MRI contrast agents and ProCAs were simulated based on Solomon-Bloembergen-Morgan Equations[36-38, 40, 42] according to Equations 1-2 to 1-9. The detailed Equations for this simulation are show in Chapter 1. The simulation were done in Microsoft Excel software using the given values of different τ_R (100 ps for clinical MRI contrast agents and 10 ns for ProCA), τ_m (0.1, 1, 10, and 100 ns), τ_v (10 ps), and Δ^2 (5×10^{19} s^{-2}). q is assumed to be 1 and the agent concentration (C) is 0.001 M. The following values are used in the calculation: the gyro-magnetic constant for proton $\gamma_I = 2.675 \times 10^8$ $T^{-1}s^{-1}$; g = 2.0; $\mu B = 9.274 \times 10^{-24}$ J T^{-1}; S = 7/2; $\mu_0 = 1.257 \times 10^{-6}$ N A^{-2}; $r_{GdH} = 3.0 \times 10^{-10}$ m. A relaxivity simulator (Appendix 3) were generated by Microsoft Excel and different relaxivity in a broad range of magnetic field can be generated by changing τ_R, τ_m, τ_v, Δ^2, q, r_{Gd-H} and other parameters.

2.2 Molecular Cloning, Site-direct mutagenesis

2.2.1 Constract parvalbumin expression vector

Rat α-parvalbumin (PV) in pcDNA3.1 vector is a gift from Dr. Emmy Lee at Emory University. PV was double digested by restriction enzyme: *nde I and xho I* (New England Biolabs) and then transferred in to bacteria expression vectors such pET-22b, pET-20b and pRSETb vector. The successfully cloning of PV in these vectors were confirmed by DNA sequencing at GSU core facility.

2.2.2 Site directed mutagenesis and DNA insertion

The general procedures for site directed mutagenesis and DNA insertion are shown in Fig. 2-1. Mutations on S56D, E60D, G99D and F102W and peptide insertions of PV are achieved by site directed mutagenesis using the primer listed in Table 2-1. Polymerase chain reaction was applied under following condition: 95 ˚C denatured for 10 min, then 94 ˚C for 30 seconds, 58 ˚C for 45 seconds and 72 ˚C for 10 min with 30 cycles. The products were finally elongated at 72 ˚C for 15 min. The PCR products were analyzed by agarose gel electrophoresis and the DNA with correct size were phosphorylated by PNK (New England Biolabs), ligated by T4-ligase (New England Biolabs) and the successful ligations were amplified by by E coli. DH5α strains. The corrected plasmid constructs were finally confirmed by DNA sequencing at GSU core facility or Genewiz Company.

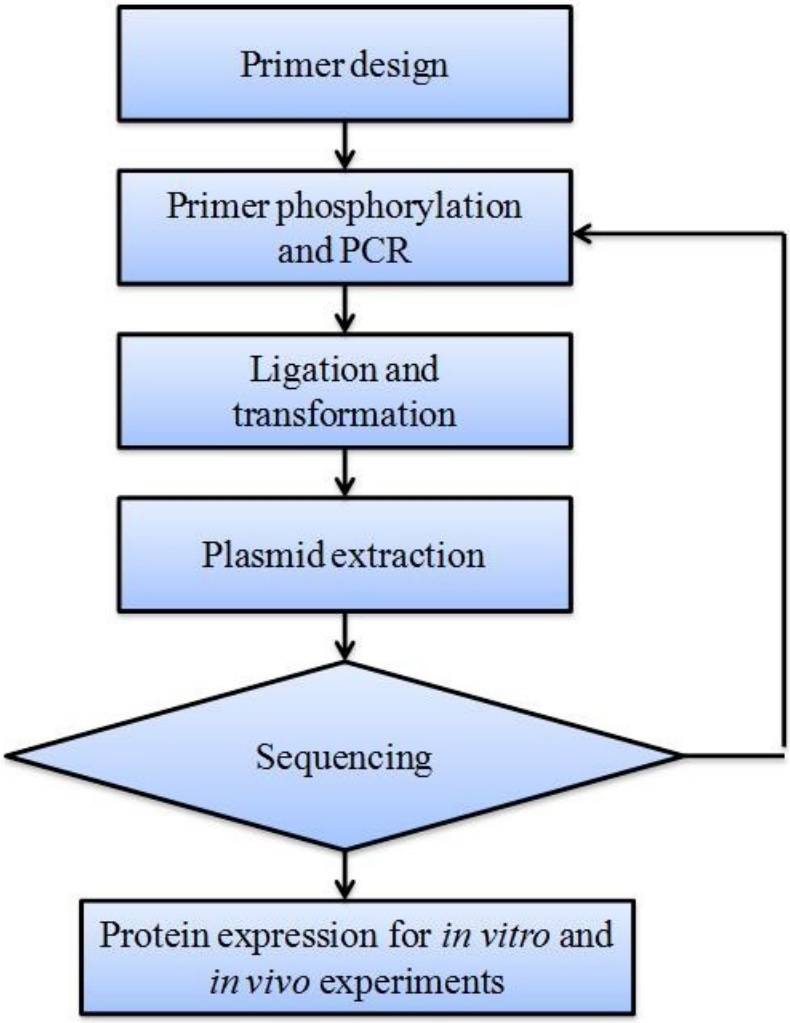

Figure 2-1. General procedures for site direct metagenesis and DNA insertion for PV.

Primers were first phosphorylated before performing PCR. Then, the linear DNA obtained from PCR was linked to circulcualr plasmid by T4-ligase. Then, the DNA was transorformed to E. coli after ligation. The E. coli harbored corrected plasmid were growned on LB solid medium. The plasmids were extracted from these E. coli and send for DNA sequencing. If the desired mutations or insertions are confirmed via DNA sequencing analysis, the new plasmids could be further used for protein expression and purification. Subsequently, the purified protein can be used for various *in vitro* and *in vivo* experiments. Modified from [112].

Table 2-1. Primer design for ProCA construction.

Primer name	Sequence	Mutation/insertion in PV
PVE60D_for	TTCATTGACGAGGATGAGCTGGG	E60D
PVE60D_Rev	GCCGTCTTTGTCTTTGTCCAGAAT	E60D
PV99103_for	AAGATTGACGTTGAAGAATGGTCCACT	G99DF103W
PV99103_Rev	GCCGTCCCCGTCCTTGTCTC	G99DF103W
F103W_for	GAA GAA TGG TCC ACT CTG GTG GC	F013W
F103W_Rev	AAC CCC AAT CTT GCC GTC CCC	F013W
F103WG99D_for	GAA GAA TGG TCC ACT CTG GTG GC	G99DF103W
F103WG99D_Rev	AAC GTC AAT CTT GCC GTC CCC GTC	G99DF103W
PVE60D56D_fov	TTCATTGACGAGGATGAGCTGGG	S56DE60D
PVE60D56D_Rev	GTC TTT GTC TTT GTC CAG AAT GTG GAA	S56DE60D
PV52E_For	ATTCTGGAGAAAGACAAAGACGGCTT	D52E
PV52E_Rev	GTGGAACACCTTCTTCACATCATC	D52E
PV111C_inser_For	TGTTAAGGATCCACTAGTCCAGTGTG	111C insertion
PV111C_inser_Rev	GCTTTCGGCCACCAGAGTGGA	111C insertion
PV99E103W_f	GAGGTTGAAGAATGGTCCACTC	G99EF103W

PV99E103W_r	AATCTTGCCGTCCCCGTCCTT	G99EF103W
D99E1_F	GTTGAAGAATGGTCCACTCTGGT	G99EF103W
D99E1_R	TTCAATCTTGCCGTCCCCGTCC	G99EF103W
D99E2_F	TGGTCCACTCTGGTGGCCGAA	G99EF103W
D99E2_R	TTCTTCAACCTCAATCTTGCCGTCC	G99EF103W
Selectin_CD2_for	GGGATCAACTTTGGGATCTTATGAAGGGCG GAGGTGGAGCATTTGAGATCGACGCAAA	Selectin targeting pep-tide intertion
Selectin_CD2_rev	AAGTAATATCTCCATCATACTTGCCTCCGCC CGATTTCAAAAAAGGCTTCATCTTC	Selectin targeting pep-tide intertion
RGD_CD2_for	GATGGCGGAGGTGGAGCATTTGAGATCGA CGCAAA	Integrin targeting pep-tide insetion
RGD_CD2_rev	ACCTCTATCACCTCTATCACCTCTGCCTCCGC CCGATTTCAAAAAAGGCTTCATCTTC	Integrin targeting pep-tide insetion
Primer name	Sequence	Mutation/insertion in PV
collegan_CD2_for	TTATTTTCCTCATCATTATTGTGTTTATGGAG GTGGAGCATTTGAGATCGACGCAAA	Collegan targeting pep-tide insertion
RGD_CD2_rev	GTATAACAATGCCACTTCTTGCCTCCGCCCG ATTTCAAAAAAGGCTTCATCTTC	Collegan targeting pep-tide insertion
56103aff1_for	GCAAAGAAGTTGAACGATGCTCAAGCACCT	Her-2 affibody insertion

	AAGTAAGGATCCACTAGTCCAGTGTG	part 1
56103aff1_rev	ATTGAACTTGTTGTCGACGCCGCCGCTGCC GCCGCTTTCGGCCACCAGAGTGGA	Her-2 affibody insertion part 1
56103aff2_for	GACCCTTCTCAATCAGCTAATTTACTTGCAG AGGCAAAGAAGTTGAACGATGCTCAA	Her-2 affibody insertion part 2
56103aff2_rev	TAACGCGATTTCCCAGTACGCATTACGCATT TCTTTATTGAACTTGTTGTCGACGCCG	Her-2 affibody insertion part 2
56103aff3_for	TTTATCCGTTCATTGTACGATGACCCTTCTC AATCAGCTAATTTA	Her-2 affibody insertion part 3
56103aff3_rev	GGCACGCTTTTGCTGATTGTTCAAGTTGGG CAATAACGCGATTTCCCAGTACGCAT	Her-2 affibody insertion part 3
Bomb_for	TGGGCAGTAGGCCACCTAATGTAAGGATCC ACTAGTCCAGTGTG	GRPR targeting peptide insetion
Bomb_rev	TTGGGCTCCTCCTCCGCTTTCGGCCACCAGA GTGGA	GRPR targeting peptide insetion

2.3 Protein Expression, purification and PEGlytion

ProCA varients were purified following Dr. M. Henzl's method with some modifications.[172] ProCAs were expressed in E. coli BL-21DE3 or Tuner cell strains. ProCA expression was induced by IPTG after OD_{500} reached 0.6. After IPTG induction overnight, the bacterial culture was sonicated in 10 mM Tris/ HCl buffer, pH 7.2, 100 μM PMSF and benzonuclease and followed by passing through a French pressure cell. The supernatant of cell lysate was incubated at 85 ˚C for 10 min, cooled at 4 ˚C in an ice-water bath, and centrifuged (17000 rpm, 20 min, 4˚C). The supernatant was collected for further purification. DNA was then precipitated by supplementation of 3% strepmyosin sulfate. After dialysis for 24 h at 4 ˚C against 10 mM Tris/HCl at pH 8.5, the protein mixture was further purified by the HiTrap Q column. After removing unbound proteins with 3 bed volumn of 10 mM Tris at pH 8.5, the column was eluted with a 0–1 M NaCl gradient in 10 mM Tis/HCl at pH 8.5. The protein and DNA separations were monitored by the SDS-PAGE and agarose gel, respectively. The purified ProCA32 was dialyzed against 10 mM Tris, pH8.5. Metals in ProCAs are removed by chelex-100 and metal content in ProCAs is analyzed by ICP-OES.

ProCAs were PEGlyted by the following steps: 1). ProCAs were dialyzed against 10 mM HEPES at pH 7.0-7.2 to remove all possible Tris. 2). ProCAs were mixed with PEG-NHS ester with a molar ratio of 1:3 and then incubated at room temperature for 4 hours or 4 ˚C overnight. 3). Unreacted free PEG-NHS were quenched by adding 100 mM Tris/HCl with a final concentration of 10 mM. 4) PEGlyated ProCAs were further purified by HP Q column. After removing unbound proteins with 3 bed volumn of 10 mM HEPES at pH 8.0, the column was eluted with a 0–1 M

NaCl gradient in 10 mM HEPES at pH 8.0. The PEGlyation procedures were monitored by SDS-PAGE with protein staining by coomassie brilliant blue and PEG staining by I^2.

2.4 Large scale protein expression and purification

2.4.1 Large scale expression of ProCA by fermentation

The plasmid for ProCA3 was first transferred in BL21-DE3-plysS bacteria cultured on agar plate supplemented with ECAM media. 1 ml of a glycerol stock of ProCA32 expressing bacteria were innoculated in 100 ml ECAM and left to shake at 150 rpm and 37 ˚C over night. Then, 10 ml of the bacteria was transferred to 250 ml ECAM medium and incubate at 37 ˚C and 200 rpm for 6 hours. 120 ml of these bacteria were used as an inoculum for the bioreactor.

The bioreactor were setup as follows: Initial glucose concentration 21g/L; Batch media contained 50ug/ml carbenicillin; Vessel was inoculated to give $1.5x10^{-2}$ cells; oxygen conenctration was set to 30% and maintained with stirrer (min= 160 rpm, max = 450 rpm) and Gas Mix; Air flow was constant at 10 LPM. Bacteria were harvested by continous centrifuge.

2.4.2 Exploring different methods for large scale purification of ProCA3 obtained from bio-reactor

The bacteria cell pellets were suspended by 10 mM HEPES, pH 7.0 and then broken by cell discruptor. After concentrigation at 6000 rpm for 30- 60 min, the supernatant of bacteria lysate were collected for further protein purification. In order to separate ProCA3 from other proteins or bio-moleculars, such as DNA, different concentrations of PEG-8000 were added to the supernatant of the cell lysate. Due to the differences of the solubility and molecular weight,

different proteins can be precipated at different concentration of PEG-8000. The concentration range of PEG-8000 for ProCA32 precipitation was determined by SDS-PAGE. The detailed results and discussions will be shown in Chapter 7.

To further purifiy ProCA3, ProCA3 precipitate by PEG-8000 was dissolved in HEPES buffer at pH 7.0. These protein solution were load to FPLC equipped with Hi-trap Q column. After binding to the column, the unbounded component was first washed out with 7 column volume (CV) of buffer A (10 mM HEPES buffer at pH 8.0). Then, buffer B (10 mM HEPES buffer, 1 M NaCl at pH 8.0) concentration were increase to 25 % within 7 CV. We further wash the column with 25% of buffer B for 2 CV and then increase to 100 % of buffer B of 1 CV to wash out every component bounded to the column. The fractions containing purified ProCA32 were determined by UV abs and SDS-PAGE.

At last, since ProCA32 is very stable at 90 ˚C, we further incubate the purified ProCA32 at 90 ˚C for 20 min and followed by a centrifugation at 6000 rpm for 30 min to remove residue uwanted protein.

2.5 Gd^{3+}, Tb^{3+} Ca^{2+}, Mg^{2+} and Zn^{2+}-Binding Affinity Determination

Fluorescence spectra were recorded using a QM1 fluorescence spectrophotometer (PTI) with a xenon short arc lamp at ambient temperature. Tryptophan fluorescence was monitored using excitation at 280 nm and emission between 290 and 370 nm with 2 - 4 nm slit width and phenylalanine signal was monitored by excitation at 259 nm and emission between 270 and 350 nm. Tb^{3+} luminescence resounance energy transfer (LRET) experiments were acquired by excitation of phenylalanine and tryptophan at 259 nm and 280 nm and emission from 500 to

650 nm. Fluozin-1 emission spectra were obtained at excitation 495 nm and emission between 500-600 nm.

For the equilibrium method, 10 µM ProCA32 were added in to the calcium-buffer system containing 50 mM HEPES, 100 mM NaCl, 5 mM EGTA, pH7.2. Subsequently, different calcium chloride concentrations were titrated into the buffer system. Thus, free calcium concentration was calculated based on tsein's method (K_d of EGTA is 1.51×10^{-7} M [173]) using Equation (2-1).

$$[Ca^{2+}]_{free} = Kd_{Ca,EGTA} \times \frac{[Ca-EGTA]}{[EGTA]_{free}} \quad (2\text{-}1)$$

$$f = \frac{{[Ca^{2+}]_{free}}^{n}}{{Kd_{Ca,ProCA}}^{n}+{[Ca^{2+}]_{free}}^{n}} \quad (2\text{-}2)$$

where $[CA^{2+}]_{free}$ is the free Ca^{2+} concentration in each titration point, $Kd_{Ca,EGTA}$ is the dissociation constant of GGTA to Ca^{2+}, [Ca-EGTA] is the concentration of total Ca-EGTA complex in each titration point, and $[EGTA]_{free}$ is the concentration of EGTA in each titration point.

Tb^{3+} binding affinity of ProCA were obtained by Tb^{3+} LRET-competition methods or Tb^{3+}-DTPA buffer system. For Tb^{3+} LRET-competition method, 10 µM of ProCA and 20 µM Tb^{3+} were incubated with different concentration of NTA or DTPA at room temperature over night. ProCA3 are exitated at 260 nm for phenylalanine ro at 280 nm for tryptophan. The Tb^{3+} LRET signal changes were measured by the emission at 545 nm. The apparent K_d (K_{app}) was obtained by one to one binding Equation (Equation (2-3)) and the dissociation constants of ProCA were fitted by Equation (2-3). The dissociation constants of Tb^{3+} to NTA (10^{-13} M) and EGTA (10^{-18} M) is obtained from NIST.

$$\mathrm{f} = \frac{([\mathrm{P}]_\mathrm{T}+[\mathrm{M}]_\mathrm{T}+\mathrm{Kd_{app}})-\sqrt{([\mathrm{P}]_\mathrm{T}+[\mathrm{M}]_\mathrm{T}+\mathrm{Kd_{app}})^2-4[\mathrm{P}]_\mathrm{T}[\mathrm{M}]_\mathrm{T}}}{2[\mathrm{P}]_\mathrm{T}} \quad (2\text{-}3)$$

$$Kd_{Tb,ProCA} = \frac{Kd_{Tb,NTA}}{Kd_{app} - Kd_{Tb,NTA}} \quad (2\text{-}4)$$

where f is the fractional change, Kd_{app} is the apparent dissociation constant for Tb^{3+} and $[P]_T$, $[M]_T$ are the total concentrations of the protein and Tb^{3+}, $Kd_{Tb,ProCA}$ is the dissociation constant of ProCA to Tb^{3+}, $Kd_{Tb,NTA}$ is the dissociations constant of NTA to Tb^{3+}.

For Tb^{3+}-DTPA buffer system, 30 μM of ProCA were added into Tb^{3+}-DTPA buffer system, which contains 5 mM DTPA, 50 mM HEPES, 100 mM NaCl at pH7.2. Then, $TbCl_3$ was titrated into the buffer and free Tb^{3+} concentration is calculated by Equation (2-5). ProCA3 is exciated at 280 nm and Tb^{3+}-LRET signal is observed in the emission wavelength between 500-650 nm. The $Kd_{Tb,DTPA}$ is calculated by Hill Equation (2-6)

$$[Tb^{3+}]_{free} = Kd_{Tb,DTPA} \times \frac{[Tb-DTPA]}{[DTPA]_{free}} \quad (2\text{-}5)$$

$$f = \frac{[Tb^{3+}]_{free}{}^{n}}{Kd_{Tb,ProCA}{}^{n} + [Tb^{3+}]_{free}{}^{n}} \quad (2\text{-}6)$$

where $[Tb^{3+}]_{free}$ is the free Tb^{3+} concentration calculated from buffer system, $Kd_{Tb,DTPA}$ is the dissociation constant between Tb^{3+} and DTPA, [Tb-DTPA] is the concentration of Tb-DTPA complex, [DTPA]free is the free DTPA concentration in the buffer, f is the fractional change, $Kd_{Tb,ProCA}$ is the dissociation constant between Tb^{3+} and ProCA.

LRET competition method was applied to measure the Gd^{3+} binding affinity to ProCA. 10 μM of ProCA and 20 μM Tb^{3+} were incubated with 0 to 1000 μM of $GdCl_3$ at room temperature over night. The Tb^{3+} FRET changes were measured by the emission at 545 nm. The apparent Kd were fitted by 1 to 1 binding Equation (Equation 2-3) and Kd of Gd^{3+} were calculated by Equation (2-7),

$$Kd_{Gd,ProCA} = Kd_{app} \times \frac{Kd_{Tb,ProCA}}{Kd_{Tb,ProCA} + [Tb^{3+}]_T} \quad (2\text{-}7)$$

where $Kd_{Gd,ProCA}$ is the dissociation constant between Gd^{3+} and ProCA, Kd_{app} is the apparent Kd for Gd^{3+}, ProCA between and ProCA obtained from Equation (2-6) and $Kd_{Tb,ProCA}$ is the dissociation constant between Tb^{3+} and ProCA calculated from Equation (2-4) and $[Tb^{3+}]_T$ is the total concentration of Tb^{3+} in the competition experiments.

Fluozin-1 competition experiments were applied to calculate the Zn^{2+} binding affinity of ProCA according to Yang's method with some modifications.[103] Briefly, 2 µM of Zn^{2+} and 1 µM of Fluozin-1 were added in 50 mM HEPES, 100 mM NaCl, pH 7.2. Then, 0-100 µM of ProCA were titrated in to the solution. The fluoresence signal changes were recorded in an equilibrium state after each titration point. Dissociation constant between ProCA and Zn^{2+} were calculated by the following Equations (2-8 and 2-9)

$$f = \frac{([P]_T+[M]_T+Kd_{app})-\sqrt{([P]_T+[M]_T+Kd_{app})^2-4[P]_T[M]_T}}{2[P]_T} \quad (2\text{-}8)$$

$$Kd_{Zn,ProCA} = \frac{Kd_{Zn,fluozin}}{Kd_{app} - Kd_{Tb,fluozin}} \quad (2\text{-}9)$$

where $Kd_{Zn,ProCA}$ is the dissociation constant between Zn^{2+} and ProCA, Kd_{app} is the apparent K_d calculated by Equation (2-8), $Kd_{Tb,fluozin}$ is the dissociation constant between Tb^{3+} and Fluozin-1 . $Kd_{Tb,fluozin}$ is measured by yang's methods[103].

2.6 Determination of r_1 and r_2 Relaxivity Values

The relaxation times (T_1 and T_2) were measured by Bruker relaxometer (1.47 T). The contrast agents with different concentration were prepared in 50 mM HEPES, 100 mM NaCl, pH 7.4. The relaxivity were calculated by the Equation (2-10 and 2-11).[113]

$$r_i = \frac{\frac{1}{T_{i_{sample}}}-\frac{1}{T_{i_{buffer}}}}{[Gd^{3+}]_T} \qquad i= 1, 2 \quad (2\text{-}10)$$

where r_i is the per Gd^{3+} relaxivity, $T_{isample}$ is the relaxation time of water after adding ProCA, Ti_{buffer} is the relaxation time of water without adding contrast agents and $[Gd^{3+}]_T$ is the total Gd^{3+} concentration in the tested solution.

2.7 Measurement of Water coordination number by Terbium Lifetime Luminescence.

The number of water ligands coordinated to Gd^{3+}-ProCA complex was determined by measuring Tb^{3+} luminescence decay in H_2O or D_2O using the previously published methods with some modifications.[174, 175] Tb^{3+} was excited at 265 nm with a Xenon Flash lamp and the Tb^{3+} emission was collected at 545 nm at a series of time in both H_2O and D_2O solutions. Luminescence decay lifetime of Tb^{3+} or Tb^{3+}-chelator complex in H_2O and D_2O solution were obtained by fitting monoexpernantial decay equation. A standard curve of water number (q) over ΔK_{obs} (the difference of the decay constant between H_2O and D_2O) were established using Tb-NTA (q=5), Tb-EDTA (q=3), Tb-DTPA (q=1) and Tb^{3+} in aqueous solution (q=9). The water number of ProCA was calculated based on the standard curve.

2.8 Serum stability

Gd^{3+}-ProCA32 (400 μM) was mixed with mice serum with 1:1 ratio, and then incubated at 37 ˚C for different time point. SDS-PAGE and mass spectrum were applied to detect the remaining Gd^{3+}-ProCA32 after incubating in the serum for each time point. The protein separated by SDS-PAGE is stained by coomassie brilliant blue or west blot. Homemade rabbit ProCA32P40 antibody is used as primary antibody with 1:3000 dilutions. For western blot detection, AP-conjugated Goat anti rabbit antibody (Bio-Rad) is used as secondary antibody with 1: 3000 dilutions.

2.9 Immunoblot and tissue homogenizes

Mouse tissue with and without ProCA32 injection were homogenized in RIPA buffer supplemented with 1 mM PMSF and 10 ul protease inhibitor cock tale. Each 300 mg tissue was homogenized in 500 µl buffer. Homogenized tissues were then mixed with 2× SDS sample buffer and loaded into SDS gel. The electrophoresis was done at 120V voltage for 1 hour. 7.5% and 15% resolving gel were used for the GRPR and ProCA, respectively. Electron transformation was done at 20 mV at 4 ˚C overnight. As primary antibody, homemade rabbit against ProCA32-P40 antibody was diluted 3000 times. Rabbits against GRPR antibody are diluted 500 times. The membranes are blocked with 0.2% non-fat milk, 4 ˚C overnight incubation with primary antibody. After washing three times with TBST buffer, AP-conjugated Goat anti Rabbit antibody are diluted 3000 times and incubated at room temperature for 1 hour. The western blots were virtualized by Bio-Rad kit with the exposure time of around 30 seconds to 3 minutes.

2.10 Immunofluorescence image

The cryoslice of tumor and normal tissue were cut with a thickness of 10 µm. The tissue were fixed with acetone for 10 min at -20 ˚C and then washed with TBST for three times. Tissues were then blocked at room temperature for 1 hour by 1% BSA in TBST, and incubated with primary antibody for 1 and half hour. Homemade ProCA32-P40 anitbody with 1:100 dilution and Rabbit anti GRPR from ABCAM were used as primary antibody in the separated slides. After washing for three times, the slides were incubated with Alaxa fluo (red) goat anti rabbit antibody (Invitrogen) as secondary antibody. The fluorescence images were obtained from Leica imaging system for 400 × amplification.

2.11 NIR labeling and NIR imaging

Protein and Cy5.5 were mixed with 5 to 1 ratio, and incubated at room temperature for 4 hours. Unreacted Cy5.5 was quenched by adding 5 times access amount of Tris at pH 7.0. For the animal injection, the final sample was dialysised against 10 mM HEPES three times and concentrated to a ProCA concentration of 5 mM. The mice cy5.5 imaging was perfomed every day after ProCA32-bombsin injection under Xengen imaging system with excitation wavelength of 640 nm and Cy5.5 filter. After finishing a continuous three-day MRI experiments, the mice are scarified, and tumor, liver, kidney, muscle, spleen and heart were taken out and imaged under NIR imaging system. Along with these NIR images, bright field are also taken each time.

2.12 Mice MRI image

CD-1 mice or tumor baring nude mice of about 20-30 g were selected for the MR imaging. MR angiography of mice after injection of ProCA3M was collected by Varian MR scanner (4.7 T) at Emory University. 0.03 mol/kg MRI ProCA32M were injected into the mice and scanned with 3D gradient echo sequence (TR = 40 ms, TE = 2.9 ms). The field view was 8 cm × 4 cm × 6.4 cm with matrix of 384 × 192 × 64 MR images were obtained before ProCA injection and 0.7, 3, 44 and 54 h post injection of contrast agents. The images were analyzed by Image J and MRI croN. The intensities of blood, liver and kidney were plotted over time. T_1-weighted 2D MRI of mice or phantom were collected before and after injection of contrast agents using spin echo sequence with TR = 400 ms, TE = 11 ms, FOV = 4 × 4 cm, matrix =512 × 512, thickness = 1 mm. T_2-wegithed 2D MRI of mice or phantom were collected before and after injection of MRI contrast agents using fast spin echo with TR = 5 s, effective TE = 28 ms FOV = 4 × 4 cm, matrix =512 × 512, thickness = 1 mm. The ratiometric imaging MRI were then calculated by the ratio of MRI

signal intensity of T_2-weighted fast spin echo and T_1-weighted spin echo sequence. A threshhold was setup to further eliminate extremely low intensity from background (air).

Bi-brililant MRI were collected by T_2-weighted inversion recovery sequence with long TE by fast spin echo sequence (TR = 5 s, effective TE = 28 ms, FOV = 4 × 4 cm, matrix =512 × 512, thickness = 1 mm) and spin echo sequences (TR = 5 s, TE = 11 ms, FOV = 4 × 4 cm, matrix =512 × 512, thickness = 1 mm). After the injection of ProCA, inversion time to null liver signal was determined by a series of inversion recovery sequence with different inverstion time. We then applied bi-brilinat MRI with this inversion time to collect the MR imaging from live animal and liver tissue using both fast spin echo sequence (TR = 5s, effective TE = 28 ms, FOV = 4 × 4 cm, matrix =512 × 512, thickness = 1 mm) and spin echo sequences (TR = 5s, TE = 11 ms, FOV = 4 × 4 cm, matrix =512 × 512, thickness = 1 mm).

MR images of GRPR in tumor were collected by Varian MR scanner (7 T) at the University of Georgia. H441 and PC3 cells were implanted in the flank of nude mice in the animal facility of Georgia State University. MR image were collected after the tumor size reached to 1 cm^3. MR images were collected with spin echo sequence (TR = 500 ms, TE = 14.52 ms). The field view was 3.5 cm × 3.5 cm with matix of 128 × 128 and slice of 1 mm in thickness. One of MR images were collected before ProCA3 injection followed by 0.02 mol/kg ProCA32.bomb into the nude mice through the tail vain. Tumor MR Images were acquired at the following time points: 30 min, 2 hr, 1 day, 2 days. MR images were analyzed by Image J and MRI croN.

Dynamic contrast enhanced-MRI (DEC-MRI) data were acquired using Varian 7 T MR scanner. A 26 G catheter was implanted into the tail vein of the mice before the scanning. Two group of mice were used for the DCE-MRI experiments at UGA. Each mouse was acquired three

slices in kidney with proton density map, T_1 map and DCE-MRI sequence. T_1 map of 3 slices of mice kidney were acquired before contrast agents injection by saturation recovery FSEMS sequence with different length of TR (mice injected with Gd-DTPA: TR=350, 500, 700, 900, 1200, 2000, 3000, 5000; Mice injected with ProCA32: TR=350, 500, 700, 900, 1000, 2000, 3000, 5000) matrix: 256 x 256, fov=4 cm × 4 cm and thickness=2 mm. Then, DCE-MRI was applied with FLASH sequence with 150 repeated scanning. 20 scans were acquired before contrast agent injection as baseline. For Gd-DTPA group, DCE-MRI are acquired with following parameters TR=18.80 ms, TE=2.95 ms, Flap Angel=25 °, average=1; gain=20. Data were acquired every 2.3 second. 0.2 mmol/kg Gd-DTPA (100 µl) was quickly injected after 20 scan followed with the quick injection of 150 µl Saline. For ProCA32 group, DCE-MRI were acquired with following parameters TR=18.80 ms, TE=2.95 ms, Flap Angel=25 °, average=3; gain=25. Data was acquired every 7 second. 0.015 mmol/kg ProCA3 (100 µl) was quickly injected after 20 scan followed with the injection of 150 µl Saline. 20 round of scannings were acquired as baseline before the injection of contrast agents, and then a total volume of 100 µl of DTPA (0.2 mmol/kg) or ProCA3 (0.015 mmol/kg) were injected in to the mice during scanning with an injection rate of 10 µl per second. Total 150 rounds of scannings were finally acquired with a 2.3 s for Gd-DTPA and 7 s for ProCA in each round. MRI were acquired by FLASH sequence with TR= 18.80, TE=2.95 ms, flip angel 25 ˚. The field view was kept to be 4 cm ×4 cm with matrix of 128×128 and slice of 1 mm thickness.

2.13 Detection limits study

PCR tubes filled with buffer or different concentration of the contrast agents were scanned in 7 T Varian scanner. MR images were collected with spin echo sequence (TR = 300,

500, 600, 700 and TE=13.82). The field of view was 10 cm × 8 cm with matrix of 128 × 128 and thickness of 1 mm.

T_1 maps were acquired with inversion recovery FSEMS sequence with TR = 7000 ms, effective TE= 48 m (esp = 12 ms, etl = 8, kzron = 4, average = 2), Ti = 0.01, 0.05, 0.1, 0.3, 0.5, 0.7, 0.9, 1, 2, 3, 4 s. The field of view was 10 cm × 8 cm with matrix of 128 × 128 and thickness of 1 mm.

CD1 mice of about 20-30 g were injected with different concentration of contrast agents. MR imaging were acquired under 7 T Varian MRI scanner by two different sequences. The kidney enhancements were collected with spin echo sequence with TR = 300 - 700 ms and minimum TE. The field view was 4cm × 4cm with matrix of 128 × 128 and thickness of 1 mm. 3 D image of the mice were collected by gradient echo sequence (TR = 40 ms, TE = 2.48 ms). The field view was 8 cm × 4 cm × 4 cm with matrix of 128 × 128 × 64.

2.14 Blood retention, tissue distribution and toxicity

2.14.1 Short term and long term Gd^{3+} distribution and toxicity study by ICP-OES

Mice with a body weight of 20-25 g were injected with 0.2 mmol/kg of Gd-DTPA, 0.0016 mmol/kg of $GdCl_3$ or 0.0008 mmol/kg of ProCA3 variants, respectively. Blood were collected from saphenous vein at different time point from 10 min to 14 days. Tissues from mice were collected after the mice were euthanized at 10 min or 14 days after injection of Gd-DTPA, $GdCl_3$ or ProCA3 variants.

To determine Gd^{3+} concentration in tissues, the collected tissue and blood samples were digested with 70% HNO_3 at 130 ˚C overnight. The HNO_3 with tissue digestions were collected

the next day and diluted with 2% HNO_3 to 10 ml. The sample was analyzed by ICP-OES (Varian 720-ES) at Gadolinium wavelength of 342.76 nm. ICP-OES was running at the following conditions: Pwr for 1.2 kW, PlasFlow at 15 L/min, AuxFlow at 1.50 L/min, NebFlow at 0.90 L/min, Replicate Time for 10 s, Stable Time for 15 s, Sample Uptake for 30 s, Rinse Time for 10 s, Pump Rate at 15 rpm. A standard curve with different concentration of Gd^{3+} was generated to calculate the Gd^{3+} concentration in testing samples. 2 ppm of YCl_3 was used as internal reference. For pharmacokinetics and biodistribution study, different tissues from at least 5 mice in each group were analyzed.

2.14.2 Clinical chemistry study of ProCA variants

Mices with a body weighted of 25 – 30 g were I. V. injected with 0.03 mmol/kg of ProCA variants. The bloods of the mice were collected two days post injection using heparin-coated capillary. The sera of the blood were obtained by centrifuge at 3000 rpm at 4 ˚C for 10 min. About 300 µl of mice serum were collected for clinical chemistry study in IDEXX Laboratories. The clinical chemistry evulate the liver, kidney, heart functions based on the levels of enzyme, proteins, glucose and ions in the serum.

3 DESIGN, EXPRESSION, PURIFICATION OF PROTEIN-BASED MRI CONTRAST AGENTS

3.1 Introduction

As discussed in Chapter 1, there is a strong need to develop MRI contrast agents for patient diagnosis and diseaseprognosis. In order to design protein contrast agents with superior *in vivo* applications, protein based MRI contrast agents must have several key features. 1). Protein-based MRI contrast agents must be stable, which means engineered proteins resistances to protease cleavage to prevent degradation *in vivo*, and Gd^{3+}-must bind to protein tightly to avoid competition by physiological cations and inions. Free Gd^{3+} is toxic, with LD_{50} = 0.2 mmol/kg,[104] thus, Gd^{3+} must binds with protein contrast agents and avoid free Gd^{3+} release before excreted out. 2). Protein-based MRI should have high relaxivity to increase the dose efficiency. In this way, total injection dosage of Gd^{3+} can be decreased to reduce to the toxicity caused by free Gd^{3+} release. High relaxivity also improve the sensitivity for the molecular imaging to biomarkers with limited expression level. 3). Protein contrast agents must have a proper size for optimized organ/tissue distribution and blood retention time. Good contrast agents must have fast accumulation in the organ/tissue of interests and should be quickly excreted to reduce the toxicity. 4). As protein imaging reagents, the immunogenicity must be decreased. Thus, PEGlytion of ProCA is very important. 5). Protein contrast agents are preferred to incorporate with targeting moieties to improve the imaging specificity and enable quantitatively imaging tumor biomarkers. Previous members in our lab have shown that by designing a Gd binding site into a scaffold protein CD2 is able to increase of relaxivity by tuning τ_c and other factors, such as secondary coordination shell contributors.[169] However, further increase of metal binding affini-

ty, stability as well as additional metal binding sites to increase payload is challenging.[99, 155, 164, 169]

In order to design protein contrast agents with high binding affinity, we carefully analyzed the metal binding sites in protein and small contrast agents. Like other lanthanide such as Tb^{3+} and Eu^{3+}, Gd^{3+} use oxygen and nitrogen as metal binding ligands and oxygen ligand is the most preferred ligand in protein to interact with Gd^{3+} with an average coordination number of 7.2. EF-hand motif in Ca^{2+} binding proteins is one of the most promising candidates for the design Gd^{3+} binding pocket due to highly similarity of ligand type and ionic radius between Ca^{2+} and lanthanide. For example, Tb^{3+} and Eu^{3+} are usually applied as a fluorescent probe for Ca^{2+} binding. Native Ca^{2+} binding pockets in proteins are usually form penta-bipyramid structure with oxygen ligands, which provide good candidate for the design Gd^{3+} binding proteins. Lanthanide usually binds to EF-hand with ambient binding affinity. The dissociation constant (K_d) for Tb^{3+} binding affinity to grafted calcium binding loop in CD2 protein is always less than 1 μM. The design CCMV particles with CaM EF hand motif only have Gd^{3+} K_d around 3 nM.[109] Carnavan construct Helix-loop-helix contrast agents, while the Gd^{3+} affinity is still not strong enough for *in vivo* applications. To date, there are no successful applications using EF-hand to design MRI contrast agents due to the undesired low Gd^{3+} binding affinity.[108] All of these initial attempts have a Gd^{3+} binding constant far weaker than the estimated stability constant 1.8×10^{-21} M of Gd-DTPA with requires in vivo applications. Additional challenges for developing protein based contrast agents are arised from the lack of accurate methods for determing metal bining afifnity and selectivity with in vivo application. This question will be addressed in Chapter 4.

Our central hypothesis: We hypothesize that a Gd^{3+} binding protein with high relaxivity, metal stability can be achieved by modifying natural metal binding proteins based on key determinants for metal selectivity and relaxivity and our knowledge in protein design and modifications.

In this chapter, I will first introduce our stretegies for design a novel class of ProCAs, named ProCA3. Then, we will show our results on the cloning, expression, purification and modification of ProCA3 variants. Next, I will introduce our studies on structural characterization of this novel class of MRI contrast agents. The other properties, such as metal stability and relaxivity, will be shown in Chapter 4. Further modification of our protein contrast agents by pegylation and large scale production of these developed reagents will be discussed in Chapter 9.

3.2 Results

3.2.1 Design of ProCA3 variants with high metal binding affinities and relaxivities

Based on these requirements for ideal contrast agents, we carefully designed a novel protein-based MRI contrast agents based on a new scarfold protein, PV. Fig. 3-1 shows the modeled structure of designed protein contrast agent (ProCA) ProCA3 based on following rationales. First, to achieve maximal value of r_1 relaxivity of Gd contrast agent at medical field strength, a correlation time of the Gd binding around 10 ns is needed. This can be achieved by embedding a Gd^{3+} binding site in a fixed protein frame with a size between 10 - 20 kDa. Based on our simulation in Chapter 1, protein environment has the addition of secondary water shell that also contributes to the increase of relaxivity. We also achieve high r_2 relaxivity by improving the three key factors of τ_c, q, and outer coordinate shell contributions. PV is a small globular

protein with a molecular weight of about 11 kDa with a rigid structure. The τ_R of Ca^{2+} binding site is similar to the overall τ_R of PV, which provide a great advantage to decrease the τ_R of Gd^{3+}-vector when the Ca^{2+} binding site is engineered as Gd^{3+} binding sites.Second, the engineered metal binding sites should have strong metal binding affinity for Gd and metal selectivity for Gd over physiological metal ions such as Ca^{2+}, Mg^{2+} and Zn^{2+}. Ideally metal binding affinity constants especially for metal selectivity (or kinetic selectivity) should be comparable or stronger than clinical approved ones to overcome NSF effect associated with the Gd toxicity. To design a MRI contrast agent from protein with high thermodynamic stability, we carefully selected PV as the scaffold protein. This protein is very stable at high temperature, resistance to protease cleavage, and has strong Ca^{2+} binding affinities. This protein is a Ca^{2+} buffer protein with K_d for calcium about nM and its metal binding affinity can be modified. [176] PV is distributed in the cytosol of neuronal and muscle cells without any interactions with other proteins.[177] PV also has high thermostability, high solubility, high resistance to the enzyme cleavage, and high tolerate mutations. Based on extensive analysis of structural parameters such as the ligand types, coordination numbers, water numbers, bond angles and lengths of different classes of metal binding sites in proteins [98, 178] and small chelators and key determinants for metal binding affinity, selectivity, conformational change, and dynamic properties of metalloproteins[87, 100, 103, 179-182], we proposes that addition of one more negatively charged ligand at S56D at position 5 in EF-hand motif 1 of PV is able to convert this calcium binding site to Gd^{3+} binding site with desired Gd relaxation properties. A F103W was introduced to allow the determination of metal binding affinity by Tb-FRET. Third, modifying protein surface by PEGylation allows to increase blood retention time and to increase liver preference based on previous studies by us and others.

PV has two EF-hand Ca^{2+} binding sites. EF-hand I in wild type PV has four carboxyl ligands (D52, D54, E60 and E63). EF-hand II of PV WT are formed by the four carboxyl group (D91, D93, D95, E102) and one water ligand (G99) to bind Ca^{2+}. One noncharged oxygen liagnd (S56) directly interact with Ca^{2+}. X-ray structure (Fig. 3-1 and Fig. 3-2) and other technique shows that position 9 in EF-hand I (E60) of PV directly use side chain carboxyl group as oxygen ligand to interact with Ca^{2+}, however, most other EF-hand protein use water as oxygen ligand to interact with Ca^{2+}. X-ray structure of Ca^{2+} indicates that this mutation use one water ligand to bind Ca^{2+}, while carboxyl side chain in this position moved away. Earlier studies from Yang lab and others have show that the metal selectivity for Ln^{3+}/ Ca^{2+} can be achived by increasing numbers of charged residues in the metal coordination shell.[87, 100, 103, 180] To further verify our hypothesis for tuning metal selectivity by charged residues, we further studied the effects of pentacarboxylate EF-hand on Gd^{3+} binding affinity. We created two S56D variant with a modified Gd^{3+} binding site by E60D mutation in both WT and S56D mutant. By this way, total carboxyl group for metal binding in EF-hand I is expected to be decreased. G99D mutants are generated to study the charge effects on the metal selectivity of EF-hand II. Table 3-1 summarizes 6 variants with mutations at the metal binding sites we designed to use to create protein contrast agents with additional modifictions such as and complex formation and Pegylation (Chapter 9).

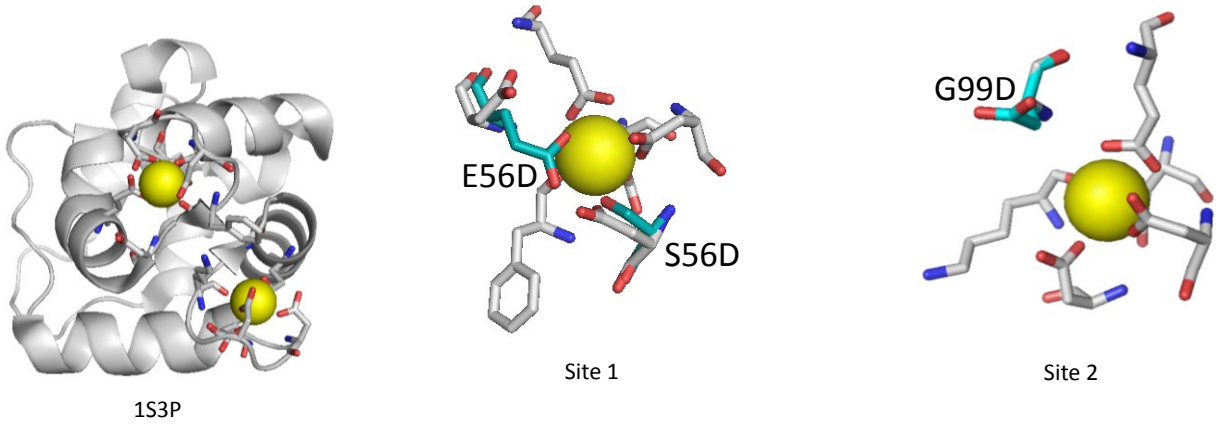

Figure 3-1. The design of Gd^{3+} binding protein based on PV.

Two Gd^{3+} binding pockets were generated on the wild type PV by mutations at S56D, E60D, and/or G99D.

Table 3-1. Design of PV-based contrast agents.

Mutations in EF-hand motifs are labeled with grey background.

Contrast agent	Site 1 (52-63)	Site 2 (91-102)	Tryptophan mutation
PV (ProCA30)	DKDKSGFIEEDE	DKDGDGKIGVEE	N/A
PV (ProCA31)	DKDKSGFIEEDE	DKDGDGKIGVEE	F103W
PV (ProCA32)	DKDKDGFIEEDE	DKDGDGKIGVEE	F103W
PV (ProCA33)	DKDKSGFIDEDE	DKDGDGKIGVEE	F103W
PV (ProCA34)	DKDKSGFIEEDE	DKDGDGKIDVEE	F103W
PV (ProCA35)	DKDKDGFIDEDE	DKDGDGKIGVEE	F103W

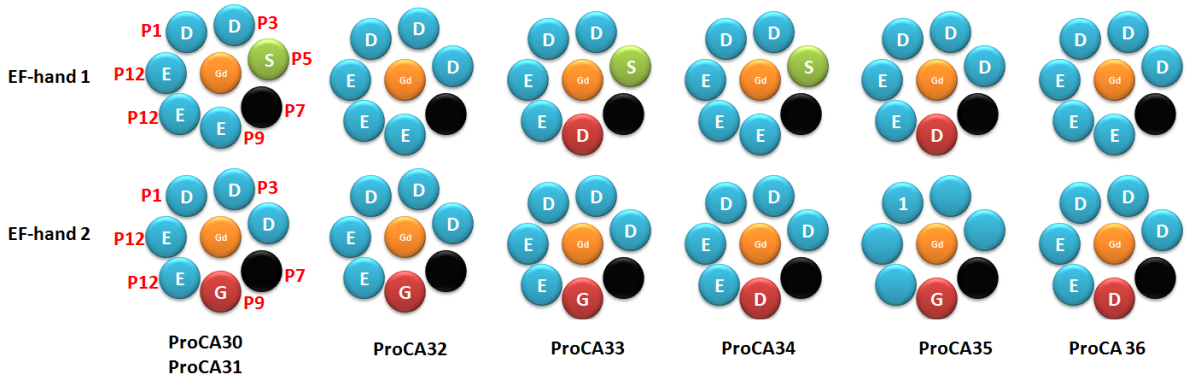

Figure 3-2. Schematic representation of designed Gd^{3+} binding protein.

Two Gd^{3+} binding pockets were generated on the CD and EF-loop of helix-loop-helix structure in wild type PV by mutations at S56D, E60D, and/or G99D. Organ dots stand for Gd^{3+} ion, blue dots stand for charged oxygen ligand for Gd^{3+} from carboxyl group, black dots stand for oxygen ligand for Gd^{3+} from protein main chain, green dots stand for non-charged oxygen ligand for Gd^{3+} from Ser, and red dots stand for oxygen ligand for Gd^{3+} from brighted water molecule. P1, P3, P5, P7, P9 and P12 are the residue postions in EF-hand.

3.2.2 Constructing ProCA3 expression vector

The general procedures for constructing ProCA3 are shown in Fig. 3-3. The Rat a-PV in pcDNA 3.1(+) vector was a generally gift from Dr. Amy Lee at Emory University. In order to construct bacteria expression vector for PV, the plasmid were first inserted the *Nde I* cleavage sequence (CATATG) by DNA insertion methods shown in Chapter 2 and then the new plasmid was double digested by *Nde I* and *Xho I* (New England Biolab). The plasmids of pET20b-7E15, pET22b-A7 and pRSETb were also digested with *Nde I* and *Xho I*. As show from Fig. 3-3 b, pcDNA3.1-PV, pET-20b-7E15, pET-22b-A7 and pRSETb vector were successfully digested by these two enzymes. Then, the double digested PV was subcloned into these vectors by T4-ligase. After insertion, we sequenced the plasmids to make sure that full length of PV was inserted into the corrected location of the plasmids. As shown from Fig. 3-4 a, PV was successfully inserted in to the pET22b plasmids (named pET22b_PV). We next translated the DNA sequence into protein sequence. Sequence alignment (Fig. 3-4 b) shown that protein sequence translated from pET22b-PV is identical with rat PV sequence in the protein data base. These results indicate that PV is successfully inserted into the pET-22b vector. Using similar procedure, we also successfully inserted PV into pET20b and pRSETb vector (data not shown).

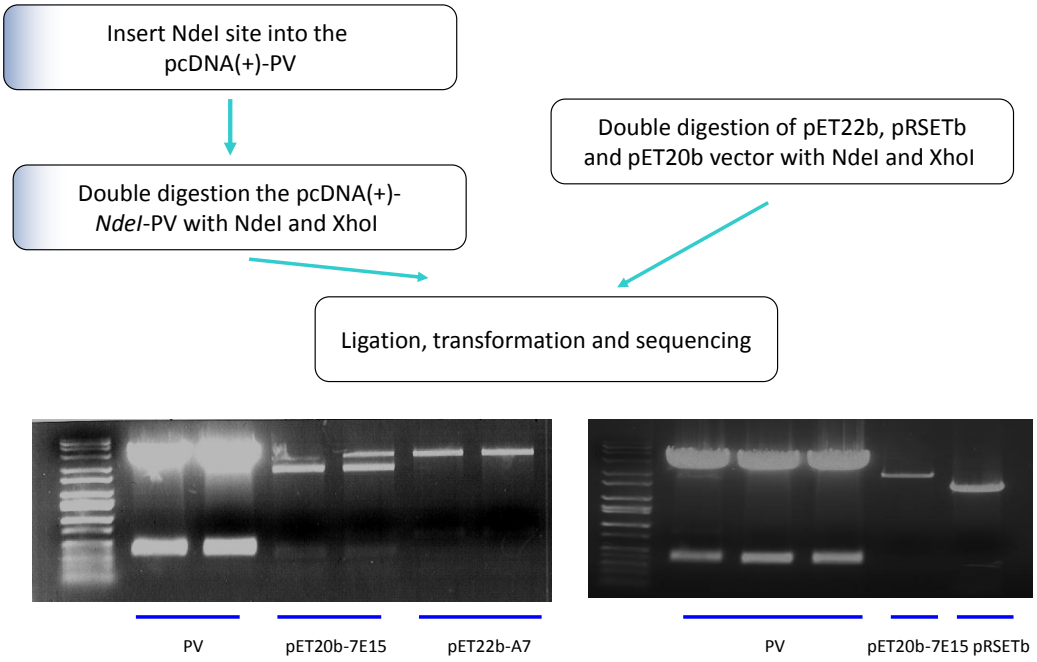

Figure 3-3. Construction of expression vector of PV.

pRESTb, pET20b, pET22b vector and pcDNA3.1 (+)-PV DNA were double digested by NdeI and xhoI restriction enzyme. The digestion products were further separated by electrophoresis (bottom). PV and vectors were further linked by T4 ligase.

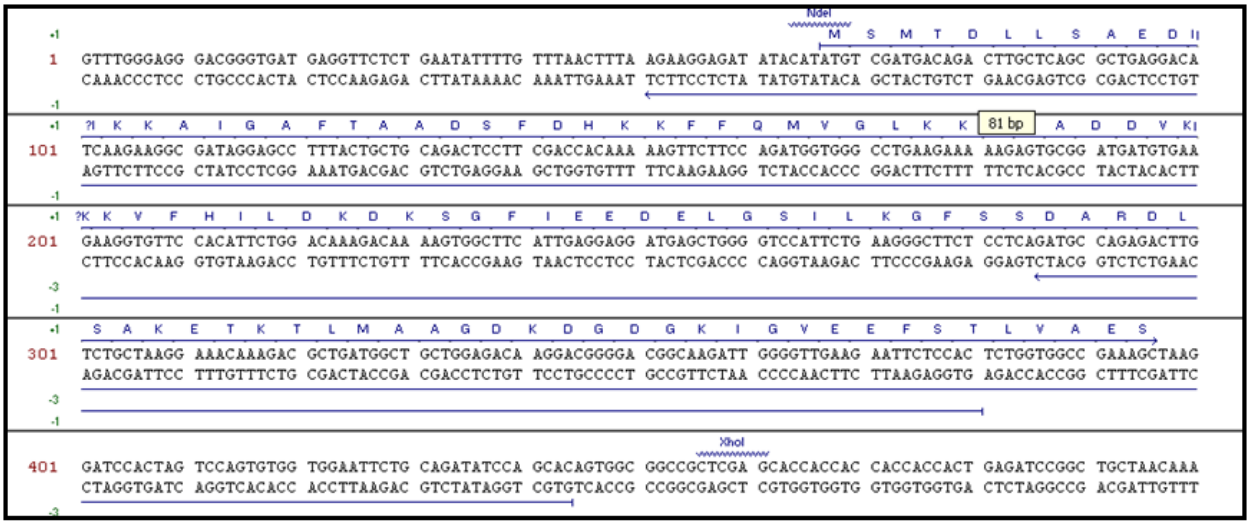


```
pET22b_PV       MSMTDLLSAEDIKKAIGAFTAADSFDHKKFFQMVGLKKKSADDVKKVFHILDKDKSGFIE 60
PV_Rat          MSMTDLLSAEDIKKAIGAFTAADSFDHKKFFQMVGLKKKSADDVKKVFHILDKDKSGFIE 60
                ************************************************************

pET22b_PV       EDELGSILKGFSSDARDLSAKETKTLMAAGDKDGDGKIGVEEFSTLVAES 110
PV_Rat          EDELGSILKGFSSDARDLSAKETKTLMAAGDKDGDGKIGVEEFSTLVAES 110
                ***************************************************
```

Figure 3-4. DNA and protein sequence of PV.

DNA and protein sequence of PV in pET-22b vector were analyzed by vector NTI (top). The protein sequence of PV in pET22b vector (pET22b_PV) shows 100% identity as rat PV sequence in the PubMed (Bottom).

3.2.3 Protein expression and purification

3.2.3.1 Protein expression

We next test the expression conditions of PV in pET22b and pRSETb vectors. PV in two different vectors (pRETb-PV and pET22b-PV) were expressed in LB medium (Fig. 3-5). When the OD_{500} reached to 0.8, the bacteria were induced with 0.1 mM, 0.5 mM or 1 mM IPTG. As shown in Fig. 3-5, the protein greatly expressed after 3 hours induction and same level of expression were observed after IPTG induction overnight. For pRSETb-PV vector, the best IPTG concentration for PV expresion is 0.5 mM and the protein expression level decreased when IPTG concentration increase to 1 mM. However, the best concentration of IPTG for the expression PV in pET22b vector is different from that in pRSETb vector. As shown in Fig. 3-5, 1 mM IPTG can induce the highest level of PV expression in pET22b vector. Compared with the expression levels of PV with different IPTG concentration and in two vectors, we found that the best PV expression condition is pET22b vector and induced at 1 mM IPTG for 3 hr or overnight.

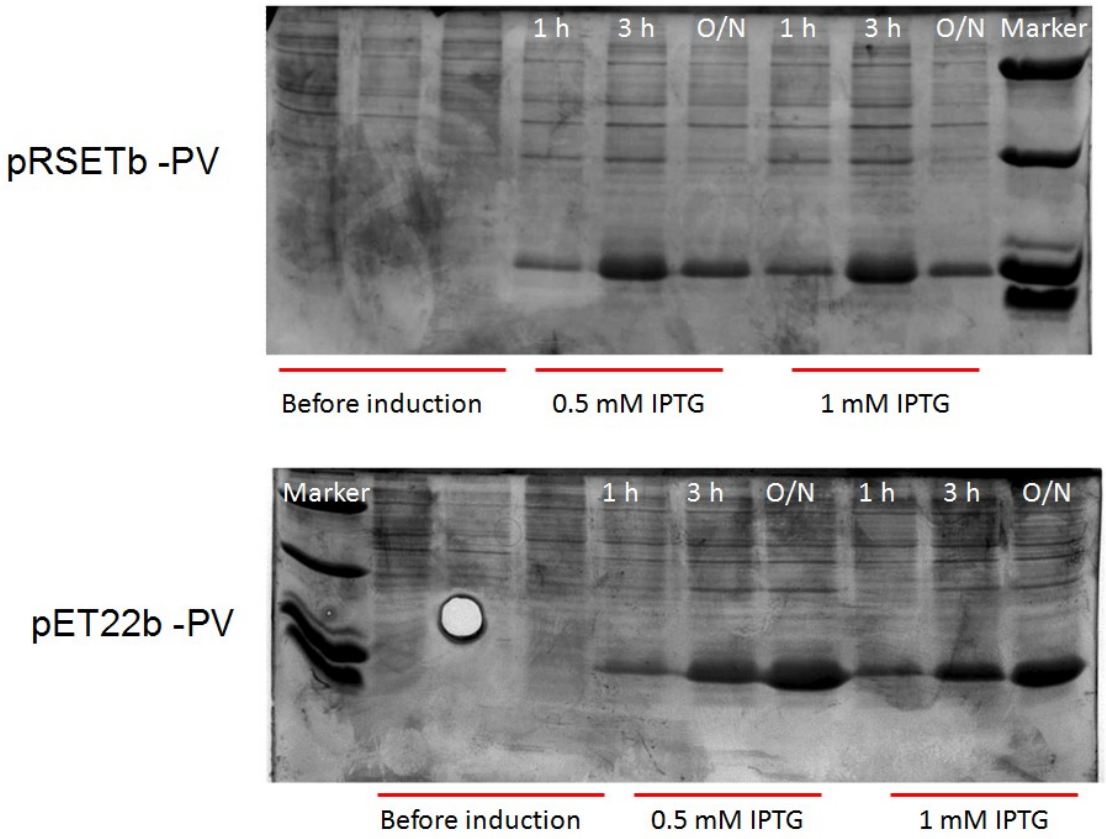

Figure 3-5. The expression of PV by *E. coli*.

pRESTb-PV (left top) and pET22b-PV (left bottom) plasmids were transferred into bacteria BL21-DC3-plysS strain and were further expressed in LB-medium with IPTG induction.

3.2.3.2 Early procedure for PV purification (Protocol 1)

Fig. 3.6 shows the early procedure for PV purification. BL21 plysS bacteria with pET22b-PV transformation were expressed in 2 liter LB medium. When the optical density (OD) reached to 0.8, the bacteria were induced with either 1 mM IPTG. The protein greatly expressed after 3 hours induction. High amount of proteins were expressed in pET22b vectors after cultured at 37 ˚C overnight. After that, the proteins were purified followed by Henzl's [172] protocol with modifications. SDS-PAGE and DNA agarose gel were used to monitor the PV purification. To purify this protein, the bacteria with PV expresion were lysated by French press or sonication. As shown from the SDS-PAGE in Fig. 3-7, PV mainly exists in the supernatant after spinning down at 13000 rpm for 10 min. The purification of PV took the advantage of high thermal stabilities of this protein. The supernatant of bacterial lysate were incubated at 85 ˚C for 5-20 min. After heating and centrifugation, most of the PV was in the supernatant while other proteins were denatured and precipitated by high temperature (Fig. 3-7 A). We then ran two set of FPLC equipped with Hi-Trap Q column to further purify PV. The PV in the first round of FPLC were eluted by 10 mM Tris/HCl, pH7.6, 3 mM EGTA and 1 M NaCl. As shown in the SDS-PAGE in Fig. 3-7 B, the fractions 12 and 13 contains PV with 95% purity. However, DNA agarose gel indicates that fractions 12 and 13 contains DNA and RNA (Fig. 3-7 B), although major DNA peak is shown in fraction 15 and 16. To further purify PV, we collected fraction 12 and 13, added 6 mM $CaCl_2$ and then injected into FPLC. As shown from Fig. 3-7, fraction 4-8 contains PV with high purity. After purified by second round of FPLC, PV with more than 99 % purities were obtained (Fig. 3-7).

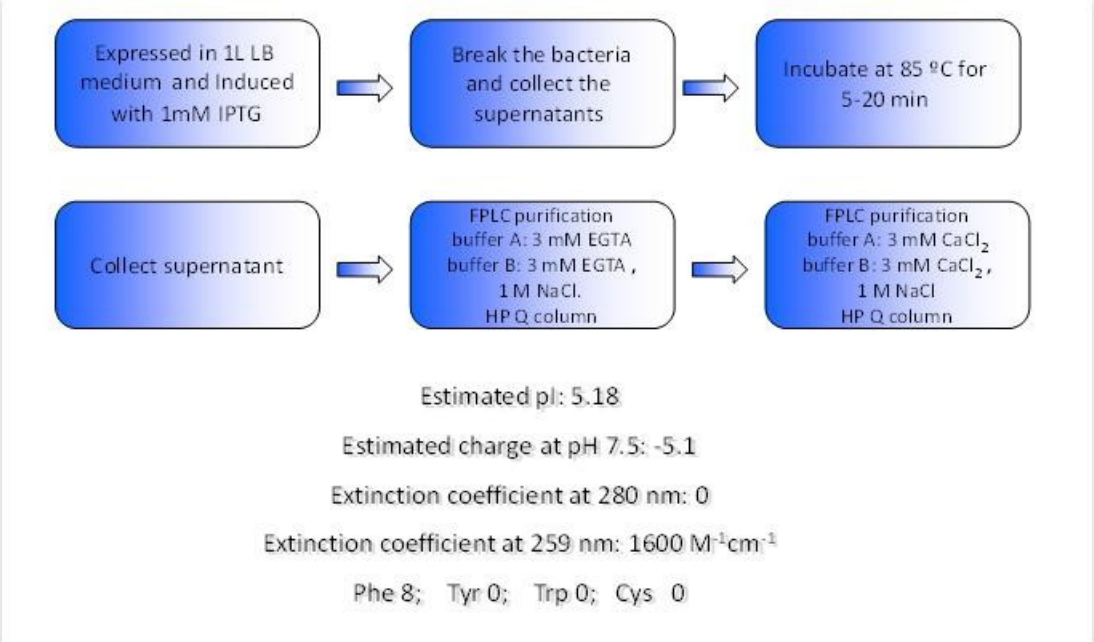

Figure 3-6. Schematic representation of initial strategies for PV purification (Protocol 1).

PV is expressed in *E. coli* after IPTG induction. Then, the bacteria were breaked by sonication and/or French press. The supernatant of bacteria lysate were incubated in a water bath at 85 ˚C for 5-20 min. The bacteria were further purified by two round of FPLC with different elution buffer. For the first round of FPLC, buffer A contains 3 mM EGTA in HEPES buffer at pH 7.2, buffer B contains 3 mM EGTA, 1 M NaCl in HEPES buffer at pH7.2. All the fractions of PV were further purified with second round of FPLC with 3 mM $CaCl_2$ instead of EGTA in both buffer A and buffer B.

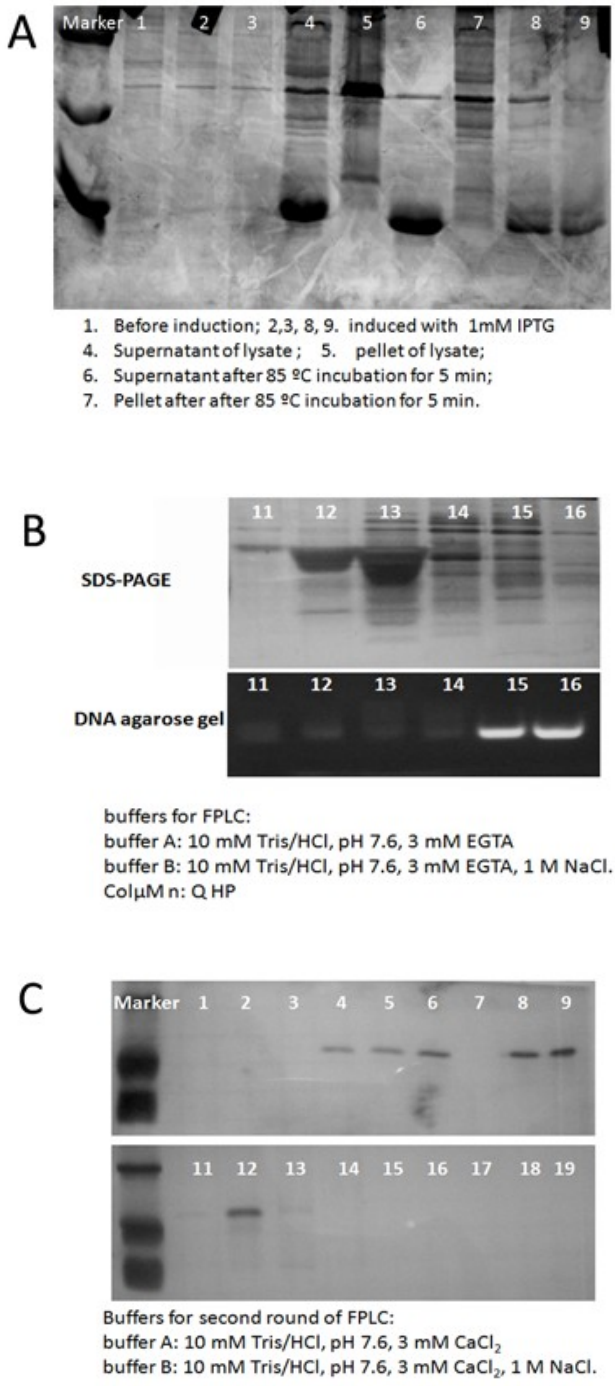

Figure 3-7. Purification of PV with two round of FPLC.

The purification of PV using stretegies shown in Figure 3-6 monitored by SDS-PAGE (A, C and B (top)) and agarose gel (B (bottem)). A. Expresion of PV induced by IPTG and purification of PV

by frech press and heat incubation. B. Different fractions from first round FPLC purification with HP Q colume, monitored by SDS-PAGE (top) and DNA agarose gel (bottem); C. Different fractions from second run FPLC purification equated with Q HP column.

3.2.3.3 Structural characterization of purified PV variants

We next scan the UV absorbance spectra of PV and it mutants. Since pavalbumin wild type doesn't have trptophan and tyrosine, the UV absorbance peak is mainly from Phe at 259 nm. As shown from Fig. 3-8 A, PV wild type has the maximum peak at 259 nm, which is consistent with literature reported carp PV absorbance spectrum.[183] PV variants with tryptophan showed the UV absorbance peak at 280 nm and a sharp peak at 285-290 nm (Fig. 3-8B, C, D), which is also consistent with literature reported absorbance spectrum of PV with F103W mutation[184]. UV absorbance spectrum also indicates that purified PV variants do not have DNA or RNA contamination.

We further perform MALDI-mass analysis to verify our purified PV (Fig. 3-9). The molecular weight of the purified protein is 11776.8 kDa, which is consistent with the calculated value of PV (11776 kDa).

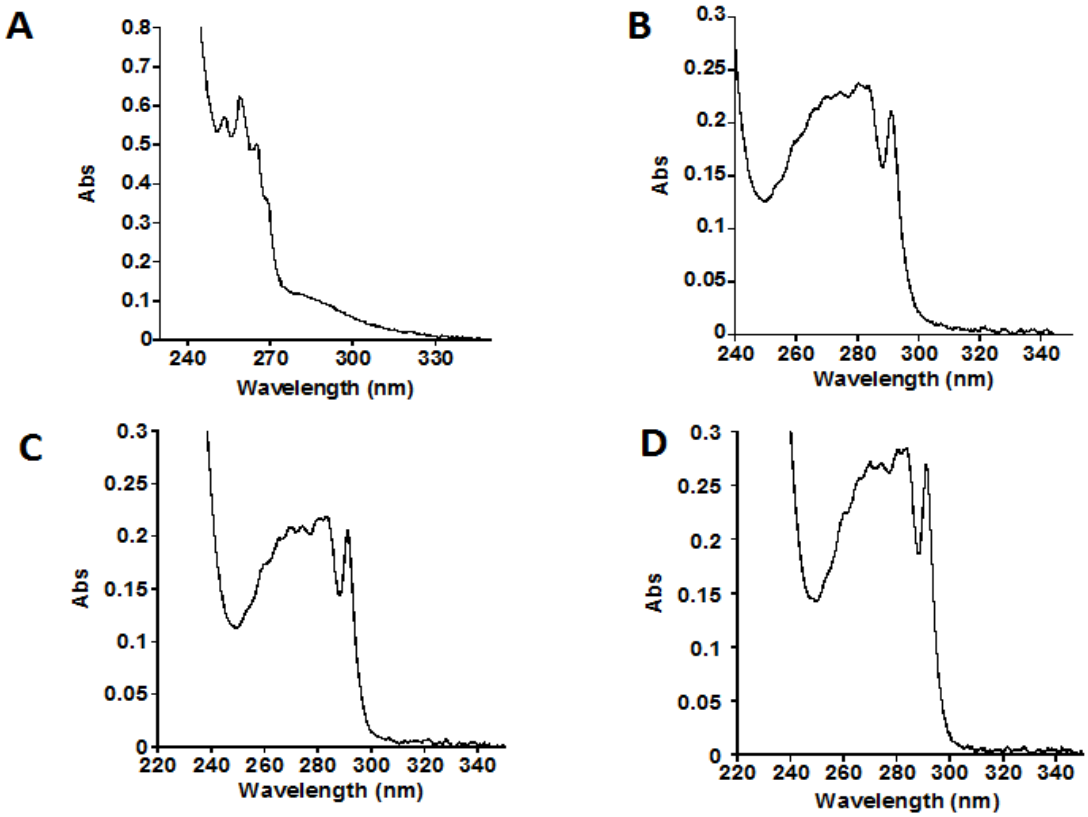

Figure 3-8. UV spectra of PV.

UV spectra of PV wild type (A) and its variants: PVF103W (ProCA31) (B), PVS56DF103W (ProCA32) (C), and PVS60DF103W (ProCA33) (D).

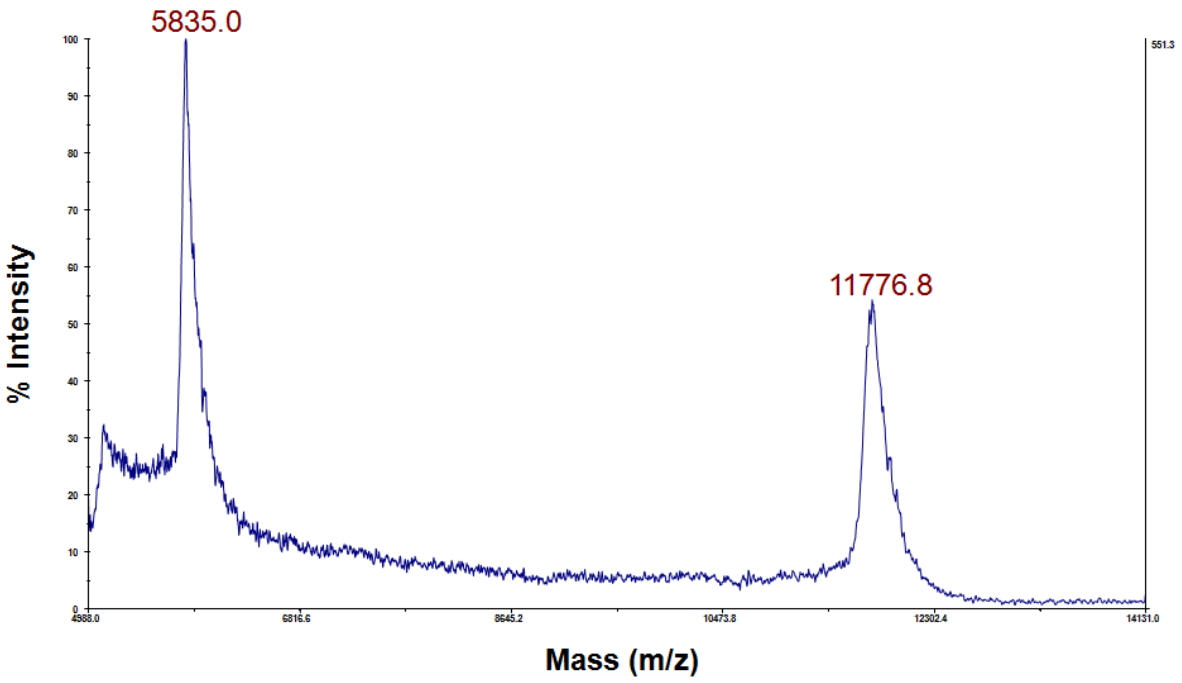

Figure 3-9. Mass spectra of PV.

The expected MW of PV is 11776 kDa. The MALDI measured molecular weighte of PV is 11776.8 kDa.

3.2.3.4 Further optimization and simplification of for PV purification (Protocol 2)

Previously, we are able to obtain the recombinant PV and its variants using heating combined with two round of FPLC in the present or absent of Ca^{2+} (Fig. 3-6). Using this method, we are able to obtain PV with 99% purity. However, lots of proteins were lost during these two sets of FPLC. In order to improve the yield of PV, remove DNA contamination more efficiently and simplify the purification procedure, six major modifications were made based on previous purification protocol (Fig. 3-6). 1). We added additional step before FPLC for DNA precipitation. We added 3 % streptomycin sulfate and incubated at 4°C overnight. After spin down at 13000 rpm for 10 min the supernatant were incubated at 85°C for 5 min. After spin down, the supernatant was dialysis against 10 mM Tris/HCl at pH 8.0 before injecting into FPLC column. 2). We increased the buffer pH 7.5 to 8.0. Since the Q column is anion exchange column, increasing the pH of buffer improves the binding of PV to the column. 3). We found that our protein can be eluted out from Q column at 200 mM NaCl, therefore, we decrease the percentage of buffer B (containing 1 mM NaCl) during elution from 70% to 25% of buffer B. 4). The flow rate of FPLC was decreased from 5 ml/min to 2 ml/min to improve the binding of the pavalbumin to Q column. 6). We use 9 column volumes to let buffer B slowly increase from 0% to 25% (Fig. 3-10). The very slow increase of salt gradient further facilitates the separation between PV and DNA. After FPLC remaining small fragment of DNA can be further removed by concentrating protein using through 3 kDa membrane.

The FPLC prufication curve is shown in Fig. 3-11A. The UV absorbance at 280 nm from FPLC detector shows four peaks during buffer B elution. Each peak were collected and then tested by UV spectroscopy, SDS PAGE and agarose gel. As show from Fig. 3-11A, the third frac-

tion (28-30) has a single band at 11 kDa, which is consistent with the molecular weight of PV. UV spectrum of this frection is the same as the PV F103W mutants in the old methods in 3.2.3.2. The first and second peaks do not have any protein and the last peak contains protein with a molecular of 30 kDa. DNA and UV absorbance data show that the peak 1 and peak 4 has a lot of DNA/RNA because these frections have high obsorbance at 260 nm. The final yield of this protein is about 50-70 mg per liter bacteria expression in LB medium. Taken together, this new method simplified PV purification procedure with much higher yield compared with the early purification methods described in section 3.2.3.2.

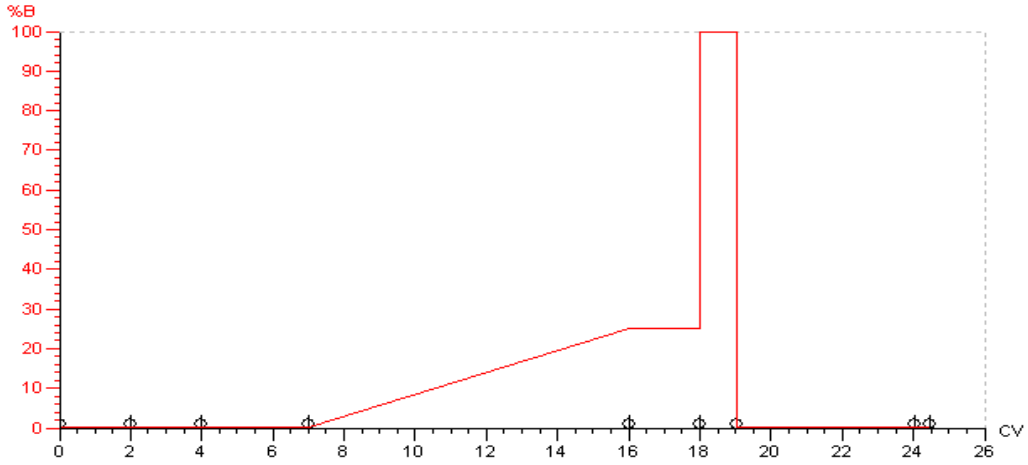

Figure 3-10. The FPLC program for ProCA3 variants purification.

After binding to the column, the unbounded component were first washed with 7 column volume (CV) of buffer A (10 mM HEPES buffer at pH 8.0). Then, buffer B (10 mM HEPES buffer, 1 M NaCl at pH 8.0) concentration was increase to 25 % within 7 CV. We further wash the column with 25% of buffer B for 2 CV and then increase to 100 % of buffer B of 1 CV to wash out every component bounded to the column. At last, the column was requilibriated with 100% buffer A for 5 CV.

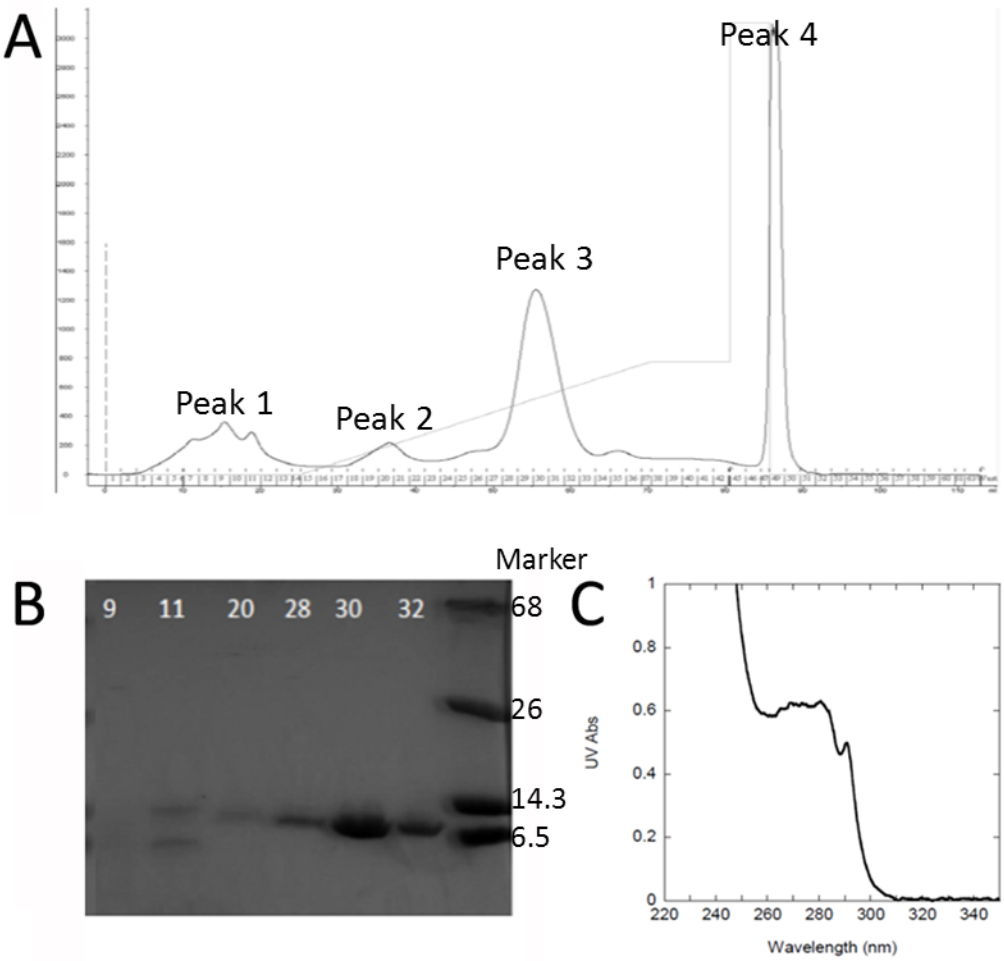

Figure 3-11. FPLC fractions, SDS-PAGE and UV absorbance spectrum analysis of ProCA3 purification with improved protocol.

Only one round of FPLC are required in this new purification method. There are four major peaks during FPLC purification (A). SDS-PAGE results (B) show that the fractions 28-32 contain ProCA3 with more than 99% purity. UV spectrum of fraction 28-32 (C) shows the typical spectrum of ProCA3, which has the maximum absorbance at 280 nm and a shoulder peak at 285 nm. The UV absorbance at 260 nm is lower than that at 280, indicating the DNA concentration in these fractions are very low.

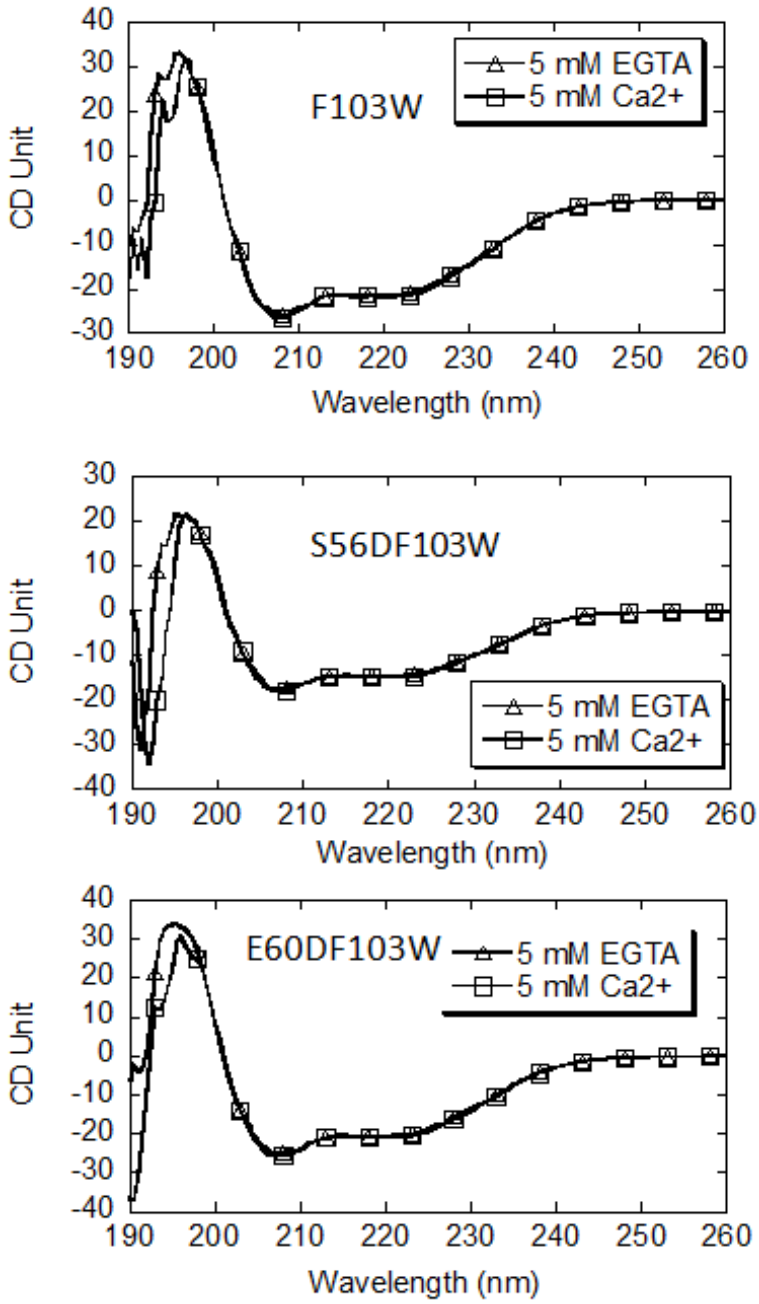

Figure 3-12. Conformational analysis of ProCA3 variants in the presence Ca^{2+} or EGTA by CD.

The ProCA3 variants shows typical helix structure in CD and the secondary structures of proCA3 variants do not change in the presence Ca^{2+} or EGTA at 10 mM Tris buffer at pH 7.2.

3.3 Discussion

3.3.1 Selection of scaffold protein

The selection of scaffold protein is essential for the design of protein based MRI contrast agents. The scaffold protein must have above unique features: 1). The scaffold must stable and resistant to the enzyme cleavage; 2). The scaffold protein should have very good solubility; 3). To engineer metal binding pocket, scaffold protein must tolerate to mutations; 4). The scaffold should have no interference of its nature function such as interacting with cell membrane receptors to trigger signaling pathway; 5). The scaffold should have a molecular size between 10 kDa and 20 kDa to have good tumor penetration and proper blood retention time.

Due to above requirement, we choose PV as our scaffold protein to develop new generation of protein-based MRI contrast agents. PV is a small calcium buffer protein abundant in the central neuron system and muscle cells. The main biological role of this protein is to serve as a buffer to modulate cytosolic Ca^{2+} concentration. There is no reported interaction between PV and any other protein. This protein also doesn't have extracellular cellular functions. PV is very stable, and it does not precipitated even in boiling water. This protein is also resistant to enzyme cleavage.

3.3.2 Design Gd^{3+} binding pocket in PV

We next design Gd^{3+} binding sites into PV. We named these PV variant as ProCA3. PV has two Ca^{2+} binding sites with high binding affinity. Unlike other calcium binding proteins, Ca^{2+} binding to PV do not induce large conformational changes. Henzl et al.,[185] report that the Ca^{2+} binding affinity of some PV variants is higher than EGTA. Since lanthanide usually bind to pro-

tein much stronger than Ca^{2+}, we hypothesis the PV also has higher Gd^{3+} binding affinity than that of Ca^{2+}. We use two strategies to design optimized Gd^{3+} binding affinity: 1) introducing more negative charge in the metal binding pocket (S56D, G99D); 2) change the ligand types (S56D, E60D). Henzl et al.,[185-187] reported that mutating key residues in EF-hand can alter the Ca^{2+} binding affinity. Double mutation S56DE60 in PV dramatically increase Ca^{2+} binding affinity ($K_1 = 1.65 \times 10^9\ M^{-1}$ $K_2 = 3.0 \times 10^8\ M^{-1}$ for S56DE60D mutant, and $K_1 = 1.2 \times 10^8\ M^{-1}$ $K_2 = 1.2 \times 10^8\ M^{-1}$ for WT PV). Therefore, we want to further study the effects of these mutations on Gd^{3+} binding affinity.

In addition, we want to study the relaxivity of PV with different Gd^{3+} binding ligands. Mutations on EF hand could also change the water coordination number. The position 9 in EF-hand usually interacts with Ca^{2+} through one bridged water molecular.[112, 115, 188] The EF-hand I of PV, however, use side chain of Glu to bind to Ca^{2+}. We designed E60D mutant to introduce more water ligand into the Gd^{3+} binding pocket.

The metal binding affinity, relaxivity and water number of designed ProCA3 variants will be tested in Chapter 4 since these experiments reqires methodology development.

3.3.3 ProCA3 expression, purification and PEGlytion

After obtaining the ProCA3 variants mutants, we established the protein expression and purification protocol. Since ProCA3 is very stable at high temperature, it is very easy to separate this protein from other proteins by incubating at 85˚C for 5-20 minutes. However, we face a big problem to separate ProCA3 from DNA/RNA, since DNA/RNA is also soluble at high temperature. We use two round of FPLC to completely separate between ProCA3 and DNA/RNA.

Since two rounds FPLC in Protocol 1 is time consuming and decrease the yield of ProCA3, we further simplified the purification procedure for ProCA3 in Protocol 2. Since streptomycin sulfate precipitates DNA, we add 3% streptomycin sulfate to precipitate DNA. Our results indicate that streptomycin indicate precipitate large amount of DNA. By adding this step, we greatly reduced the DNA concentration before injection to the FPLC. Since DNA concentration is decreased, we only need one round of FPLC to separate ProCA3 and DNA. As shown from Fig. 3.10, we successfully purified ProCA3 with one round of FPLC. Optimization of ProCA3 purification greatly increases the yield and decreases the time and efforts for the ProCA3 purification.

3.3.4 Standard protocol for PV purification

After explore different methods for PV purification, we established the standard protocol for PV purification. This protocol contains several steps: lyate the bacteria, 85˚C incubation, DNA precipitation and FPLC separation.

Since this protein is a super dissolving and super stable protein (shown later), the protein is always in the supernatant even heat at 85˚C for 5-20 min. However, DNA is also very stable at 85 ˚C and it is very hard to separate the DNA from PV. We added 3% of streptomycin sulfate to precipitate DNA. After try different conditions of FPLC, we found that Q column is the most efficient column to separate DNA and PV. The SDS-PAGE shows that the fractions 28 to 32 are the major peak for PV, although the small peak around fraction 20 also contains our proteins. The last peak (47-50) are DNA/RNA and some protein peak, which can be detected by agarose gel with EB staining or SDS-PAGE with Commassie brilliant blue staining (data not shown). According the UV absorbance and $\varepsilon_{280} = 7200\ M^{-1}cm^{-1}$, the highest yield of ProCA32 we can get from 1 liter LB medium is 50-70 mg.

3.3.5 Secondary and teriary strucure analysis of PV mutants

Far-UV CD spectra of PV variants were detected in the present or absent of Ca^{2+}. As show in Fig. 3-12, these mutants share the same alpha-helical structure, characterized by the low CD signal peak at 208 nm and 225 nm. We also compared with the secondary conformational changes in the present or absent of calcium. The CD signal of F102W, S55DF102W and E60DF103W do not have significant conformational changes, which is consistent with the reported NMR and X-ray structure of apo- and holo-PV variants.[187, 189, 190]

3.4 Summary

To design novel protein-based MRI contrast agents (ProCA3), we carefully selected PV as our scaffold protein based on our criteria for an ideal contrast agent. This protein is well packed, highly stable, highly soluble, tolerant to mutations, have a rigid structure and metal binding sites. There is also no reported interaction between PV and other proteins.

We have designed 7 variants with mutations on the metal binding sites to improve Gd^{3+} binding affinity, metal selectivity by tuning charged numbers in the coorinaton shell and relaxivity of ProCA3 by altering water number q associated to ligand total numbers. We have constructed vectors for the bacteria expression.

We have optimized the bacterial expression and tag-less purification procedures of ProCA3 by selecting expression straints and removal of DNA contaimnations.

After obtaining purified ProCA3, we are able to test the metal selectivity, relativity, metal coordination ligands, and serum stabiltiy of ProCA3. We are also able to purify and PEGylate ProCA3 variants (also refer to Chapter 9) for *in vivo* study, such as MR imaging, molecular imaging, biodistribution and toxicity.

4 STABILITY, METAL SELECTIVITY AND RELAXIVITY OF PROTEIN-BASED MRI CONTRAST AGENTS

4.1 Introduction

As discuessed in Chapter 1, to develop contrast agents with superior safety profile, the contrast agents must have high Gd^{3+} stability, high metal selectivity and relaxivity. Long term toxicity of the contrast agents generally coming from the free Gd^{3+} release due to the competition of other physiological cations and ionons, such as Zn^{2+}, Mg^{2+} and PO_4^{3+}. Gd^{3+} has ionic radius of 0.93 Å, which is similar to the ionic radius of Ca^{2+}. Thus, Gd^{3+} can bind to the physiological Ca^{2+} binding sites. Such binding disrupt the dynamic function of calcium binding proteins. Besides, long term accumulation of Gd^{3+} could cause NSF (Nephrogenic systemic fibrosis), a lethal disease in the renal impaired patients.[125] A safe MRI contrast agent with high metal stability and Gd^{3+} selectivity is highly needed to reduce the toxicitiy caused by MRI contrast agent injection.

Tradditionally, pH titration methods were used to determine the meal binding affinities for the small chelators (refs). Small chlators, such as DTPA, has a Gd^{3+} binding affinity of 1.8 x 10^{-21} M. Due to multiple protonations of residues in proteins, traditional methods such as pH titration can not be applied to determine the K_d between ProCA and Gd^{3+} or other metals. Tb^{3+}- or Eu^{3+}- FERT methods are used to measure protein-metal binding affinity measurement. However, these methods are only sensitive to determine a K_d of around 1 μM or above. Due to this limitation, the metal binding affinity for Tb^{3+} for ProCA1 we previously reported as around 10^{-7} M. To date, while several other methods such as the Ca^{45} flow dialysis, equilibrium dialysis, florescence dye titration and NMR were been applied to determine metal binding afifnities for

calcium binding proteins [185, 191], the Gd^{3+} binding affinity of EF-hand binding proteins are not accurately reported. The Ca^{2+} binding affinity of all EF-hand proteins such as PV can reach to 10^{-9} M. Thus, a method to accurately mesure Gd^{3+} binding affinity in the range between 10^{-22} and 10^{-18} M should be developed to study the Gd^{3+} affinity to ProCA variants.

Relaxivity is another key parameter for MRI contrast agents as discussed in Chapter 1. The MRI signals are generated based on the different relaxation properties of protons. However, such differences are very small among organs *in vivo*. The contrast and sensitivity of MRI can be improved by administrate the contrast agents. MRI contrast agent works as "catalyst" to catalyze the relaxation properties of each water molecule. By differential distribution *in vivo*, MRI contrast agents make the relaxation properties difference in each organ. The relaxivity of clinical MRI contrast agent is around 5 mM^{-1} s^{-1}. The therotical maxium relaxivity, however, is about 100 mM^{-1} s^{-1}. There is a strong need to develop MRI contrast with high relaxivity.

In this chapter, we first report our efforts in developing a sensitive new method to evaluate metal binding affinity and selectivity of metalloporteins. We then report our studies on determining Gd^{3+} binding affinity and selectivity of our developed protein contrast agents ProCA3 series designed in Chapter 3 based on determinants for metal binding. We further measured the water number of these contrast agents to test the hypothesis of tuning relaxivity by tuning water number without trading off metal binding affinity.

4.2 Results

4.2.1 Thermodynamic stability study and metal selectivity of protein based MRI contrast agents.

We developed metal-chelator buffer system to control of the free metal ion in solution. In this way, we can successfully obtain the accurate K_d between ProCA3 variants and metal ions such as Ca^{2+}, Mg^{2+} and Tb^{3+}.

4.2.1.1 Determine Ca^{2+} binding affinity of ProCA variants using Ca^{2+}-EGTA buffer system.

Some of the ProCA3 variants has been reported to have strong K_d around 10^{-9} M to Ca^{2+},[191] which is even stronger than EGTA. We hypothesis that our ProCA3 variants also has similar Ca^{2+} binding affinity compared with these reported ProCA3 variants. However, such strong K_d cannot be accurately measured by the regular fluorescent titration methods due to the limitation of background free metal in solutionand the sensitivity of this methods. In principle, an accurate method for Kd determination requires the use of protein and metal concentration close to the K_d. However, Tb^{3+} and other durect method requires protein and metal concentration to be nM or above. To overcome these limitations, we developed metal chelator buffer system to control the free Ca^{2+} concentration between 10^{-13} M to 10^{-8} M, and then we can use the fluorescence change of Phe or Trp to probe the Ca^{2+} binding affinity at extremely low concentration of free Ca^{2+}.

Fig. 4-1 shows our experimental procedure of Ca^{2+}-EGTA buffer system. This buffer system contains 5 mM EGTA, 100 mM KCl, 50 mM HEPES at pH 7.2. ProCA3 variants were added into this system to a final concentration of 5 μM before the experiments. As we can see, this

system contains 1000-times high concentration of EGTA than ProCA3. Therefore, majority of ProCA3 variants should maintain app-form. We then titrated different concentration of Ca^{2+}. We can calculate free Ca^{2+} concentration according to Equation (2-1). Ca^{2+} binding to ProCA3 variants cause the fluorescent intensity changes, therefore, we are able to derive the fraction of the Ca^{2+} bonded ProCA3 variants based on the fluorescent signal changes in each titration point (Fig. 4-1 B). We then fit the titration points (Fig. 4-1 C) using Hill Equation (Equation (2-2)).

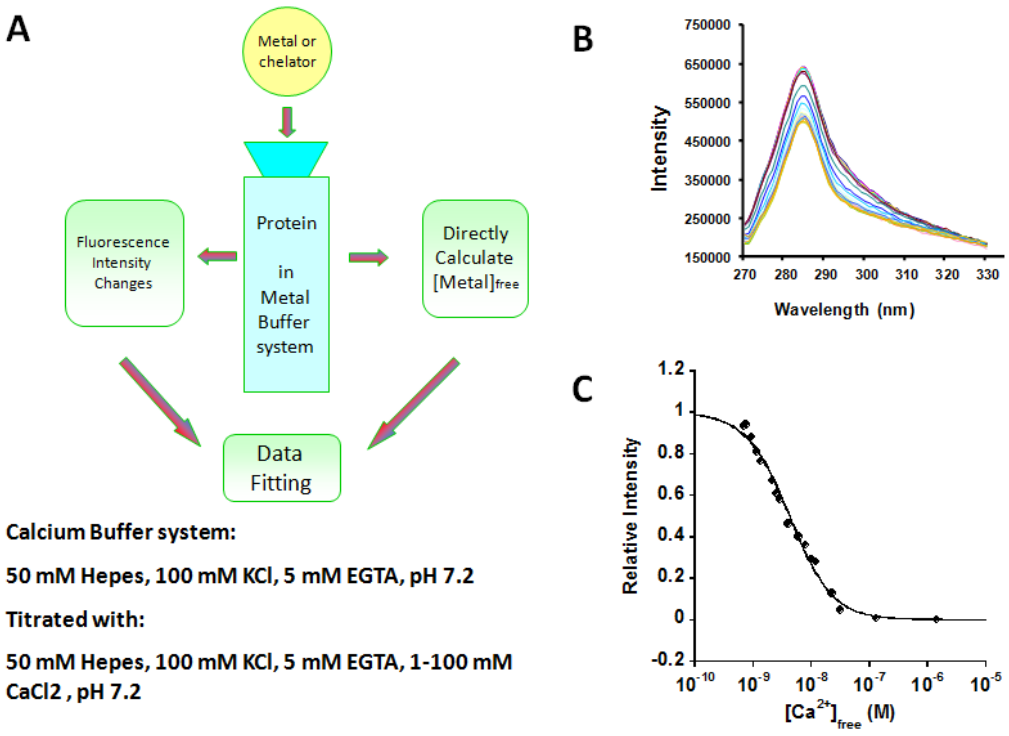

Figure 4-1. Determine Ca2+ binding affinity to ProCA variants by metal chelator buffer.

This buffer system contains 2-20 µM of ProCA variants, 5 mM EGTA, 100 mM KCl, 50 mM HEPES at pH 7. This system contains 1000-times high concentration of EGTA than ProCA3. Due to strong K_d of EGTA to Ca^{2+} and high concentration of EGTA, the majority of ProCA3 variants should maintain apo-form. When we titrated different concentration of Ca^{2+} in this system, the majority of Ca^{2+} binds to EGTA. Due to dynamic equlibium, low concentration of Ca^{2+} will be stay as free form. These "free" Ca^{2+} can bind to ProCA variants. We can calculate free Ca^{2+} concentration according to Equation (2-1). Ca^{2+} binding to ProCA3 variants cause the fluorescent intensity changes, therefore, we are able to know the fraction of the Ca^{2+} bonded ProCA3 variants based on the fluorescent signal changes in each titration points (B). We then fit the titration points using Hill Equation (B, Equation (2-2)).

Fig. 4-2 shows how we calculate the free Ca^{2+} concentration based on total concentration of Ca^{2+} in the Ca^{2+}-EGTA buffer system. The total Ca^{2+} of the buffer system contains three major sources: (1) residue Ca^{2+} in the buffer, even after dialysis with Chelex-100 bag to deprive Ca^{2+}; (2) Ca^{2+} which originally binds to ProCA3 variants were introduced to the system when adding ProCA variants before titration; (3) Ca^{2+} titrated in to the system. The total residue Ca^{2+} concentration, $[Ca^{2+}]_{Residue}$ were measured by Fura-2 dye, which is around 10^{-7} - 10^{-6} M after chelex-100 treatment. According to Equation (2-1), $[Ca^{2+}]_{residue}$ contributes 10^{-12} - 10^{-11} M of free Ca^{2+} when total EGTA concentration is 5 mM. We add 5 μM ProCA3 variants in experiments. If $Kd_{ProCA\ to\ Ca}$ is 10^{-9} M, then we introduced 10 μM of total Ca^{2+} into the system, which further contribute 7.37×10^{-10} M of free Ca^{2+} in the system. The total Ca^{2+} concentration in each titration point is tightly controlled, and we know the exact total Ca^{2+} concentration have been titrated into the system. For example, if we titratated 100 μM of total Ca^{2+} in the system, it generates 7.51×10^{-9} M free Ca^{2+} in the system according to Equation (2-1).

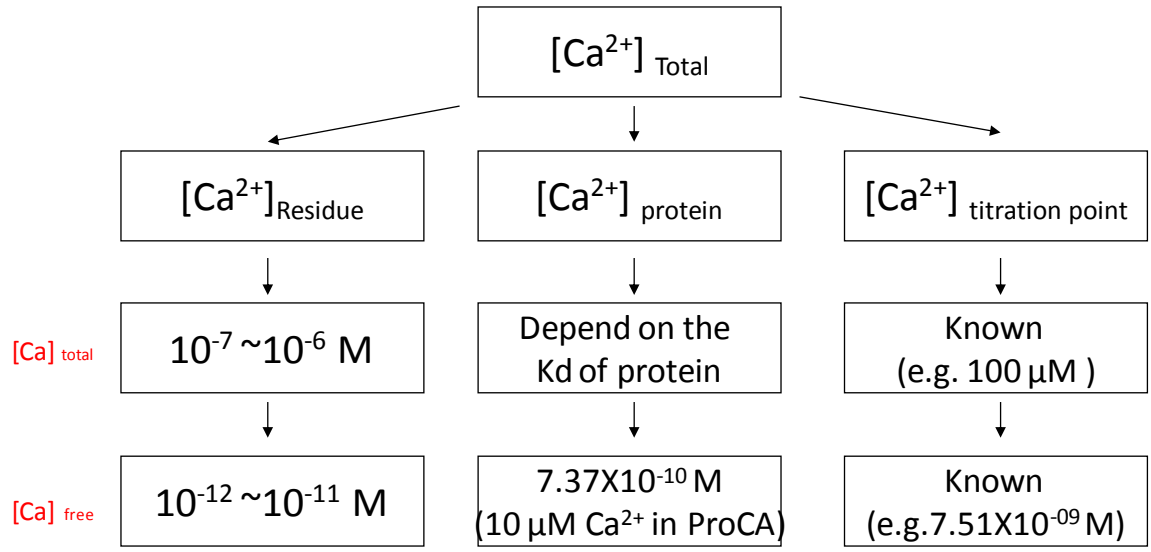

Figure 4-2. Schematic demonstration of free Ca^{2+} calculation in Ca-EGTA buffer system.

Ca^{2+} in our system is contributed from three major sources: residue calcium in the buffer, calcium introduced by adding ProCA variants and calcium added during titration. According our calculation by Equation 2-1, residue calcium in the buffer contribute 10^{-12}-10^{-11} M free calcium to the Ca-EGTA buffer system. Since ProCA3 variants has a K_d to Ca^{2+} around 10^{-8} M, adding calcium bounded ProCA3 variants also introduce free Ca^{2+} in the system. For example, 10 µM Ca^{2+} in ProCA introduce 7.37×10^{-10} M free calcium in the buffer system. The total calcium tritrated in the system is know and well controlled during titration, we can then calculate free Ca^{2+} concentration in the system during titration. For example, adding 100 µM total Ca^{2+} will generate 7.5×10^{-9} M free Ca^{2+} in the system.

Fig. 4-3 shows Ca^{2+} titration results of ProCA3 variants using Ca^{2+}-EGTA buffer system as described above. ProCA30 has 10 Phe residues and do not have Trp and Tyr. Therefore, we excite the Phe fluorescence at 260 nm and collect emission fluorescence spectrum between 270-320 nm. As we can see from Fig. 4-3 A, the fluorescence signal decreases during the titration and finally reaches the plateau. ProCA31, ProCA32, ProCA33 has one Trp residue of each. Thus, we exite the Trp fluorescence at 280 nm and collect emission spectrum between 290-370 nm (or 300-340 nm). The fluorescent signalsincrease during the titration and finally reach the plateau (Fig. 4-3 B,C,D).

Table 4-1 shorws the Ca^{2+} binding affinity of ProCA3 variants. Wild type PV (ProCA30) has a Ca^{2+} binding affinity of 8.35×10^{-9} M. F103W mutation (ProCA31) increase Ca^{2+} binding about 2 folds. Introducing one more negative charged ligand (S56DF103W) in EF-hand I does not change Ca^{2+} binding affinity, while replacing Glu ligand to water ligand (E60DF103W) decreases calcium binding affinity when compared with F103W mutant.

4.2.1.2 Determine Mg^{2+} binding affinity of ProCA variants using Mg^{2+}-EGTA buffer system.

Similar to Ca^{2+}-EGTA buffer system, we use Mg^{2+}-EGTA buffer system to determine the Mg^{2+} binding affinity to ProCA3 variants (Fig. 4-4). ProCA30 and ProCA31 has similar K_d to Mg^{2+} about 2×10^{-5} M. Interestingly, ProCA32 has 10 times stronger K_d to Mg^{2+} than ProCA31 and ProCA32. Such dramatic increase of K_d to Mg^{2+} of ProCA32 may caused by one more negative charged residue in EF-hand I of ProCA32.

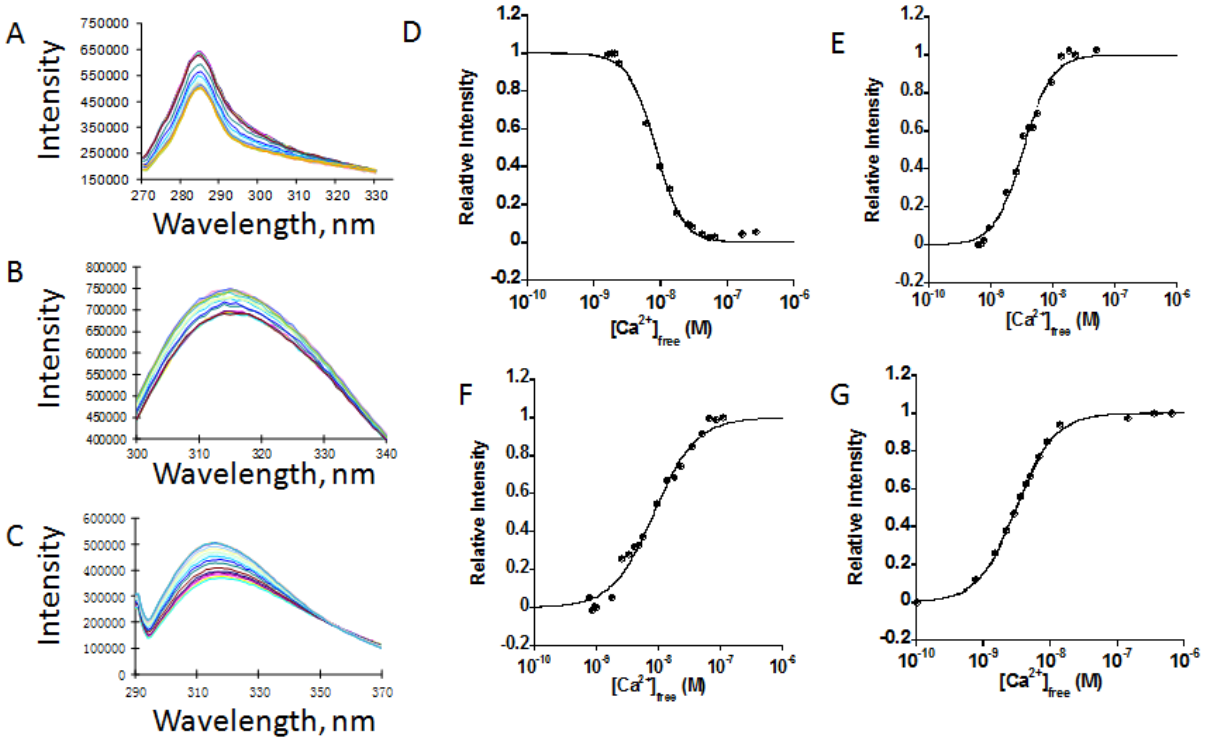

Figure 4-3. Determine K_d of Ca^{2+} to ProCA3 variants.

K_d of Ca^{2+} to ProCA3 variants were determined by Phe (A)/ Trp (B, C) fluorescence titration using Ca-EGTA buffer system in 50 mM HEPES 100 mM NaCl at pH 7.2. Phe fluorescence decrease (A, D) in wild type ProCA3 or Trp fluorescence increase in ProCA3 mutant (B,E: ProCA31; C,F: ProCA32, G: ProCA33) were observed when increase total Ca^{2+} concentration in the system. Free Ca^{2+}concentration were calculated according to the method described by Fig. 4-1 and 4-2. The K_d of Ca^{2+} to ProCA3 variants were calculated by Hill equation (Equation 2-2).

Table 4-1. The Ca^{2+} binding affinity of ProCA3 variants.

	Kd	Ka	lg Ka	n
ProCA30	8.35E-09	1.20E+08	8.08	2.1
ProCA31	3.32E-09	3.01E+08	8.48	1.9
ProCA32	3.07E-09	3.26E+08	8.51	1.5
ProCA33	8.83E-09	1.13E+08	8.05	1.2

The binding affinities of ProCA3 variants were determine at in 50 mM HEPES 100 mM NaCl at pH 7.2.

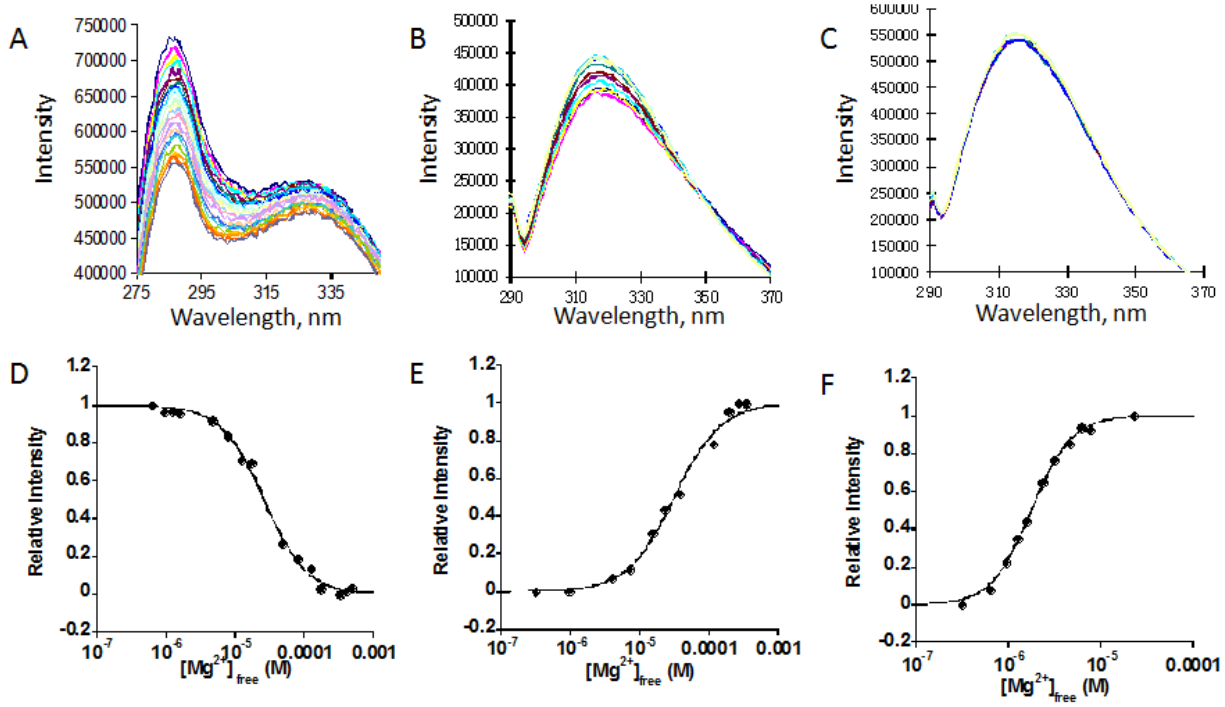

Figure 4-4. Determine Kd of Mg^{2+} to ProCA3 varants.

K_d of Mg^{2+} to ProCA3 variants were determined by Phe (A, excitation at 260 nm)/ Trp (B, C, excitation at 280 nm) fluorescence titration using Mg-EGTA buffer system in 50 mM HEPES 100 mM NaCl at pH 7.2. Phe fluorescence decrease (A, D) in wild type ProCA3 or Trp fluorescence increase in ProCA3 mutant (B, E: ProCA31; C,F: ProCA32) were observed when increase total Mg^{2+} concentration in the system. Free Mg^{2+}concentration were calculated according to the method described by Fig. 4-1 and 4-2. The K_d of Mg^{2+} to ProCA3 variants were calculated by Hill equation (equation 2-2).

4.2.1.3 Determine Tb^{3+} and Gd^{3+} binding affinity of ProCA3 variants using Tb^{3+}-chelator buffer system and competition methds.

Next we applied metal-chelator buffer system to measure the ProCA3 variants to lanthanide metals. Lanthnide usually binds to EF-hand calcium binding proteins with a K_d between 10^{-11} - 10^{-9} M. Our first generation of ProCAs, ProCA1 has a K_d to Gd^{3+} around 10^{-12} M. Nitrilotriacetic acid (NTA) has a K_d of 5.62×10^{-12} M to lanthanide, and NTA-lanthanide buffer system can maintain the free lanthanide concentration between 10^{-13} - 10^{-10} M, which is the proper range of free lanthanide concentration for titration. We use Tb^{3+} luminescence energy transfer methods to probe the binding between ProCA3 variants and Tb^{3+}. We excited Trp residue in ProCA3 variants at 280 nm, it usually has the fluorescence emission at 315 nm. However, if Tb^{3+} binds to ProCA3, Tb^{3+} will be excited by Trp emission fluorescence signal and have an emission peak at 545 nm (Fig. 4-5). After obtaining the K_d between ProCA3 variants, we can calculate the K_d between Gd^{3+} and ProCA3 variants by competition methods.

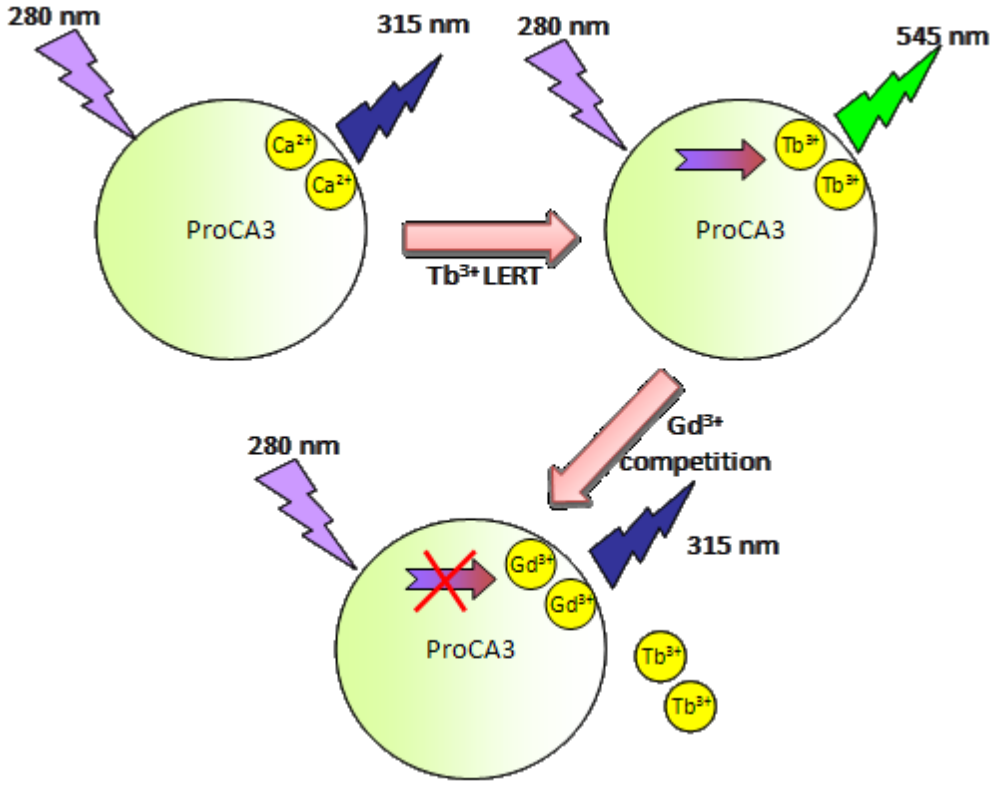

Figure 4-5. Trp-Tb^{3+} LRET assay.

Carton demonstration of Trp-Tb^{3+} LRET assay to characterize the interaction between ProCA3 variants and metal ions such as Ca^{2+}, Tb^{3+} and Gd^{3+}. ProCA3 varients (except wild type) all have one Trp mutation (F103W). ProCA3 variants have an emission peak at 315 nm, when they were excited at 280 nm. If Tb^{3+} binds to these metal binding sites, the emission from Trp are transferred to Tb^{3+} and have a fluorescence/luminescence emission at 545 nm. In the competition assay,10 µM Tb^{3+} was pre-loaded into 5 µM ProCA3 variants. We added Gd^{3+} in the system. Since Gd^{3+} and Tb^{3+} binds to ProCA3 variants in the same site, Gd^{3+} competes Tb^{3+} out of the metal binding pockets. Since there is no energy transfer between Gd^{3+} and Trp, the emission at 545 nm decrease and emission at 315 nm increases.

Fig. 4-6 shows the Tb^{3+} LERT fluorescence spectrum changes by changing the free Tb^{3+} concentration in the presence and absence of ProCA31. The buffer initially contains 1 mM Tb^{3+}, 1 mM NTA, 50 mM HEPES, 100 mM KCl and 30 µM ProCA31. We then titrated different concentrations of NTA to decrease the free Tb^{3+} concentration in the system. As we can see from Fig. 4-6, the fluorescence decrease to a plateau when adding NTA, which indicate that Tb^{3+} is dissociated from ProCA31 then the free Tb^{3+} concentration decrease (adding NTA decrease free Tb^{3+} concentration). On the contrary, the system without ProCA31 has very low fluorescence and such low fluorescence does not have obvious intensity changes. We then calculate the free Tb^{3+} concentration using Equation (2-5) and then calculate K_d between ProCA31 and Tb^{3+} by Hill Equation. Similarly, we also use this method to obtained the Kd between ProCA33 and Tb^{3+} (5-9). ProCA31 and ProCA33 have K_{dTb3+} of 4.3×10^{-12} and 1.55×10^{-12} M.

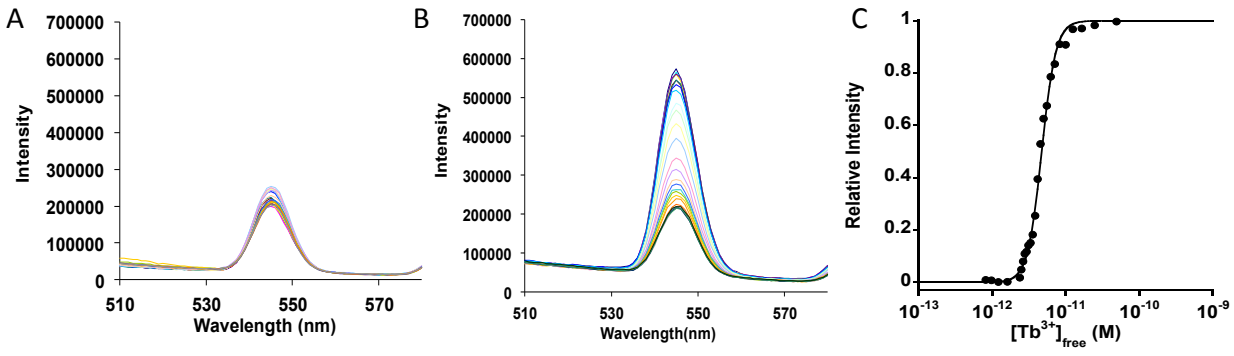

Figure 4-6. Determine Kd of ProCA31 to Tb^{3+} by Tb-NTA buffer system.

The Tb-NTA system contains 50 mM HEPES at pH 7.2, 100 mM KCl, 1 mM Tb^{3+} and 1 mM NTA and 30 µM ProCA31. Due to the strong binding between ProCA31 and Tb^{3+}, the metal binding pockets in ProCA31 were occupied by Tb^{3+}. After titrating NTA in the buffer system, Tb^{3+} will release from ProCA31 due to the free concentration of Tb^{3+} decrease (B). In a control experiments without, no significant fluorescen change after adding NTA (A). In the control experiments without ProCA3, the fluorescence signal doesn't change due to the lack of FRET (A). The K_d of ProCA31 to Tb^{3+} was calculated by Hill Equation based on the relative fluorescence intensity vs. free Tb^{3+} concentration plot (C).

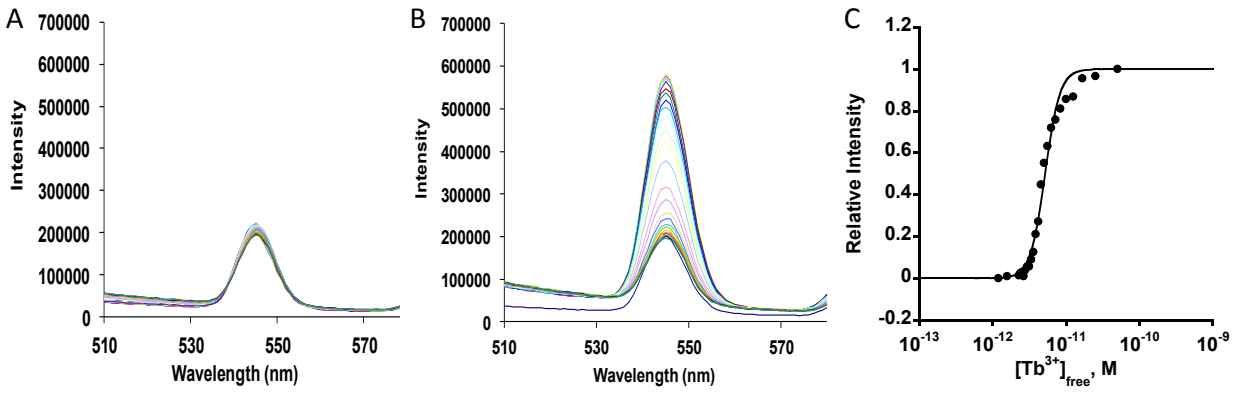

Figure 4-7. Determine Kd of ProCA33 to Tb^{3+} by Tb-NTA buffer system.

The Tb-NTA system contains 50 mM HEPES, 100 mM KCl, 1 mM Tb^{3+} and 1 mM NTA and 30 µM ProCA33. Due to the strong binding between ProCA33 and Tb^{3+}, the metal binding pockets in ProCA33 were occupied by Tb^{3+}. After titrating NTA, Tb^{3+} will release from ProCA31 due to the concentration of free Tb^{3+} decreases (B). In the control experiments without ProCA33, the fluorescence signal doesn't change since there is no LRET phanamana occured in the control experiments (A). The K_d of ProCA33 to Tb^{3+} was calculated by Hill Equation based on the relative fluorescence intensity vs. free Tb^{3+} concentration plot.

To our surprise, we failed to observe the fluorescence decrease in the NTA-Tb^{3+} buffer system when applied to ProCA32 and after adding NTA. We reasoned that ProCA32 has much stronger affinity for Tb^{3+} than other ProCA3 variants and ProCA32 is always saturated by Tb^{3+} when the free Tb^{3+} concentration is between 10^{-13} M to 10^{-11} M. To test our hypothesis, we did dye competition experiments to explore the Kd of ProCA32 to lanthanide. Table 4-2 shows the Gd^{3+} binding affinity of fluoresce dyes determined by our previous lab members Dr. Jin Zou and Dr. Jie Jiang. Fura-2 has the strongest Gd^{3+} binding affinity (K_d = 1.5 × 10^{-14} M) among these dyes. We then test if ProCA32 is able to compete Gd^{3+} out of the Fura-2. 18 μM $GdCl_3$ and 20 μM Fura-2 were added in 10 mM Tirs/HCl, pH 7.4. Then, ProCA32 or CaM was titrated in to the cell with different concentration. The fluorescence spectra were obtained with λ_{ex} 250-450 nm and λ_{em} 510 nm. As shown from Fig. 4-8, the fura-2 fluorescence peak shift from 380 nm to 340 nm after adding 18 μM Gd^{3+}, which indicates that Fura-2 binds to Gd^{3+}. Then, different concentration of ProCA32 or CaM were titrated into the system. As shown in Fig. 4-8, The fura-2 fluorescence dramatically decreases after adding ProCA32, and the fluorescence peak shift to 380 nm with the same intensity of apo-fura-2 when titrated 10 μM ProCA32 (20 μM of total Gd^{3+} at two binding sites). Thus, 10 μM ProCA32 is able to completely compete Gd^{3+} out of fura-2, which indicate that ProCA32 has a much greater Gd^{3+} binding affinity than Fura-2 (($Kd_{fura\text{-}2,Gd}$ = 1.5 × 10^{-14} M)). As a control experiment, we also titrate calmodulin in a parallel experiment, CaM cannot compete Gd^{3+} out of fura-2 even at much higher concentration (20 μM of Calmodulin or 80 μM of Gd^{3+} binding pocket).

Table 4-2. Excitation, emission and Gd3+ binding affinities of fluorescent dyes determined by Gd-chelator buffer system. *

Fluoresence Dye	Excitation (nm)	Emission (nm)	Gd^{3+} binding affinity (K_d, M)
Fura-2	340/380	510	1.5×10^{-14}
Fura-6F	340/380	510	8.4×10^{-12}
Fluo-5N	488	520	3.8×10^{-12}
Mag-Fura-2	340/380	510	2.4×10^{-9}
Rhod-5N	550	580	2.5×10^{-9}

* Experimental data from Dr. Jin Zou and Dr. Jie Jiang.

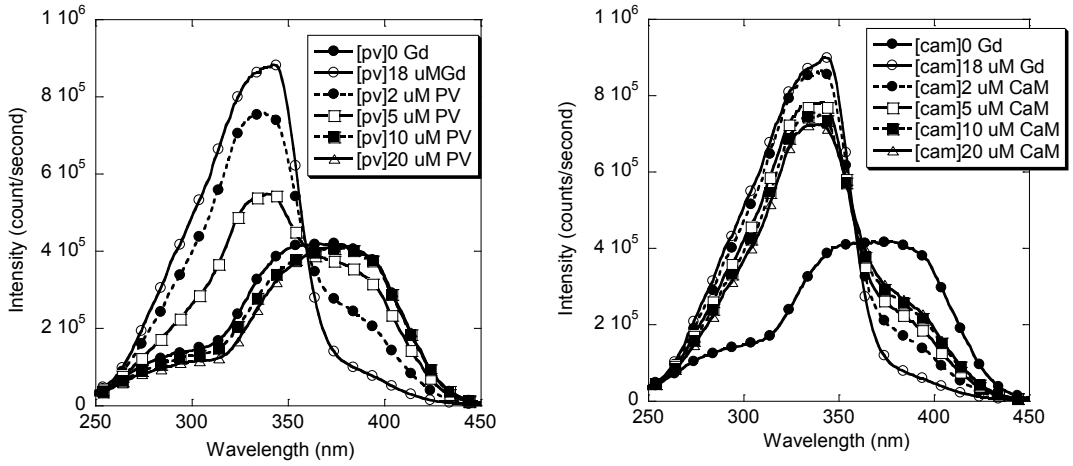

Figure 4-8. Evaluation of Gd^{3+} binding affinity to ProCA32 and calmodulin by fura-2 competition assay.

20 µM of fura-2 were added into 50 mM HEPES, 100 mM NaCl at pH 7.0. Fluorescence changes were collected after adding 18 µM Gd^{3+}, and different concentration of ProCA32 or CaM by excitation between 250 – 450 nm, and emission at 510 nm using PTI.

To determine the exact lanthanide binding affinity of ProCA32, we developed Tb^{3+}-DTPA buffer system. This system contains 5 mM DTPA, 30 μM ProCA32, 0.06 μM Rhod-5N, 5 mM HEPES, and 100 mM NaCl, pH7.2. DTPA has a K_d to Tb^{3+} of 9.55×10^{-22} M. Tb-DTPA is able to generate a buffer range between 10^{-24} and 10^{-18} M of free Tb^{3+}. As a low-affinity-metal indicator, the fluorescene of Rhod-5N can increase when free [Tb^{3+}] is higher than 10^{-6} M. We added Rhod-5N as an internal standard and make sure that that DTPA is not saturated by Tb^{3+}. Fig. 4-9B shows Tb-ProCA32 LERT signal changes during Tb^{3+} titration. In a parallel experiment, 5 mM DTPA without ProCA32 were titrated with Tb^{3+} as background control (Fig. 4-9A). Rhod-5N signal were also monitored at each titration point (Fig. 4-9C). As shown in Fig. 4-9AB, Tb^{3+}-ProCA32 LERT happened in the Tb-DTPA buffer system, which indicates that ProCA32 is able to bind to Tb^{3+} concentration is between 10^{-23} and 10^{-19} M. We next calculated the K_d using Hill equation (Fig. 4-9E). Interestingly, ProCA32 has a $Kd_{ProCA32,Tb}$ of 1.21×10^{-21} M.

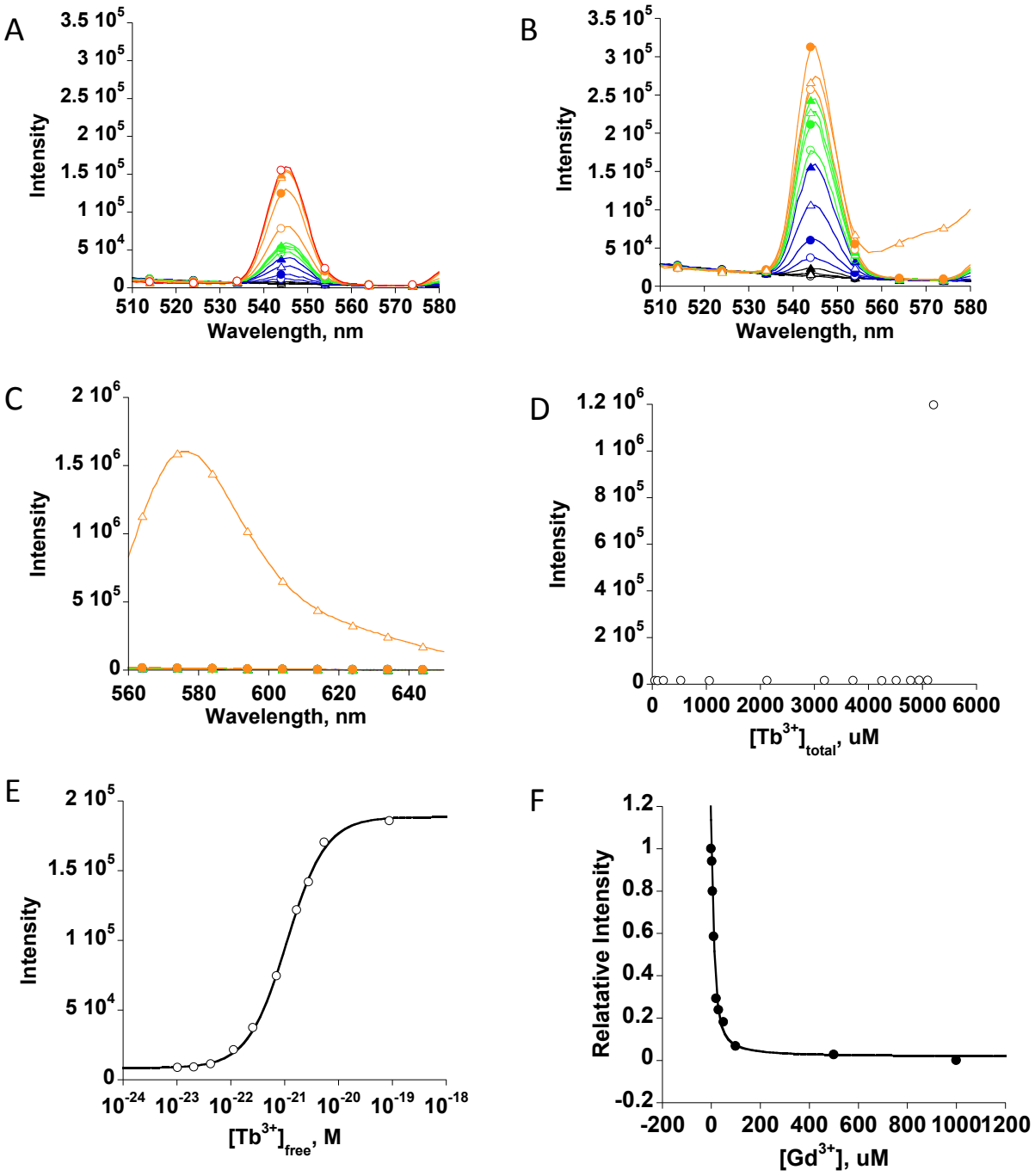

Figure 4-9. Determine Tb^{3+} and Gd^{3+} binding affinity to ProCA32 by Tb^{3+}-DTPA buffer system and Gd^{3+} competition assay.

Terbium fluorescence spectrum changes after adding Tb^{3+} into 5 mM DTPA with out protein in 50 mM HEPES with 100 mM NaCl. B. Terbium fluorescence spectrum changes after adding Tb^{3+}

into 5 mM DTPA with 30 μM ProCA3 in 50 mM HEPES with 100 mM NaCl at pH 7.2. C. Rhodmin 5N fluorescence changes after adding Tb^{3+} into 5 mM DTPA with 0.06 Rhodmin 5N in 50 mM HEPES with 100 mM NaCl. D. Fluorescence intensity does not change during Tb titration in Rhodmin 5N and DTPA. E. Fluorescence intensity with background subtraction increases during Tb^{3+} titration in ProCA32 and DTPA. The K_d of Tb^{3+} to ProCA32 was calculated by Hill Equation. F. Determine Gd^{3+} binding affinity to ProCA32 by Gd^{3+} competition assay.

We next determined Gd^{3+} binding affinity to ProCA3 variants by completion experiments. 10 μM of Tb^{3+} and 5 μM ProCA3 variants were incubated with different concentrations of Gd^{3+} at room temperature over night. The Tb-FRET fluorescence signal changes were measured the next day at excitation 280 nm and emission at 545 nm. As shown in Fig. 4-9 F, Gd^{3+} can compete Tb^{3+} out of ProCA32 with a decrease of FRET upon graduately addition of Gd with an apparent K_d (K_{app}) of 5 μM. We then calculated K_d between Gd^{3+} and ProCA3 variants. As shown from Table 4-3, the Gd^{3+} binding affinity of ProCA30, ProCA 31, ProCA 33, ProCA35 has Kd_{Gd} around 10^{-12} M, while ProCA32 has a Kd_{Gd} of 2.79×10^{-22} M. This is an exciting result because ProCA32 has very similar Gd^{3+} stability compared with most clinical MRI contrast agents, such as Gd-DTPA, multihance, and Eovist. and much higher Gd-stability than Ominiscan and optimark.

4.2.1.4 Determine Zn^{2+} binding affinity of ProCA3 variants using Fluozin-1 competition.

Zn^{2+} is another physiological metal ion potentially inducing transmetallation for contrast agents. We determined the Zn^{2+} binding affinity to ProCA3 variants using Fluozin-1 competition methods.[103] Zn^{2+} and Fluozin-1 were first incubated in 50 mM HEPES, 100 mM NaCl, pH 7.2. Then, ProCA3 variants were titrated into the solution. The Fluorescence signals of Fluozin-1 were collected in each titration point. Due to competition, Zn^{2+} will be removed from Fluozin-1 during ProCA titration and the fluorescence intensity of Fluozin-1 deceased until reach to a plateau (Fig. 4-10). Interestingly, Zn^{2+} binding affinity of ProCA32 variants varies from 6.0×10^{-8} M to more than 1×10^{-5} M (Table 4-3). Interestingly, ProCA32 has the highest Zn^{2+} binding affinity, which may caused by additional negatively charged mutation (S56D) inducted in EF-hand I.

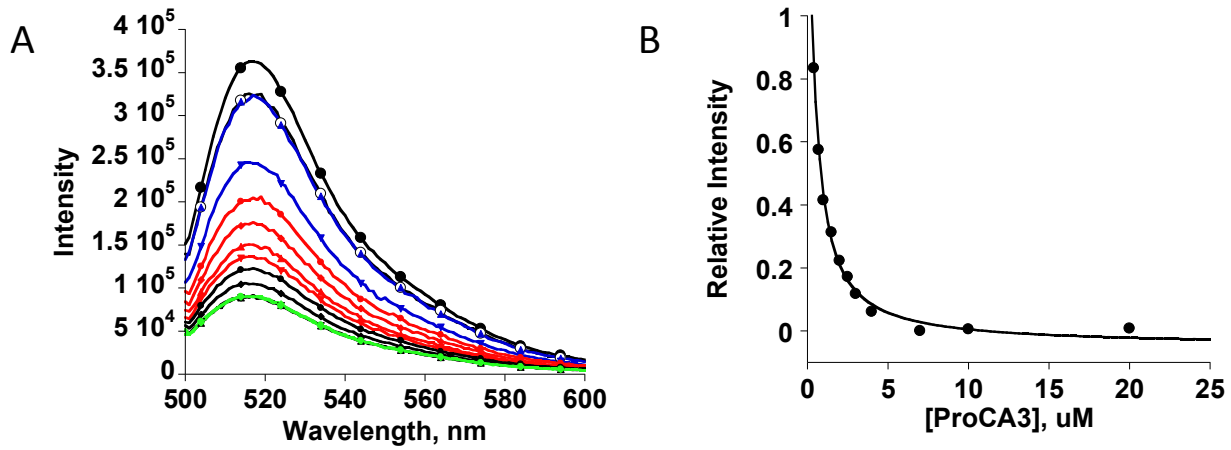

Figure 4-10. Determine Zn^{2+} binding affinity to ProCA32 by Fluozin-1 competition assay.

A. Fluozin-1 fluorescence spectrum changes during ProCA32 titration. The solution contains 50 mM HEPES, 100 mM NaCl and 1 µM Fluozin-1 at pH 7.2. B. Fluorescence intensity changes during ProCA32 titration. The apparent Kd of Tb^{3+} to ProCA32 was calculated by competition equation (equations 2-8 an 2-9).

Table 4-3. Metal binding affinity and selectivity of PV-based MRI contrast agents.

K_d	Tb^{3+} (M)	Gd^{3+} (M)	Ca^{2+} (M)	Mg^{2+} (M)	Zn^{2+} (M)	Log (K_{Gd}/K_{Ca})	Log (K_{Gd}/K_{Zn})
Gd-DTPA	9.55×10^{-22}	1.86×10^{-21}	1.51×10^{-10}	2.75×10^{-9}	6.31×10^{-19}	10.91	2.53
ProCA30	$6.29 \pm 0.13 \times 10^{-11}$	$6.37 \pm 0.50 \times 10^{-11}$	8.35×10^{-9}	1.96×10^{-5}	2.05×10^{-6}	2.1	4.5
ProCA31	$1.79 \pm 0.33 \times 10^{-12}$	$2.55 \pm 0.09 \times 10^{-11}$	$3.91 \pm 0.96 \times 10^{-9}$	2.49×10^{-5}	$1.3 \pm 0.5 \times 10^{-7}$	2.2	3.7
ProCA32	$1.21 \pm 0.33 \times 10^{-21}$	$2.79 \pm 0.36 \times 10^{-22}$	$3.57 \pm 0.01 \times 10^{-9}$	1.72×10^{-6}	$6.0 \pm 2.0 \times 10^{-8}$	13.1	14.3
ProCA33	$5.34 \pm 0.34 \times 10^{-11}$	1.24×10^{-11}	$1.05 \pm 0.09 \times 10^{-9}$	N/A	$> \times 10^{-5}$	2.9	n/a
ProCA35	$1.68 \pm 0.04 \times 10^{-11}$	$1.51 \pm 0.21 \times 10^{-11}$	N/A	N/A	6.91×10^{-5}	N/A	7.7

The binding affinities of ProCA3 variants were determine at in 50 mM HEPES 100 mM NaCl at pH 7.2.

4.2.1.5 Metal selectivity ProCA3 variants.

Contrast agents with high metal stabilities are highly desired for the development of contrast agents, since other physiological ions could compete Gd^{3+} out of the binding pocket. After obtained the binding affinity of ProCA variants to metal ions such as Zn^{2+}, Ca^{2+} and Gd^{3+}, we calculated their metal selectivities. Our best contrast agent, ProCA32, has pGd/pCa of 13.1 and pGd/pZn of 14.3, which is much higher than all of the clinical MRI contrast agents and the first generation of ProCA, ProCA1. These results indicate that ProCA32 could be resistant to transmetallation *in vivo* and ProCA32 could be much more stable than clinical MRI contrast agents injected *in vivo*.

4.2.1.6 In vitro transmetallation study of ProCA32 and clinical MRI contrast agents

In the physiological condition, Zn^{2+} and Po_4^{3-} are the major molecules to compete Gd^{3+} from contrast agents. To study the transmetalizaiton of ProCA3, we measured the relaxation rate changes over time of contrast agents in the presence of Zn^{2+} and Po_4^{3-}. Consistant with literature data (Fig. 4-11A), clininial MRI contrast agents has different transmetallation rate in this solution. The linear noncharged MRI contrast agent, Ominiscan, has highest transmetallation, while macrocyclic non-charged MRI contrast agents, such as Gadavist and Prohace, have no trasmetalization in the presence of Zn^{2+} and PO_4^{3-} for at least 4 days based on the study reprted by Laurent et al,.[192] Intestertingly, different ionic linear MRI contrast agents has different transmetallation rate, even through the number of negative charge and ligand type are very similar.

We applied the similar experiemnts to test the transmetallation properties of ProCA32 in the presence of Zn^{2+} and PO_4^{3-}. Due to the high relaxivity, 25 times lower Gd^{3+} concentration,

25-50 times lower chelator concentration was used in this study. To better compare the transmealization properties of ProCA32 with clinical MRI contrast agent, we apply this study using 25 time lower concentration of Zn^{2+} and PO_4^{3-}. As show from Fig. 4-11B, the relaxation rate of ProCA32 is not changed in the presence of Zn^{2+} and PO_4^{3-} for at least 4 days, indicating that ProCA32 has no transmelization at this condition.

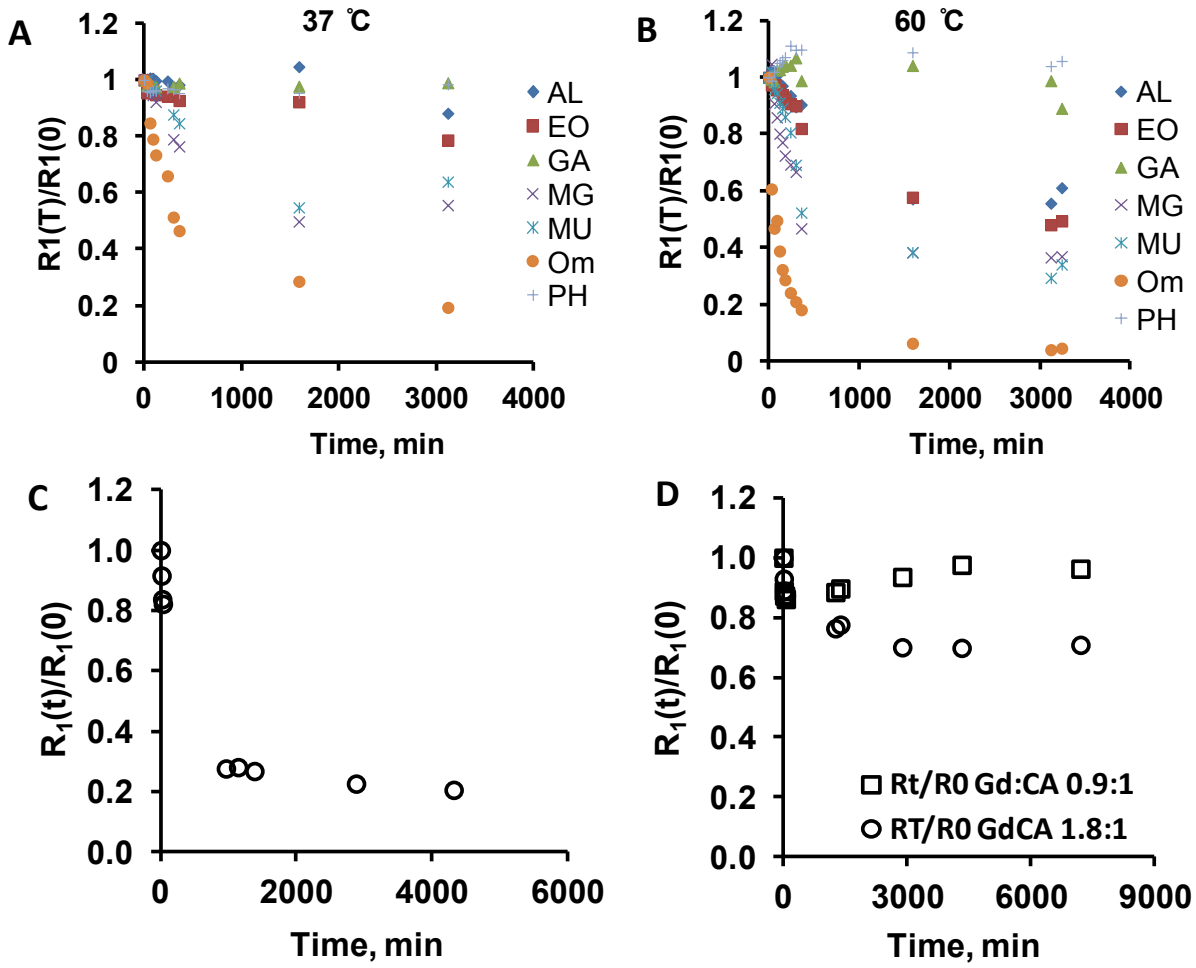

Figure 4-11. Transmetallation study of clinical MRI contrast agents and ProCA32.

Transmetallation study of clinical MRI contrast agents (A. at 37˚C, B. at 60˚C) and ProCA32 (C. 50 µM of ProCA32, 100 µM Gd^{3+}, 2.5 mM Zn^{2+}, and 30 mM PO_4^{3-}; D. 55 µM (open dots) or 110 µM (open square) of ProCA32, 100 µM Gd^{3+}, 100 µM Zn^{2+}, and 1.2 mM PO_4^{3-}).

4.2.2 Relaxivity study of ProCA3 variants

The relaxivity of ProCA3 variants were measured in the buffer containing 50 mM HEPES, 100 mM NaCl, pH 7.2 at 37 ˚C. We fixed the Gd^{3+} concentration as 100 μM and mixed with different concentration of ProCA3 variants from 5 μM to 200 μM. We then calculate the per Gd^{3+} relaxivity of each fixed contrast agent concentration. The final relaxivity were calculated when the ratio between Gd^{3+} and ProCA3 were 2:1.

5.2.3.1 The relaxivity of ProCA30 at 37 ˚C 1.4 T

Fig. 4-12 shows the r_1 and r_2 measurement of ProCA30. We fixed Gd^{3+} concentration at 100 μM. r_1 and r_2 started with 5 and 22 $mM^{-1}s^{-1}$, respectively, which is the relaxivity of free Gd^{3+} without any ProCA30. After adding 5-25 μM of ProCA30, the r_1 and r_2 keep increase. Since ProCA30 has two Gd^{3+} binding sites, r_1 and r_2 measured in these conditions should be the combination of both free Gd^{3+} relaxivity and Gd^{3+}-ProCA30 complex relaxivity. All of the Gd^{3+} bind to ProCA30, when ProCA30 concentration is equal to or above 50 μM. In such conditions, the r_1 and r_2 is the per-Gd relaxivity of Gd^{3+}-ProCA30 complex. Interestingly, the per Gd^{3+} r_1 and r_2 of ProCA30 is 32 and 42 $mM^{-1}s^{-1}$, which is about 8 fold higher than clinical MRI contrast agents with r_1 = 3.5 $mM^{-1}s^{-1}$ and r_2 = 5 $mM^{-1}s^{-1}$.Since ProCA30 binds two Gd^{3+}, the per particle relaxivity is 64 for r_1 and 84 $mM^{-1}s^{-1}$ for r_2 (Fig. 4-12).

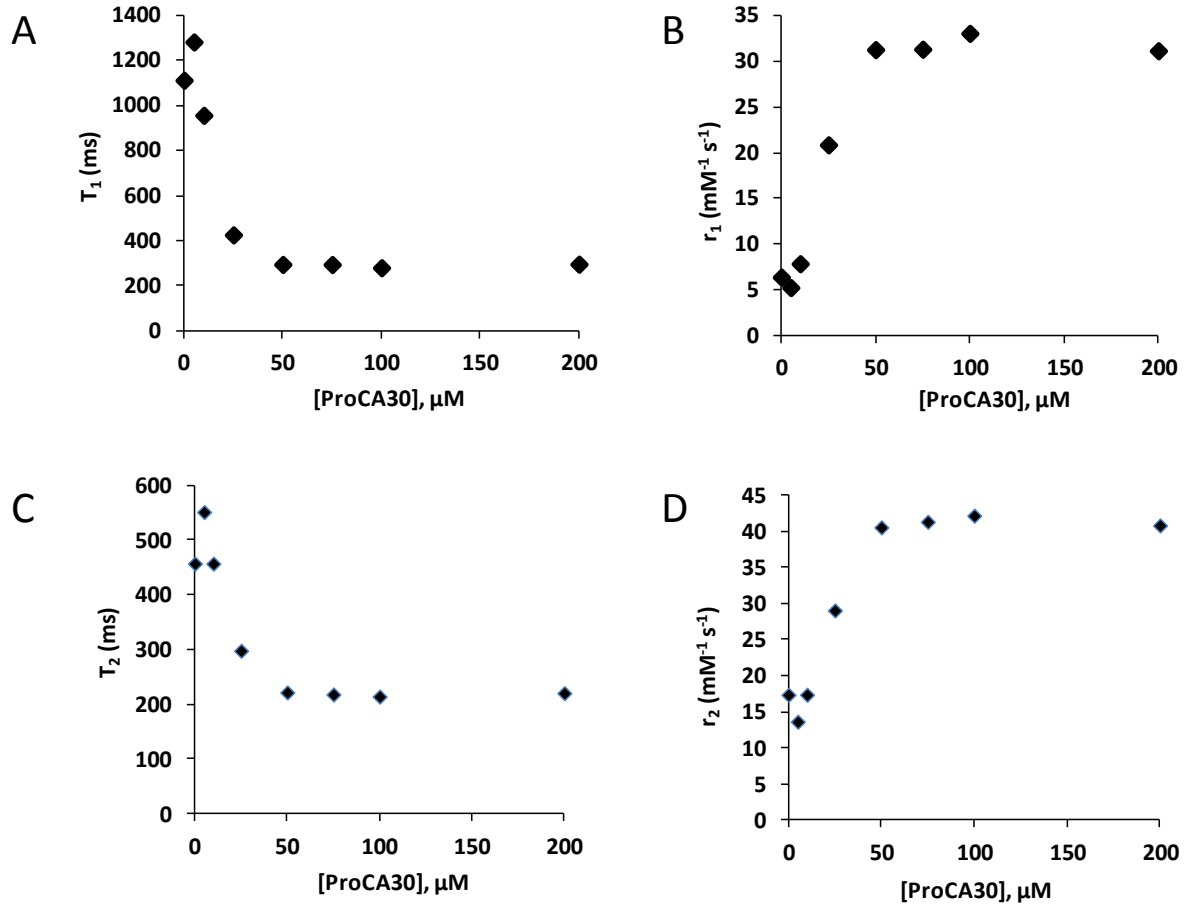

Figure 4-12. Relaxivity of ProCA30.

r_1 and r_2 relaxivities of 50 µM Gd^{3+} at different concentration of ProCA30 were measured by 1.4 T relaxometer in 50 mM HEPES 100 mM NaCl at pH 7.2. A T_1 relaxiation time of 50 µM Gd^{3+} at different concentrations of ProCA30 in 50 mM HEPES 100 mM NaCl at pH 7.2. B. r_1 relaxiavity of 50 µM Gd^{3+} at different concentration of ProCA30 in 50 mM HEPES 100 mM NaCl at pH 7.2. C. T_2 relaxiation time of 50 µM Gd^{3+} at different concentrations of ProCA30 in 50 mM HEPES 100 mM NaCl at pH 7.2. D. r_2 relaxiavity of 50 µM Gd^{3+} at different concentrations of ProCA30 in 50 mM HEPES 100 mM NaCl at pH 7.2.

4.2.2.1 The relaxivity of ProCA32 at 1.4 T 37 ˚C.

We next determined the r_1 and r_2 of ProCA32 at 1.4 T, using similar methods at 37 ˚C to minic animal body temperature. Gd^{3+} concentration of the each testing conditions was fixed at 100 μM. We then measured T_1 and T_2 of the water in the presence of 100 μM of Gd^{3+} and different concentration of ProCA32. As shown from Fig. 4-13, the T_1 and T_2 relaxiation time of water decrease when titrating ProCA32. However, when Gd^{3+} is saturated by ProCA32 ([ProCA32]=50 μM), continuing titrating ProCA32 increase the relaxation time. The r_1 and r_2 relaxivity first increase, then when ProCA32 concentraion is larger than 50 μM, the r_1 and r_2 decrease when adding ProCA32. These results indicate that ProCA32 has different Gd^{3+} binding sites when compare to ProCA30. When Gd^{3+} concentration is higher than that of the Gd^{3+} binding pocket in ProCA32, all of the Gd^{3+} binding pockets in ProCA32 are occupied, which cause the shorter relaxiation time and high relaxivity. The relaxivity of ProCA32 at this condition is similar to that of ProCA32. The lowest T_1 and T_2 were achieved when the Gd^{3+} concentration is the same as the concentration of Gd^{3+} binding pocket in ProCA32. Then r_1 and r_2 determined at this concentration is the r_1 and r_2 of ProCA32. As shown from Fig. 4-13, ProCA32 has the similar relaxivity comparing the WT ProCA32. Per Gd^{3+} r_1 and r_2 of ProCA32 are 30 and 40 $mM^{-1}s^{-1}$, respectively. Similar as ProCA30, ProCA32 has two Gd^{3+} binding sites. Therefore, the per particle r_1 and r_2 of ProCA32 are 60 and 80 $mM^{-1}s^{-1}$, respectively.

Interestingly, the T_1 and T_2 increase when ProCA32 concentration is higher than 50 μM (corresponding to 100 μM of the Gd^{3+} binding pocket in ProCA32). T_1 and T_2 reached to plateau, when ProCA32 concentration is higher than the Gd^{3+} concentration. Fig. 4-13 also shows that when ProCA32 binds to one Gd^{3+}, the relaxivity is much lower than that of ProCA32 which binds

two Gd^{3+}ions. These results indicate that Gd^{3+} binding patterns to ProCA32 are different when it binds to one or two Gd^{3+}. ProCA32 may have two very different Gd^{3+} binding pockets. One of the Gd^{3+} binding pockets may have high relaxivity but low Gd^{3+} binding affinity and another Gd^{3+} binding pocket may have low relaxivity but high Gd^{3+} binding affinity. It is also possible that Gd^{3+} binding to two binding sites changes overall metal affinity due to coopertivity.

4.2.2.2 The relaxivity of ProCA35 at 1.4 T 37 ˚C.

Fig. 4-13 shows the relaxivity of ProCA35. These ProCA32 variant has three mutations at S56D, E60D and F103W. Same measurement conditions, like Gd^{3+} concentration, HEPES buffer and salt strength were applied to determine the relaxivity of ProCA35. T_1 and T_2 decrease is much more significant than that of ProCA30 and ProCA32, and it reachs to a plateau when the protein concentration is equal to or higher than Gd^{3+} concentration (100 μM). Interestingly, the per Gd r_1 of ProCA35 are 57 and 53 $mM^{-1}s^{-1}$ when $[Gd^{3+}]$/[ProCA] are 1 to 2 and 1 to 1, repectively. The per Gd r_2 of ProCA35 is 77 and 70 $mM^{-1}s^{-1}$ when $[Gd^{3+}]$/[ProCA] are 1 to 2 and 1 to 1,respectively. As discussed in Chapter 3, we hypothesize that mutation E60D introduces one more additional water ligand to ProCA3. These results support our hypothesis, since increased water number will increase relaxivity as shown from Equation 1-2.

4.2.2.3 The relaxivity of other ProCA3 variants at 1.4 T 37 ˚C.

The relaxivity of ProCA31, ProCA33 and ProCA36 were also measured by this method with the exactly same conditions (Fig. 4-13). ProCA31 only has F103W mutation. There is no modification of Gd^{3+} binding pocket in ProCA3. The relaxivity of ProCA31 is very similar to that of ProCA30. The per Gd^{3+} r_1 and r_2 for ProCA31 is 32 and 42 $mM^{-1}s^{-1}$ when $[Gd^{3+}]$/[ProCA] are 1

to 2 and 1 to 1. The per Gd^{3+} r_2 of ProCA32 is 31 and 40 $mM^{-1}s^{-1}$ when [Gd^{3+}]/[ProCA] are 1 to 2 and 1 to 1. These results indicate that F103W mutation does not change the relaxivity of ProCA3 variants.

ProCA33 has two mutations at E60D and F103W. Position of EF-hand I of ProCA33 is modified by mutation E60D. We hypothesis that E60D replace the side chain ligand for Gd^{3+} at position 9 to be water ligand, which cause increased relaxivity. Consistent with our hypothesis, the per Gd^{3+} relaxivity of ProCA33 is much higher than that of ProCA30 and ProCA31. The per Gd^{3+} r_1 and r_2 for ProCA31 is 43 and 57 $mM^{-1}s^{-1}$ when [Gd^{3+}]/[ProCA] are 1 to 2 and 1 to 1. The per Gd r_2 of ProCA33 is 40 and 52 $mM^{-1}s^{-1}$ when [Gd^{3+}]/[ProCA] are 1 to 2 and 1 to 1.

ProCA34 has two mutations at G99D and F103W. G99D is the mutation at position 9 of EF-hand II. We hypothesis that this mutation make all the binding ligand in EF-hand II same as EF-hand I with S56D and E60D double mutant (ProCA33). However, G99D mutation does not change the ligand type for Gd^{3+} in the EF-hand II. Consistent with our hypothesis, the per Gd^{3+} r_1 and r_2 for ProCA31 is 32 and 42 $mM^{-1}s^{-1}$ when [Gd^{3+}]/[ProCA] are 1 to 2 and 1 to 1. The per Gd r_2 of ProCA34 is 31 and 40 $mM^{-1}s^{-1}$ when [Gd^{3+}]/[ProCA] are 1 to 2 and 1 to 1. These relaxivity values are the same as that of ProCA30 and ProCA31, indicating that mutation G99D does not change the Gd^{3+} binding pocket in EF-hand II.

ProCA36 contains three mutations: S56D, G99D and F103W. The mutations on ProCA36 is the combination of ProCA32 and ProCA34. The relaxation time changes of ProCA36 during titration are very similar to that ProCA32. Both T_1 and T_2 decrease when ProCA36 concentration increases. However, when ProCA36 concentration is higher than 50 μM, continue adding ProCA36 increase both T_1 and T_2. The per Gd^{3+} r_1 and r_2 for ProCA36 is 32 and 42 $mM^{-1}s^{-1}$ when

$[Gd^{3+}]$/[ProCA] are 1 to 2 and 1 to 1. The per Gd r_2 of ProCA36 is 20 and 28 $mM^{-1}s^{-1}$ when $[Gd^{3+}]$/[ProCA] are 1 to 2 and 1 to 1. Both ProCA32 and ProCA36 contains S56D mutation indicating that S56D mutation cause the relaxivity decreasing at high concentration of ratio between ProCA and Gd^{3+}.

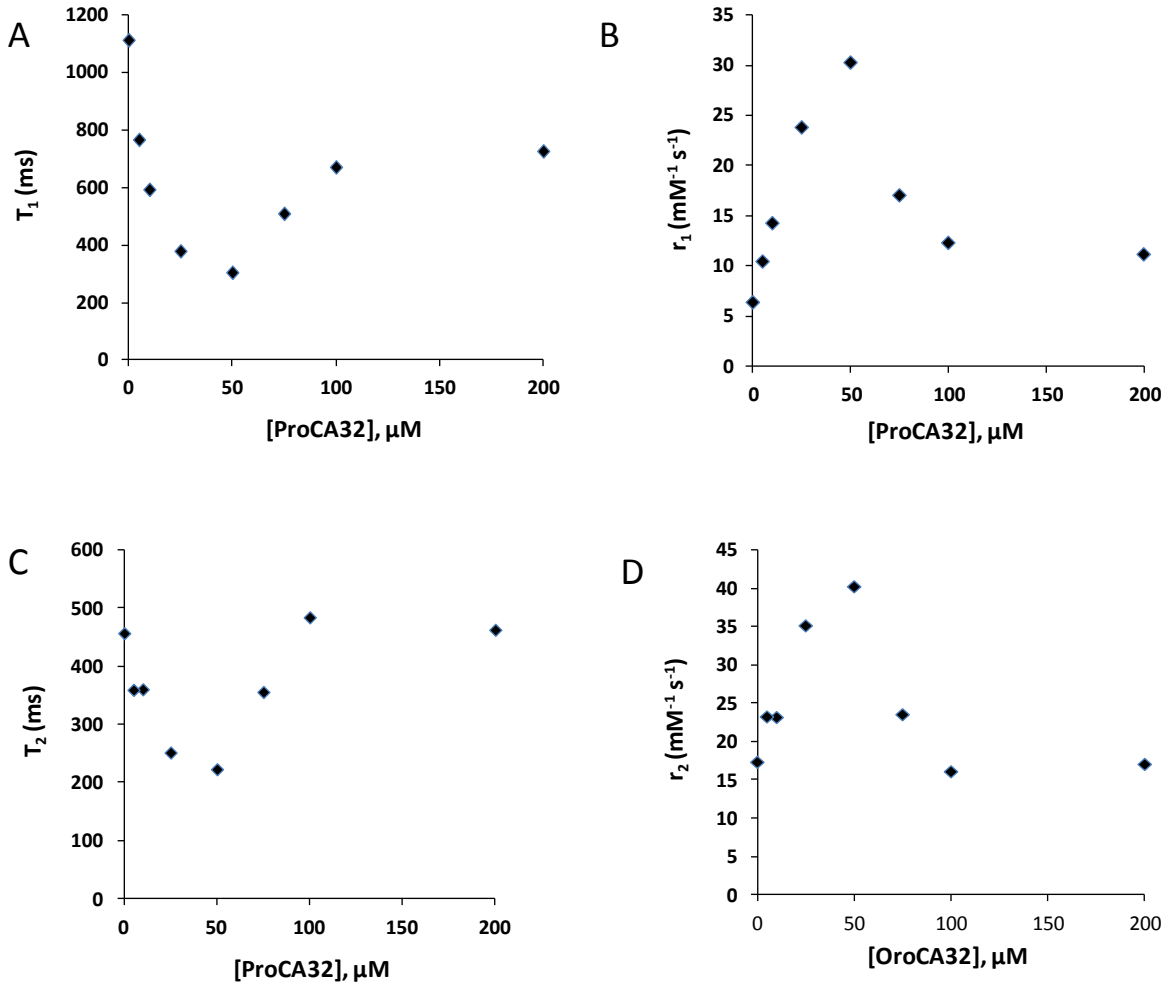

Figure 4-13. Relaxivity of ProCA32.

r_1 and r_2 relaxivity of 50 µM Gd^{3+} at different concentrations of ProCA32 in 50 mM HEPES 100 mM NaCl at pH 7.2. A T_1 relaxiation time of 50 µM Gd^{3+} at different concentrations of ProCA32 in 50 mM HEPES 100 mM NaCl at pH 7.2. B. r_1 relaxiavity of 50 µM Gd^{3+} at different concentrations of ProCA32 in 50 mM HEPES 100 mM NaCl at pH 7.2. C. T_2 relaxiation time of 50 µM Gd^{3+} at different concentrations of ProCA32 in 50 mM HEPES 100 mM NaCl at pH 7.2. D. r_2 relaxiavity of 50 µM Gd^{3+} at different concentrations of ProCA32 in 50 mM HEPES 100 mM NaCl at pH 7.2.

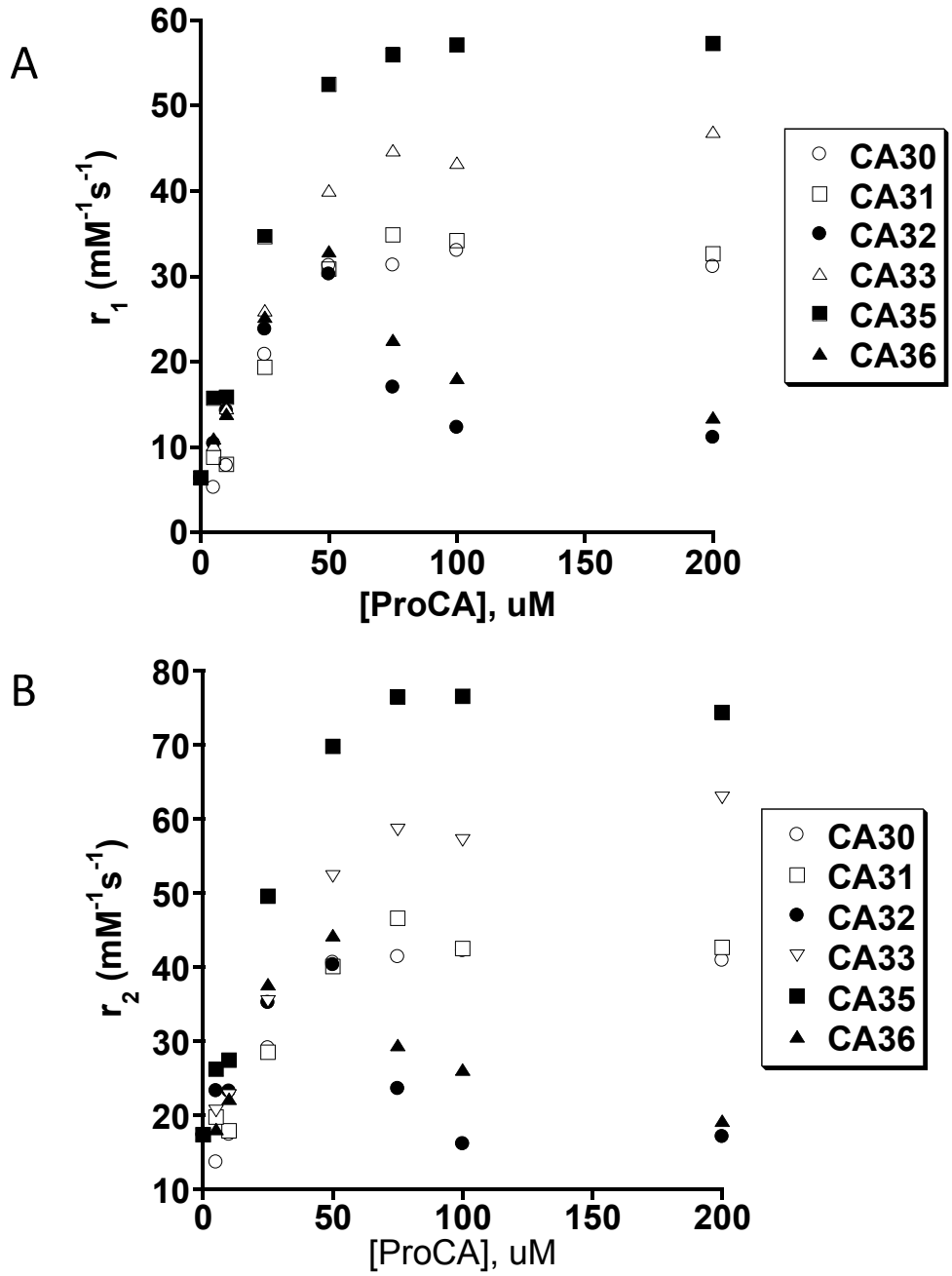

Figure 4-14. Relaxivity of ProCA3 variants.

r_1 (A) and r_2 (B) relaxivity of 50 µM Gd^{3+} at different concentrations of ProCA3 variants in 50 mM HEPES 100 mM NaCl at pH 7.2 using 1. 4 T relaxometer at 37˚C

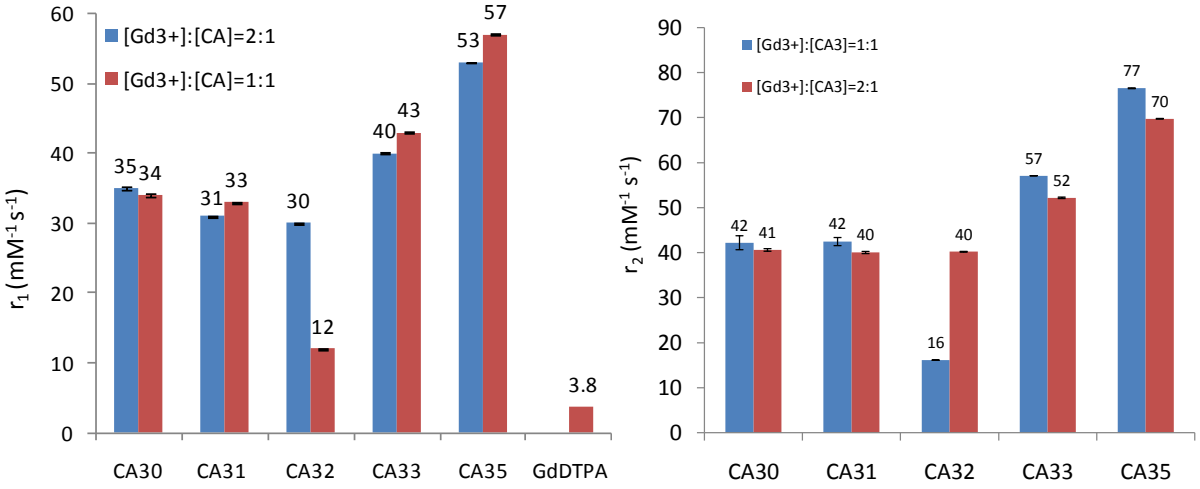

Figure 4-15. r_1 and r_2 relaxivities ProCA3 variants incorporated with 1 or 2 Gd^{3+} ions.

Therelaxivities were measured variants in 50 mM HEPES 100 mM NaCl at pH 7.2 using 1. 4 T relaxometer at 37˚C

4.2.2.4 The relaxivity of ProCA32 after PEGlytion.

Since ProCA32 has highest Gd binding affinity and metal binding selectivity, it could be potentially used as MRI contrast agents. PEGlytion of protein could optimize the biocompatibilities of protein drugs including increasing the solubility and decreasing immunogenicity. We previously reported that PEGlyation of ProCA1 can increase both r_1 and r_2 at different field strength, so we test whether PEGlytion of ProCA32 also increase the relaxivity.

ProCA32 was PEGlyated using the methods described in Chapter 2. 3-5 PEG-40 was conjugated to ProCA32 through lysine residues. The PEGlyted ProCA32 is called ProCA32-P40 (or ProCA32M). The r_1 and r_2 of ProCA32-P40 were measured at 1.4 T 37 ˚C using similar methods for ProCA32. Gd^{3+} concentration of the each testing condition were fixed at 100 μM. We then measured T_1 and T_2 of water in the presence of 100 μM of Gd^{3+} and different concentration of ProCA32-P40. As shown from Fig. 4-16, the T_1 and T_2 relaxiation time of water decreased when titrating ProCA32-P40. However, when Gd^{3+} is saturated by ProCA32-P40 ([ProCA32-P40] = 50 μM), continuing titrating ProCA32-P40 increase the relaxation time. The r_1 and r_2 relaxivity first increase, then when ProCA32-P40 concentration is larger than 50 μM, the r_1 and r_2 decrease when adding ProCA32-P40. As shown from Fig. 4-16, ProCA32-P40 has the similar relaxivity comparing with the ProCA32-P40. The per Gd r_1 and r_2 for ProCA32-P40 is 30 and 40 $mM^{-1}s^{-1}$ when [Gd^{3+}]/[ProCA] are 1 to 2 and 1 to 1. The per Gd r_2 of ProCA32-P40 is 12 and 16 $mM^{-1}s^{-1}$ when [Gd^{3+}]/[ProCA] are 1 to 2 and 1 to 1.

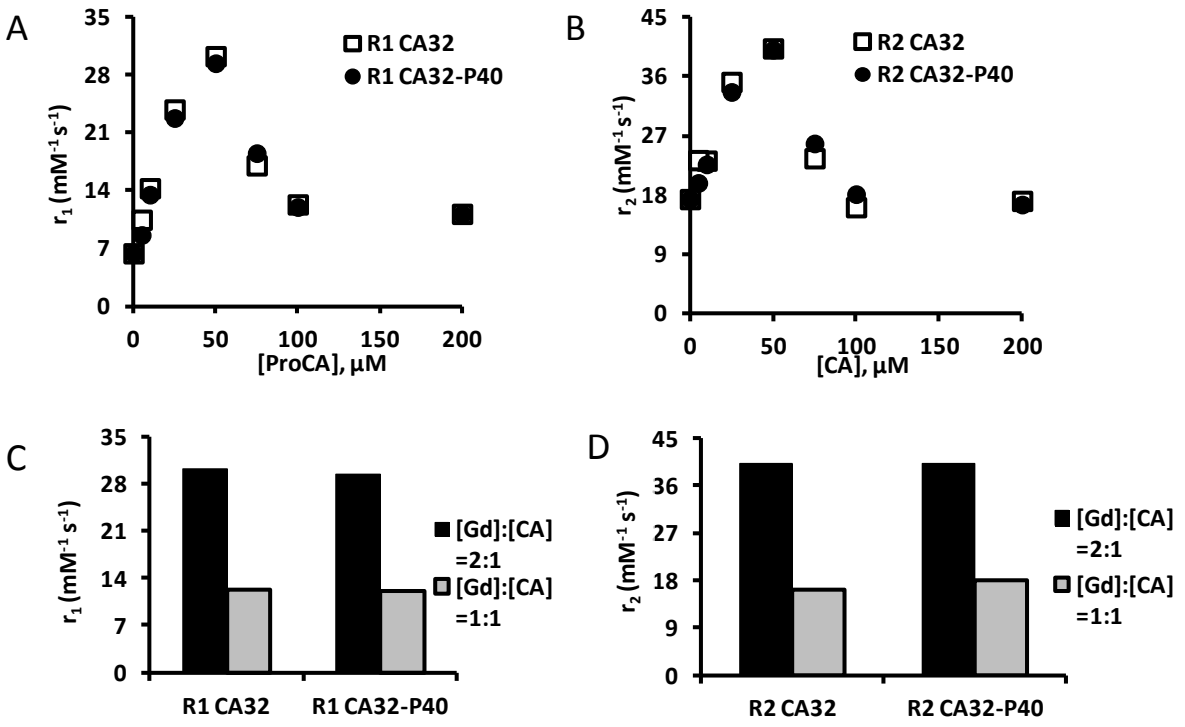

Figure 4-16. Effects of PEG conjugation on the relaxivity of ProCA32.

A. r_1 relaxiavity of 50 µM Gd^{3+} at different concentration of ProCA32 or ProCA32-P40 in 50 mM HEPES 100 mM NaCl at pH 7.2 at 37˚C. B. r_2 relaxiavity of 50 µM Gd^{3+} at different concentration of ProCA32 or ProCA32-P40 in 50 mM HEPES 100 mM NaCl at pH 7.2. C, D. r_1 (C) and r_2 (D) relaxivity of PEGlyated and non-PEGlyted ProCA32 with 1 or 2 Gd^{3+} molecular.

4.2.2.5 The relaxivity of ProCA32 at high magnetic field

With the improvement of technology, MRI scanner with high magnetic field strength has been applied for both clinical and preclinical studies. The currently developed MRI contrast agents, however, are mainly focused on the application at regular magnetic field (0.5 T – 1.5 T). However, the relaxivity and sensivity of these contrast agents has dramatic drop at high magnetic field. Thus, there is an urgent need to develop MRI contrast agents with high relaxivity at high magnetic field (3 T – 9.4 T). According to the SMB theory, we carefully simulated the relaxivity of MRI contrast agents at high magnetic field using different τ_R and τ_m, and a τ_R of 0.5-2 ns is optimized for the high relaxivity of MRI contrast agents at high magnetic field (3 T – 9.4 T). We next compared the relaxivity of ProCA32 and Gd-DTPA at 7 T MRI. We prepared a set of phantom containing different concentration of Gd-DTPA or ProCA3 varianrs. The T_1 relaxiation time were measured by inversion recovery sequences with different inversion time. Then, the relaxivity were calculated based on different relaxiation time in certain concentrations. The relaxivity ProCA32 is around 18 $mM^{-1}s^{-1}$ (Fig. 4-17), which reach the theorical maxium value of relaxivity at high magnetic field. Due to unoptimized τ_R and τ_m, the relaxivity of Gd-DTPA is only around 4 $mM^{-1}s^{-1}$. Thus, ProCA32 is promising to be applied as a sensitive MRI contrast agent at high magnetic field.

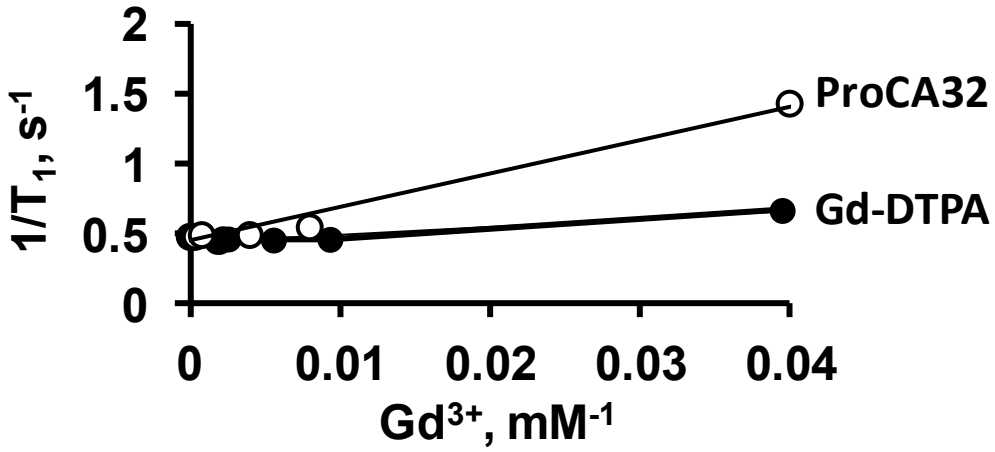

Figure 4-17. Relaxiation time differences between GdDTPA and ProCA32 at different concentration in the 7 T MRI scanner.

Inverstion recovery with different inversion time were used to calculate the relaxation time of water containing different concentration of Gd-DTPA or ProCa32. Then, the relaxivities of ProCA32 and Gd-DPTA were calculated by fitting the linear equation using $1/T_1$ as y-axis and Gd^{3+} concentration as x-axis.

4.2.3 Water number study of ProCA3

The relaxivity of contrast agents is influenced by water number, the number of water molecular interact with Gd^{3+} at the same time. The water number measurement also reveals the special arrangement of the Gd^{3+} binding ligands. To test our hypothesis that the relaxivity and metal binding affinity of ProCA3 variants can be tuned by changing water number, the water number of ProCA3 is measured by the Tb^{3+} luminescence life time experiments.[172, 173] As shown in Fig. 4-18, the fluorescence decay of the Tb^{3+} is caused by the radiative decay (Γ) and non-radiative decay (K). Non-raditive decay contains many factors, such as molecular collation, quenching, energy transfer. H_2O is one of the major factors which causes the non-radiative decay of the Tb^{3+} fluorescence, whereas D_2O does not cause non-radiative decay of Tb^{3+} fluorescence. Therefore, the difference of the decay rates of Tb^{3+} in the presence of H_2O and D_2O (ΔK_{obs}) reflects the number of water molecular interact with Tb^{3+}-ProCA3.

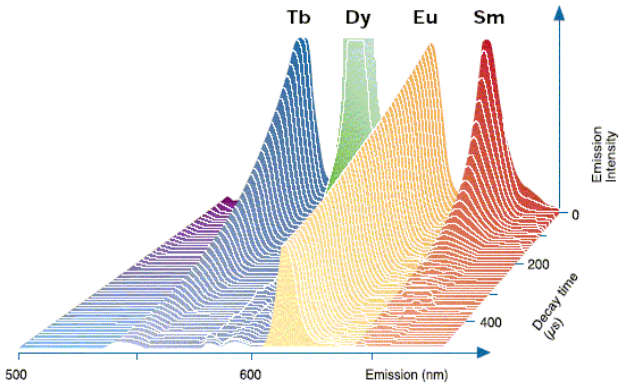

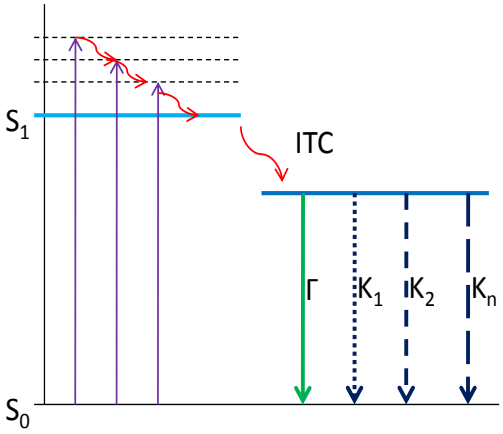

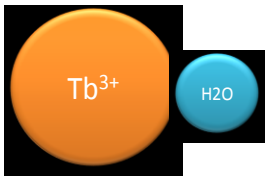

$$K_{obs}=\Gamma+K_1+K_2+\ldots+K_n \qquad \text{Equation 3-1}$$

$$K_{obs}=\Gamma+K_{nonrad}+K_{H_2O}x_{H_2O} \qquad \text{Equation 3-2}$$

$$\Delta K_{obs}=K_{obs}H_2O-K_{obs}D_2O=K_{H2O} \qquad \text{Equation 3-3}$$

http://www.case.edu/med/pathology/faculty/cobblab/TRF.html

Figure 4-18. The mechanism of water number determination by luminescence life time experiments.

The fluorescence decay of the Tb^{3+} is caused by the radiative decay (Γ) and non-radiative decay (K). Non-raditive decay contains many factors, such as molecular collation, quenching, energy transfer. H_2O is one of the major factors which cause the non-radiative decay of the Tb^{3+} fluorescence, whereas D_2O does not cause non-radiative decay of Tb^{3+} fluorescence.[172, 173] Therefore, the difference of the decay rates of Tb^{3+} in the presence of H_2O and D_2O (ΔK_{obs}) reflects the number of water molecular interact with Tb^{3+}-ProCA3.

To determine the exact number of water number of ProCA3 variants, we use organic chelators (NTA, EDTA, DTPA) and Tb^{3+} in aqueous solution to make a standard curve. The number of NTA, EDTA, DTPA and Tb^{3+} and aqueous solution were reported in literature, where the water numbers of these chelators were determined by X-ray diffraction. [172, 173]

To determine the standard curve, Tb-DTPA, Tb-EDTA, Tb-NTA and free Tb^{3+} are prepared in H_2O and D_2O solution. Tb^{3+} fluorescence were excited at 280 nm and the fluorescence decays were measured at 545 nm. The fluorescence decay was fitted by single exponential decay Equation. The decay rate (Kobs) and life time (τ) of Tb^{3+} in H2O and D2O were calculated by this fitting (Fig. 4-19). We then draw the standard curve based on the reported water number of these chelators and difference of Kobs in H_2O and D_2O (ΔK_{obs}).

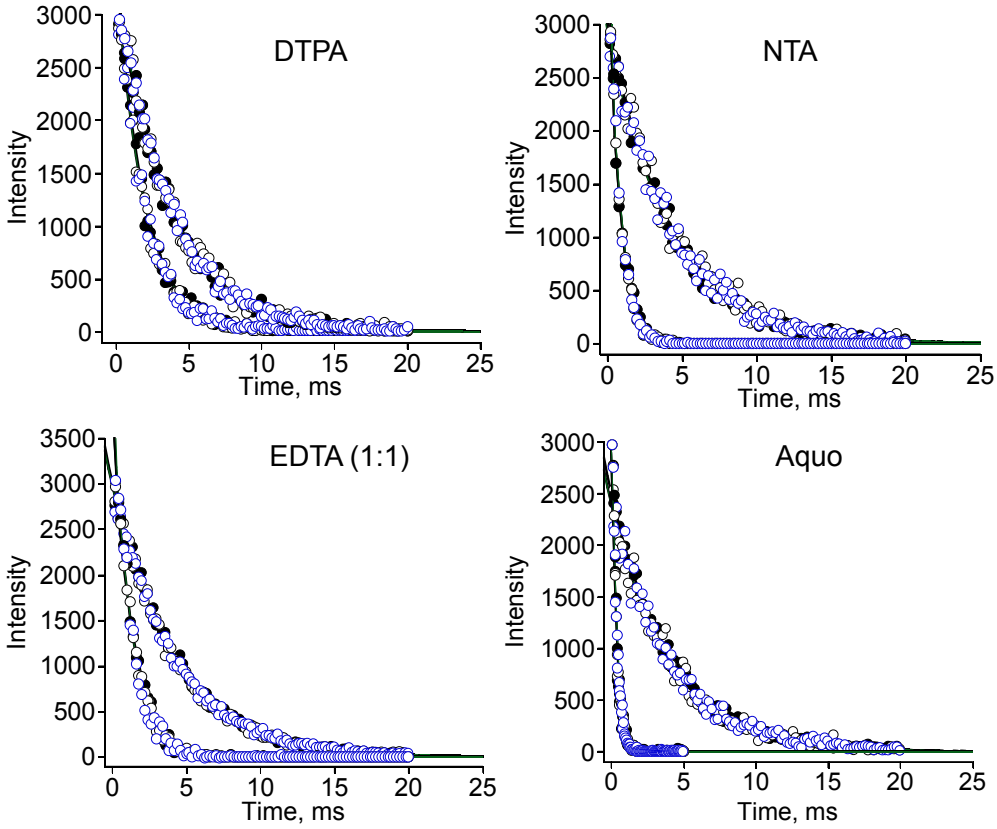

Figure 4-19. The luminescence decay of Tb^{3+} in H_2O or D_2O in aqueous solution or chaleted by DTPA, EDTA or NTA.

Tb^{3+} and chelators were mixed with 1 to 1 ratio. The final concentration for Tb^{3+}-chelators were 20 µM in H_2O or D_2O at pH 7.0. The experiments were performed at PTI fluorometer in H_2O or D_2O in aqueous solution without any salt.

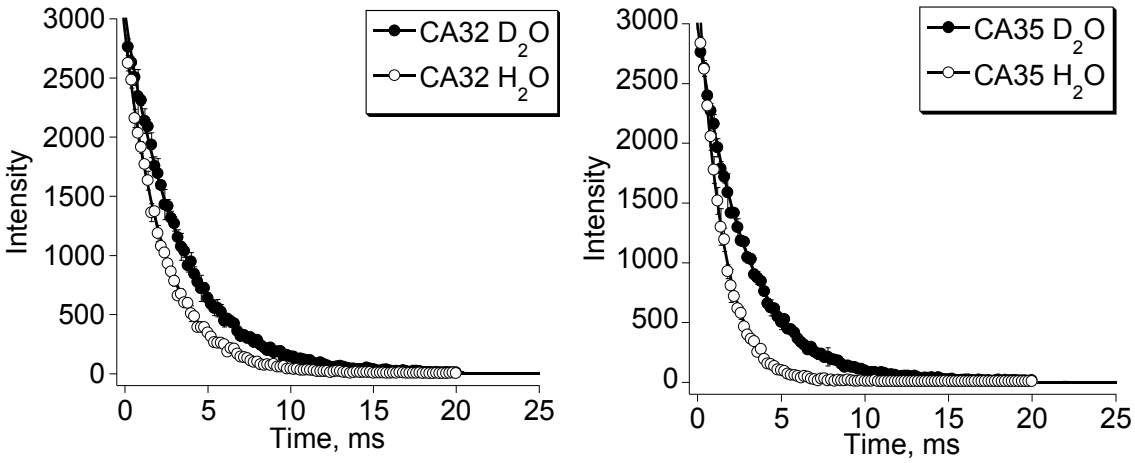

Figure 4-20 The luminescence decay of Tb^{3+} in H_2O or D_2O chaleted by ProCA32 (left) or ProCA35 (right).

Tb^{3+} and ProCA3 variants were mixed with 2 to 1 ratio. The final concentration for Tb^{3+}-ProCA3 variants were 20 µM in water at pH 7.0. The experiments were performed at PTI fluorometer in H_2O or D_2O in aqueous solution without any salt. To prepare ProCA3 variants in D_2O. 20 µM of ProCA3 variants in H_2O were first freeze at -80˚C and then all the water was removed by spin vacuum. The protein powder was then dissolved in the same volume of D_2O. This process was repeated three times to completely remove of H_2O.

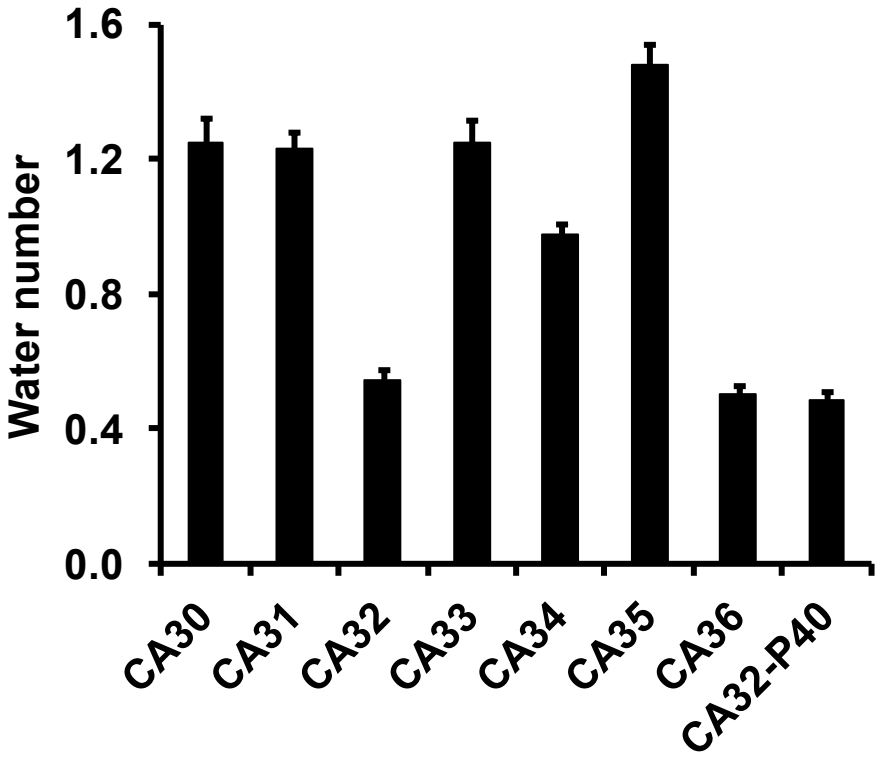

Figure 4-21. Water number of Tb^{3+} loaded ProCA3 variants.

Tb^{3+} and ProCA3 variants were mixed with 2 to 1 ratio. The final concentration for Tb^{3+}-ProCA3 variants were 20 μM. The experiments were performed at PTI fluorometer in H_2O or D_2O in aqueous solution without any salt at pH 7.0.

The ΔK_{bos} of Tb^{3+} in ProCA3 variants were determined using the similar methods. Then the water number of the ProCA3 variants were calculated based on the standard curve and ΔK_{obs} of each varients (Fig. 4-20). WT PV has averaged water number of 1.3 (Fig. 4-21), which is consistent with reported value.[174] Interestingly, the water number of ProCA35 increase to 1.6, the increase of water number in ProCA35 is consistent with the increase of relaxivity in ProCA35. To our surprise, the water number of ProCA32 (introducing S56D mutation) decreases from 1.3 to 0.4 (Fig. 4-20), while the relaxivity of ProCA32 (S56DE60D) does not decrease. All these results indicate that mutation of S56D introduces more ligands from protein to interact with Gd^{3+}, which increase Gd^{3+} binding affinity and decrease the number of water to interact with protein.

4.2.4 In vitro serum stability study of protein based MRI contrast agents

Since ProCA32 shows the best metal stability and good relaxivity, ProCA32 and PEGylated ProCA32 is promising to be applied as a novel MRI contrast agents. It is extremely important that the ProCA3 will not be cleaved by the enzyme in the serum and maintain intact structure before secreted out of the body. In order to evaluate the stability of ProCA32 and PEGylated ProCA32, ProCA32 and PEGylated ProCA32 were incubated in the 50% serum and then detected by SDS-PAGE, western blot and Mass spectrum. ProCA32 is very stable in the serum for at least 3 days (Fig. 4-22). After three day, the native protein in the blood began degrading, but ProCA32 still existed in the blood serum even after 12 days. Immuno blot and Mass spectrum are also applied to detect the ProCA32 and P40CA32 serum stability. All of these data indicates that ProCA32 and PEGylated ProCA32 are stable in serum for at least three days. As shown in Fig. 4-22, ProCA32 and PEGylated ProCA32 and stable for even up to 12 days. All these data indicate that ProCA32 and PEGylated ProCA32 are very stable in the serum, and PEGylated

ProCA32 has a half-life of 2.9 hours in the blood, most ProCA32 is excreted out one day after injection. Thus, it is very important that ProCA32 is stable for at least 2 days in order to the safely used *in vivo*.

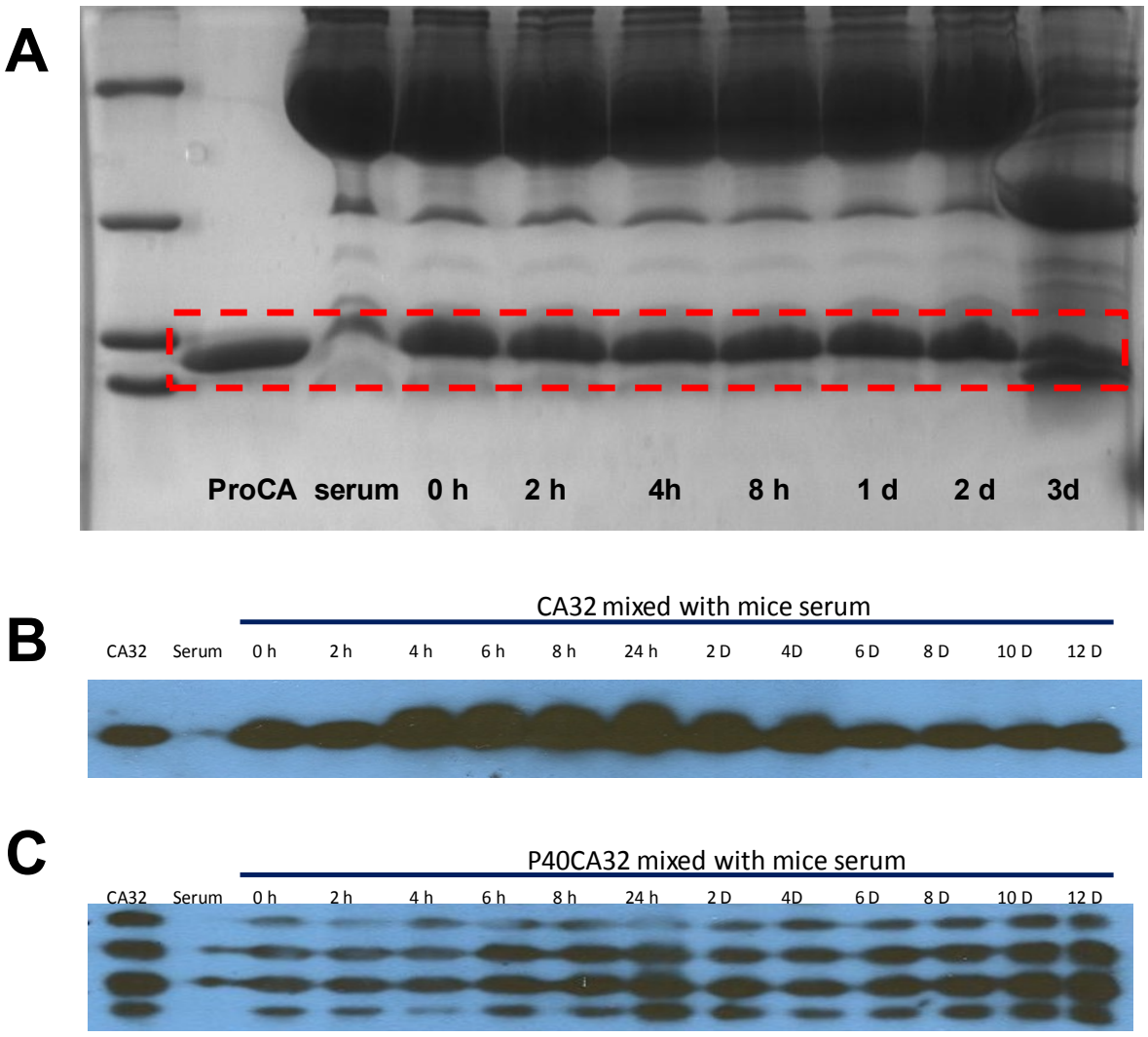

Figure 4-22. Serum stability of ProCA32 or ProCA32-P40.

A, B. Serum stability tests of ProCA32 by SDS-PAGE (A) or immune-blot (B). C. Serum stability tests of ProCA32-P40 by immune-blot. Gd^{3+}-ProCA32 (400 µM) was mixed with mice serum with 1:1 ratio, and then incubated at 37 ˚C for different time point. SDS-PAGE and immunoblot were applied to detect the remaining Gd^{3+}-ProCA32 after incubate in the serum for each time point. The protein separated by SDS-PAGE is stained by coomassie brilliant blue or immunoblot.

4.3 Discussion

4.3.1 Developed new metal binding methods using metal-chelator buffer system allow us to acuately measure strong metal binding affinity.

EF-hand I in wild type PV has four carboxyl ligands (D52, D54, E60 and E63) and one noncharged oxygen liagnd (S56) to interact with Ca^{2+}. X-ray structure (Fig. 3-1) and other technique showed that position 9 in EF-hand I (E60) of PV directly use side chain carboxyl group as oxygen ligand to interact with Ca^{2+}, however, most other EF-hand proteins use water as oxygen ligand to interact with Ca^{2+}. Mutation S56D introduces additional one more negative charge to form pentacarboxylate structure. Since charge is one of the key determinants for the metal binding affinity, we further studied the effects of pentacarboxylate EF-hand on Gd^{3+} binding affinity. Fluorescence competition methods and metal buffer system methods are applied to determine the dissociation constant between Gd^{3+} and ProCA3 (Fig. 3-2). Interestingly, introducing one negative charge dramatically increases Tb^{3+} and Gd^{3+} binding affinity for more than 10^6 folds, which indicates the desired Gd^{3+} binding pocket in protein are formed by introducing more negative charged residues in EF hand I. We further modified the Gd^{3+} binding sites by E60D mutation in both WT and S56D mutants. X-ray structure of Ca^{2+} indicates that E60D introduced one water ligand to interact with Ca^{2+}, while carboxyl side chain in this position moved away. By this way, number of carboxyl groups for metal binding in EF-hand I decreased. PVE60D does not show dramatic metal binding affinity change compared to wild type, while PVS56DE60D showed the increase of Ca^{2+} binding affinity and dramatically decreased Gd^{3+} and Tb^{3+} binding affinity compared with PV S56D and WT. EF-hand II of PV WT are formed by the four carboxyl group (D91, D93, D95, E102) and one water ligand (G99) to bind Ca^{2+}. G99D and

G99E mutants are generated to study the charge effects on the metal selectivity of EF-hand II. We hypothesize that G99E directly interacts with metals, while G99D, like WT, utilizes one additional water ligand instead of carboxyl group. EF-hand II of G99E is very similar to S56D in EF-hand I. Interestingly, since EF-hand II of G99D is very similar to the EF-hand I of S56DE60D, the binding affinity of G99D is very similar to that of mutants. Zn^{2+} binding affinity of PV variants are measured by Fluozin-1 competition methods. PV-based MRI contrast agents shows excellent metal selectivity between Gd^{3+} and Zn^{2+} with log(pGd/pZn)= 10.5 for ProCA32. All these data indicates that pentacarboxylate structure in EF-hand is strongly favorable to bind to Gd^{3+} and Tb^{3+} over Ca^{2+} and Zn^{2+}. Interestingly, ProCA32 has a much higher metal selectivity than DTPA and ProCA1, which is essential for the *in vivo* application because Zn^{2+} is considered as one the the major metal ion to compete Gd^{3+} out of chelators.

Tb^{3+} luminescent life time decay in H_2O and D_2O solvents is measured to characterize the water number of the inner sphere of metal binding sites. WT PV has averaged water number of 1.3, which is consistent with reported value. Interestingly, the water number of ProCA35 increases to 1.6, the increase of water number in ProCA35 is consistent with the increase of relaxivity in ProCA35. To our surprise, the water number of ProCA32 decreases from 1.2 to 0.4, while the relaxivity of ProCA35 does not decrease. All these results indicate that the mutation of S56D introduce more ligands from protein to interact with Gd^{3+}, which increase Gd^{3+} binding affinity and decrease the number of water to interact with protein. The per Gd^{3+} and per particle relaxivity of ProCA32 with improved metal binding affinity and decreaed water number do not decrease compared with ProCA30 is very interestingThese results suggest ind that different

from first coordination shell, secondary hydration shell or /and reduction of local motion by improved metal binding affinity may be further contribute to the increase of relaxivity.

4.3.2 Tune the relaxivity of ProCA3 variants by protein design.

We are able to tune the relaxivity of ProCA3 variants through protein design. Positions 1, 3 5, 7, 9 and 12 in EF-hand are the key residues for metal binding. Among them, positions 1, 3, 5 and 12 usually use side chain oxygen as metal ligand. Position 9 of EF-hand always bridges with one water molecular. Glutamate 60 is located in the position 9 in the EF-hand I of PV. Interestingly, X-ray structures of PV shows that Glutamate acid 60 directly interact with metals without water bridge, we hypothesis that mutation of E60D will introduce water ligand to position 9. Consistent with our hypothesis, the water number of S56DE60D increase to 1.8, while the WT PV only has a water number of 1.3. Interestingly, the relaxivity of ProCA35 (S56DE60DF103W) dramatically increase to 57 and 77 $mM^{-1}s^{-1}$, which is increase about 100% comparing the ProCA30 (wild type PV) , ProCA31 (PV with F103W mutations) and ProCA32 (PV with S56D F103W mutations). This is the first time that we can increase the realxivity by directly control the the ligand coordination of ProCA3. Interestingly, r_1 and r_2 of ProCA33 increased about 50%, the increase of the relaxivity could also be caused by the introducing water ligand in the position 9.

Position 9 of EF-hand II in PV is occupied by a water ligand. Interesting, mutations in G99D in EF-hand II decrease the water number. These results indicate that aspartic acid in EF-hand II decrease the water binding in position 9. However, the relaxivity of this mutant is the same as WT PV, suggesting that second shell of coordination water plays important roles on the relaxivity.

4.3.3 The advantage of ProCA3 for MR imaging due to high relaxivity.

The MRI signals are generated based on the different relaxation properties of protons. However, such differences are very small among organs *in vivo*. As we can imagine, changing the water relaxation properties is not a trivial task, since water has a concentration of 18 M, and the relaxivity different of organs could be very similar. Because of this reason, the contrast agent and sensitivity of MRI is much lower than other imaging modalities, such as PET/SPECT. The contrast and sensitivity of MRI can be improved by administrate the contrast agents. MRI contrast agent works as "catalyst" to catalyze the relaxation properties each water molecule. By differential distribution *in vivo*, MRI contrast agents made the relaxation properties difference in each organ.

In order generate considerable contrast *in vivo*, the relaxation time of water should be decrease to 100 ms. For clinical MRI contrast agents, such as Gd-DTPA has a relaxivity less than 5 mM^{-1} s^{-1}, the effective concentration of Gd-DTPA should be as high as 100 μM in order see the clear differences between each tissue.[10] The lowest concentration of clinical MRI contrast agents is 30 μM in order to clearly show the difference. In order generate such high Gd^{3+} concentration *in vivo*, the clinical contrast agents is recommended to injection 0.1-0.2 mmol/kg body weight.[10]

The application of MRI for molecular imaging is jeopardized by the detection limits of MRI contrast agents, since the disease biomarker usually has very low concentration. The biomarker expression level is usually less than 10^6 biomaker/cell. Assuming a cell has a volume of 1000 μm^3, the local concentration of this biomarker is only 1 nM.[136] Such low expression of biomarker made molecular imaging very hard for MRI. It would still be very hard even if consid-

ering the effects of endocytosis. Sherry simulated the relationship between relaxivity and detection limits. The detection limits for clinical MRI contrast agents is more than 10 μM with *r1* relaxivity of less than 5 mM^{-1} s^{-1}. The detection limits of contrast agents are pushed to about 1 μM, when the relaxivity of the contrast agent is about 20 mM^{-1} s^{-1}. When the relaxivity of the contrast agent is higher than 100 mM^{-1} s^{-1}, the detection limits of MRI contrast agents is further pushed to less than 1 μM.[45]

Improving the relaxivity of the contrast agents has two advantages. First, increase the relaxivity of the contrast agents can decrease injection dosage required, which could potentially decrease the Gd^{3+} accumulation *in vivo*. Second, improve the relaxivity can potentially improve the detection limits for MRI contrast agent, which greatly benefits the molecular imaging using MRI.

As shown from Fig. 1-1, the relaxivity of the contrast agents can be influenced by many factors. Water molecular directly interacts with metal ion such as Gd^{3+} to change the relaxiation properties. Based on the distant between water molecule and Gd^{3+}, the relaxivity can be further divided into inner sphere relaxivity, second sphere relaxivity and outer sphere relaxivity. The overall relaxivity of the contrast agents is the combination of inner sphere, secondary sphere and outer sphere relaxivity. The inner sphere and second sphere relaxivity can be characterized by SMB equation.[10] The outer sphere relaxivity of the contrast agents can be characterized by hard-sphere model, when the water is considered as passive diffusion.[10] In general, relaxivity of the contrast agents are influenced by τR, τ_m and q. For example, the bioresponsive contrast agents were designed based on the changes of these parameters at different physiological conditions.[10]

To develop a MRI contrast agent with high sensitivity, high relaxivity is highly desired. ProCA3 has more than 10 times higher relaxivity than commercial contrast agents at clinical MRI field (1.4 T), which provides a more sensitive tool for the MR imaging for clinical and pre-clinical diagnostics. Furthermore, due to careful design, the T_R of the ProCA3 was optimized for the use in the high magnetic field. The r_1 relaxivity of ProCA3 is 18 $mM^{-1}s^{-1}$ at 7 T, which is up to the theoretical relaxivity value of Gd^{3+} based MRI contrast agents. The relaxivity of ProCA3 decrease at high temperature, which indicates that ProCA32 also has optimized fast water exchange. Only 2.5 μM of ProCA3 in the test tube can be detected, which is much lower dosage than that of Gd-DTPA. High relaxivity of ProCA3 at both clinical and high magnetic field will have two advantages. First, increased relaxivity improves the detection of MRI which will benefit the molecular imaging using MRI, since biomarkers always shows limited expression levels and only can be detected by very sensitive probes. Second, increased relaxivity of ProCA3 can effectively reduce the injection dosage, which could decrease the metal release caused toxicity.

4.4 Summary

First, we have developed a novel method to determine metal binding affinity and selectivity using metal-buffer sytem and Tb-LET of proteins with stronger metal binding affinity and selectivity constants that can not be accurately determined by current avalibale methods. Currently there is no valaible assay allows to determine high metal stability strongly required in the clinical diagnostics for the MRI contrast agents. This developed method can be used for determining metal binding affinities and selectivity for other metalloproteins or macromolecules.

Second, we have determined all the metal binding affinity and selectivity of designed ProCA3 variants. We have shown that ProCA32 with mutation S55D on the metal binding sites

has extremely high Gd^{3+} binding affinity (Kd = 2.8 ± 0.3 × 10^{-22} M) that is improved than ProCA1 and is similar to clinical approved contrast agents DTPA etc. More important, ProCA32 has metal selectivities for Gd over physiological metal ions such as Zn^{2+}, Mg^{2+} and $Ca^{2+}$are more than 10^{11}, 500, 150 fold greater than DTPA. Pegylation of ProCA32 does not change metal stability. Serum stability studies also further support that ProCA32 and ProCA32-P40 is stable in blood and resistant to the enzyme cleavage, which provide another solid support for the clinical application of ProCAs with high safety.

5 PROCA3 ENHANCED MRI OF MUTIPLE TISSUE ORGANS AND TUMOR METASTASIS

5.1 Introduction

A contrast agent with high relaxivity is essential for improving the detection limits of the MRI contrast agents. Dr. Sherry and his colleagues[45] found that a contrast agents with an r_1 = 5 $mM^{-1}s^{-1}$ has a lowest detection limits above 20 μM, and the detection limit improved to 680 nM, when the relaxivity increase to above 100 $mM^{-1}s^{-1}$.

Improvement of the detection limits of the MRI contrast agents could be essential for MRI. It dramatically reduces injection dosage and decreases the toxicity of the MRI contrast agents. It also improves the sensitivity of the MRI contrast agents for the molecular imaging. Since the biomarkers usually have low expression level in the range of nM or pM, imaging biomarker using MRI is largely hampered by the lack of MRI contrast agents with high relaxivity, low detection limits and targeting specificity.

Due to the selective tissue distribution, MRI contrast agents are applied for the imaging of kidney, CNS, liver and blood. Clinical MRI contrast agents are also applied to evaluate lesions, infrared, stroke and tumor due to its unique distribution in these tissues *in vivo* compared to the normal tissue. However, due to the lower detection limits, non-specific distribution, and not optimized pharmacokinetics, the clinical MRI contrast agents are not optimized for imaging these tissues. Dynamic contrast enhanced-MRI (DCE-MRI) is a usefully methods to evaluate tumor vasculature. The reliability and stability of this technique, however, is affected by the inaccurate measurement of the real-time concentration of the contrast agents in serum due to the short blood retention time and low relaxivity of contrast agents.

As discussed in chapter 1, MR imaging of tumor metastases has great advantage than other imaging techniques. For example, MR imaging of liver provides more sensitivity and reliability than other imaging techniques.[14, 193-196] In principle, MRI can also non-invasively evaluate tumor properties, such as size, oxygen level, water diffusion, and blood vasculature. Gadolinium compounds are the most frequently used MRI contrast agents due to high paramagnetic property and asymmetric electronic ground state of Gd^{3+}, rendering the ability to create bright MR images by decreasing T_1 without causing substantial line broadening. However, clinical MRI contrast agents, such as Gd-DTPA, have relaxivities less than 5 mM^{-1} s^{-1} which require high injection doses of 0.025-0.2 mmol/kg of clinical MRI contrast agents to generate a detectable contrast with a local Gd^{3+} concentration of about 100 μM. This is significantly lower than theoretical value around 100 $mM^{-1}s^{-1}$ for one water molecule coordinated in the Gd^{3+} inner shell.[197] They suffer a risk of Nephrogenic Systemic Fibrosis (NSF) due to metal toxicity for patients with renal dysfunctions.[22] There are additional challenges for developing contrast agents for liver imaging due to its fast circulation. Gd-EOB-DTPA (Evoist US; Primovist, Europe, Bayer) and Gd-BOPTA (Multihance, Bracco) with 50% and 5% hepatocyte up take, respectively, are the most commonly used clinically approved liver contrast agents. In addition to similar per Gd relaxivity (r_1) values around 4-6 $mM^{-1}s^{-1}$, their very short retention time in the liver (1 min for Multihance and 30 min for Eovist) largely restrains a narrow time widow to achieve high quality MR imaging and limited time for MRI-guided liver intervention and local treatment. On the other hand, iron oxide nanoparticle contrast agents such as Ferumoxides are taken up by functioning Kupffer's cells creating T_2 /T_2* effects on the normal liver, however it is less applicable due to imaging artifacts. Increasing relaxivity of small metal chelators by increasing exchangeable water num-

ber q in the Gd coordination shell often resulting the tradeoff metal stability. Increasing correlation time τ_c by conjugating to the polymer or macromolecules do not yield expected increase of relaxivity. Therefore, there is an urgent need to develop contrast agents with significantly improved relaxivity and metal stability, pharmacokinetics to enable the detection capability of smaller size tumor extending to less than 1 cm with good confidence.

Challenges in developing contrast agents with high relaxivity in *in vivo* imaging capability of liver metastasis are due to several criteria: 1). An ideal MRI contrast agents should have high relaxivity 2). An ideal MRI contrast agents should have high distribution in liver. 3). An ideal MRI contrast agents should have permeability to the liver tissue but low permeability to the metastatic tumor tissue. These features can improve ratio of MRI liver signal intensity to tumor signal intensity. 4). An ideal MRI contrast agents should be able to alter the signal from both T_1- and T_2- weighted MR images, so that detected tumor under T_1 weight MRI can be further validated by T_2- weight MRI. If the tumor too is small, T_2-weighted MRI without contrast agent is not able to show the tumor enhancement, a MRI contrast agent with good r_2 is able to decrease the liver signal which can improve the tumor detection using T_2 weighted MRI sequences. 5). An ideal MRI contrast agents should have stability and strong metal selectivity to avoid Gd^{3+} release. 6). An ideal MRI contrast agents should have good pharmacokinetics. 7) An ideal MRI contrast agents should have no toxicity.

Our previous work shows that the protein-based MRI contrast agents has more than 10 times higher r_1 and r_2 relaxivities, optimized blood circulation, good solubility and biocompatibilities. Protein-based MRI contrast agents were also fused with targeting moieties, such as HER-2 affibody or GRP peptide, for in vivo MRI of biomarkers by target tumor bi-

omarkers with high specificities and high affinity. However, such study is only limited to T_1-weighed MRI. In addition, these contrast agents only embrace one Gd3+ binding sites and the purification methods for ProCA need to be further improved. In my Ph. D. study, I developed a new class of MRI contrast agents with multiple Gd^{3+} binding sites, extremely high affinity, optimized blood and liver retention time for in vivo MRI of multiple organs. I also optimized the expression purification and GMP-like procedures for ProCA production. In addition, the paharmacokinetics of different protein-based MRI contrast agetns were carefully studied. Because ProCAs has both high r_1 and r_2 relaxivity, we further applied the T_2/T_1 ratiometric imaging and bi-briliant imaging for the MRI of primary and metastatic tumors in the liver with high confidency. These works are of great vaule for the clinical diagnosis of disease by MRI with improved MRI contrast agents and impoved methodology.

Our work discussed in Chapter 4 has shown that ProCA3 variants have 10 fold higher r_1 relaxivity than that of clinical contrast agents at 1.47 T. More strikingly, due to the optimization of τ_R, τ_m, ProCA3 reached the maximum value of r_1 at high magnetic field, such as 7 T. As shown in Fig. 5-1, since ProCA32 variants has high relaxivitiy with r_1 = 30 $mM^{-1}s^{-1}$ at 1.4 T and r_1 = 19 $mM^{-1}s^{-1}$ at 7 T, it should has much lower detection limits for MRI imaging than clinical MRI contrast agents. These unique features made ProCA3 as one of the most suitable candidates as sensitive MRI contrast agents not only for clinical application but also good for the preclinical application at high magnetic field.

In this chapter, we will first explore the lowest detection limits of ProCA32 under MRI. Then, we will report mice imaging of ProCA32 of multiple organs, such as kidney, liver, blood

vessel imaging. At last, we will report our progress of imaging liver metastases of unveal melanoma using ProCA32 with bi-briliant dual weighted MRI methodology.

5.2 Results

5.2.1 In vitro detection limit of ProCA3

Less contrast agents are acquired to acquired good image enhancement when the relaxivity of the contrast agent improved. Since our contrast agents show about 10 times higher relaxivity at 1.4 T and more than 4 times higher relaxivity at 7 T compared with that of Gd-DTPA, we further studied the detection limits *in vitro* and *in vivo*. To test the *in vitro* detection limits, ProCA3 with different concentrations were scanned using T_1-weighted spin echo sequence (spin echo sequence with TR = 500 ms, TE = minimium, thickness = 1 mm) at 7 T. As shown from Fig. 5-1, 2.5 μM of ProCA3 showed much higher signal intensity compared with buffer only. This result indicates the detection limits for ProCA3 is at least 2.5 μM, which is more than 10 times sensitive than that of clinical MRI contrast agents.

5.2.2 In vivo detection limits of ProCA3

We further tested the *in vivo* detection limits for the detection of kidney, liver and blood enhancement by injection of a series concentration of ProCA3 in different mice. To optimize the best conditions for MRI data collections, The MRI images of kidney were collected at different repetition time (TR) from 300 ms to 700 ms. 400 ms to 600 ms TR shows the best enhancement of the ProCA3 in kidney. Then, the MR images of kidney were collected by varian 7 T MRI scanner using spin echo sequence with TR = 500 ms. The mice without injection of ProCA3 or other

contrast agents were used as control. Different concentrations of ProCA3 were injected in mice through tail vein, and then kidney MR images were collected 10 min post injection of the contrast agents. Clear kidney enhancement were obtained with a injection dosage of 0.8 μmol/kg ProCA32M, a concentration more than 100 times lower than the clinical injection of Gd-DTPA. As a comparison, 1.6 μmol/kg Gd-DTPA was injection in a separate mice, which has the same Gd^{3+} concentration as 0.8 μmol/kg of ProCA32M. Interestingly, 1.6 μmol/kg Gd-DTPA do not show any significant kidney enhancement under MRI. These results indicate that ProCA32 has much lower detection limits than Gd-DTPA *in vivo*.

To determine the lowest injection dosage of ProCA3 for liver and blood, 0.8 - 33 μmol/kg of ProCA3M were injected into CD1 mice (25 – 30 g) through tail vein. The blood and liver images were collected at 20 min post injection of ProCA3M using 3D-gradient echo sequence (TR = 40 ms, TE = 2.9 ms, slice thickness = 1 mm). 3D MRI of liver shows that the liver is heterogeneously enhanced with the injection of 1.6 μmol/kg of ProCA3M. Thus, using the injection dosage of 1.6 μmol/kg of ProCA3M, we are able to detect liver enhancement.

Although 1.6 μmol/kg of ProCA3M is able to enhance the liver, such injection dosage can not enhance the blood vessel. 3D MRI of liver shows that the lowest injection dosage to enhance the blood vessel is 33 μmol/kg of ProCA3M. However, the MRI signal in blood is highly dependent on the time point after injection, and we could see the blood vessel signal changes with lower injection dosage at earlier time point.

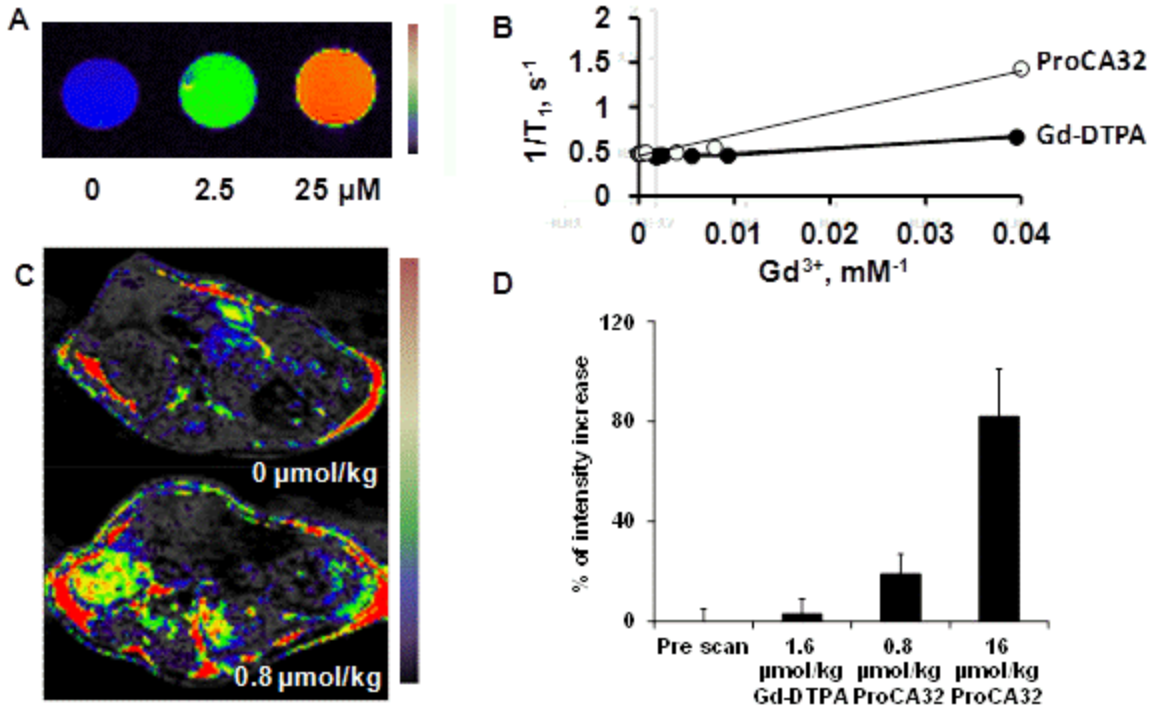

Figure 5-1. The relaxivity, detection limits of ProCA32 *in vitro* and *in vivo*.

A. *In vitro* study of MRI in the phantom of ProCA32 in different concentration. B. Relaxiation time differences between GdDTPA and ProCA32 at different concentration in the 7 T MR scanner. C. *In vivo* MRI of the mice kidney before and after injection of 0.8 µmol/kg ProCA32. D. percentage of signal increase in mice kidney after injection of 0.8, or 16 µmol/kg ProCA32 or 1.6 µmol/kg Gd-DTPA. The MRI images were processed by MRIcro. The MRI signal intensity of kidney were measured from at least three slides. The error bar refers to the standard deviation of MRI intensity increase measured from at least three slides.

5.2.3 MR angiography (MRA) before and after injection of ProCA32M

To investigate ProCA32 on MR imaging for different organ, 3D MR images were acquired at pre injection, 50 min, 2 hr, 25 hr and 49 hr post injection of 33 μmol/kg of ProCA32M using 3D gradient echo sequence (TR = 40 ms, TE = 2.9 ms, slice thickness 1mm, matrix 256 × 256 × 64, Fov 8 cm × 4 cm × 6.4 cm). ProCA32M shows excellent enhancement of blood vessel even at 50 min post injection (Fig. 5-2 at 4.7 T). Interestingly, ProCA32M is able to enhance the blood vessel with a diameter less than 1 mm. No blood vessel was enhanced before injection of ProCA32M, and the blood vessel is immediately enhanced at the first time point of data collection. The blood vessel enhancement dramatically decreased 2 hr post injection of the ProCA and the blood vessel intensity returned to the original stage when the data were collected 1 day and 2 day post injection. We then analyzed the Gd^{3+} distribution and ProCA32M protein distribution by ICP-OES and immune blot respectively (Please see chapter 7 for details). These results indicate that ProCA32M is a good contrast agent for MRA, and ProCA32M can be potentially used as a powerful diagnostic tool for the blood vessel disease.

5.2.4 MR imaging of kidney, bladder and liver before and after injection of ProCA32M using T1-weighted 3D gradient echo sequence

Using the same procedures as 3D gradient echo (3DGE) sequence image of blood vessel, the kidney of the mice was enhanced after injection of ProCA32M. However, the enhancement of the kidney is much slower than that of the blood vessel (Fig. 5-2). The highest enhancement for kidney was observed at 1 day post injection of ProCA32M. The signal of kidney returned to the original state 2 days post injection of contrast agents. 3DGE image shows great enhancement of bladder at 50 min post injection of ProCA, which indicate ProCA32M started excretion

through kidney. Liver also got enhancement after injection of the ProCA32M. The liver is immediately enhanced after injection of ProCA32M and the signal return to the original state 2 day after injection of ProCA32M. These results indicated that ProCA32M has great potential for the imaging of liver and kidney disease, such as liver metastasis and renal malfunction.

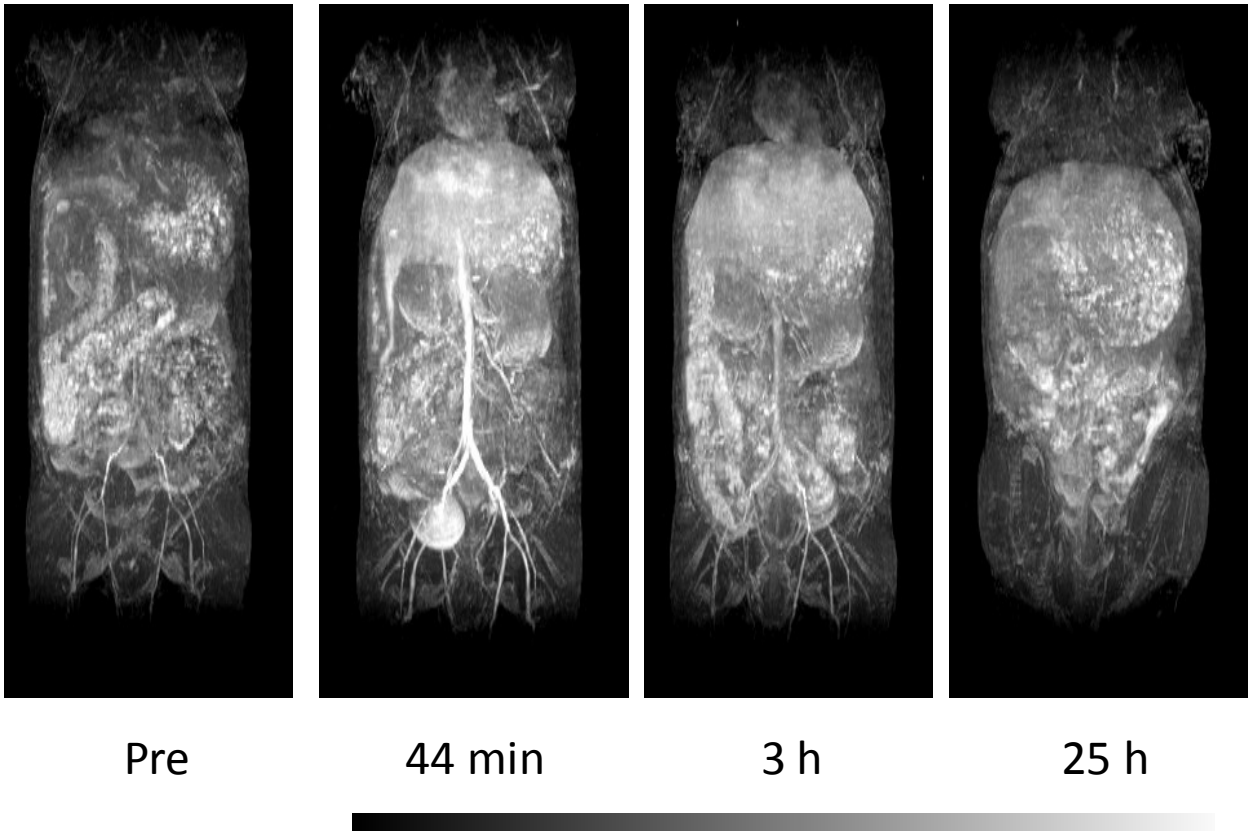

Figure 5-2. Maxmium intensity projection images of three dementional MRI before (Pre) and after injection of ProCA32M for different length of time (44 min, 3 h, and 25 h).

MRI were colletected at 4.7 T MRI scanner before and after injection of ProCA32M (0.02 mmol/kg) with 3D gradient echo echo sequence with TR = 40 ms and TE = 2.9 ms.

5.2.5 Imaging normal mice liver using T_1-weighted or T_2-weighted sequences

Since r_2 of ProCA32 is 40 $mmol^{-1}$ s^{-1}, ProCA3 could also be applied for the T_2-weighted MRI image. Fig. 5-3 shows that the liver of the mice became darker two hours after injection imaged by T_2-weighted sequence at 3 T clinical scanners. Interestingly, the liver of the same mice shows enhancement using T_1-weighted sequence at 3 T clinical scanners. These results indicate that ProCA32M can be as both T_1-weighted MRI contrast agents and T_2-weighted MRI contrast agents.

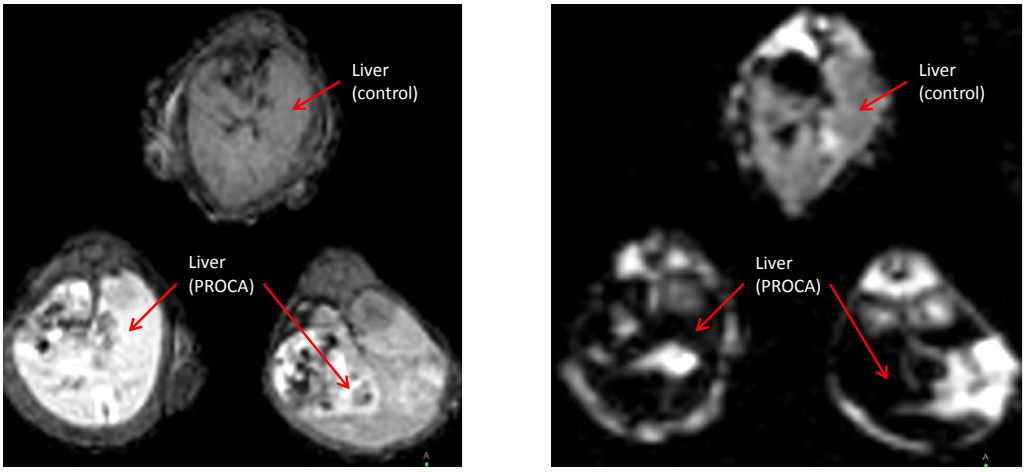

T1W MRI of liver (axial view) **T2W MRI of liver (axial view)**

Figure 5-3. T_1 or T_2 weighted MRI with and without ProCA32M injection.

Images of dead mice were collected at 3 T clinical MR scanner with ProCA32 M (0.02 mmol/kg) injection for 2 hours or without ProCA32M injection. T_1-weighted MRI shows signal enhancement in the mice liver (left) and T_2-weighted MRI shows signal decrease in the mice liver (right). Data collected from University of Alabama at Birminham with the help from Drs. Kim and Zhai.

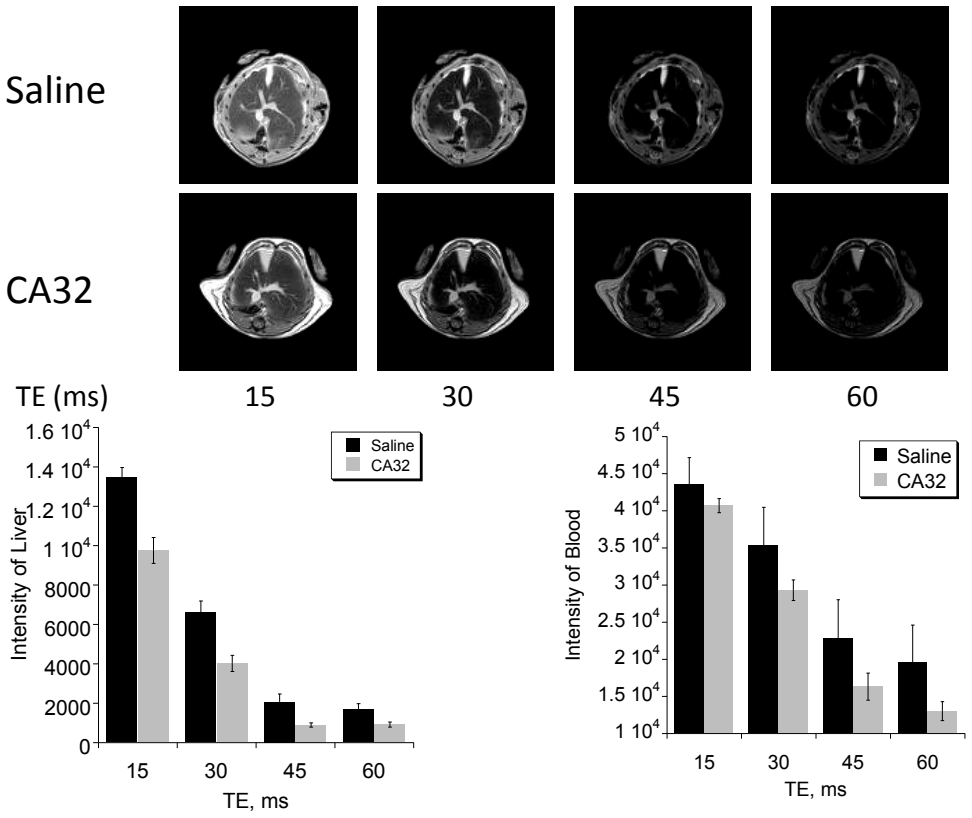

Figure 5-4. T_2 mapping of mice liver with and without injection of ProCA32M.

T_2-weighted MEMS image the mice liver with different TE. B. Liver intensity of mice with and without injection of ProCa32M at 15, 30, 45 or 60 ms of TE. C. Blood intensity of mice with and without injection of ProCa32M at 15, 30, 45 or 60 ms of TE.

Similarly, T_2-weighted MRI images of mice liver were collected at 7 T Varian MRI scanner. The mice were scanned after injection of 0.02 mmol/kg ProCA32 or saline for 30 min. T_2-weighted MEMS sequence (Multi-echo-multi-slides sequence) with different echo time (TE) were applied to acquire MRI images of liver. As shown from Fig. 5-4, the liver the mice became darker after injection of ProCA32M. The biggest differences of the liver between ProCA32M injected mice and saline injected mice were obtained using MEMS with TE=15 or 30 ms. We also compared the blood vessel signal differences in T_2-weighted MR images. The optimized TE to see the differences of blood vessel in ProCA32M injected mice and saline injected mice are 45 and 60 ms. In summary, ProCA32M is able to decrease the signal of liver after injection of ProCA32M in both 3 T clinical scanner and 7 T preclinical scanner. Thus, ProCA32M can also be used as T_2-weighted MRI contrast agents due to high r_2 relaxivity.

5.2.6 Imaging liver metastasis using ProCA

Liver is one the major organ for the tumor metastasis, such as melanoma, breast cancer and pancreatic cancer. Our preliminary data shows that ProCA32M is able to accumulate liver and imaging liver with high intensity, high efficiency and low injection dosage. We next evaluate if ProCA32M can detect tumor metastasis in liver. The mice melanoma cells were implanted in the eye of the PEDF knockout mice. The tumor implanted mice were continuously grown for two weeks. We then imaged the mice liver under MRI with T_2-weighted fast spin echo and T_1-weighted spin echo sequence. The mice were imaged before and injection of the contrast agents. Liver metastasis of melanoma cannot be detected without injection of the contrast agents. We clearly see more than 10 liver metastasis in liver after injection of ProCA32 with hypo-intensity of tumor in T_1-weighted spin echo (Fig. 5-5 B, E) and hyper-intensity of tumor in T_2-

weighted fast spin echo sequence (Fig. 5-5 A, D). Interestingly, the MR imaging of liver metastasis correlates well with HE staining (Fig. 5-5 C, H), where the tumor in dark blue/purple color and normal liver is pink color. The location of the tumor under MRI were further confirmed by IHC staining of S100 (Fig. 5-5 I), which is a typical biomarker for melanoma. To further explore the mechanism of hypo-intensity of tumor under MRI, the optical (Fig. 5-5 J) and fluorescent (Fig. 5-5 K) images of mice liver with melanoma metastasis were taken by fluorescent dissecting microscope 30 min post I.V. injection of fluorescein-labeled ProCA32M. The liver tissue showed enhanced green fluorescence, while melanoma matastasis doesn't show any fluorescence. These results indicate that after injection for 30 min, ProCA32M is accumulated in liver tissue, while due to lack of blood vessel, no ProCA32M can be penetrated in to the melanoma. Moreover, we are able to clearly detect liver metastasis with a size less than 0.25 mm, while most of current MRI test can only detect tumor with a size more than 10 mm with high accuracy. Thus, ProCA32M shows the great advantages for the imaging tumor metastasis in liver. Thus, ProCA32M show great potential for the early diagnostics of liver metastasis. Early diagnosis of liver metastases is essential for the effective drug treatment of tumor.

We further compared the MRI liver ehance of Evoist and ProCA32 in mice under the T_1-weighted spin echo sequence (Fig. 5-6). With the injection of same concentration of Eovist or ProCA32, ProCA32 has significant high liver enhancement at 10 min and 50 min post injection of the contrast agents. The intensity for Eovist decreases very fast. As show from Fig 6-6B, more than 50% liver signal decrease after injection of Evoist 50 min. ProCA32, however, shows much stable liver enhancement. There are no significant signal entensity differences after injection for 10 min and 50 min. ProCA32 is also able to be applied for T_2-weighted MRI with improved

tumor detection. Taken together, ProCA32 show great potential as a promising MRI contrast agents for the imaging of liver and liver metastasis with a size more than 10 times less than that of clinica MRI contrast agents in the clinical tumor diagnostics.

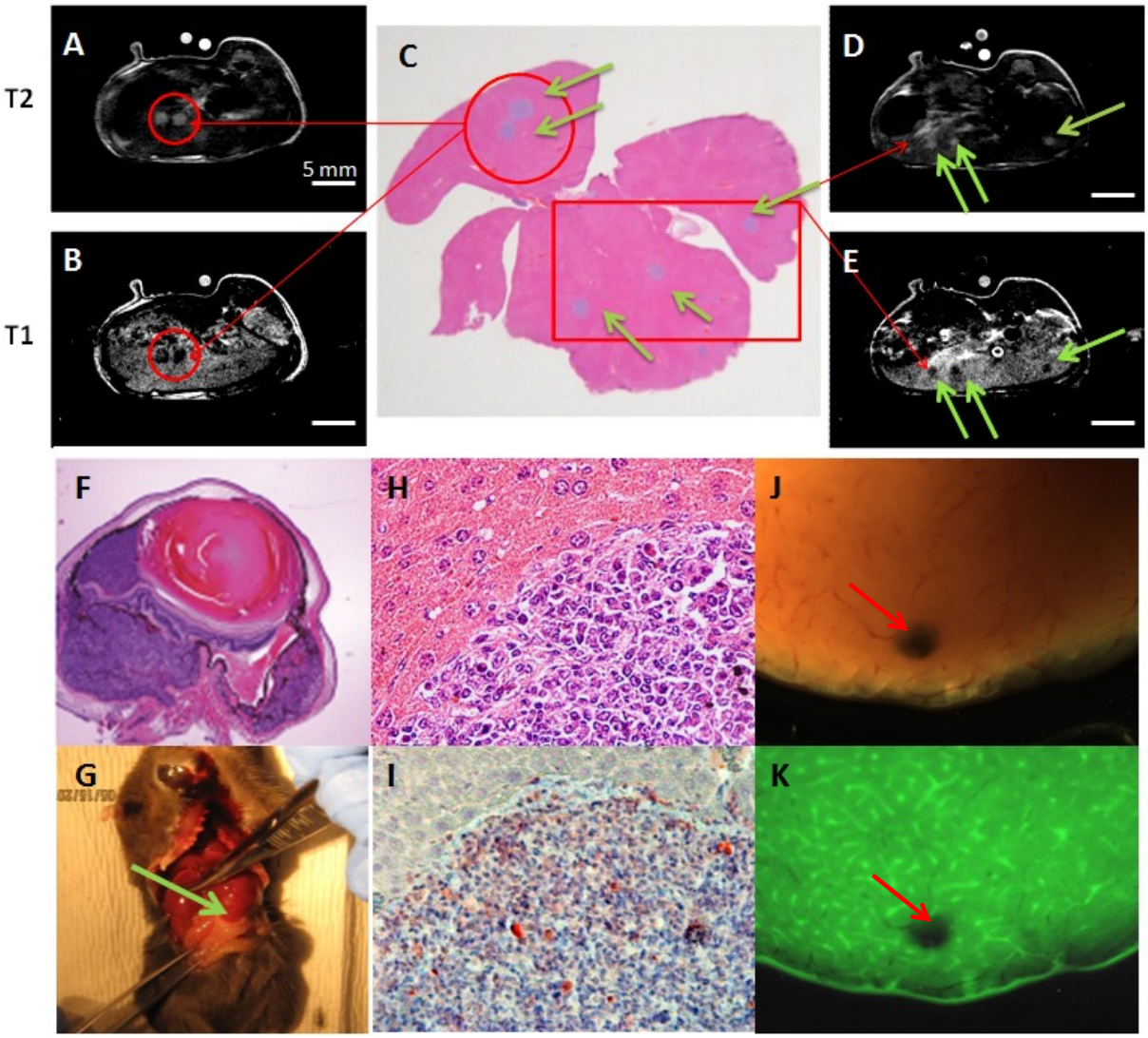

Figure 5-5. MR imaging of melanoma metastasis to liver with a size less than 2 mm after injection of ProCA32M.

A, D. T_2-weighted fast spin echo sequence after injection of ProCA32M with hyper-intensity of tumor metastasis. B, D, T_1-weighted spin echo sequence after injection ProCA32M with hypo-intensity of liver metastasis. A and C are the same position of mice liver imaged by two difference MRI sequences. B and D are the same position of mice liver imaged by two difference MRI sequences. Tumor metastasis were indicated by red cycle (A, B) or green arrows (D, E). C and H.

HE staining of liver with melanoma metastasis. Melanoma metastasis shows dark blue color/ purple colorF. primary melanoma implanted in the eye of eye mice. G. The mice with melanoma metastasis to the liver, one the of tumor can be visualized on the liver surface (green arrow). H. is the enlarged picture of HE staining of liver. Image was collected with 40x magnification. I. Immunohistochemistry staining of S100A in the liver metastases. S100A (dark brown color) is a biomarker for melanoma. Positive staining of S100A indicate that this liver tumor is metastasis from uveal melanoma. J. Dissecting microscope imaging of liver with melanoma metastasis. Melanoma metastases is indicated by red arrow. K. Fluorescence imaging of liver with melanoma metastasis (same position as J). The mice were euthanized 30 min post injection of fluorecein-ProCA32M. Fluorescence imaging was taken with excitation at 488 nm with fluorecein filter. ProCA32M is distributed in the liver tissue, while no ProCA32M is distributed in tumor due to the low permeability of melanoma to ProCA32M. These results confirm that hypo-intensity of tumor and hyper-intensity of liver under T_1-weighted MRI post injection of ProCA32M for about 30 min.

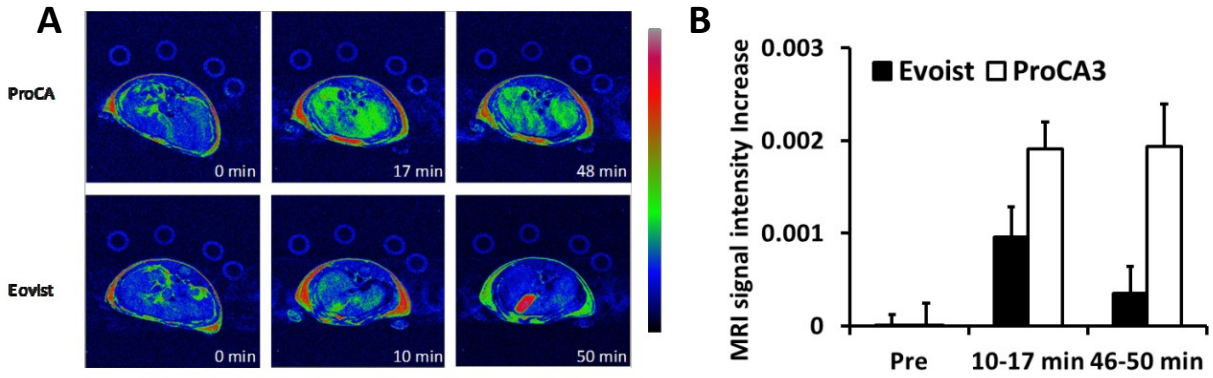

Figure 5-6. Comparision of the liver enhancement of MRI before and after injection of ProCA3 or Evoist.

MRI images at 4.7 T (left) show that ProCA32 has much higher liver enhancement than that of Eovist at both 10-17 min and 48-50 min. ProCA32 has siginificant higher MRI signal intensity than that of Evoist (right) and liver enhanment is much stable than Evoist. At 48-50 min Evoist has more 50 % drop of the enhanced MRI signal intensity, while ProCA3 has no MRI signal decrease compared with 10-17 min post injection.

5.2.7 T_2/T_1 Ratiometric imaging for the early diagnosis of metastatic tumors in the liver

One of the major chellagenes of MRI is lack of contrast between tissues and interested lesions with desired dynamic range and signal to noise ratio. In addition, soft tissues such as liver and heart are largely suffered from motion artifact. As shown in Fig.4-15, since ProCAs has both about 10 times higher r_1 and r_2 relaxivities than that of clinical MRI contrast agents, ProCAs could be potentially used as either T_1-weighted MRI contrast agents or T_2-weighted MRI sequence based on the different settings of TR and TE. In the section 5.2.5 and 5.2.6 of this chapter, we demonstrate that ProCA3 variants can be used as T_1-weighted MRI and T_2-weighted MRI for liver imaging and liver shows increased signal intensity in T_1-weighted MRI and decreased intensity in T_2-weighted MRI, while the tumor intensity doesn't change mainly due to the low contrast agent uptake within 1 hour. This is a great achievement because Gd^{3+} based MRI contrast agents are mainly used as a T_1-weighted MRI contrast agents, and Gd^{3+}-based MRI contrast agent are not used as T_2-weighted MRI contrast agents in general.

We hypothesize that ProCAs can function as T_2-weighted MRI contrast agents with decreased MRI signal because of the high r_2 relaxivity and a ratiometric method can increase the dynamic range of MRI signal. To test this hypothesis, we simulated the MRI signal intensity of phantom filled with different concentrations of MRI contrast agents in typical T_1-weighted and T_2-weighted MRI sequence. Fig. 5-7 shows our simulation results based on the relaxivity theory. Consistant with experimental data, both Gd-DTPA and ProCA32 shows enhanced MRI signal in the T_1-weigthed MRI (TR= 500 ms, TE = 13 ms), and the signal enhancement of ProCA32 is much higher than that of Gd-DTPA. In the T_2-weighted MRI sequence, ProCA32 shows a small increase of MRI signal intensity at a Gd^{3+} concentration less than 20 μM and shows a dramatic signal de-

crease the Gd^{3+} concentration is increased to more than 50 µM. On the other hand, Gd-DTPA shows small increase of MRI signal intensity in the T_2-weighted MRI when the Gd^{3+} concentration increased from 0 to 100 µM. The T_2-weighted MRI signal in 200 µM of Gd^{3+} is still higher than water without MRI contrast agents.

Our the simulation results shown in Fig. 5-8 suggest that ProCA32 can be used as both T_1-wieghted and T_2-weighted MRI contrast agents, while clinical MRI contrast agents, such as Gd-dTPA, can only be used as T_1-weighted MRI contrast agents. To test our simulation, we scanned T_2-weighted MRI of phamtom filled with different concentration of MRI contrast agents (Eovist, Magnevist and ProCA). Consistant with simulation, Eovist and Magnevist shows enhanced MRI signal when the Gd^{3+} concentration increase, while ProCAs shows the decreased MRI signal when the concentration of the contrast agents increased to more than 20 µM.

Because ProCA variants can increase the signal in T_1-weighted MRI and decease the signal in T_2-weighted MRI, we hypothese that the ratio of T_1/T_2 or T_2/T_1 (named as T_1/T_2 or T_2/T_1 ratiometric imaging) after injection of ProCA can further increase the dynamic range of MRI. According to the simulation of liver intensity of different concentration of MRI contrast agents in Fig. 5-8, increasing Gd^{3+} concentration of ProCA32 from 0 µM to 50 µM Gd^{3+} decreases MRI signal from 0.45 to 0.40, while the T_2/T_1 intensity ratio decreases from 1.4 to 0.8. On the contrary, Gd-DTPA shows the T_2 MRI signal decrease from 0.45 to 0.43 and T_2/T_1 signal decrease from 1.4 to 0.8, when Gd-DTPA concentration increase from 0 µM to 50 µM. Thus, this simulation results support our hypothesis that ratio of T_1/T_2 or T_2/T_1 ratiometric imaging method can dramatically increase the dynamic range of MRI compare with T_1-weigthed or T_2-weighted MRI.

Next, we examed the T_2/T_1 ratiometric imaging *in vivo*. As shown in Fig. 5-5, ProCA32M can enhance the liver in T_1-weighted MRI and suppress the liver signal in T_2-weighted MRI, while the tumor signal did not change in both T_1-weighted and T_2-weighted MRI due to the less accumulation of MRI contrast agents within 1 hour. We hypothesis that ratiometric imaging can further improve the tumor detection because of the larger dynamic range (Fig 5.9 A). Fig. 5-9 B, C, D, E shows the MRI of mice liver with melanoma metastasis before and after injection of MRI contrast agents. After the ratio of T_2/T_1, the liver signal dramatically suppressed and tumor shows much higher enhancement (Fig 5.9 F) than T_2 weighted MRI (Fig 5.9 D). Fig 5.10 shows T1 weigthed, T_2-weighted and T_2/T_1 ratio imaging of other slices of the same mice. All these images shows that T_2/T_1 ratiometric imaging has the best enhancement of the tumor by supress the liver signal. Interesting, we are able to identify small tumors with a size less than 0.25 mm be-cause of the improved dynamic range. Thus, ratiometric MRI with the injection of ProCA32M can improve the tumor detection in liver by dramatically decrease the liver signal.

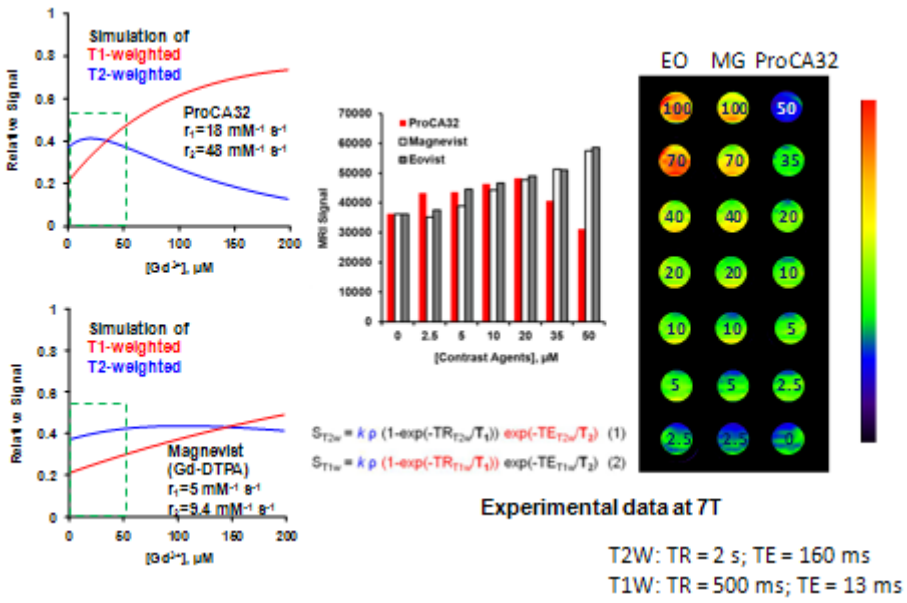

Figure 5-7. Simulation and experimental data of the phantom filled with different concentration of MRI contrast agents.

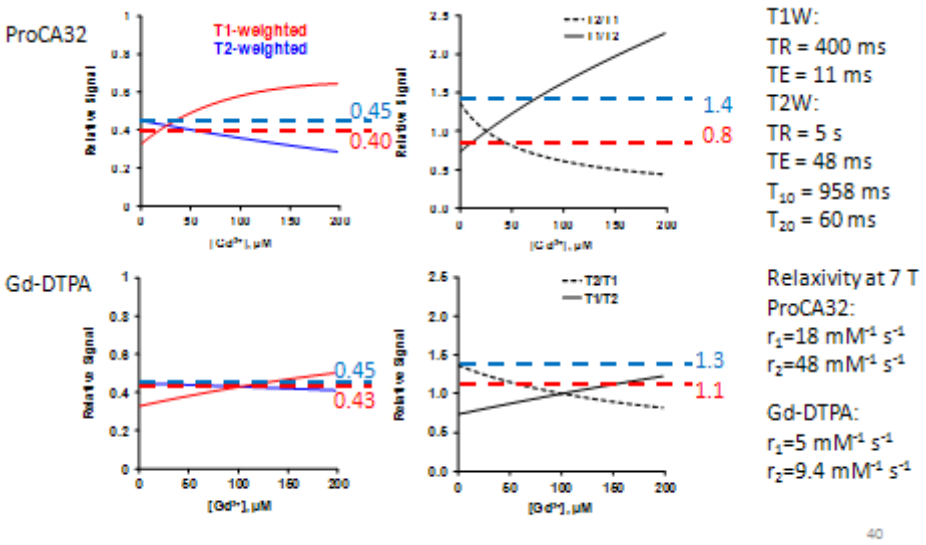

Figure 5-8. Simulation of MRI signal changes in the liver with different concentration of Gd-DTPA or ProCA32.

The dynamic range of these methods are defined as the differences between signal intensity with 50 μM of Gd^{3+} in Gd-DTPA or ProCA32 (red dash line) and the signal intensity without any contrast agents (blue dash line).

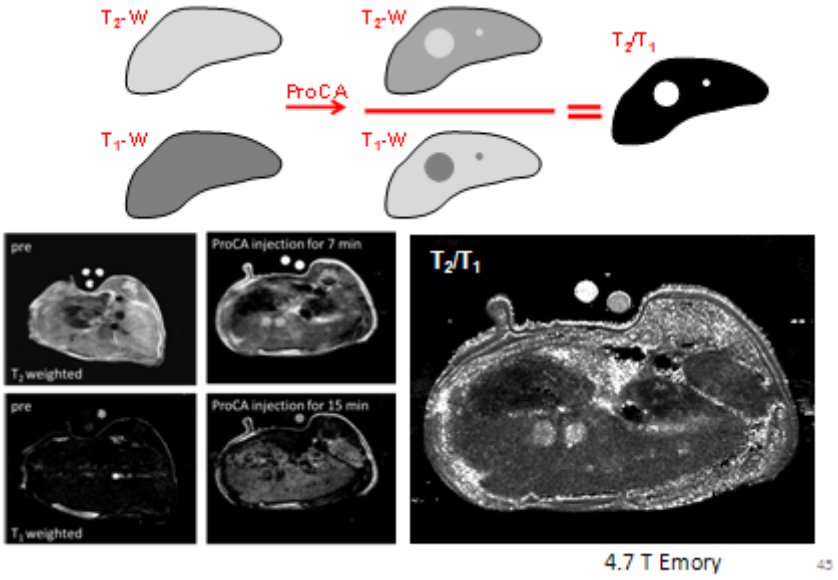

Figure 5-9. Liver tumor detection by T_2/T_1 ratiometic changes after injection of ProCA.

If live and tumor has similar T_1 and T_2, then we are not able to differeciate the MRI signal between liver and tumor without injection of the MRI contrast agents in neither T_1-weighted MRI nor T_2-weighted MRI. After injection of ProCA, the T_1 and T_2 of liver decreased because 1) ProCA has 10 times higher r_1 and r_2 compared with clinical MRI contrast agents; 2) Liver has more ProCA than tumor within one hour post injection of ProCA. Thus, tumor shows hypo-intensity in T_1-weighted MRI and shows hyper-intensity in T_2-weighted MRI.The ratio of the MRI intensity of T_2-weigthed MRI over T_1-weighted MRI further improves the signal differences between liver and tumor in both model and real experimental data.

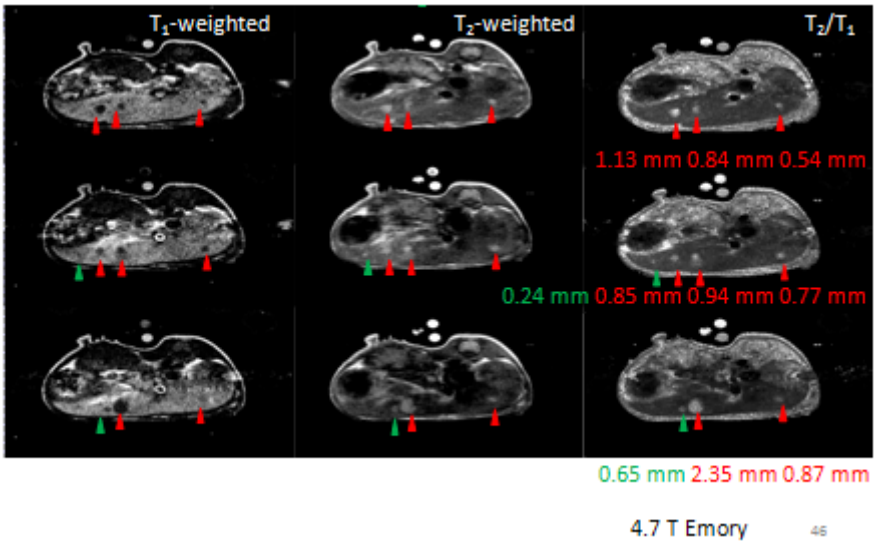

Figure 5-10. Ratiometic MRI can detect tumors less than 0.25 mm in liver.

Uveal melanoma was implanted in the eye of the PEDF knockout mice. These melanoma metastasis to liver two days after implantation. To imaging these metastatic melanoma, ProCA32M were injected from the mice tail vein and MRI were done before and after injection of ProCA32M. T_1-weighted spin echo sequence and T_2-weighted fast spin echo sequences were applied in the same section of the liver. Then we did the ratio of T_2/T_1 intensity. Row 1, 2, and 3 stand for three different slice of mice tumor and column 1, 2, and 3 stand for T_1-weighted, T_2-weighted, and T_2/T_1 ratiometric imaging of MRI of liver slices, respectively.

5.2.8 Dual weighted Bi-brilant imaging of tumor detection with improved dynamic range.

As show in the previous sections, ProCA variants can alter the MRI signal in T_1-weighted MRI and T_2-weighted MRI. The ratio of T_2/T_1 or T_2/T_1 intensity after injection of ProCA further improves the dynamic range of MR signal. With the help of Dr. Xiaoping Hu in Emory University, we developed a novel MRI sequence with encoded both T_1 and T_2 feature of the MRI contrast agents. We call this MRI sequence as dual weighted bi-briliant imaging.

The dual weighted bi-briliant MRI sequences can be described as an inversion recovery (IR) seuqnces with a special inversion time (TI) and long TE (Fig. 5-12). The TI of inversion recovery sequence is carefully selected to decrease the organ with contrast agents. The TI time is influenced by the contrast agent concentration and the r_1 relaxivity of the contrast agents. Because of the decrease T_1 value of the tissue due to ProCA accumulation, the MRI signal of ProCA accumulating organs could be suppressed to extremely low level in certain TI in the IR sequences. Because ProCA accumulating tissues has short T_2, long TE in this dual weighted bi-briliant MRI sequence further decrease MRI signal. Thus, theortically, the dual weighted bi-briliant MRI sequence can further show the difference between ProCA accumulating tissue and ProCA-non-accumulating tissue.

To test this dualweighted bi-briliant sequence, Evoist and ProCA32 with different concentration and water were immobilized in argar plate and scanned for T_1-weighted spin echo, T_2-weighted fast spin echo and bi-briliant sequence with differnet TI. As show in Fig. 5-13, ProCA3 shows much enhanced MRI signal than that of Eovist in T_1-weighted MRI. 75 μM of ProCA3 shows decrease MRI signal in T_2-weighted MRI, while Eovist does not decrease MRI signal even concentration of Eovist increase to 150 μM. This result indicate that ProCA3 can be

used for both T_1-weighted MRI and T_2-weighted MRI, while Eovist can only be applied in the T_1-weighed MRI. In addition, we scanned dual weighted bi-briliant MRI with different TI time (0.001 ms, and 0.251 ms). The phantom with 75 μM of ProCA shows extremely low signal intensity at TI = 0.251 ms compared with Eovist and water.

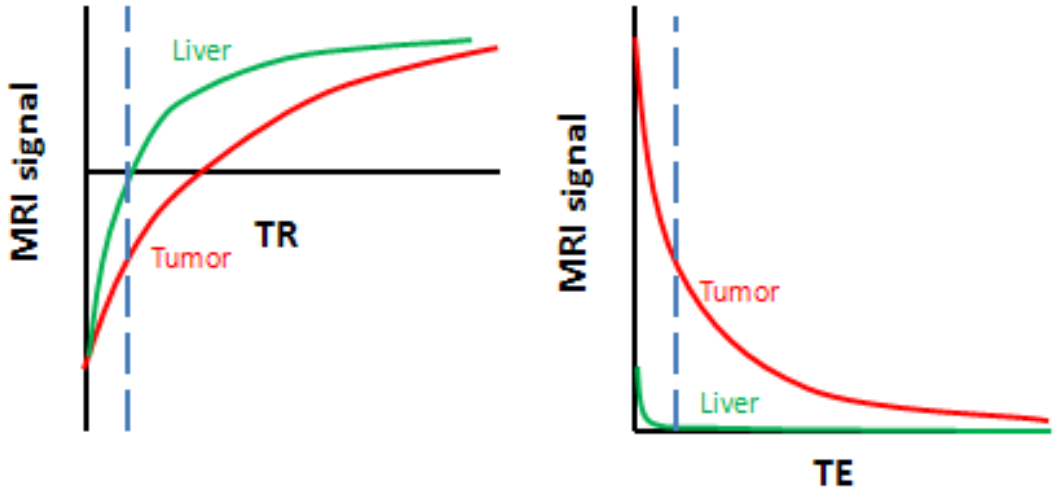

Figure 5-11. A demenstrion of Bi-briliant MRI sequence.

The bi-briliant sequence contains an inversion recovery sequence (left) followed by long TE (right). If liver accumulates more ProCAs than that of tumor, liver has much shorter T_1 and T_2 relaxiation time in liver than that of tumor. By apply an inversion recovery sequence with TI = T_{1liver}*ln2, (T_{1liver} stands for the T_1 of liver tissue), the liver signal is suppressed. After inversion recovery sequence, the MRI was collected with long TE. Because liver has shorter T_2 than that of tumor, long TE will further decrease liver signal. By ProCAs injection and applying inversion recovery sequence with long TE, we will be able to double suppress the liver signal and enhance the tumor signal.

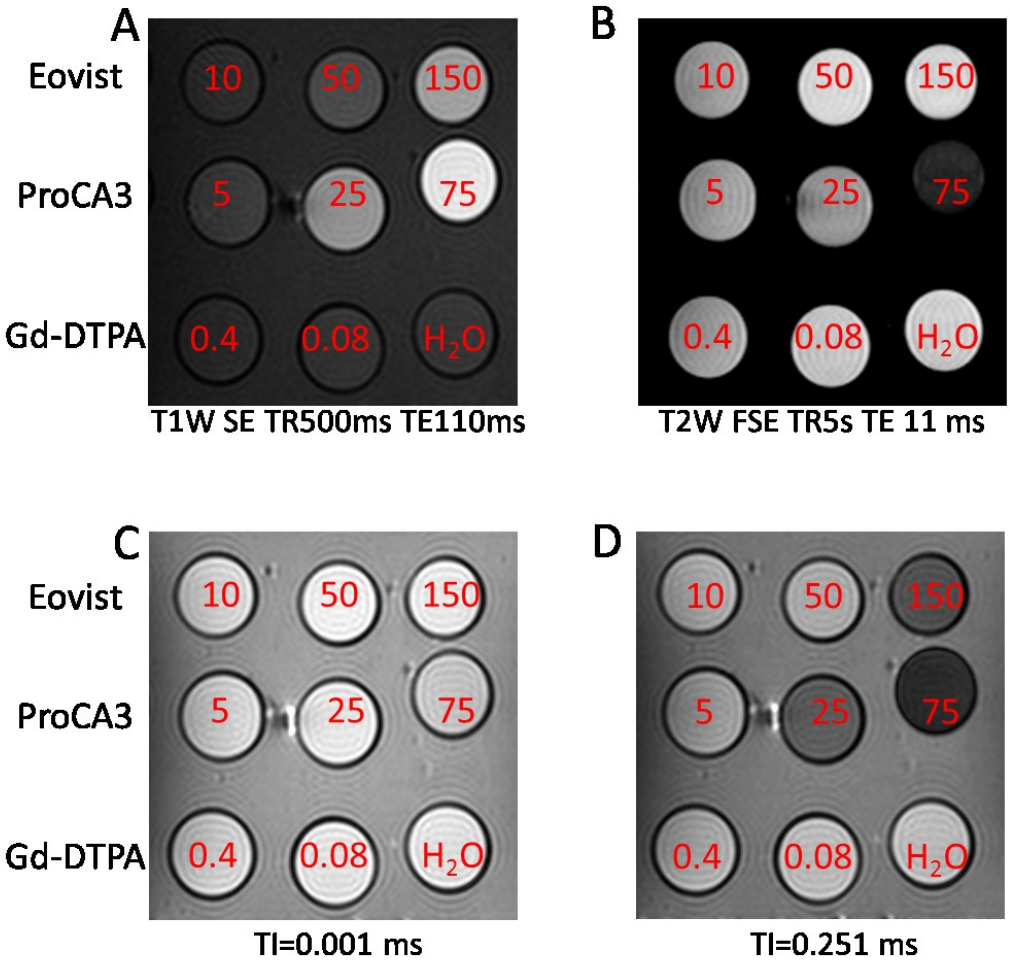

Figure 5-12. *in vitro* study of bi-briliant imaging with diffent concentration of Eovist, Gd-DTPA and Eovist.

MRI of phantom with different concentrations of contrast agents labeled on top(μM) or water were collected by T1-weighted spin echo sequence (A), T_2-weighted fast spin sequence (B), and bi-briliant sequence with TI= 0.001 ms (C) and TI= 0.251 ms (D).

Next, we tested the dual weighted bi-briliant methodology *in vivo* using melanoma implanted model. The melanoma mice model was generated by following the animal protocols from IACUC in Emory University. Melanoma cells were dierectly injected into the liver the mice, and liver will generate tumors with a size between 5 mm to 20 mm within two weeks after injection. 0.03 μmol/kg of ProCA35 were I.V. injected in mice with implanted melanoma in liver. As show in Fig 5-14, ProCA35 shows the enhanced liver signal in T_1 weighted MRI and shows the decrease liver signal in T_2-weighed MRI. As a result, melanoma can be identified in both T_1-weighted MRI and T_2-weighted MRI after injection of ProCA. Because of the intrinsic properties of tumor, this malanoma also shows higher intensity than that of liver even without injection of the MRI contrast agents. The differences between tumor and liver increased in T_2-weighted MRI after injection of ProCA35, which is very helpful to confirm the tumor.

After scanning, we euthnised the mice and take the liver out for MRI scanning. This liver already has high concentration of ProCA35. The tumor implanted liver tissue also shows hyperintensity of liver and hypo-intensity of tumor in T_1-weighted MRI and hypointensity of liver and hyperintensity of tumor in T_2-weighted MRI. Thus, the T_1 and T_2 of liver decreased after injection of MRI contrast agents. We next tested the dual weighted bi-briliant methodology of the same melanoma implanted liver tissue. As shown in Fig 5-14, bi-brilant MRI shows more dramatic difference differences between liver and tumor compared with that of T_1-weighed or T_2-weighted MRI.

Interesting, because ProCA35 accumulating liver has much short T_2 than that of tumor, bi-briliant imaging with longer TE (28 ms) shows much lower liver signal than that of shorter TE (11 ms). These results indicating that by utilizing both high r_1 and r_2 relaxivity of ProCA variants,

dual weighted bi-briliant MRI methodology shows great advantage in improving the tussue contrast differences after injection of ProCAs. This dual weighted bi-briliant MRI methodology is very promising for the early and sensitive detection of metastatic tumors.

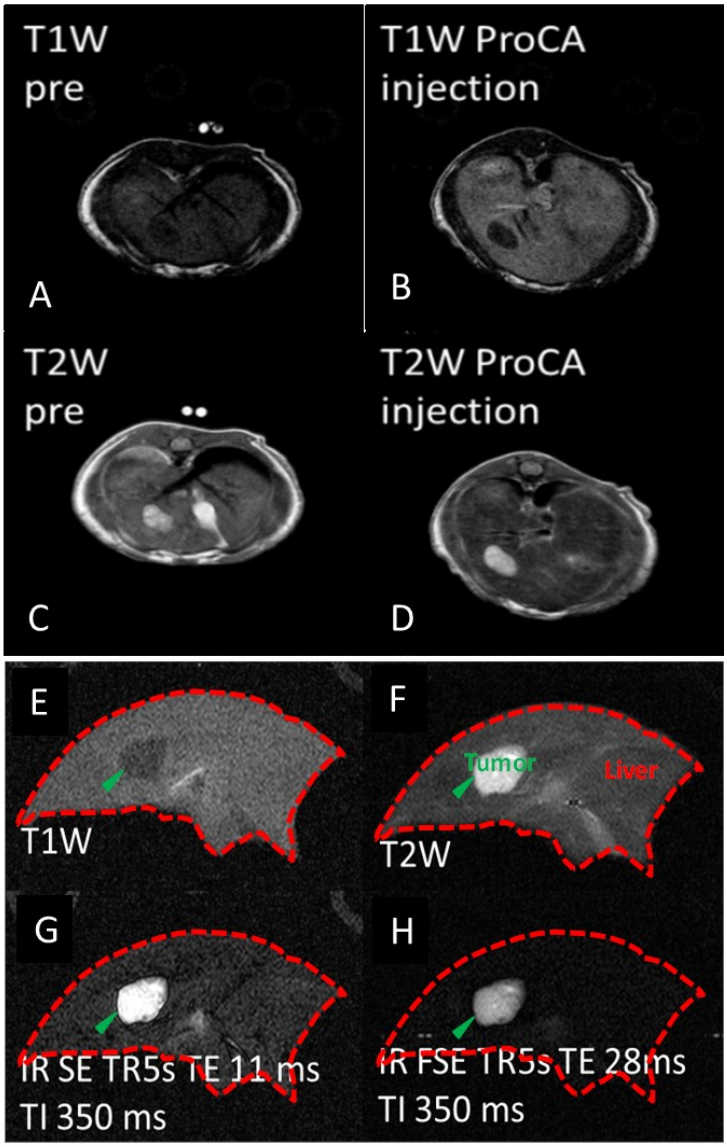

Figure 5-13. Bi-briliant imaging for the detection of liver cancer.

MRI imaging of mice liver with transplanted melanoma before (A for T1W, C for T2W) and after injection of MRI contrast agents using T_1-weighted spin echo (B for live animal, E for liver tissue), T_2-weighted fast spin echo (D for live animal, F for liver tissue), bi-brilliant methodology with two different TEs (G, H). The liver signal is dramatically suppressed, while the tumor signal does not decrease dramatically. The difference between tumor and liver improved ~8 times by this method. Green arrow stand for tumor.

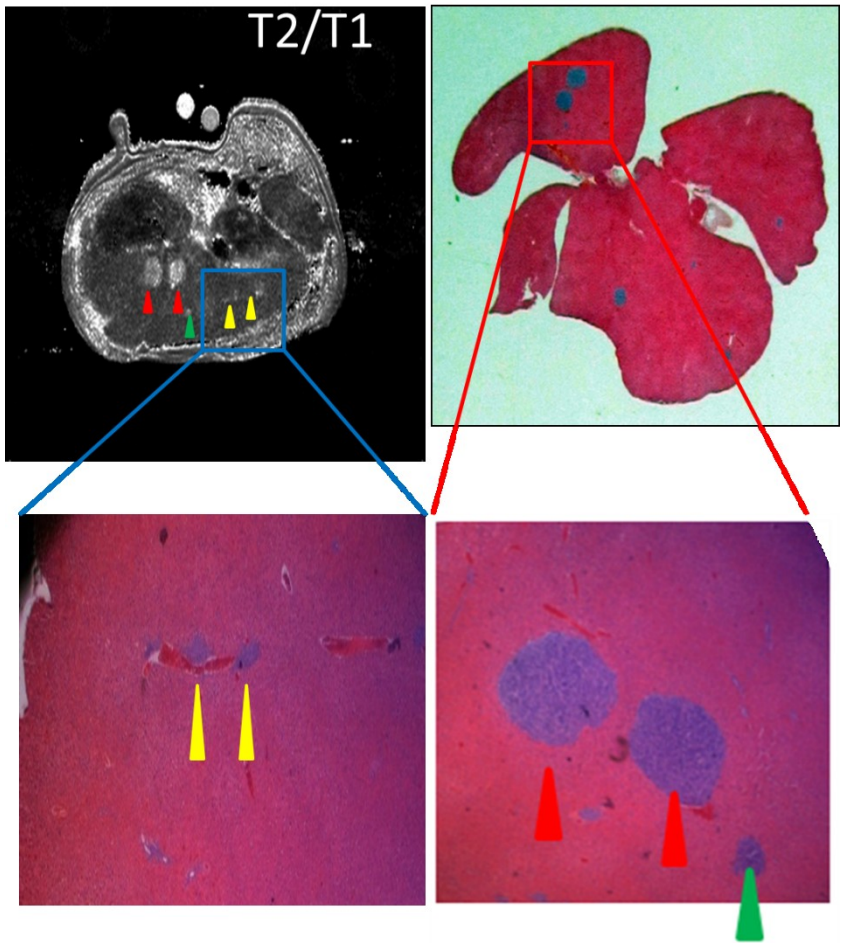

Figure 5-14. MRI and histology correlation study for metastatic melanoma detection.

Liver specific MRI contrast agent MRI helps to detect liver metastasis but cannot detect tumor size <10 mm with accuracy. ProCA enables to detect early mouse melenoma liver metastasis (mediametastases) tumor size from > 2 cm to 0.25 mm or less (blue and red arrows) with high sensitivity using both T2/T1 ratiometric (top left) imaging at 4.7 T. The HE staining of the same mice liver section (top right and bottom right) shows similar tumor size and location as MRI images (red and green arrows). In addition, tumors with a less than 0.25 mm can be detected in MRI (yellow arrows), which can also be confirmed from HE staining (yellow arrows on bottom left).

5.3 Discussion

Since ProCA32 has high relaixivity and stability, it is promising to apply ProCA32 *in vivo* for the disease diagnosis. With 10 times lower injection dosage than that of clinical MRI contrast agents, ProCAs is able to image blood vessel, liver, kidney. The small blood vessels with a diameter of less than 1 mm are able to be clearly imaged; therefore, ProCA32 has great potential for MRA. Supported by both 3DGE images and DCE-MRI, ProCA32 has much longer blood circulation time. Longer blood circulation of ProCA will benefit molecular imaging of tumor biomarkers, since the interaction between targeting moieties and biomarkers requires optimized blood circulation time. Long blood circulation time of ProCA32 in blood also promising for the application of DCE-MRI. AIF in DCE-MRI experiment is the key experiment for successful calculating tumor permeability. However, it is hard to accurate determine AIF of clinical MRI contrast agents, since the blood circulation time of clinical MRI contrast agents is too short[198]. ProCA32 has longer blood circulation time, and AIF of ProCA32 is easily to be determined by both MRI and blood sampling. Thus, ProCA32 will be a powerfully and reliable probe for tumor permeability using DCE-MRI.

ProCA32 is able to enhance the kidney in all type of T_1-weighted MR images. 3DGE images show that the kidney is enhanced after injection of ProCA32, and the highest enhancement were obtained 2 day post injection. After 2 days, the kidney intensity decrease to the original intensity without injection of ProCA32. Thus, ProCA32 is promising to be applied to evaluate the kidney lesions and kidney tumors. Kidney intensity changes function of time in DCE-MRI of kidney can be applied for the evaluation of renal function.

We are also able to image the contrast agent accumulation in bladder indicating that contrast agents were able to be excreted out through renal clearance. DCE-MRI of kidney also shows that ProCA32 start to enhance the kidney within 1 minute post injection, which is a strong evidence of ProCA32 excretion through kidney.

Liver tissue is evenly enhanced under T_1-weighted MRI after ProCA32 injection. Since ProCA32 also has high r_2, livers also show decreased intensity under T_2-weighted MRI post ProCA32 injection. Due to such unique features, ProCA32 is superior for the imaging of liver tumors with both T_1- and T_2- weighted sequences. We evaluated the imaging capability of ProCA32 on the liver tumor diagnostics. Mice melanoma was implanted in the eye of the mice, and the tumor metastasis to liver organ 2 weeks after tumor implantation. With 10 times lower injection dosage of than clinical MRI contrast agents, ProCA were able to image the liver metastasis in both T_1- and T_2- weighted images. Since liver metastasis has less penetration to ProCA32, liver metastasis shows hyper-intensity in T_2- weighted MRI and shows hypo-intensity in T_1-weighted MRI. Interestingly, we are able to detect tumor metastasis with a size less than 0.25 mm, whereas clinical diagnostics only can detect liver metastasis with a size larger than 10 mm with high confidence. Thus, ProCA32 proved a very good diagnostic tool for the early detection of liver metastasis.

5.4 Summary

First, we have shown that the the lowest detection concentration of ProCA32 can reach 0.8 μM at 7 T using T_1-weighted spin echo sequences due to the high relaxivity. This largely extended the reported detection limit of 30 μM for [Gd(HP-DO3A)(H2O)] by Wedeking.[18]

Second, we have shown that the the lowest injection dose for us to detect in vivo mouse kidney is 0.0008 μmol/kg that is more than 100 fold lowever injection dosage than that of clinical MRI contrast agents (0.1 - 0.2 mmol/kg).

Third, ProCA32 shows great potential for assess blood vasculature properties of tumor using the DCE-MRI due to its high relaxivity and longer blood circulation time.

Fourth, based on detailed histologic analysis and imaging analysis, ProCA32M is able to detect liver uveal melanoma metastases with a size less than 0.16 mm with high accuracy using both T_1 and T_2 ratiometic methd we developed in this chapter. These detected tumor sizes are correlated to the micrometastasis which are 10 - 100 times smaller than the reported detection size. Current detection with good confidence for liver human metastasis or primary tumor are at about 2 cm that are at late stages of cancer (stage 3 or 4 out of 4). Thus, our developed contast agents and methodology are expected to fill in the major gap for early diagnosis and treatment of liver metastases.

6 DYNAMIC-CONTRAST ENHANCED MRI (DCE-MRI) WITH INJECTION OF PROCA3 VARIENTS

6.1 Introduction

Tumor has abnormal blood vasculature than normal tissue. The growth rate of the tumor is much faster than blood vessel, therefore the rapid proliferation of tumor cells force blood vessel apart. The leakage size of the tumor vasculature varies in different tumors, and it could be reached to more than 100 μm. Tumor and stroma cells also secret enzymes and growth factors, such as VEGF, to facilitate the formation of new blood vessel and rebuilt extracellular matrix. This process called angiogenesis. On the other hand high interstitial fluid pressure in tumor forms a barrier for drug and imaging reagent penetration to the tumor from blood vessel[199].

Dynamic-contrast enhanced MRI (DCE-MRI) is a non-invisive tool to probe tumor vasculature by methmatically modeling and calculating contrast accumulation in the tumor over time. The clinical MRI contrast agents, such as Gd-DTPA has been applied to evualte the tumor vasculature of many types of cancers, such as breast cancer, pancreatic cancer [200]. This technique is very helpful to monitor the tumor vasculature changes of the patients after tumor treatment with angiogenesis drugs. DCE-MRI is also widely applied as an advanced technique in the preclinical field to evaluate the effects of angiogenesis drugs[200]. Due to the non-invissive properties, applications of DCE-MRI decrease the number of animals and cost in preclinical drug development.

Current DEC-MRI methods still have some limitations. First, in order to accurately calculate the blood volume and blood vessel permeability, most DCE-MRI methods requires having accurate measurement of arterial input function (AIF), the artery contrast agents concentration

at different time points post injection. The AIF of clinical MRI contrast agent, however, is extremely difficult to be measured very accurately due to their fast excretion of clinical MRI contrast agents[198]. For example, the blood half life for Gd-DTPA is only 2 min in mice and 10 min in human. It has a lot of technique difficulties to deterime accurate contrast agents in such a short time. Second, due to the small size and fast tumor penetration, DCE-MRI is not able to differentiate the leakage size using clinical MRI contrast agents. Third, clinical MRI contrast agnets has short time accumulation and short time release in tumor, which retrict enough data collection in the limitate time period.

In order to evaluate tumor vasculature with high accuracy and high reliability, ideal MRI contrast agents for DCE-MRI requires following features: 1). The contrast agents concentration in blood should be relatively stable, so that arterial input function can be accurately determined. 2). The contrast agents should have a tumor size between 2 – 10 nm, so that contrast agents can selectively penetrate to the tumor based on the size of leakage of the tumor blood vessel. If the contrast agents are too small, then they will penetrate to the tumor without any capability to reflect the size of derentiating tumor blood vessel leakage. On the other hand, if the contrast agents are too big, its penetration to the tumors with small vessel leakage is largely limited. 3). The contrast agents should have high relaxivities, so that trace amout of contrast agents distribution in tumor can be detected.

Compared with clinical MRI contras agents, ProCAs has their own advantages for the DCE-MRI study. 1). The contrast agents concentration in the blood is relatively stable, which made it easier to measure AIF with small error. 2). ProCA3 should have much longer accumulation and release time in tumor. Since the blood contrast agents always gave lowerer than tumor

contrast agent's concentration for at least 2 hours post injection of ProCAs, the mathmetical model for DCE-MRI can be simplified. 3) Due to the larger size, ProCA can only selective pass through blood vessel with a leakage larger than ProCAs (Fig. 6-1). 4) ProCAs has higher relaxivity, which could improve the sensitivity and dose efficiency of contrast agents. Taken together, ProCAs is a promising probe for the DCE-MRI of tumor blood vessel. Since DCE-MRI can also be applied to imaging other abnormal tissue, ProCAs can also be used for the imaging the DCD-MRI of the abnormal blood vessel of other type of diseases, such as stroke and liver kidney[201, 202].

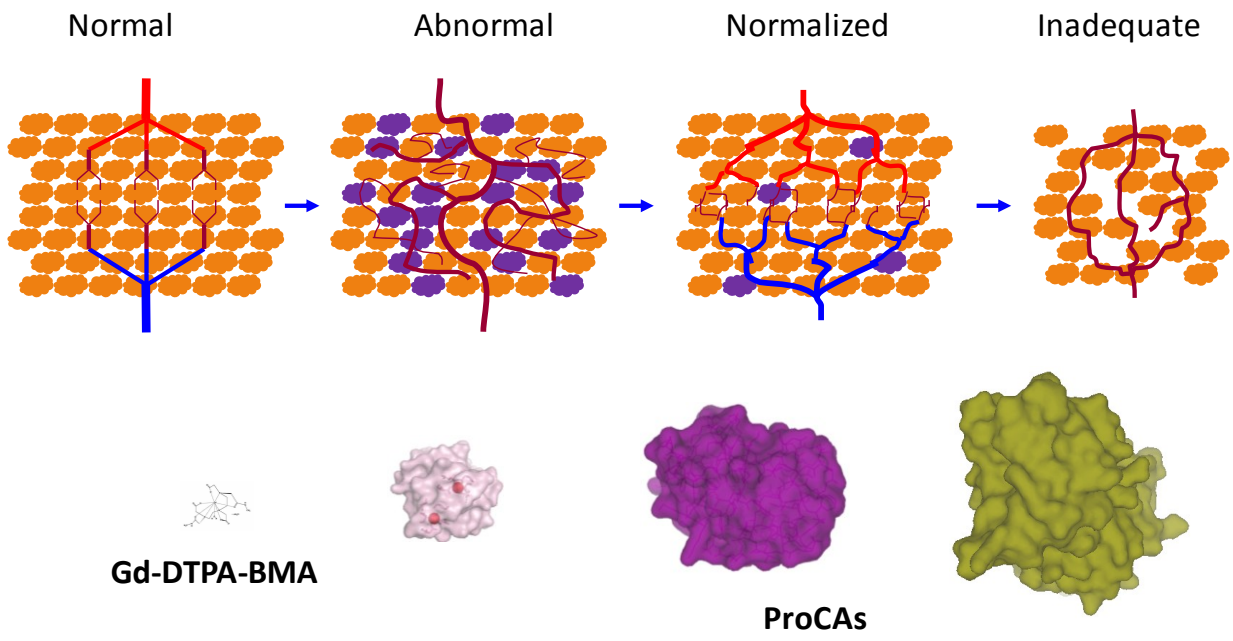

Figure 6-1. Carton demonstration of the application of ProCA variants and Gd-DTPA-BMA for the evulation of blood vessel abnormalities using DCE-MRI.

Normal tissue has well organized blood vasculature, while tumor tissue has abnormal vasculature due to angiogenesis. After treatment with anti-angiogenesis drugs, the blood vescular in tumor tissue can be normalized. Hoever, after treatment with anti-angiogenesis drugs, tumor can reduce the blood vessel desity as a way resistant to the drug treatment. DCE-MRI is a promising technique to to evaluate blood vesculture. Due to large sizer size, ProCA has great potential to be applied to DCE-MRI for the evaluation of tumor vasculature.

6.2 Results

6.2.1 DCE-MRI by ProCA32 or Gd-DTPA

Since ProCA32 has high relaxivity and sensitivity at high magnetic field than than of nanoparticles and small molecular MRI contrast agents. We measured the AIF differences of mice at 9.4 T bruker MRI scanner. Five baseline images without injection of contrast agents were collected before injection of MRI contrast agents. Then, 0.025 mmol/kg ProCA were injected in mice throught tail vein. MRI imagings were continuously collected by another 85 min. As shown from Fig. 6-2, ProCA32 has very clear AIF. The blood vessel of the mice is enhanced for at least 85 min. On the other hand, Gd-DTPA only has very short AIF with a half life less than 1 min (Fig 7-2 C). Due to such fast decrease of Gd-DTPA in blood vessel, it is extremely hard to collect AIF of Gd-DTPA correctly for DCE-MRI study[198]. Thus, ProCA32 has a trenmendous advantage for the evlautation of tumor vasculartur by DCE-MRI.

We next compared the in vivo properties between ProCA32 and Gd-DTPA to probe blood vessel and kidney enhancement by DCE-MRI. To evaluate the dynamic enhancement of ProCA32, T1 map of the same slice are collected by FESMS sequence with different length of TR (Fig. 6-3). Then, MR images are collected every 7 seconds by FLASH sequence (TR = 18.44 ms, TE = 2.83 ms, thickness=2 mm, matrix 128 × 128, Fov 4 cm × 4 cm). After collecting 20 slides as baseline, 0.015 mmol/kg ProCA32 were injected in mice followed by an injection of 150 µl saline through tail vein (Fig. 6-4). 130 slices were continuously collected. The concentration of ProCA3 in tissue are calculated based on the relaxivity of ProCA3 at 7 T and the signal intensity differences between the baseline images and images post injection of the contrast agents. The ProCA3 concentration in blood reached to the plateau within 2 min post injection of ProCA3

and the contrast agent concentration keep constant for at least 10 min and ProCA3 concentration decrease after 10 min post injection with blood retention half life around 15 min in mice. As comparison, 0.2 mmol/kg Gd-DTPA were for DCE-MRI in mice. Due to the short blood retention time, the peak enhancement of blood post injection of Gd-DTPA is not observed, which was mainly caused by the extremely short blood retention time for Gd-DTPA. Compared with Gd-DTPA, our contrast agents shows extremely good blood vessel enhancement with much longer blood retention time. This is extremely significant, our contrast agent can enhance the blood vessel image with longer time and with 1/10 dosage of injection of contrast agent compared with Gd-DTPA. We compared MR images of kidney after injection of Gd-DTPA (0.2 mmol/kg) or Gd-ProCA32 (0.02 mmol/kg). The time of kidney enhancement by Gd-DTPA is very short. The enhancement of cortex and modulla reach to maximum within than 1 min then half of the signal decreased to less than 50% within the next 1 min, which left only limited time window for data acquirement. The enhancement of kidney by ProCA3.2 is slower than that of Gd-DTPA. The cortex enhancement reached to the maximum after 1 min post injection and modulla enhancement is slower, which take 2 min to reach to the maximium. The half of the ProCA3 image is much longer. The slow kenetics of ProCA32 in kidney provide new insight to devolvement to study kidney function.

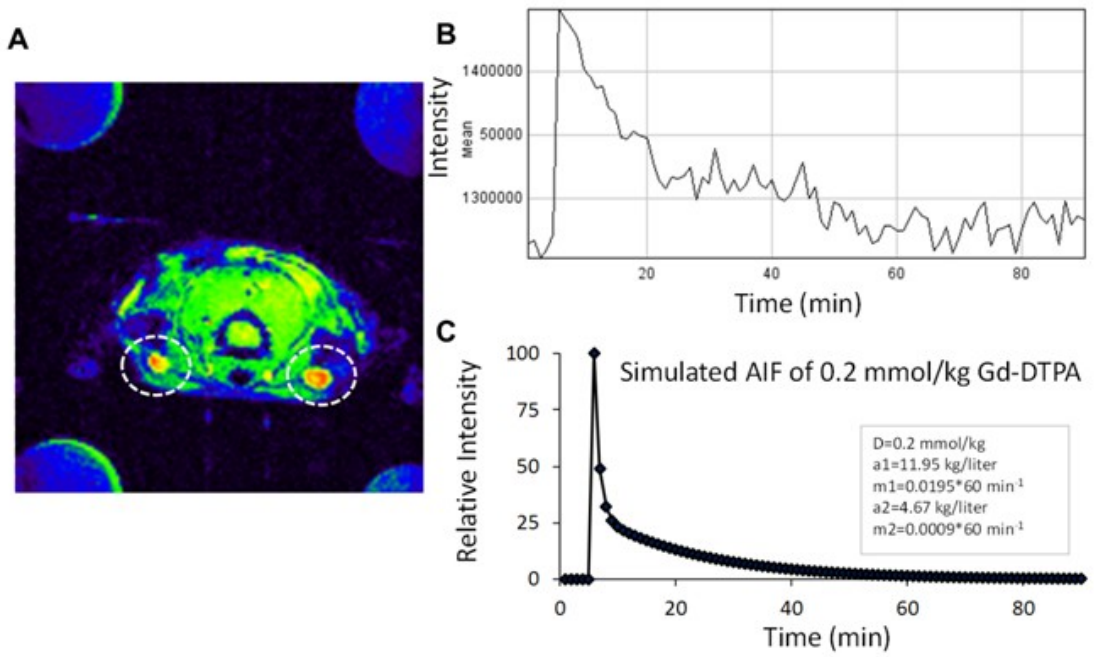

Figure 6-2. Aterial imput function study of ProCA and Gd-DTPA.

A. MRI signal enhancement of the vein in the nick of mice. MRI imaging were collected every 1 min. Five baseline images without injection of contrast agents were collected before injectionfo MRI contrast agents. Then, 0.025 mmol/kg ProCA were injected in mice throught tail vein. MRI imagings were continuously collected by another 85 min. B. Aterial input function of ProCA in mice. The MRI signal intensicity changes of the vein during DCE-MRI study before (0-5 min) and after (5-85 min) injection of ProCA. C. Simulated aterial input function of Gd-DTPA in mice with compartmental model for Gd-DTPA ($Cp(t)=D[a_1 \exp(-m_1 t) + a_2 \exp(-m_2 t)]$) by Toft et al., [203] (D is the injection dosage, a1 and a2 are the amplatudes of the compatments, m1 and m2 are the rate constant for Gd-DTPA).

6.2.2 T_1 Map calculation

FSEMS saturation recovery sequence was applied to measure T_1 map of mice with the same slices previous used for DCE-MRI study. To aquire T_1 value of each picsle, multiple TR were applied in the FSEMS saturation recovery sequence (TR=0.35, 0.5, 0.7, 0.9, 1, 2, 3, 5 (s)). We then use Equation (6-1) by imageJ plugin to fit the T_1 value of each pixel:

$$\mathrm{Sn} = \mathrm{S0}\left(1 - \exp\left(-\frac{\mathrm{TRn}}{\mathrm{T1}}\right)\right) \tag{6-1}$$

A cutoff of 4 s was applied for T_1 map measurement. This is because T_1 value of tissue is usually less than 4 s at 7 T in mice temperature. Fig. 6-3 shows our calculated T_1 map from one slide of mice. The kidney has a T_1 value between 1-1.5 s, which is consistant with reported value.[202, 204-206]

I then calculated the relaxation time of tissue based on DCE-MRI and T_1 map. After got T_1 map, I use the Equation (6-5) to calculate T_1 and $1/T_1$ from each DCE-MRI scan. The Equation 6-5 is obtained from Equation (6-2) and (6-3).

$$\mathrm{S0} = \mathrm{k}\,\rho\left(1 - \mathrm{e}\left(-\frac{\mathrm{TR}}{\mathrm{T10}}\right)\right)\mathrm{Sin}\theta\,\frac{\mathrm{e}\left(-\frac{\mathrm{TE}}{\mathrm{T2}*}\right)}{1-\mathrm{Cos}\theta*\exp\left(-\frac{\mathrm{TR}}{\mathrm{T10}}\right)} \tag{6-2}$$

$$\mathrm{Sx} = \mathrm{k}\,\rho\left(1 - \mathrm{e}\left(-\frac{\mathrm{TR}}{\mathrm{T1x}}\right)\right)\mathrm{Sin}\theta * \frac{\mathrm{e}\left(-\frac{\mathrm{TE}}{\mathrm{T2}*}\right)}{1\mathrm{Cos}\theta*\exp\left(-\frac{\mathrm{TR}}{\mathrm{T1x}}\right)} \tag{6-3}$$

Then (2)/(3),

$$\frac{\mathrm{S0}}{\mathrm{Sx}} = \frac{\left[\mathrm{k}\rho\left(1-\mathrm{e}\left(-\frac{\mathrm{TR}}{\mathrm{T10}}\right)\right)\mathrm{Sin}\theta*\frac{\mathrm{e}\left(-\frac{\mathrm{TE}}{\mathrm{T2}*}\right)}{1-\mathrm{Cos}\theta*\exp\left(-\frac{\mathrm{TR}}{\mathrm{T10}}\right)}\right]}{\left[\mathrm{k}\rho\left(1-\mathrm{e}\left(-\frac{\mathrm{TR}}{\mathrm{T1x}}\right)\right)\mathrm{Sin}\theta*\frac{\mathrm{e}\left(-\frac{\mathrm{TE}}{\mathrm{T2}*}\right)}{1-\mathrm{Cos}\theta*\exp\left(-\frac{\mathrm{TR}}{\mathrm{T1x}}\right)}\right]} \tag{6-4}$$

Equation (6-4) was further simplified to be Equation (6-5).

$$\frac{S0}{Sx} = \frac{\left[\frac{1-e\left(-\frac{TR}{T10}\right)}{1-Cos\theta*exp\left(-\frac{TR}{T10}\right)}\right]}{\left[\frac{1-e\left(-\frac{TR}{T1x}\right)}{1-Cos\theta*exp\left(-\frac{TR}{T1x}\right)}\right]} \quad (6\text{-}5)$$

Where, S_0 is the signal intensity of ROI before injection of the contrast agents, Sx is the signal intensity of the RIO of each slides after injection of the contrast agents. $T1_0$ is the T1 of RIO in the T_1 map.T_{1x} is the T_1 of RIO after injection of the contrast agents. Θ=25 degree.

From Equation (6-5), we can see that S_0, S_x, T_{10}, and Cosθ is known. We can calculate $T1_x$ based on Equation (6-5) in the attached excel file. Fig. 6-4 shows the signal intensity of blood, kidney center, kidney cortex and muscle. After calculation of the relaxation time of ROT in tissues and T_1 map values, the T_1 and R_1 values changes of these organs in every 7 s before and after injection of contrast agents. $[Gd^{3+}]$ changes at each time point were also calculated based on the relaxivity Equation (2-10).

Fig. 6-4 C and Fig. 6-5 shows the Gd^{3+} concentration changes in the blood vessel, kidney (center and cortex) and muscle at each time point. Due to the quick injection of ProCA, Gd^{3+} in blood has a sharp increase of the Gd^{3+} concentration to above 120 µM, and then quickly decreases to less than 20 uM. The Gd^{3+} concentration in blood then gradually increase to a stable stage with a concentration around 40 µM for about 8 min. Then the Gd^{3+} concnetation gradually decrease. The blood Gd^{3+} concentration decrease to 20 µM 15 min post injection of ProCA32. Kidney is the major organ for the Gd^{3+} excretion. As shown from Fig. 6-5, Gd^{3+} concentration in kidney cortex and centrer gradually increase to 10 and 20 µM respctively with in first 2-3 min after injection of ProCA3. Then, Gd^{3+} concentration in kidney is always around 10 - 20 µM in the next 12 min. Since kidney is the major organ, these results provide another the evidence that ProCA3 is excreted from kidney. Fig. 6-4 also shown that Gd^{3+} in the muscle is usually very low,

which is also consistent with our distribution data. In the future, I will explore the potention application of ProCA in kidney function and disease by applying our dynamic imaging data to renal DCE-MRI model.

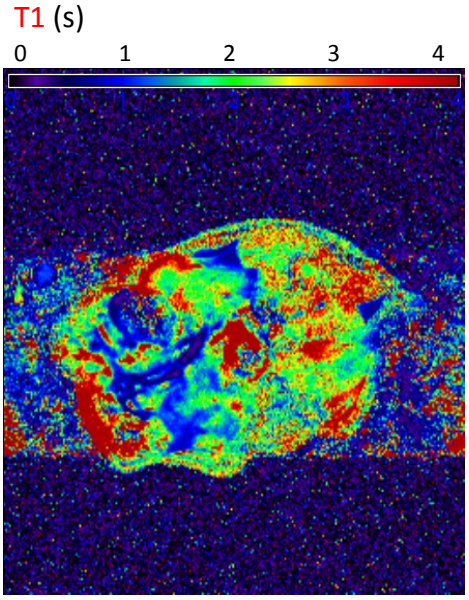

Figure 6-3. T_1 map of mice kidney section without injection of MRI contrast agents.

To calculate T_1 map of the mice, the mice kidney sections were by FSEMS saturation recovery sequence with multiple TR (TR=0.35, 0.5, 0.7, 0.9, 1, 2, 3, and 5 (s)). We then use the following Equation by imageJ plugin to fit the T_1 value of kidney imaging:

$$\mathrm{Sn} = \mathrm{S0}\left(1 - \exp\left(-\frac{\mathrm{TRn}}{\mathrm{T1}}\right)\right)$$

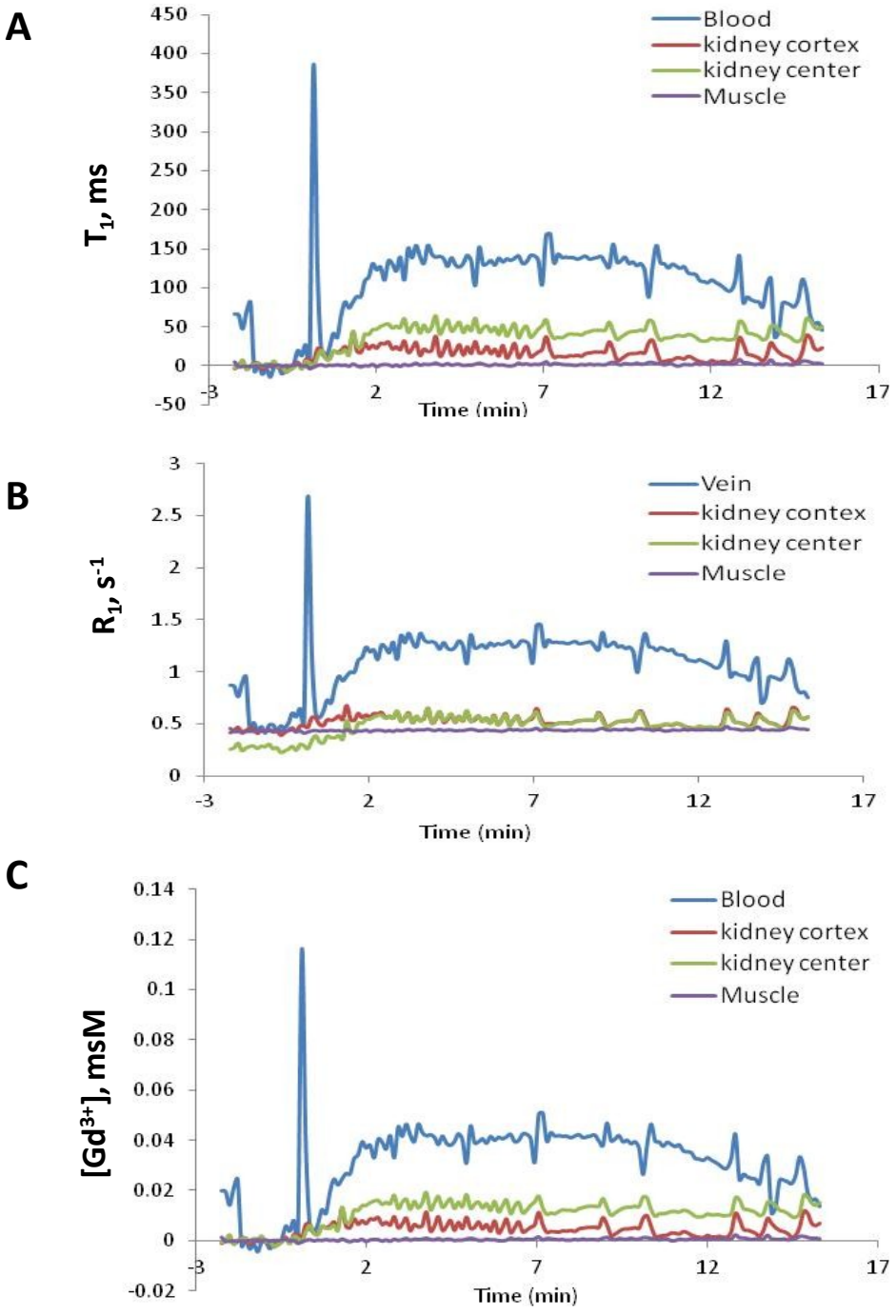

Figure 6-4. Relaxiation time (A), relaxiation rate (B) and Gd^{3+} concentration (C) changes of mice organ during DCE-MRI experiements with ProCA32 injection.

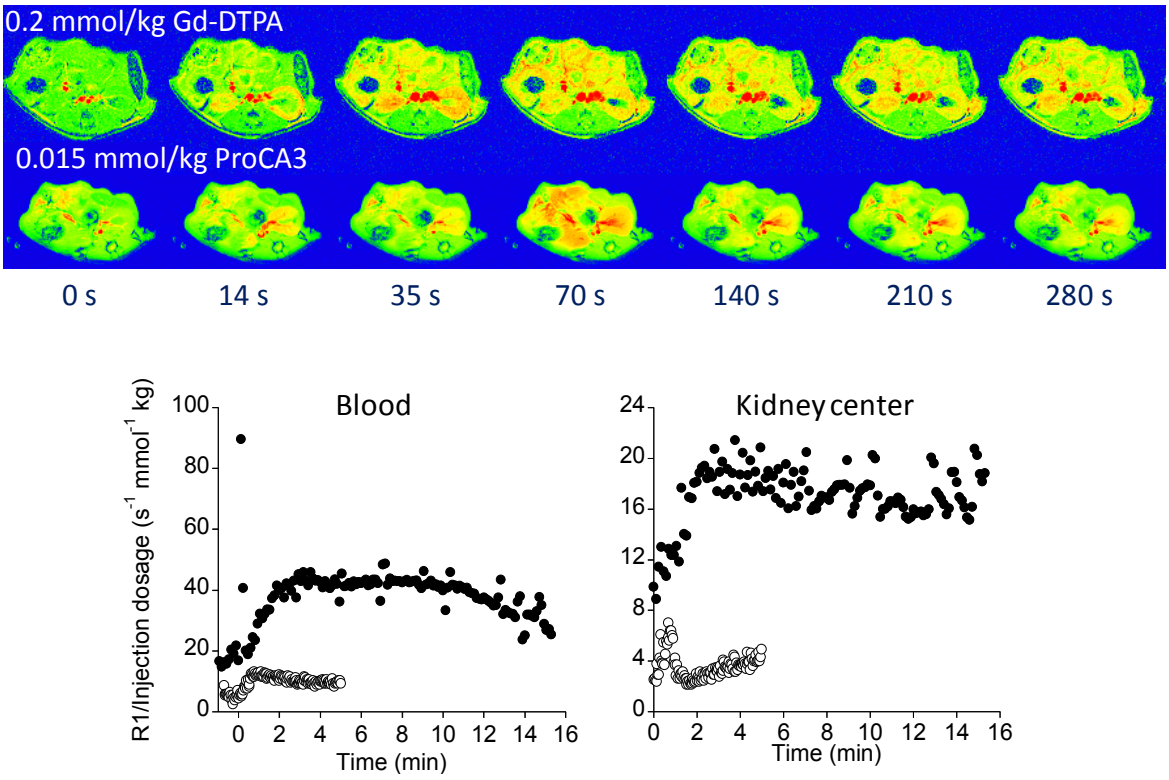

Figure 6-5. MRI enhancement of kidney over time before and after injection of (0.015 mmol/kg) ProCA32 or (0.2 mmol/kg) Gd-DTPA.

Top: DCE-MRI of mice kidney before and after injection of (0.015 mmol/kg) ProCA32 or (0.2 mmol/kg) Gd-DTPA.

Bottom: the R_1 / injection dosage of blood and kidney over time. Black dots stands for ProCA32 signal. Open dots stand for Gd-DTPA signal.

6.3 Discussion

Angiogenesis is an essential process for the tumor development and metastasis. Inhibition of angiogenesis is an effective way for the tumor therapy. However, the discovery of anti-angiogenesis drugs is hampered by the lack of sensitive methods for monitor the drug treatment for the patients. DCE-MRI is a promising technique to monitor the tumor structure changes under drug treatment. The evaluation of tumor vasculature by DCE-MRI is achieved by the permeability rate and volume of contrast agents from blood to tumor tissue after a bolus injection of MRI contrast agents. Clinical MRI contrast agents, such as Gd-DTPA, have been extensively applied to evaluate tumor vasculatures of brain tumors in mice, rat, dogs and human patents[198, 207, 208]. DEC-MRI is also extensively applied for the development of novel anti-tumor drugs[209, 210]. However, the contrast agents used in DCE-MRI, Gd-DTPA, have many disadvantages. 1). A reliable DCE-MRI evaluation is highly dependent on arterial input function, the real-time contrast agents' concentration in blood after a bolus injection of MRI contrast agents. However, clinical MRI contrast agents has very small size and very short half-life in blood, and arterial input function of clinical MRI contrast agents is extremely hard to measure correctly. A MRI contrast agents with prolonged half-life can improve the AIF measurement, which can further improve the accuracy and reliability of MRI contrast agents in blood. 2). An ideal MRI contrast agents should have high relaxivity and high sensitivity. The currently MRI contrast agents, however, only have a relaxivity around 5 $mM^{-1}s^{-1}$. In order to be detected by DCE-MRI, a local contrast agent concentration of 30 μM is required. If the relaxivity of MRI contrast agents increase to 100 μM, only a local concentration 0.69 μM of contrast agent is sufficient to be de-

tected under DCE-MRI. Therefore, a MRI contrast agent with longer circulation time and high relaxivity is strongly required for the DCE-MRI field[208].

In this study, we demonstrate that protein-based MRI contrast agents is a promising contrast agents for DCE-MRI due to signicant longer blood circulation time and significant higher signal intensity. The blood half life of ProCA3 in mice is more than 100 times long than that of Gd-DTPA, which made AIF, the date set for DCE-MRI analysis, easier to obtain with high accuracy and reliability than that of Gd-DTPA. As shown from Fig. 6-5, the blood signal intensity is dramatically improved after injection of ProCA3 instead of Gd-DTPA. ProCA3 also shows about 5 times higer signal intensity in kidney, indicating a potential application of ProCA3 for the evaluation of kidney function by DCE-MRI.

In our current study discussed in Chapter 5, our contrast agents can detect liver tumor with a size less than 0.25 mm, which is 80 time higher resolution than smallest size of tumor which can be detected by any non-invasive imaging technique. Since brain is one of the major organs for tumor metastases, primary tumors also developed in brain with high frequency, we would like to explore the capability of ProCA to brain tumor detection and assessment. Angiogenesis is an essential process for the tumor development and metastasis. Inhibition of angiogenesis is an effective way for the tumor therapy. However, the discovery of anti-angiogenesis drugs is hampered by the lack of sensitive methods for monitor the drug treatment for the patients. DCE-MRI is a promising technique to monitor the tumor structure changes under drug treatment. However, the contrast agents used in DCE, Gd-DTPA, have many disadvantages. This small chelator-based contrast agent after injection changes too fast to capture the details in the region of interests. In addition, small molecular MRI contrast agents. Therefore, a contrast

agent with longer circulation time and high relaxivity is strongly required for the DCE-MRI field[208]. Our preliminary data shows that ProCA has more than 10 times higher r_1 relaxivity than that of Gd-DTPA. Since r_2 of ProCA is more than 120 $mM^{-1}s^{-1}$, ProCA can also be applied for T_2-weighted MRI. The clinical MRI contrast agent, such as Gd-DTPA, usually is not good for T2 weighted MRI. In addition, ProCA has a blood half-life of 2.8 hours in mice, while Gd-DTPA has a blood half-life less than 30 seconds in mice. Thus, AIF of ProCA is much easier to be collected, which provide another advantage for the DCE-MRI with improved reliability. Since ProCA has much longer blood half-life than that of Gd-DTPA, we easily obtained the AIF after injection of ProCA. On the contrary, the AIF cannot be easily obtained by Gd-DTPA injection, even 10 times higher injection dosages of Gd-DTPA than that of Ca2+ were administrated.

We hypothesis that ProCA can be applied to evaluate blood vasculature of brain tumor and follow the drug treatment related with tumor vasculature changes with higher sensitivity and reliability than that of Gd-DTPA.

In the future, we will test our hypothesis by evaluating brain tumor blood vasculature in U-87 MG xenograft and othotrpic mice model by DCE-MRI using clinical MRI contrast agents and our novel designed ProCA. We will first study the ProCA biodistritbuion and tumor accumulation at different time points using MRI and ICP-OES. We will also compare the smallest tumor we can detect by Gd-DTPA or ProCA in the xenograft model; we will also determine the lowest injection dosage for ProCA and Gd-DTPA for the tumor detection. Then, we will compare the AIF and K^{trans}, V_e of clinical MRI contrast agents and ProCA in both U-87 MG xenograft and orthotropic mice model. We will further use avastin as a chemotherapy model to evaluate the potential application of non-targeted ProCA on monitoring the drug treatment. Each mouse will

be implanted with two U-87 MG tumors. We will first scan U-87 MG xenograft mice under MRI to evaluate the tumor size and structure. We will further measure the tumor blood volume and blood vessel permeability by dynamic enhanced MRI technique. To evaluate the chemotherapy effects, mice with/without avastin treatment will be imaged under MRI using previously described process. Dr. Dhamala will collaborate with us for the MRI data analysis. In the meantime, we are exploring the GMP-like methods for large scale expression and purification of ProCA. With the collaboration of Dr. Zhao and Platt in UGA, we are in a good position to full explore the DCE-MRI properties of ProCA for the evaluation of brain tumors in dogs.

6.4 Summary

The application of DCE-MRI for disease diagnostics is limited by the lack of MRI contrast agents with high relaxivity, high metal binding affinity and selectivities, proper blood retention time. Clinical MRI contrast agents all have very limited relaxivity, and very short blood half-life, which made the DCE-MRI data collect very unreliable. Our current develop MRI contrast agents has more than 10 times high relaxivity, a blood half-life of 2.8 h, with a size about 2-4 nm. In this chapter, we show that ProCA3 has longer blood circulation time, which made more easy and quantitative to accurately measure AIF. In addition, we are able to calculate ProCA3 concentration in different tissues based on the DCE-MRI data and T_1 map. These features made ProCA3 as the ideal candidate for evaluate tumor vasculature, renal perfusion by DCE-MRI.

7 BIODISTRIBUTION, PHARMACOKINETICS AND SAFETY STUDIES OF PROTEIN-BASED MRI CONTRAST AGENTS

7.1 Introduction

Contrast-enhanced magnetic resonance imaging using MRI contrast agents is an exciting method with many clinical applications. The biodistribution, safety profile and pharmacokinetics of clinical MRI contrast agents are well studied. Based on the distribution, clinical MRI contrast agents can be divided into three classes: non-specific MRI contrast agents, liver specific MRI contrast agents, and blood pool MRI contrast agents. Magnevist, Omniscan, ProHance, Optimark, Dotarem belongs to the non-specific MRI contrast agents. Due to the small size and no interaction with biomolecules, these contrast agents is distributed mainly in blood vessel and extracellular-extravesicular spaces with a blood half live less than 5 min in mouse and less than 30 min in human. These contrast agents were mainly accumulated in kidney for the renal excretion. Therefore, these contrast agents can be applied to image kidney with high efficiency. This class of MRI contrast agents also accumulated in the lesions and disease tissues with blood vessel damage. Such properties are applied to image disease such as cancer, and stroke.

Multihance and Eovist are liver specific MRI specific MRI contrast agents. The difference between these contrasts and non-specific MRI contrast agents is that Multihance and Eovist is covalently incorporated with one hydrophobic moiety, which facilitates liver accumulation of these contrast agents. Clinical study shows that, 10% Multihance and 50% of Eviost is excreted from liver.[13] Another liver specific MRI contrast agent is Mn-DPDP. Since DPDP has the similar structure as vitamin A, it can be uptake by liver cells. The accumulation of Mn-DPDP dramatical-

ly increases the MR signal in liver. However, it is unclear if DPDP is degreed in the liver and cause Mn^{2+} release.[211]

MS-325 is a new FDA approved blood pool MRI contrast agents, which reversibly binds to serum albumin. The binding of albumin increase the relaxivity of the contrast agents and binding of albumin also elongate the blood circulation time of the contrast agents. Due to such unique blood distribution, MS-325 has been approved to imaging blood vessel abnormalities.[212]

Besides clinical MRI contrast agents, nano-sized MRI contrast agents, such as dendrimers, liposome, nanotubes, and emulsions were developed with dramatically different pharmacokinetics and distributions. The pharmacokinetics, distribution and excretion of these contrast agents were largely influenced by the size, charge and targeting moieties of the contrast agents. Contrast agents with a size larger than 7 nm cannot be eliminated from renal filtration, and the blood retention time for these contrast agents are dramatically increased. Due to the phagocytosis of immune-cells, liver and spleen are the major organs to accumulate these nanoparticles. Nanoparticles with molecular weight larger than 30 kDa is accumulated in the tumor tissue due to EPR effects.[34, 169]

Pharmacokinetics is closely related with the safety of the MRI contrast agents. Long retention *in vivo* faces the risk of free Gd^{3+} release. NSF[24], a disease found in the patients with impaired renal function after administration of clinical MRI contrast agents. Impaired renal function in these patents dramatically increased the blood retention time of the MRI contrast agents, which further cause free Gd^{3+} release from the contrast agents. Low kinetic stability of the contrast agents is another key factor related with NSF. Contrast agents with low kinetic stability, such as Omniscan, release more Gd^{3+} in the serum than the contrast agents with high

kinetic stability such as ProHance. This result is consistent with *in vivo* Gd^{3+} rentention in mice and correlates well with the clinical reported with the cases of NSF.

Pharmacokinetics and blood retention time are essential for the success design of the MRI contrast agents for the molecular imaging of biomarkers of disease. Most biomarkers are expressed deep in the disease tissue. In order to the image these biomarkers, MRI contrast agents incorporated with biomarker targeting moieties should be able to penetrate to the disease tissue and then bind to these biomarkers. Unbounded MRI contrast agents should be easily washed away to reduce the background. Unbounded MRI contrast agents should be excreted efficiently to avoid unnecessary toxicity. Contrast agents with very fast clearance may not have sufficient time to reach the disease tissue and interact with biomarkers. On the other hand, contrast agents with long *in vivo* retention could increase the background signal and cause undesired toxicity. Thus, pharmacokinetics is essential for the design of the MRI contrast agent for the molecular imaging of biomarkers.

With high relaxivity, high blood circulation time and tumor targeting properties, Protein-based MRI contrast agents is promising for the clinic diagnostics for liver metastases, blood vessel abnormalities and renal functions. Understanding the biodistribution, pharmacokinetics and safety profile of the protein-based MRI contrast agents is the key step to push this class of contrast agents for clinical applications. In this chapter, we will show our recent study of the biodistriton, and safety profile of ProCA3 variants. We will also compare the pharmacokinetics of different MRI contrast agents.

7.2 Results

7.2.1 Toxicity of MRI contrasts agents.

7.2.1.1 Cytotoxicity of ProCA3

To evaluate the cytotoxicity of the ProCA3, H441 and PC3 cells precultured on 96 well plates (10^3 cells /per well) are incubated with 30 or 50 μM Gd-DTPA and ProCA3.2. The cell variabilities after incubation over night were tested by MTT assay (Fig. 7-1). No significant difference is observed between nontreated group and the groups incubated with ProCA3, ProCA3-Gd, which indicate that ProCA3 is not toxic for H441 and PC3 cells.

7.2.1.2 Acute toxicity of ProCA3

The acute toxicity of ProCA3 to CD1 mice were analyzed with the injection of 0.012 mmol/kg ProCA3. The bloods of the mice were collected two days post injection. The blood from CD1 mice without injection of contrast agents were used as control. Based on the results from IDEXX from 2 mice in each group, there was no significant differences on creatine, ALT, ALP, cholesterol, triglycerol level differences between the control group and the group injected with ProCA3 indicating the kidney, liver, heart function were not affected by ProCA3 (Fig. 7-2). The albumin and total protein, total bili, K^+, Na^+, Ca^{2+}, and Cl^- level were at the same level as those of the control control. All these data indicates that ProCA3 has low chronic toxicity.

7.2.1.3 Long term toxicity of ProCA3

The long term toxicity of the contrast agents are associated with Nephrogenic systematic fibrosis (NSF), a serious syndrome find in renal impaired patients with the Gd^{3+} release after injection of clinical contrast agents. To assess the long term toxicity of the contrast agents, long

term Gd^{3+} retention in mice tissue were evaluated after injection of ProCA3. Since only injection of 0.8 µmol/kg of ProCA3 (equal to 1.6 µmol/kg of Gd^{3+}) can clearly enhance contrast of MR images of kidney, 0.8 µmol/kg ProCA3, were injected in three groups of the mice. As a comparison, 1.6 µmol/kg of GdCl3 or 200 µmol/kg of Gd-DTPA was injected in the parallel group, respectively. ICP-OES analysis indicates that Gd^{3+} retention in blood, liver, lung, kidney, spleen 14 day post injection of ProCA3 was much less than that of Gd-DTPA and $GdCl_3$. The Gd^{3+} retention in skin and bone were comparable with that of Gd-DTPA and $GdCl_3$. These results indicate that by increasing the dose efficiency and decreasing injection dosage, less Gd^{3+} will be accumulated in mice after injection of ProCA3 which cause less long term toxicity compared with Gd-DTPA.

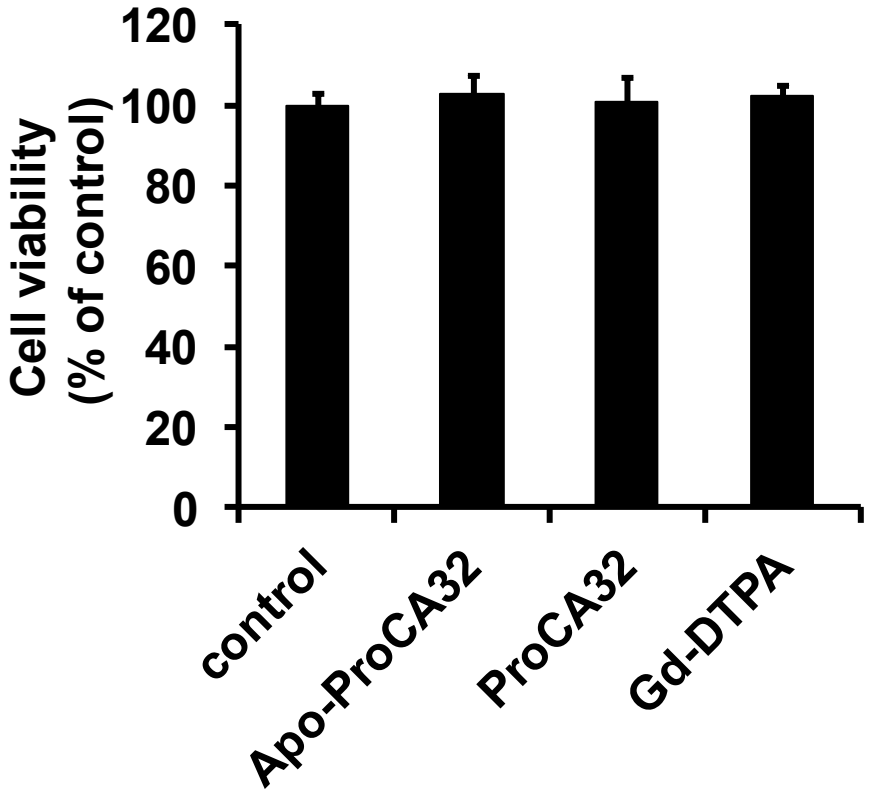

Figure 7-1. Cyto-toxicicity study of ProCA32 and Gd-DTPA.

The survival of H441 cells after incubation of 50 μM contrast agents overnight are analyzed by MTT assay (n = 3).

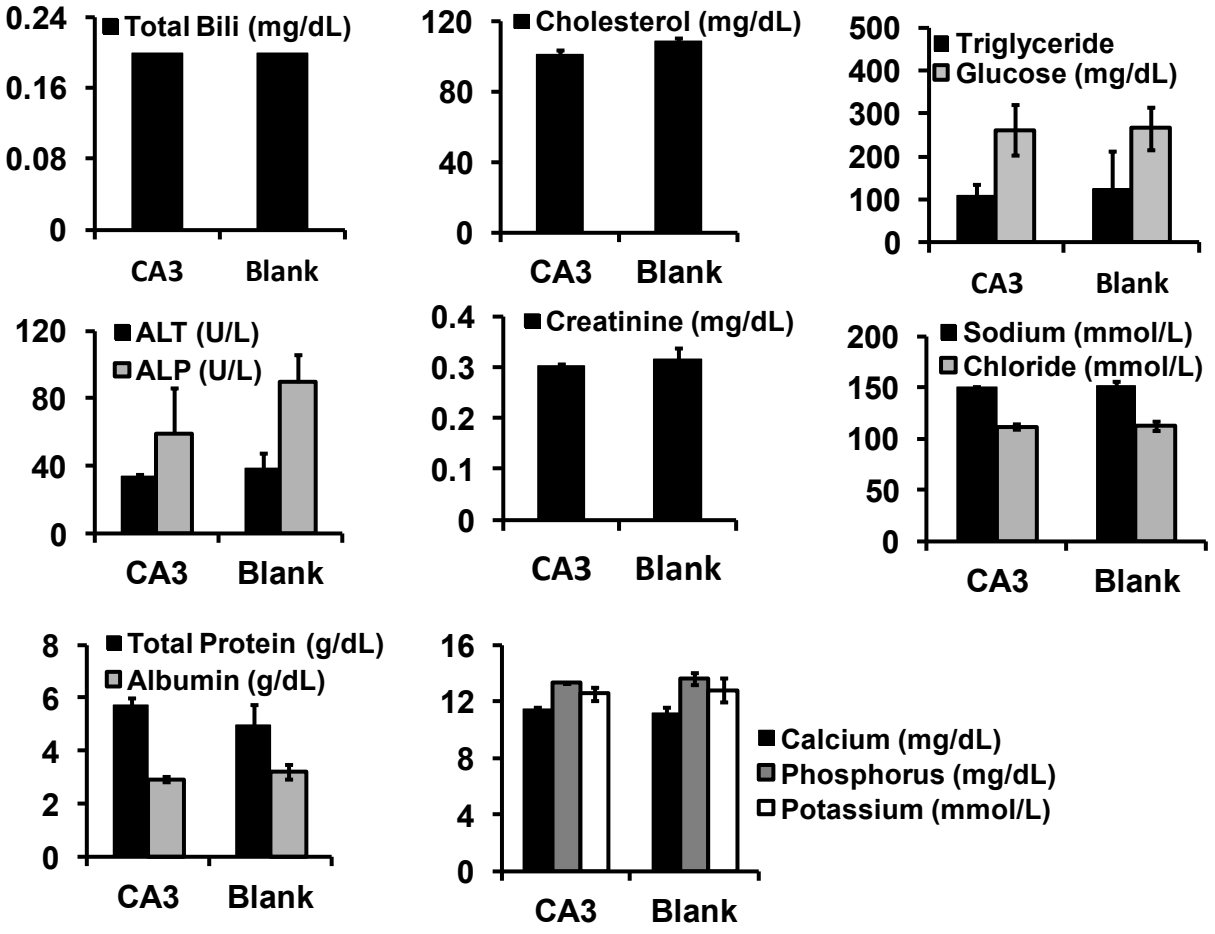

Figure 7-2. The acute toxicity study of ProCA3.

The acute toxicity of ProCA3 obtained by the serum sample 2 days post injection of ProCA3 (0.012 mmol/kg body weigtht). Results were collected from IDEXX using 2 mice in each group. Error bars stand for the standared deviation calculated based on the values of two repeats in each test.

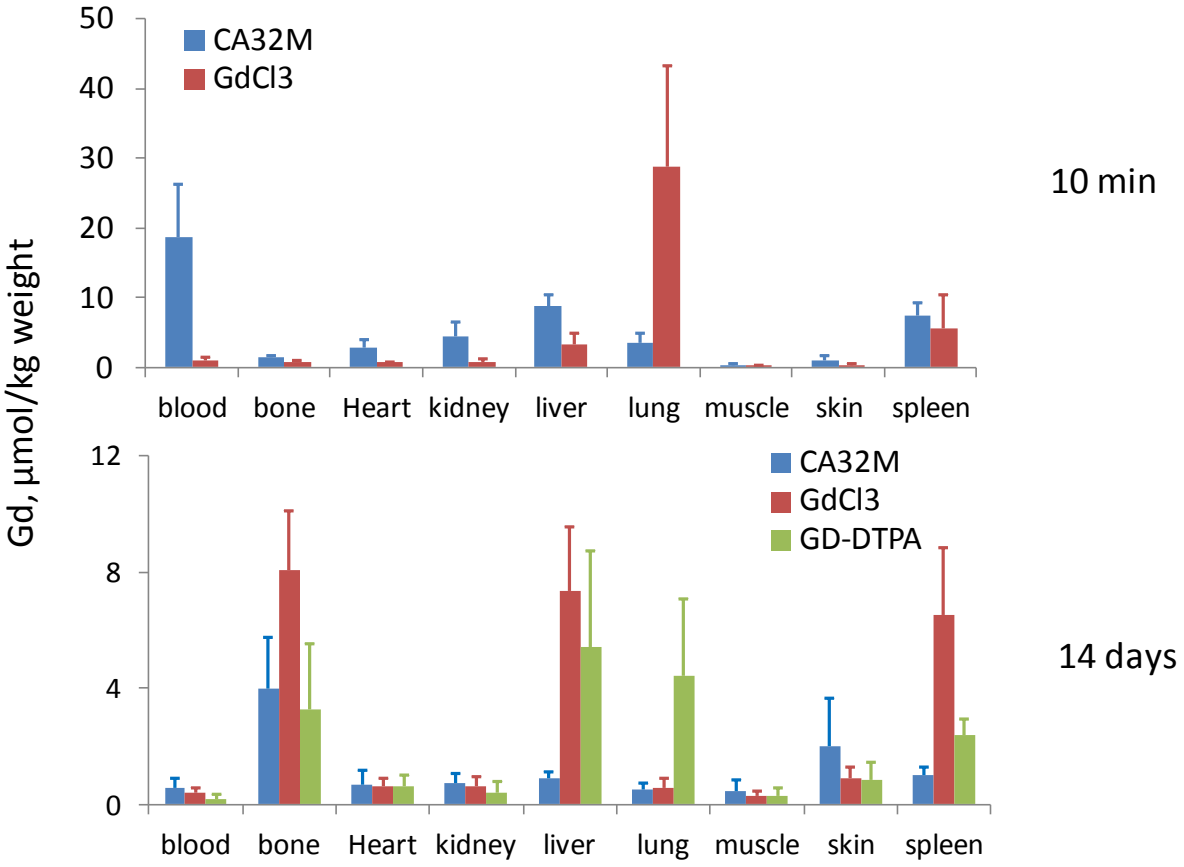

Figure 7-3. Short term (top) and long term (bottem) Gd^{3+} distribution in mice after injection of GdCl3, ProCA32M or Gd-DTPA.

0.8 M of ProCA32M (CA32M), 1.6 µmol/kg of GdCl3 or 200 µmol/kg of Gd-DTPA were injected in the parallel group, respectively. Gd^{3+} retention in blood, liver, lung, kidney, spleen for 10 min or 14 day post injection of ProCA3 were measured by ICP-OES. The average and standard deviation were calculated based on the values measured from 5 mice in each group.

7.2.2 Biodistribution of ProCA in mice

7.2.2.1 Biodistribution of ProCA measured by MRI signal intensity

As shown Fig. 5-2 in Chapter 5, 3D MR imaging was acquired to obtain the imaging enhancement of the organ at different time points after injection of ProCA. As shown from Fig. 7-4, ProCA3M is distributed in blood, liver, kidney and bladder. The blood had highest Gd^{3+} distribution of 15 and 50 min post injection, the blood intensity rapidly decrease. No blood imaging enhancement was observed one day post injection of ProCA3M. These results indicate the ProCA3 distribution kinetics in blood, with an estimated half life around 1 hour.

The imaging enhancement of liver reached the highest intensity in 15 and 50 min, however, the degree of the enhancement from MR imaging is much less than that of blood. The enhancement of the liver also decreases 2 hrs post injection of ProCA3. After 2 days of injection, the liver intensity decreased to a value similar to that of prescan. These results indicate that ProCA3M distributed and low concentration of ProCA3 remains in liver two day post injection of ProCA.

The images of kidney also enhanced 50 min post injection of ProCA3M. The enhancement of kidney reached the highest intensity in 1 day after injection of ProCA. After 2 days of injection, the kidney intensity decreased to a value similar to that of prescan. These results indicate that ProCA3M slowly accumulated in kidney and then decreased slowly. We clear see the enhancement of bladder at 44 min, which is an evidentce to support that ProCA3M is excreted from Kidney.

7.2.2.2 Biodistribution of ProCA measured by ICP-OES

The distribution of Gd^{3+} and ProCA32 were analyzed by ICP-OES and western blot with antibody against PV. For ICP-OES studies, tissues were collected 30 min and 4 hr after injection of ProCA32. 30 min post injection of ProCA32, both of the Gd^{3+} and ProCA32 were mainly distributed in liver and blood, while some accumulation was also found in kidney(Fig. 7-4). The Gd^{3+} and protein distribution are consistent with 3D MR enhancement (Fig. 7-4). The similar distribution of ProCA32 and Gd^{3+} after injection also indicates that Gd^{3+} and ProCA32 exist in a complex form *in vivo*. The distribution of Gd^{3+} in mice after injected with 0.015 mmol/kg of ProCA32 or 0.2 mmol/kg of Gd-DTPA for 4 h are analyzed by ICP-OES. Gd^{3+} was mainly detected in liver. While the Gd^{3+} concentration in blood is dramatically decreased from 0.2 mM at 30 min to 0.04 mM at 4 h. Since Gd-DTPA has very fast excretion time, the Gd^{3+} in tested tissues except kidney are very low.

7.2.2.3 Biodistribution of ProCA measured by immunochemistry methods

The distribution of the ProCA32 was also analyzed by western blot with antibody against PV. Consistent with MRI intensity, western blot shows the strongest bands in the serum, strong band in the tissue extracts of liver, kidney, heart and spleen, and not in the muscle (Fig. 7-4 D). The western blots are also consistent with the analysis of Gd^{3+} distribution (MRI and ICP-OES study) in such organs at the same time points, and protein of ProCA3M and Gd^{3+} distributed in the same location, indicating that ProCA3M is stable *in vivo* (Fig 7-5).

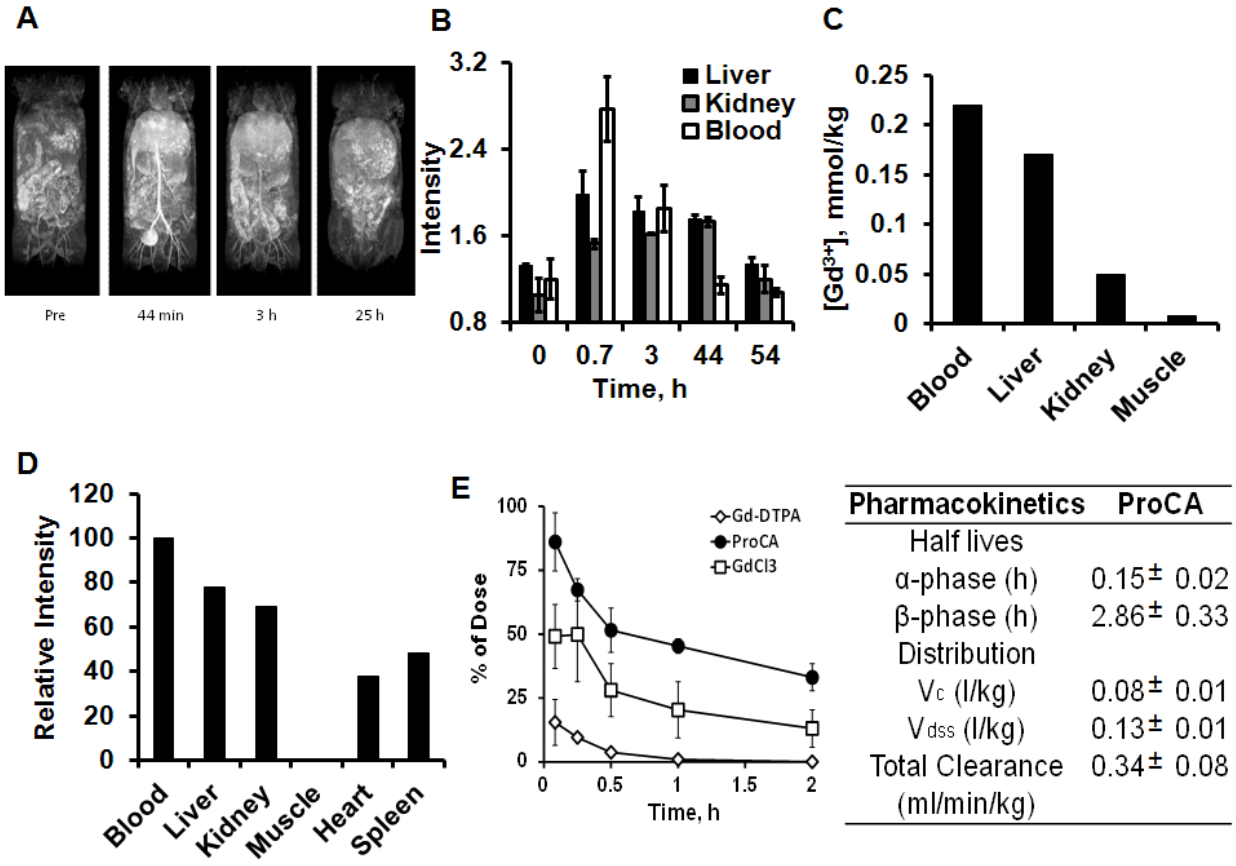

Pharmacokinetics	ProCA
Half lives	
α-phase (h)	0.15± 0.02
β-phase (h)	2.86± 0.33
Distribution	
V_c (l/kg)	0.08± 0.01
V_{dss} (l/kg)	0.13± 0.01
Total Clearance (ml/min/kg)	0.34± 0.08

Figure 7-4. MRI image (A), biodistribution (B-D) and pharmacokinetics of ProCA32 (E).

Biodistribution of ProCA32 are analyzed by MRI intensity (B), Gd^{3+} concentration by ICP-OES(C) and immunoblot with ProCA32 antibody (D).

7.2.3 Pharmacokinetics of ProCA3

Pharmacokinetics of ProCAs, Gd-DTPA and GdCl3 were studied in mice. After injection of ProCAs, GdCl3 or Gd-DTPA, blood of the mice was collected from the vein. The Gd concentration in plasma was determined by ICP-OES. We calculated the half lives and volume distribution of ProCAs or GdCl3 by two compartment model. Clearance of ProCAs or GdCl3 were determined by Equation 7-1,

$$\mathrm{CL} = \frac{\mathrm{AUC}}{\mathrm{D}} \tag{7-1}$$

where CL is the clearance, AUC is the area under the curve, and D is the injection dosage.

7.2.3.1 Parmacoknetics of ProCA1.affiM

ProCA1.affi is HER-2 biomarker targeted protein based MRI contrast agents with a molecular weight of 17 kDa. This contrast agents is further modified with PEG-40, named ProCA1.affiM, to improve solubility, relaxivity and to decease immunogenicity. As show from Fig. 7-5, the blood retention of ProCA1.affiM is much longer than that of the other MRI contrast agents. The distribution half ProCA1.affiM is 0.6 hours and the elimination half life for ProCA1.affiM is about 89 hours. Long blood circulation time allow ProCA1.affiM to have sufficient time to deeply penetrate in to the tumor and to interact with HER-2 biomarkers. On the other hand, such long circulation time may cause undesired background signal and toxicity. ProCA1.affiM has an initial volume distribution (V_c) of 0.05 l/kg, which further increase to 0.09 l/kg in the steady state phase (V_{dss}). The value of V_c and V_{dss} indicate that ProCA1.affiM is initially distributed in the blood vessel and then it restricted in the blood vessel and some extracellular extra-vascular space. Compare to other ProCAs, ProCA1.affiM has a low clearance value, indicating that ProCA1.affiM requires longer time to be excreted.

7.2.3.2 Parmacoknetics of ProCA2.affi

ProCA2.affi is the second generation of protein-based MRI contrast agents with four Gd^{3+} and one HER-2 target sequence in one molecule. This contrast agent has a molecular weight of 23 KDa. ProCA2.affiM is ProCA2.affi modified with PEG-40 to improve *in vivo* properties.

As show from Fig. 7-5, ProCA2.affiM has a shorter blood circulation time than that of ProCA1.affiM and longer blood circulation time than that of ProCA3M and GdCl3. As show in Table 7-1, ProCA2.affiM has a distribution half life of 0.2 hour and elimination half life of 12.0 hours. ProCA3.affiM has similar V_c and V_{dss} similar to that of ProCA1.affiM. V_c and V_{dss} of ProCA2.affiM is 0.05 and 0.09 l/kg, indicating that ProCA2.affiM may have similar distribution as ProCA1.affiM, and ProCA2.affiM was initially distributed in the blood circulation and restricted in the blood vessel and some extracellular extra-vascular space at equilibrium state. The clearance of ProCA2.affiM is much faster than ProCA1.affiM but slower than ProCA3M.

7.2.3.3 Pharmacokinetics of ProCA3M

ProCA3 is a non-targeted proteins based MRI contrast agent with two Gd binding sites and molecular weight about 11 kDa. ProCA3M was ProCA3 modified with PEG-40. As show in Chapter 4, PEG modification does not change the metal binding affinity and relaxivity of ProCA3. Our MRI imaging results (Chapter 5) show that ProCA3M can be used for the imaging of blood circulation, liver and kidney. The agentshows extraordinary advantage for the imaging for the early diagnosis of liver metastasis with 10 time smaller detection size than clinical diagnostics methods (Fig. 5-5).

To understand the blood retention, distribution and clearance of ProCA3M, we did pharmacokinetics study of ProCA3M. Fig. 7-5 shows the Gd^{3+} concentration in the plasma of mice at different time points after injection of ProCA3M, ProCA1.affiM, ProCA2.affiM, GdCl3 or Gd-DTPA. ProCa3M had much shorter blood retention time than that of ProCA1.affiM and ProCA2.affiM but much longer blood retention time than that of GdCl3 and Gd-DTPA. ProCA3M has a distribution half life of 0.15 hour and elimination half life of 2.8 hours, which are much shorter than that of ProCA1.affiM and ProCA2.affiM. The volume distribution of ProCA3M is 0.08 l/kg and 0.13 l/kg V_c for V_{dss}, respectively, indicating ProCA3M is mainly distributed in the blood circulation and some extracellular extravascular space, but the distribution of ProCA3M is larger than that of ProCA1.affiM and ProCA2.affiM. Interestingly, ProCA3M also has shorter clearance than that of ProCA1.affiM and ProCA2.affiM. Thus, ProCA3M has good pharmacokinetics allowing sufficient time for data collection and effect to excretion to prevent free Gd^{3+} release.

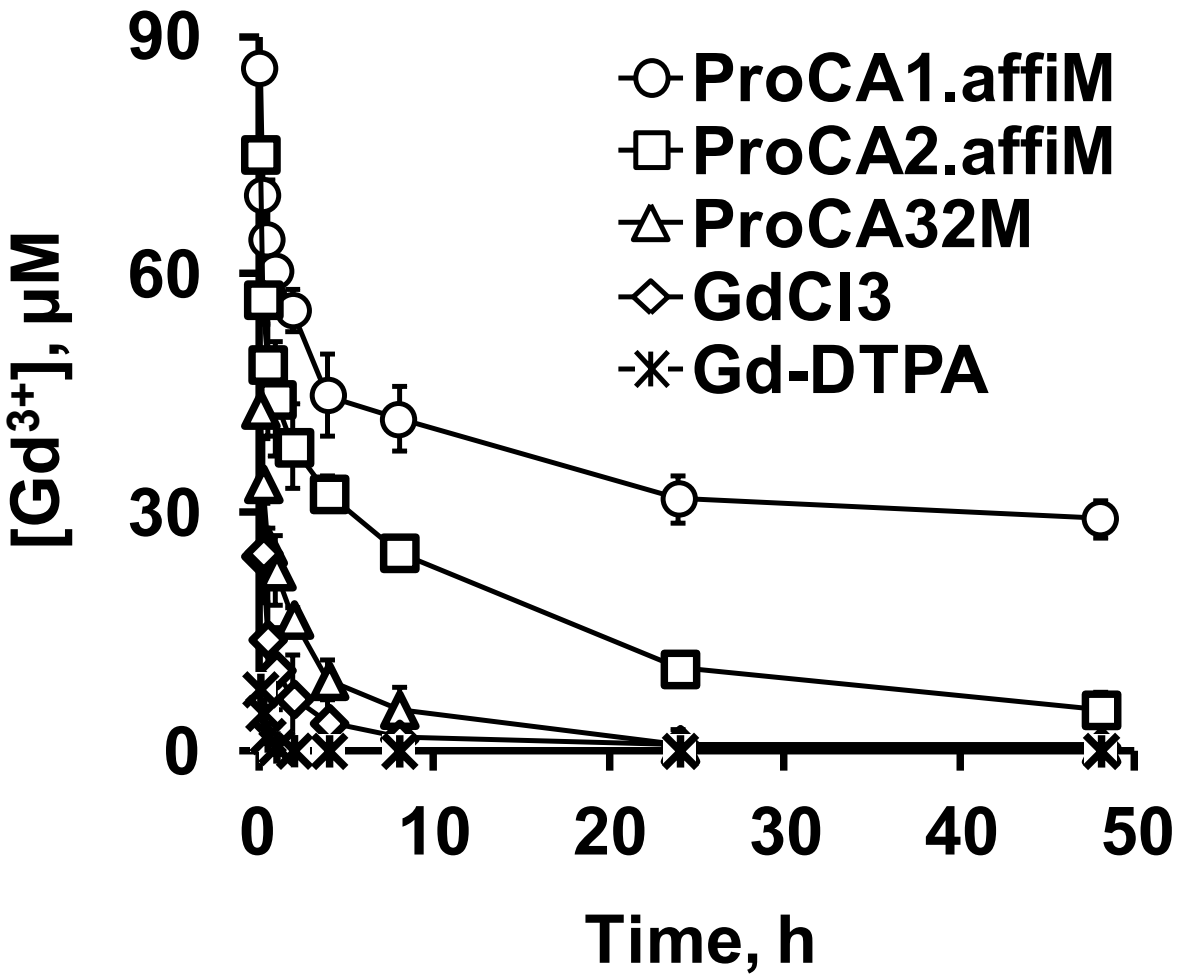

Figure 7-5. Gd^{3+} concentration in the blood of mice post injection of of ProCAs, Gd-DTPA and $GdCl_3$ at the diffent length of time.

Table 7-1. Pharmacokinetics of ProCAs and $GdCl_3$.

	$GdCl_3$	ProCA3M	ProCA1.affM	ProCA2.affiM
Half lives (h)				
α-phase	0.35 ± 0.07	0.15 ± 0.02	0.60 ± 0.47	0.20 ± 0.11
β-phase	11.43 ± 0.15	2.86 ± 0.33	89.17 ± 2.50	12.03 ± 1.92
Distribution (l/kg)				
V_c	0.14 ± 0.04	0.08 ± 0.01	0.05 ± 0.00	0.05 ± 0.00
V_{dss}	0.79 ± 0.51	0.13 ± 0.01	0.09 ± 0.01	0.09 ± 0.01
Total Clearance (ml/min/kg)	0.76 ± 0.3	0.34 ± 0.08	0.044 ± 0.02	0.089 ± 0.02

The pharcokinetics were calculated using two compartment model based on the Gd^{3+} concentration in serum at difference time points after injection of $GdCl_3$ or ProCA variants. The data were collected from 3 mice in each group.

7.2.4 Excretion pathways and clearance of ProCA

Like other drugs, MRI contrast agents can be excreted from renal and hepatointestinal excretion systems. Among 9 approved Gd^{3+} contrast agents, 2 of them are excreted from both renal and hepatointesinal excretion systems and other contrast agents are excreted only from renal excretion system. 3D MR imaging (Fig. 7-4A) shows enhanced bladder and kidney indicating that ProCA3 can be excreted from renal excretion system. To further understand the excretion pathways for ProCA3M, we I.V. injected fluorescein-labeled ProCA3M in mouse and followed its distribution under fluorescent dissecting microscope. The mice were euthanized 1 hour post injection. As show from Fig. 7-6, liver and gall bladder shows high green fluorescence and gall bladder has the highest intensity, which indicate that ProCA3M can be excreted from hepatointestinal excretion system. We also observed green fluorescence in the kidney and urine of the mice post injection of fluorescein-labeled ProCA3M. Thus, ProCA3M is excreted from both renal and hepatointestinal pathways.

Gadolinium release and accumulation is believed to induce NSF. To further study the long term accumulation and clearance of ProCA3M. Gd^{3+} concentration in different organs were measured by ICP-OES 14 days post I. V. injection of GdCl3, Gd-DTPA or ProCA3M (0.0033 mmol/kg ProCA3M, 0.0067 mmol/kg GdCl3 or 0.2 mmol/kg Gd-DTPA) in mice. As show in Fig. 7-4, Gadolinium from $GdCl_3$ has much higher accumulation in bone, liver and spleen the major organs for the Gadolinium deposit. ProCA3M has lowest accumulation in liver, lung, and spleen among these three reagents. Thus, ProCA3M has lower long-term Gd^{3+} accumulation compared with GdCl3 and the clinical injection dosage of Gd-DTPA.

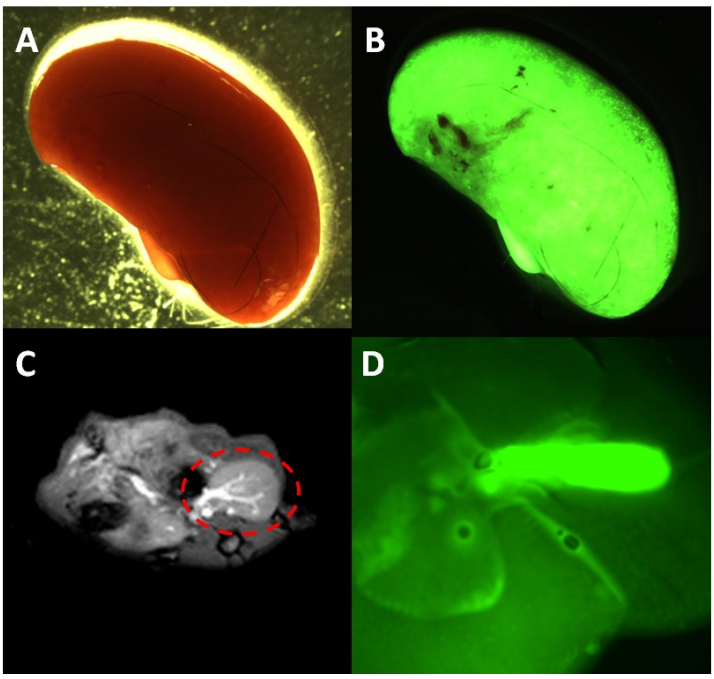

Figure 7-6. Excreation pathways of ProCA32M.

Fluorescence labeled ProCA32M were IV injected in mice. A strong enhancement of kidney (A, B) and gall blader (D) indicate that ProCA32M is excreated from both renal and hepato-intestine pathways. The fluorescence enhancement of kidney is consistant with MRI of kidney after injection of ProCA32 (C).

7.3 Discussion

The toxicity of MRI contrast agents is mainly caused by free Gd^{3+} release. Gd^{3+} has a similar ionic radius as Ca^{2+}, thus, Gd^{3+} can mimic Ca^{2+} to interact with Ca^{2+} binding proteins, such as Ca^{2+}-ATPase, channels, receptors and enzymes.[125] Gd^{3+} binding to the Ca^{2+}-binding proteins changes the activity or kinetic properties of the protein. for example, Gd^{3+} can activate calcium sensing receptor and induce inward Cl^- current.[105] Free Gd^{3+} is toxic with a LD_{50}= 0.1 mmol/kg in mice. NSF, a disease the patient with impaired rental function, is believed to be caused by the free Gd^{3+} release after administration of Gd^{3+}-based MRI contrast agents. Therefore, a safe MRI contrast agent must have no Gd^{3+} accumulation after injection To facilates further potential of clinical application, the toxicity, pharmacokinetics, biodistribution and excretion of these agents must be carefully studied.

MTT assay in H441 cells shows that ProCA3 with and without Gd^{3+} has no cytotoxivity. Our serum toxicity data shows that mice have normal liver, kidney, heart functions functions after contrast agents injection. The total protein concentration, albumin concentration, lipids concentration, Na^+, K^+, Ca^{2+}, and Cl^- level in mice are also similar to the control group injected with saline. These data provide strong evidence that ProCA3 is have no toxicity.

We further studied the distribution and pharmacokinetics of ProCAs. To design a MRI contrast agents with high safety profile and capabl ity for molecular imaging, the contrast agent must have proper pharmacokinetics. If a contrast agent excretes too fast, it will have less time to interact biomarkers. On the other hand, if a contrast agent has very long half life, it may have undesired toxicity induced by free Gd^{3+} release. ProCA1.affiM, ProCA2.affiM and ProCA3M has difference elimination half lives from 3 hours to 89 hours. Such difference is probably caused by

the different charge, molecular weight and shape of these ProCAs. Due to the large size, ProCAs are mainly distributed in the blood vessel and some extracellular extravascular spaces. Such unique distribution made ProCAs able to penetrate in the tumor for the molecular imaging and promising fro evaluate blood vasculature by DCE-MRI.

Free Gd^{3+} is accumulated in the bio-deposit site *in vivo*, such as lung, liver, spleen and bone. The accumulation of Gd^{3+} can cause serious disease, such as NSF. Thus, MRI contrast agents must excreted efficiently after imaging. Clinical MRI contrast agents are excreted from renal and hepato-intestinal excretion system. Most of these contrast agents are excreted only from renal excretion system, which made these contrast agents good for the MR imaging of kidney. Multihance and Eovist are excreted from both renal and hepato-intestinal excretion system. Due to such unique properties, Multihace and Eovist are applied for the imaging of liver disease. Our fluorescence imaging show that ProCA3M is excreted from both liver and kidney and this result is constant with MRI in mice. We further compared the Gd^{3+} long term accumulation in different mice organs after injection of GdCl3 (0.0067 mmol/kg), ProCA3M (0.0033 mmlo/kg containing 0.0067 mmol/kg Gd) and Gd-DTPA (200 mmol/kg). The reason that we use 0.0033 mmol/kg ProCA3 to study Gd^{3+} long term accumulation is that 0.0033 mmol/kg already shows good MRI enhancement in kidney. GdCl3 has the highest accumulation in the liver, spleen, lung among above three reagents and ProCA3M has the lowest accumulation in these organs. These data suggest that ProCA3M is efficiently excreted from renal and hepota-intestinal excretion system with less Gd^{3+} accumulation *in vivo* due to high stability, short elimination half life, efficient excretion, high dose efficiency and low injection dosage.

7.4 Conclusion

MRI contrast agents with good safety profiles are essential for both preclinical and clinical applications. In this chapter, the toxicity, distribution, excretion and long term accumulation of ProCAs, especially ProCA3M were carefully studied. Compared with Gd-DTPA and GdCl3, ProCAs has difference biodistribution. ProCA3M are mainly distributed in the blood, liver, kidney for the short time after injection, while ProCA3M has much lower accumulation in the Gadolinium bio-deposit sites. Lower Gd^{3+} accumulation in these sites indicate that ProCA3M has lower chance to cause NSF. Both cytotoxcity and blood test shows that ProCA3 has no toxivity in cell and *in vivo*. ProCAs has different pharmacokinetics. ProCA3M has elimination half liver around 2 hours, which is a desired for the imaging and elimination. Volume distribution studies indicate that ProCA3 and other ProCAs are mainly distributed in the blood vessel and extracellular extravascular space. In conclusion, ProCA3M has low toxicity, low Gd^{3+} accumulation, controlled distribution and such unique properties made ProCA3M a promising contrast agent for the clinical and preclinical diagnostics.

8 MOLECULAR IMAGING OF TUMOR BIOMARKERS USING PROTEIN-BASED MRI CONTRAST AGENTS

8.1 Introduction

Cancers are deadly diseases cause more 500000 deaths annually in the United States.[213] Although large effects have been made, the cancer therapy is limited by lacking of effective and reliable methods for early diagnostics and evaluation of tumor biomarkers. Therefore, it is critical to develop an effective way to detect the tumor and its biomarkers in the early stage.

Multiple approaches are applied for the tumor diagnostics. These methods include screening blood circulating biomarkers, such as VEGF, biopsy, and various imaging techniques. The blood circulating biomarkers have great potential for the tumor diagnostics. In the current stage, however, biomarker based blood test such as the PSA test, a standard for prostate cancer diagnostics, has low correlation with prostate cancer staging. Biopsy is an informative method. However, this method is invasive and with large errors due to sampling. The patients have to suffer from the great pain from the tissues are taken out from body for the analysis. The “golden-standard” the evaluation of angiogenesis is the mean vascular density (MVD), which estimate the blood vessel density by immunohistochechestry. However, tumor usually heterogeneous and MVD only quantify limited area in the collected tissue in the specific location of tumor. Thus, the MVD of biosy tissue can be missleading.[207, 214] On the other hands, imaging techniques are used to detect the angiogenesis. However, most of these techniques are not satisfy with the requirement for the tumor diagnostics. The fluorescence imaging lacks of the tissue penetration. As discussed in Chapter 1, the sensitive imaging techniques such as PET and SPECT are expensive and the number of instrument for PET and SPECT scan is limited. Be-

sides, PET and SPECT scanning use radioactive isotopes, which could be potentially harmful to the patient.[207] MRI is one of the promising techniques for the cancer diagnostics. Magnetic renascence Imaging (MRI) is an advanced diagnostic technique with high resolution, three dimensional properties. Due to the low sensitivity, 30% of the MRI tests require the administration of MRI contrast agents to improve the signal to noise ratio and obtain tissue specific images[103]. With 7 unpaired protons, high magnetic moment and long election relaxation time, Gd^{3+} became the best metal ion function as contrast agents. Gd^{3+}-based MRI contrast agents were applied for clinical diagnostics for over two decades.

One of the disadvantages of MRI is that MRI is limited by the sensitivity. To imaging the biomarkers with limited receptor number, MRI contrast agents must be incorporated with target moieties and have high relaxivity. Unfortunately, most of the current contrast agents only have very low relaxivity (less than 5 s^{-1} mM^{-1} for Gd-DTPA), and the lowest detection limits for these contrast agent is 0.1 mM[46]. Therefore, it is hard to image the expression level of certain receptors when the receptor number is low. On the other hand, in order to targeting to the receptors, these contrast agents are uaually conjugated to antibody or peptide. However, antibody has a large molecular weight. Thus, contrast agents conjugated with antibodies have low penetration capability in tumor tissue.[155] Protein based contrast agents has more than 10 fold higher relaxivity than clinical MRI contrast agents. By conjugating to small peptides or affibody, ProCA1s is able to imaging biomarkers, such as HER-2 and GRPR.

We design a new generation of protein base contrast agent with two metal binding sites with improved stability and pharmacokinetics. In this chapter, we introduce our current work for the imaging of cancer biomarkers by incorporating HER-2, GRPR or integrin targeting pep-

tide in ProCA3M by MRI. The MR imaging results is confirmed by immunostaining and ICP-OES study.

8.2 Results

8.2.1 Molecular imaging of GRPR in cancer by ProCA3.bombesin

8.2.1.1 GRPR is a biomarker for prostate, breast, small cell lung cancer

There are three groups the GPCR exist in the bombesin receptor family. Among these receptors, the group 2 receptor, GRPR, is a promising biomarker for the tumor diagnostics. Discovered in 1971 from amphibian, the natural ligand of GRPR, bombesin peptide, is found to be strongly and specifically bound to gastric-release peptide receptor (GRPR) with high affinity. Its human homolog, GRP, plays an important role on gastric acid secretion, muscle contraction, cell differentiation.[215, 216] The interaction between GRP and GRPR could activate multiple signaling pathways including tumor cell proliferation, survival and differentiation. Due to the low expression level in normal tissue and high expression levels in tumor, GRPR become a promising biomarker for the tumor diagnostics.[163, 165] The high affinity interaction between GRPR and bombesin made bombesin a promising targeting peptide for the molecular imaging of prostate cancer, breast cancer and small cell lung cancer.

8.2.1.2 in vitro testing of interaction between ProCA3.bombesin and GRPR

We linked the bombesin sequence of the C-terminal ProCA3. We expressed and purified this novel protein-based MRI contrast agents, named ProCA3.bombesin, using the methods described in Chapter 3. ProCA3.bombesin has a ProCA3 sequence, which binds two Gd^{3+} as

contracs agents. ProCA3.bombesin also has a GRPR targeting peptide, which binds to GRPR with high affinity (Fig. 8-1).

To test the interaction between ProCA3.bombesin and GRPR, ProCA3.bombesin were incubated with H441 and PC3 cells for 30 min. MR imaging of these cells were collected after robust wash by PBS. H441 has a low expression level of GRPR, while PC3 has high expression level of GRPR.[169] As shown from Fig. 8-2A, PC3 has higher MRI intensity, which means more ProCA3.bombesin binds to PC3 cells. Since PC3 cells have at least 10 fold higher GRPR expression than H441 cells, these results indicate that ProCA3.bombesin specifically binds to GRPR.

To further confirm the internaction between ProCA3.bombesin to GRPR. We did immunofluorescence staining of ProCA3 in PC3 and H441 cells after these cells were incubated with ProCA3.bombesin and robust wash. As show from Fig. 8-2B, PC3 cells has high staining of ProCA3.bombesin than that H441 cells indicate that ProCA3.bombesin specifically interact with GRPR.

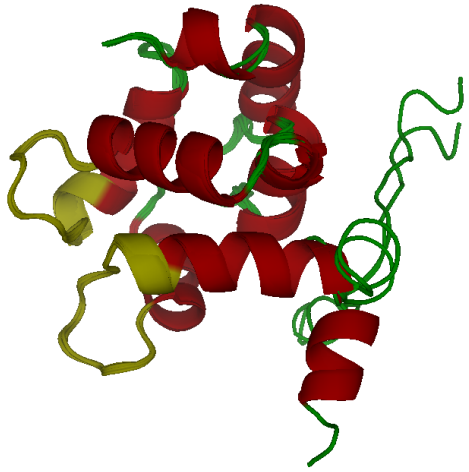

Figure 8-1. Model structure of GRPR targeted protein based contrast agent, ProCA32-bombsin.

This picture is the combination of five predicited pictures of generated from Tasser. Red region indicate Gd^{3+} binding pockets.

8.2.1.3 MR imaging of GRPR expression in xenograft mice model

We next imaged GRPR expression in xenograft mice model. H441 and PC3 nude mice xenograft are used to test the ability of tumor imaging using ProCA32.bomb. MRI experiments were carried out when the tumor size reached around 1 cm in diameter. ProCA3.bomb are labeled with Cy5.5 and PEGlytaed by PEG-40. The spin echo image (Fig. 8-3) shows that PC3 tumor brightened 1 day after contrast agents injection, and decreased there afterward. NIR image shows that both H441 and PC3 tumors brightened up 1 days post contrast agents injection (Fig. 8-3). The fluorescent intensity of tumor is consistent with the mice MRI image. Both H441 and PC3 tumor, along with kidney, spleen and liver have high cy5.5 fluorescence. Gd^{3+} distribution were analyzed by ICP-OES. Liver and spleen showed highest Gd^{3+} accumulation, PC3 tumor has slightely higher Gd^{3+} accumulation than that of kidney and H441 tumor (Fig. 8-3).

Western (Fig. 8-4 C) and imunofluorescent staining (Fig. 8-4 B) of tissue extracts and tissue sections confirms that the GRPR are highly expressed in both PC3 and H441 tumor, while it has very low expression in kidney, liver and heart. Imunofluorescent staining (Fig. 8-4) also indicate that ProCA32-bombsin are existed in PC3 and H441 tumor, liver and kidney. These data indicate the ProCA3.bembesin can be applied for the molecular imaging of GRPR in tumors.

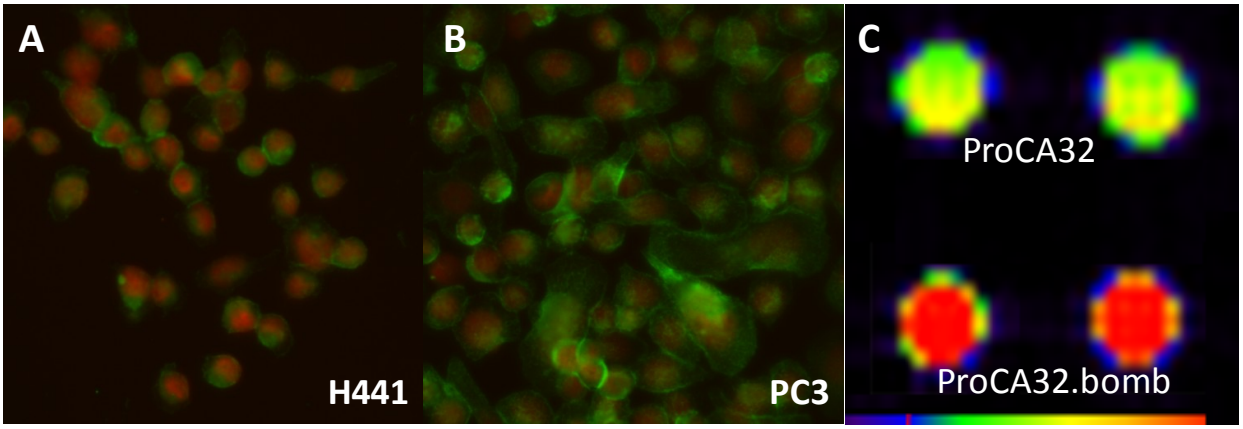

Figure 8-2. ProCA32.bomb target to GRPR high expression cells.

GRPR-specific ProCA, ProCA32.bomb, target to to GRPR expressed cells using fluoresecence microscopy (A, B) or MRI PC3 cell pellets (C). A. Fluorescence imaging of ProCA32.bomb stainig for H441 cells after incubation with ProCA32.bomb at 37 °C for 30 min. B. Fluorescence imaging of ProCA32.bomb stainig for PC3 cells after incubation with ProCA32.bomb at 37 °C for 30 min. C. MRI of PC3 cells pellets after incubation with non-targeted ProCA32 or GRPR targeted ProCA32, ProCA32.bomb, at 37 °C for 30 min followed by thoroughly washing.

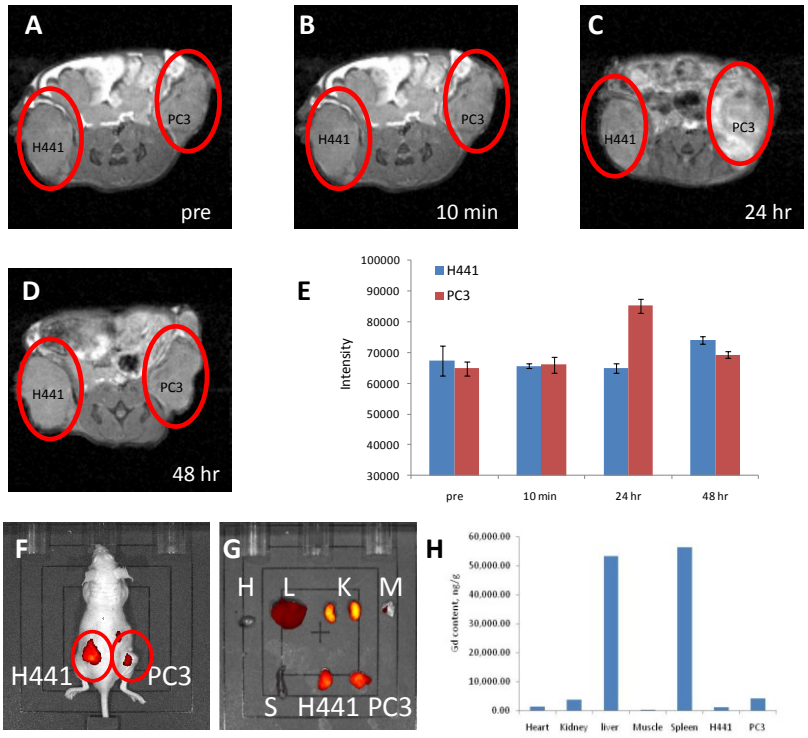

Figure 8-3. MRI (A-D) and NIR (F,G) imaging of H441 (left red circle) and PC3 (right red cycle) tumor xenograft mice.

ProCA3.bomb distribution in tumor and other tissues were analyzed by MRI signal enhancement (E), NIR imaging (G) and ICP-OES(H). PC3 tumor shows significant enhancement in MRI 24 h post injection of ProCA3.bombsin (C right red cycle). Both tumors enhanced in NIR imaging 1 day after injection (F). H441 and PC3 tumors tissue shows similar intensity under NIR imaging (G). ICP-OES study shows that PC3 higher Gd^{3+} accumulation than that of H441 tumors (H).

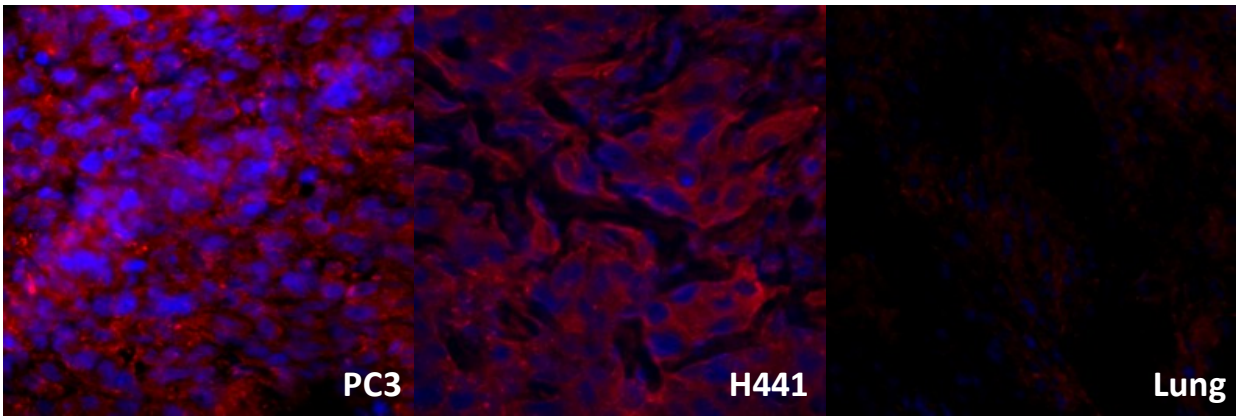

Figure 8-4. Immunofluroesence staining study of ProCA3.bomb in the PC3 and H441 tumor or lung tissue (Negative control) 48 hours post injection of ProCA32. bomb.

Red is the ProCA3.bomb stained by the home-made rabbit antibody against ProCA32 with 1:500 dilution. Blue is the nucleus staining by DAPI.

8.2.2 Molecular imaging of HRE-2 biomarker by ProCA3.affi

Breast cancers are deadly diseases. According to national cancer institute, it is estimated that 39,510 weman will be diagnosed to have breast cancer and 39,510 women will dead of the diseases. HER-2 is a major prognosis biomarker that expressed in 30% breast cancer and 60-70% of DCIS tissue. Monitoring the spatial and temporal changes of several molecular biomarkers such as HER2/EGFR sharing the same signaling pathway during cancer progression and treatment is the key for understanding the molecular basis of cancers, for early and accurate diagnosis, and for developing effective drugs with synergistic effects to treat this deadly disease. Biomarkers such as the epidermal growth factor receptors EGFR and HER2/Neu are highly expressed in various diseases such as breast and ovarian cancers and play important roles in disease progression and survival. They are also major drug targets for targeted therapy. Since the clinical application of targeted therapy is largely limited due to the limitation of current methods for assessment of these cancer biomarkers. The effectiveness of the target therapy largely depends on the pre-selection of patients with over-expressing these biomarkers. To date, one of five HER2/Neu clinical tests, including biopsy and IHC, provides incorrect results, leading to improper selection of appropriate patients for personalized treatment using biomarker targeted therapies [134, 135]. There is an urgent need to develop non-invasive and accurate methods for diagnosis and selection of patients and to monitor biomarker levels/distribution and their changes upon treatment by targeted drugs.

Instead of using HER-2 antibody for molecular imaging, we linked HER-2 affibody at the C-terminal of ProCA3, named ProCA3.affi. The procedure of purification of ProCA3.affi is very

similar to that of ProCA3 purification shown in Chapter 3. We also covalently linked PEG-40 and cy5.5 at the lysine residues of the ProCA3.affi.

We next test the MRI imaging of HER-2 biomarkers in cancer in two mouse models after injection of ProCA3.affi. In the xenograft model, SKOV-3 tumor were implanted in the flank the mouse. After the tumor size reached to about 1 cm, 0.03 mmol/kg of ProCA3.affi was I. V. injected to the mice with the tumors. MR imaging were collected before injection and different time points after injection. As shown in Fig. 8-5, the contrast of tumor edge were significantly enhanced after injection of ProCA32.affi (Fig. 8-5 B-G) and the highest enhancement were shown at 49 hr post injection of ProCA32.affi (Fig. 8-5 F). Such enhancement is still can be detect three days post injection (Fig. 8-5G), while the enhancement of other organs dramatically decreased from the original intensity. Since ProCA3.affi also carries cy5.5, ProCA3.affi can also be used for the near infrared imaging. As shown from Fig. 8-5 H, consistant with the MRI enhancement, the NIR of SKOV-3 tumor was enhanced after ProCA3.affi injection. Since ProCA3.affi enhance SKOV-3 tumor in MRI and NIR imaging, this contrast agents can be further applied non-invassively evaluate HER-2 expression levels in breast and ovarian cancers.

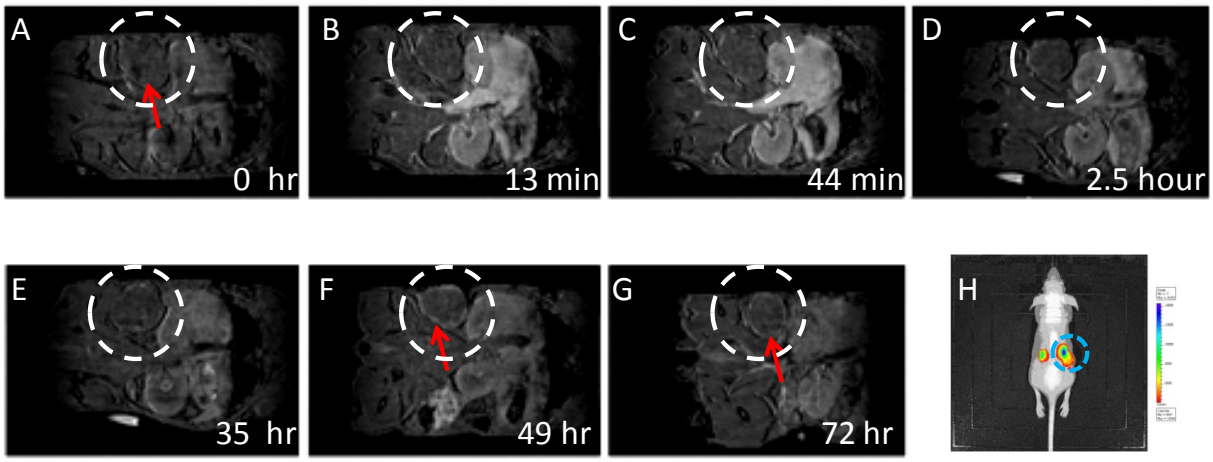

Figure 8-5. MRI (A-G) and NIR imaging (H) of HER-2 expresion in the xenografted SKOV-3 mice model.

Tumor edge under MRI (red arrow head in the circled dash line) was significantly enhanced after injection of ProCA32.affi (B-G) and the highest enhancement were shown at 49 hr post injection of ProCA32.affi (F). H. The SKOV-3 tumor in NIR imaging (blue dash cycle) is enhanced 49 hours post injection of ProCA32.affi with Cy 5.5 conjugation.

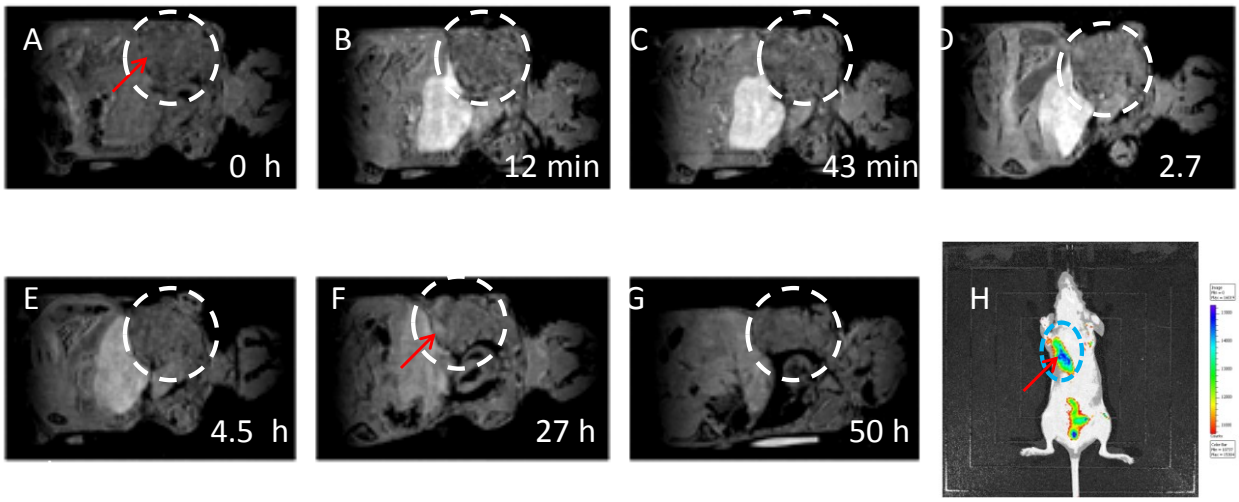

Figure 8-6. MRI (A-G) and NIR imaging (H) of HER-2 expresion in MCF10-DCIS isotropic mice model.

Small region of tumor adjacent to liver (red arrow head in the circled dash line) was enhanced at 27 hr post injection of ProCA32.affi (F). H. The SKOV-3 tumor in NIR imaging (blue dash cycle) is enhanced two days post injection of ProCA32.affi with Cy 5.5 conjugation.

We next test the MR imaging of HER-2 in the breast cancer isotropic tumor model. MCF-10DCIS tumors were implanted in the nipple of the mouse. MRI and NRI imaging were performed when tumor size is larger than 1 cm. As shown from Fig. 8-6 A-G, the MRI and MR signals of MCF-10DCIS tumor were enhanced 1 day after injection of ProCA3.affi and the imaging enhancement in MRI is consistent with those of NIR imaging(Fig. 8-6 H). These results indicate that ProCA3.affi can be used for the MRI and NIR imaging of HER-2 biomarkers. HER-2 is a prognosis biomarker for the breast cancer. Our results open a new avenue to evaluate breast cancer progression noninvasively.

8.2.3 Molecular imaging of angiogenesis by ProCA3.RGD

Tumor requires nutrition to grow. When tumor grows more than 1-2 mm in diameter, the passive perfusion of nutrient is not sufficient enough for the tumor growth. The formation of new blood vessel, angiogenesis, is essential for tumor to overcome this growth restriction. On the other hand, angiogenesis also facilitate tumor metastases.[213] It is essential to develop an effective way to monitor the tumor of angiogenesis. The methods for the angiogenesis diagnostics are also valuable for monitoring the effects of the chemotherapy against angiogenesis.

Integrins belong to a large family of integral membrane proteins expressed in animal cells. Two transmembrane subunits, α subunit and β subunit, are non-covalently interacting with each other to form functional integrin. By different combinations, they are able to form more than two dozen of different integrin pairs[217]. The extracellular domain of integrin binds to variety of proteins in the extracellular matrix, such as fibronectin, collagen, laminnin, collegan and I-CAM-1. The intracellular domain of integrin binds to signal transduction molecule and cell skeleton, such as talin, filamin, FAK. These molecule not only transfer the extracellular signal

from outside to inside of the cell, it also transfer the inside signal to the extracellular space.[218, 219] Integrin $\alpha_v\beta_3$ is expressed when the new blood vessel are formed. It is upregulated when certain tissue undergoes inflammation, wound, and necrosis and tumor formation. Integrin is one of the sensitive and high expression biomarkers of angiogenesis during tumor formation.[220] The natural ligands of integrin are vitronectin, fibronectin, fibrinogen, osteopontin. To interact with integrin $\alpha_v\beta_3$ most of these ligands contains a specific amino acid sequence, RGD. The binding affinity between RGD and integrin is about 10^{-6} M, which is strong enough to be used as a targeting peptide for the molecular imaging.[221]

To develop a MRI contrast agent for imaging of integrin $\alpha_v\beta_3$, we linked 4-repeat-RGD peptide at the c-terminal of ProCA3, named ProCA3.RGD. ProCA3 has two Gd^{3+} binding sites and the RGD peptide is linked at the C-terminal of ProCA3 by GGG linker.

We next test interaction between ProCA3.RGD to integrin $\alpha_v\beta_3$ high expression cells, UG-87-MG. Immunofluorescence results from Fig. 8-7 show that ProCA3.RGD can bind to the UG-87-MG. The cytoplasm staining of U87-MG staining by ProCA3 antibody indicates that ProCA3.RGD is robustly uptake by endocytosis. As a negative control, ProCA3 without targeting peptide was tested in a very similar conditions. These results indicate that ProCA3.RGD is a promising contrast agent for the molecular imaging of integrin $\alpha_v\beta_3$ in cancer.

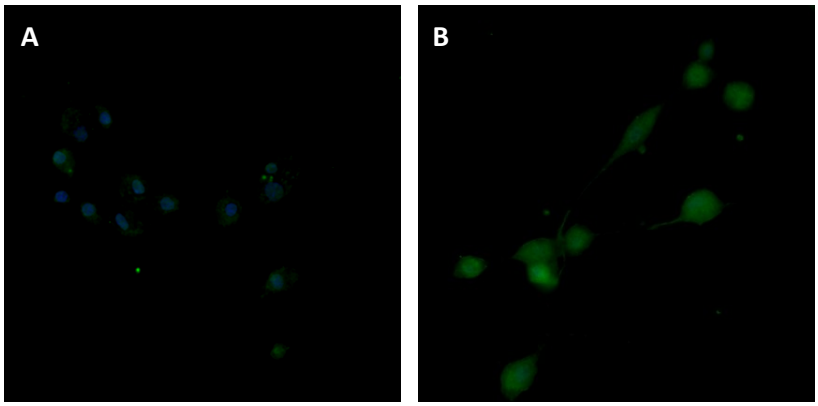

Figure 8-7. Integrin $\alpha_v\beta_3$-specific ProCA32, ProCA32-RGD4, target to to U87MG cells.

A. U87MG cells incubated with 1 µM non-targeted ProCA32 at 37 °C for 1 hour. B. U87MG cells incubated with 1 µM ProCA32-RGD at 37 °C for 1 hour.

8.3 Discussion

MRI is an advanced imaging technique which collects real time, non-invasive, three dimensional imaging with high resolution, high depth penetration. MRI not only can collect anatomic images, but also can collect functional data such as water perfusion, blood vasculature, and tissue oxygen levels. MRI is also the attractive imaging modalities for molecular imaging of disease biomarkers. The combination of these information collected by MRI will provide informative guidance for disease diagnostics.

The molecular imaging of diseases biomarkers, however, is limited by the lack of MRI contrast agents that specifically binds biomarkers and alter the signal intensities of MRI. The expression level of biomarkers is usually very low. For example, 10^5 GRPR molecules are expressed one PC3 cell. Assuming PC3 cell has a volume of 1000 μm^3 (10 μm × 10 μm × 10 μm), then the local GRPR concentration is 1.7 μM. Clinical MRI contrast agents has a detection limits above 30 μM and do not have biomarker targeting moieties. Thus, clinical MRI contrast agents cannot image this biomarker. Even the clinical MRI contrast agent is engineered with GRPR targeting peptide, the local concentration of contrast agents (1.7 μM assuming 1 to 1 binding) is lower the detection limits of clinical MRI contrast agents. Thus, MRI contrast agents with high relaxivity (low detection limits) and specific biomarker targeting sequence are essential for the success of molecular imaging of biomarker.

The detection limits of MRI contrast agent is correlated with the relaxivity. Clinical MRI contrast agents with a relaxivity less than 5 $mM^{-1}s^{-1}$ only have a relaxivity above 10 μM. When the relaxivty increase to above 100 $mM^{-1}s^{-1}$, the detection limit of the contrast agents decrease to less than 690 nM.[45] ProCA3 has a per particle r_1 relaxivity about 60 $mM^{-1}s^{-1}$. In Chapter 5, we

show that 2 μM of ProCA3 can enhance the MRI signal. Thus, ProCA3 is a good candidate for developing MRI contrast agents for the molecular imaging of biomarkers with limited expression level. ProCA3M has an elimination half-life around 3 hours. Therefore, this contrast agent have a good time window for the marker recognition, molecular imaging and excretion.

We designed three ProCA3 based MRI contrast agents for the molecular imaging of tumor biomarkers, such as GRPR, HER-2 and integrin $\alpha_v\beta_3$. ProCA3.bombesin selectively enhances PC3 tumors other than H441 tumor in xenograft mice model. Since PC3 cells have more than 10 times higher GRPR level than that of H441, this result suggests that ProCA3.bombesin can semi-quantitatively evaluate GRPR expression levels in different tumor. We also engineer HER-2 targeted ProCA3 (ProCA3.affi). ProCA3.affi is able to image HER-2 receptor in both xenograft SKOV-3 model and MCF10-DCIS isotropic model. Thus, our contrast agents can be applied for the imaging of different biomarkers by engineering different biomarker targeting moieties. Targeted ProCA3s has great potential to be applied for preclinical drug discovery and clinical tumor diagnosis and evaluation.

8.4 Summary

We developed tumor specific MRI contrast agents for the molecular imaging of tumor biomarkers. These novel targeted ProCA3s variant can binds to biomarkers such as GRPR, HER-2 and integrin $\alpha_v\beta_3$ with high specificity.

GRPR in mice tumor can be targeted by ProCA3.Bomb with high specificity of PC3 tumor cells, which has 10 times high expression level of GRPR than that of H441 cells. Because ProCA3.bomb carries a cy5.5. This probe can also be used for the NIR imaging. Consistent with MRI, PC3 tumors shows enhanced MRI signal in the NIR image.

HER-2 receptor can be imaged by ProCA3.Affi in xenograft and orthtropic mice model in both MRI and NIR, indicating that ProCA3.Affi can successfully target HER-2 receptors for the molecular imaging of HER-2 expression in tumors.

In addition, prilimiary study shows that ProCA3.RGD can selectively target integrin. Thus this probe is promising for the molecular imaging of integrin.

Molecular imaging of GRPR and HER-2 in mice model shows semi-quantitative enhancement of biomarkers in tumor. The success of MR imaging of GRPR and HER-2 suggest that targeted ProCA3s can be applied to imaging other important tumor biomarkers by engineering different biomarker targeting moieties. Integrin $\alpha_v\beta_3$ targeted ProCA32, ProCA32.RGD also able to target tumor cells with high expression of integrin $\alpha_v\beta_3$. Thus, targeted ProCA3 has great potential to detect tumor location, tumor size, evaluate tumor progression by semi-quantitavie evaluate biomarker expression levels and facilitate personalized medicine for tumor treatment.

9 PEGYLATION, FERMENTATION STUDY OF PROTEIN-BASED MRI CONTRAST AGENTS

9.1 Introduction

Several *in vivo* properties are required to be carefully considered to design protein drug for the diagnostics and therapeutics of human disease. First, the protein drug can easily cause immonugencity. Thus, the designer must carefully design and modify the desired protein drug to make sure no or low immunogenicity to limit side effects *in vivo*. Second, an effective drug must have optimized pharmacokinetics. For example, the imaging reagents must have a proper time window for imaging and excretion. Third, a commercialized drug must have reproducible and economic methods for the large scale production of the drug.

PEGylation is one of the FDA approved methods for the drug modifications. By covalent conjugation of PEG, the solubility, immunogenicity and pharmacokinetics of the drugs can be dramatically improved. Our previous data shows that PEGlytion increases the relaxivity, decrease the immunogenicity and optimize the distribution of ProCA1, while the metal binding affinity and selectivity of ProCA1 remains unaffected by PEG.[99, 155]

Humanization refers to modification of an amino acid sequence of protein drug from non-human protein sequence to human protein sequence. Humanization is essential for a protein drug to survive under the human immune system. This process is extremely important step for developing an antibody drug generated from non-human immune system.[222, 223] Since ProCA3 is derived from rat PV, it is also very important to generate humanized ProCA3 to reduce the immunogenicity of the drug.

Large scale production is another bottle neck for the commercialization of ProCA. An ideal method for ProCA3 production should contain several important features. First, the

method for the protein production should have very good repeatability so that drugs produced from differ batches have the same properties. Second, the methods for ProCA production should be easily adapted to higher volume system with no modification of the protocol. However, the ProCA3 expression methods in Chapter 3 contain heating and dialysis steps, which cannot be applied for the large scale protein purification. Third, the cost ProCA production needs to be reduced. For mice (20 - 30 g) study, 0.5 mg of ProCA3 is required as the minimium dosage for the enhancement of the kidney. Because dog and human has more than 1000 times high body weight than that of mice (20 kg for dog and 60 kg for human), by direct projection of the injection dosage by body weight, MRI requires 0.5 g and 1.5 g of ProCA3 for the injection in dog and human, respectively. Mice has much faster metabolism than that of human and dog, thus mice usually requires 20 times higher injection than that of human and dog. By considering the metabolism, it is still requires 250 mg and 750 mg of the ProCA3 as the minumium injection dosage for MRI. Thus, large scale expression and purification with GMP-like protocol is important for further potential applications of ProCA3 in large animals and human.

In this chapter will first introduce our strategies for further modification of ProCA3 by PEGlytion. I will then discuss our effort inhumanization of PrcA3 series. Next, I will introduce our efforts on the large scale expression and purification of ProCA3 based on our intial studies on protein expression and purification discussed in Chapter 3.

9.2 Results

9.2.1 PEGlytion of ProCA3 variants

PEGLytion can increase the solubility, decrease immunogenicity of the protein drugs. To improve the *in vivo* properties of ProCA3, PEG-40 was covalently linked to ProCA3 through the lysine residues. The general procedure for PEGlytion is shown in Fig. 9-1. In brief, ProCA3 were dialysised aganist PBS or HEPES buffer to completely remove Tris with free amine. PEG was mixed with ProCA3 with 3:1 ratio. The mixture was incubated at room temperature for 2 hours with constant shaking. Then, the mixture was separated by FPLC.

PEGlyted ProCA3 can be purified by High Trap Q column, after washing out the un-bounded chemicals, the PEGlyted ProCA3 was eluted with 10 mM Tris/HCl, pH 8.5, 5 mM EGTA and 1 M NaCl. Both comassie brilliant blue and iodine staining of SDS-PAGE gel were used to detect FPLC fractions. Commassie brilliant blue were used to stain the protein bands and iodine were used to stain PEG moiety. As shown in Fig. 9-2, fraction 2-9 has a very large UV absorb-ance from FPLC detector. This peak contains large amount of PEG and this peak only have very small amount of protein. Fraction 17-20 can be stained by both iodine and commassie brilliant blue, which indicate that fraction contains PEGlyted ProCA3.

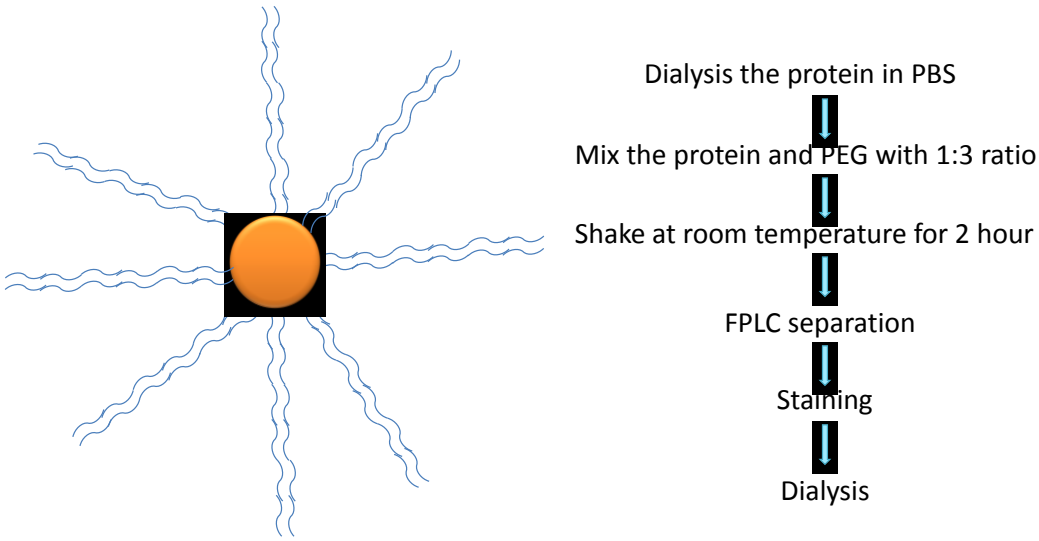

Figure 9-1. General procedure for the PEGlytion of ProCA3 varients.

ProCA3 varients were first dialyzed with PBS or HEPES buffere. Then the ProCA3 variants and PEG-NHS ester were mixed with 1:3 molar ratio and incubated at room temperature for 2 hour with constant shaking. Unreacted PEG-NHS ester were quenched by adding Tris/HCl at pH 7.0 with a final concentration of 10 mM. PEGlyted ProCA3 were further seperated by FPLC, staining by I_2 and comassie briliant blue in SDS-PAGE. The fractions contains PEGlyted ProCA3 variant dialysised and concentrated for other type of studies.

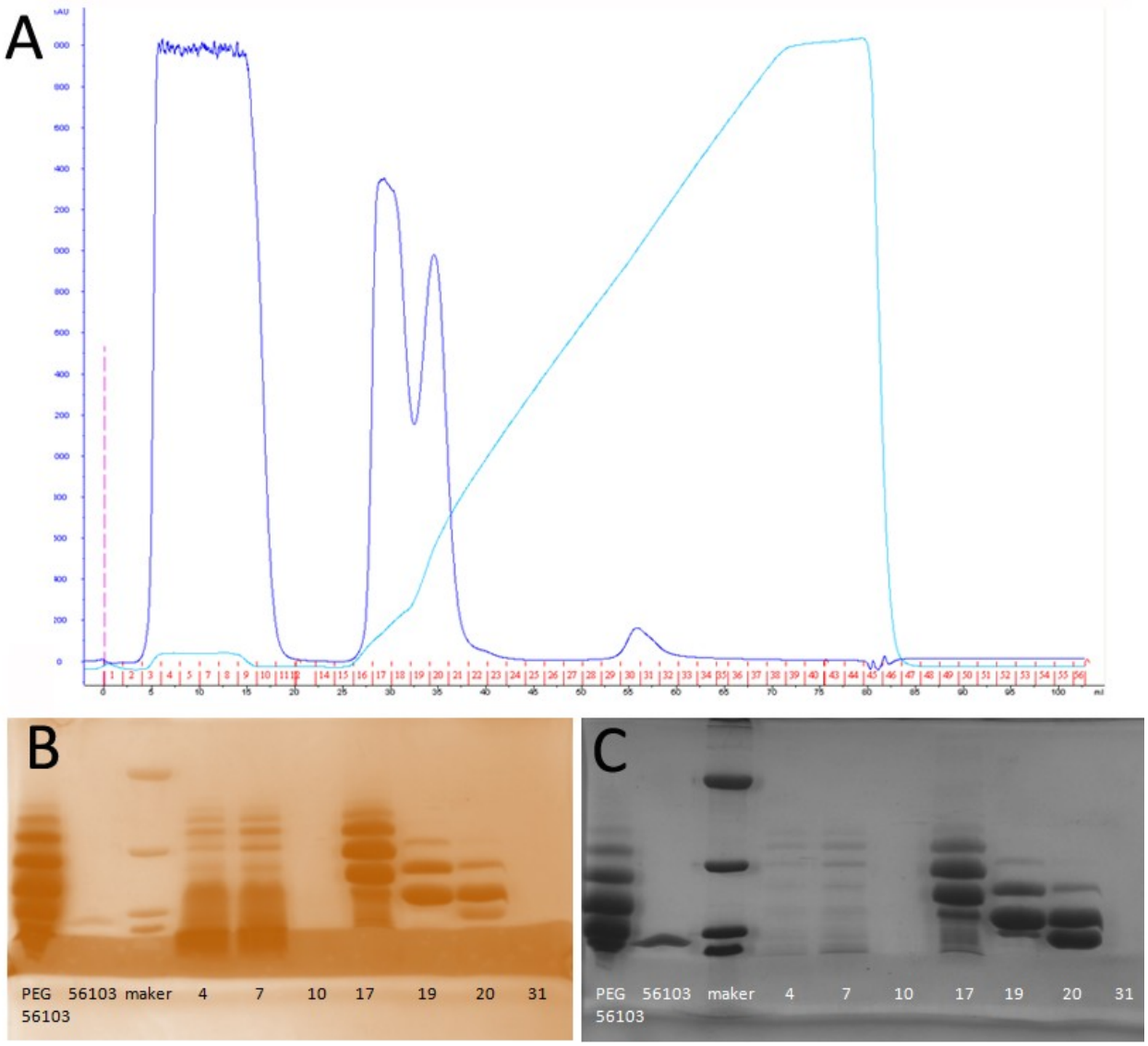

Figure 9-2. FLPC separation of PEGlyated ProCA3 variants.

The FPLC fractions were analysised by UV detector equipped in FPLC (A), SDS-PAGE by I_2 staining (B) and coomassie brilliant blue staining (C).

9.2.2 Humanization of ProCA3 variants

Since our final goal is to apply our designed ProCA in clinical, it is extremely important to avoid immunogenicity. One strategy to avoid immunogenicity is humanization of the designed protein. The original ProCA3 is derived from rat PV, and there are 9 residues differences between human and rat PV (Fig. 9-3). Among these 9 residues, only 1 residue is located on our engineer metal binding sites.

The DNA of Humanized ProCA32 was synthesized and incorporated in pBluescript plasmid by DNA synthesis. Nde I and Xho I cleavage sequences were designed at 5' and 3' terminal of ProCA32 DNA. The plasmid was amplified by E. coli DH5α strain. Humanized ProCA32 was digested by Nde I and Xho I and then inserted into PET22b vector. DNA sequencing results shows that humanized ProCA32 were inserted into pET22b vector.

Next, we will express, purify humanized ProCA32 and test its *in vitro* and *in vivo* properties such as relaxivity, metal binding affinity and selectivity. We will further evaluate its properties for MRI.

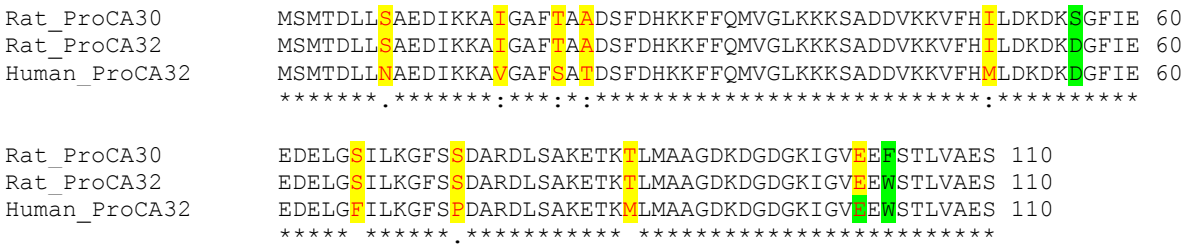

Figure 9-3. Protein sequence alignment between rat_ProCA30, rat_ProCA32 and humanized ProCA32.

Amino acids with red letter and yellow highlights indicate the amino acid difference btween human and rat ProCA32. Amino acids with green highlights indicate the key mutations in rat and human ProCA32 to improve the Gd^{3+} binding affinity.

9.2.3 Large scale expression and purification of ProCA3 variants

To study the MRI properties of ProCA3 for larger animals and applications of ProCAs in various diseases, a good manufacturing practice (GMP)-like method with high efficiency, high repeatability and low cost for ProCA3 expression and purification are highly required. However, the current expression, purification cannot meet such requirement. A GMP-like methods should be low cost, and should be able to scale up without modification of the protocols. In cooperate with Dr. Pierce at Georgia State University, we established the GMP-like protocol for the large scale expression and purification of ProCA3 variants.

9.2.3.1 Large scale expression of ProCA3 by fermentation.

To large scale expression of ProCA3, ProCA32 DNA was first transformed in BL21-DE3-plysS bacteria. ProrCA3 expressing cells were adapted to ECAM media from LB medium. 1 ml of a glycerol stock of ProCA32 expressing bacteria were then transferred to 100 ml ECAM and shake over night at 37 ˚C at 150 rpm. 10 ml of the culture was transferred to 250 ml ECAM medium and incubate at 37 ˚C and 200 rpm for 6 hours. 120 ml of these bacteria were used as an inoculum for the bioreactor.

The bioreactor were setup as follows: Initial glucose concentration 21g/L ; Batch media contained 50ug/ml carbenicillin; Vessel was inoculated to give $1.5x10^{-2}$ cells ; oxygen conenctration was set to 30% and maintained with stirrer (min= 160 rpm, max = 450 rpm) and Gas Mix; Air flow was constant at 10LPM.

Table 9-1 and Fig. 9-4 show the fermentation conditions during ProCA32 expression in bioreactor. The pH, temperature, oxygen level were kept constant during ProCA32 expression. The oxygen level was controlled by adjusting the speed of stirrer. 0.5 mM IPTG were added

when OD (AU) value reached 38. As show from Fig. 9-5, ProCA32 were expressed 1-3 hours after IPTG induction. The bacteria were harvest by Carr Powerfuge and the final yield is about 1000 g bacteria pellet from 12 liters of media.

Table 9-1. Fermentation data during ProCA32 expression in bioreactor*.

Time	pH	T (˚C)	dO_2	Air Flow (LPM)	Stir-rer(rpm)	[G] g/L	Feed rate (ml/min)	OD (AU) Spec
13:96	6.88	30.1	29.8	10.5	438	5	0	16
14:30	7:03	30		10.5	289	0	10	
14:94	6.89	30	23.4	10.5	459	0	14	
15.39	7.00	30	53.2	10.5	360	0	18	35
16.63 (I)	7.09	30	29	10.5	449	0	18	38
17.69	6.95	29.9	33.7	10.5	396	0	18	42
18.69	6.92	30	29.7	10.5-11.14	402	0	18	48
19.90	6.92	30	29	9.67-15.81	459	0	18	56

* Data were collected by Trudy and Yaoyao from Dr. Pierce's lab at GSU.

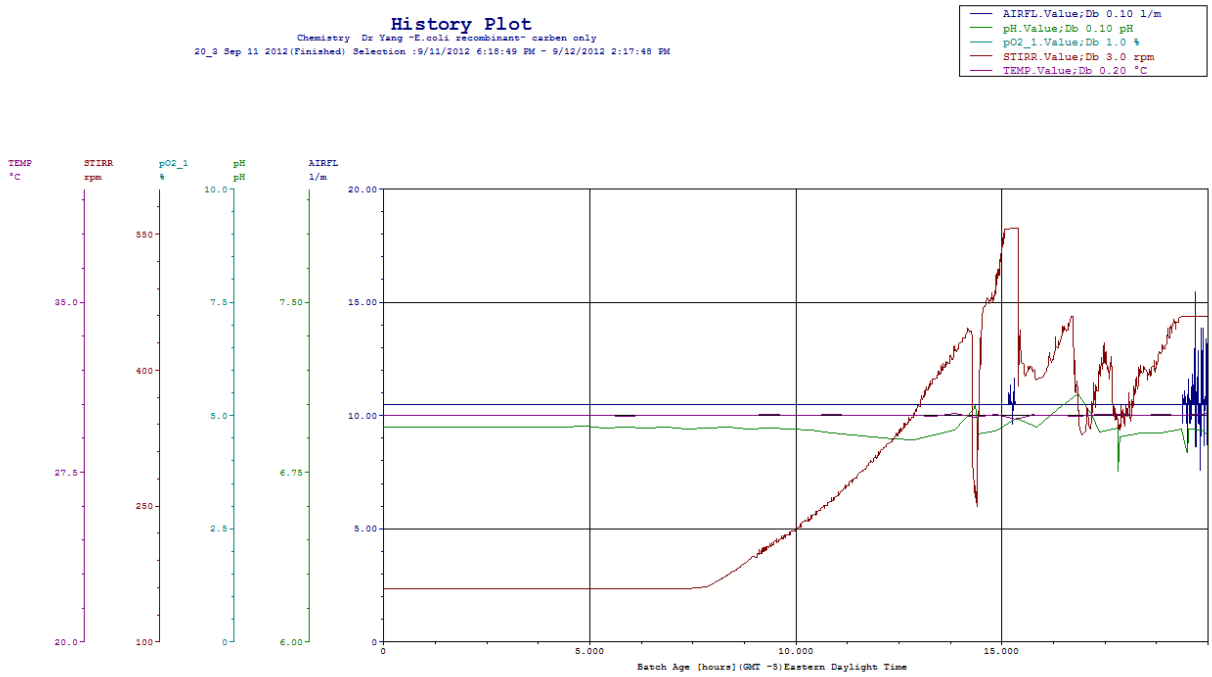

Figure 9-4. Fermentation data during ProCA32 expression in bioreactor.

Difference color shows the real time conditions of temperature, oxygen level, pH, air flow, stir rate and glucose level in the bioreactor.

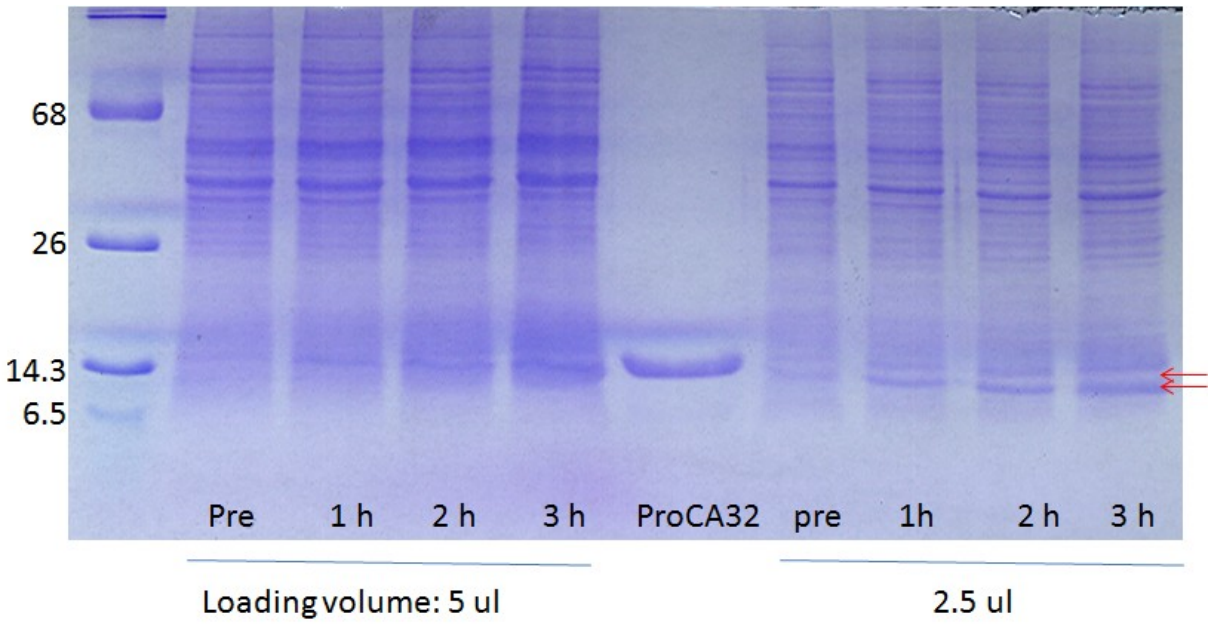

Figure 9-5. ProCA32 expression by fermentation.

No ProCA expessed before IPTG induction. ProCA32 with a molecular weight of 11 kDa pointed by arrows were expressed 1 hour post IPTG induction and highest level of ProCA32 expression can be found 3 hour post IPTG induction.

9.2.3.2 Explore the methods for large scale purification of ProCA3 by fermentation.

To ensure the production of same quality of protein, a method for large scale purification of ProCA3 variants is highly required. Such method must be easily adapted to the GMP-like system without change of the protocol. This method should also cost less. With the help from Fengkun Du from Dr. Peirce's lab at GSU, we established a new purification methods with less cost and ability to purify huge amount of protein.

Figure 4-6 shows our procedure of the new protocol for the protein purification. In brief, different concentration of PEG-8000 was added to the supernatant of the cell lysate. Due to the differences of the solubility and molecular weight, different proteins will be precipitated at different concentration of PEG-8000. The concentration of PEG-8000 for ProCA32 precipitation were determined by SDS-PAGE.

As shown from Fig. 9-7, the majority of junk proteins were precipitated at PEG-8000 concentration below 250 mg/l. ProCA32 was mainly precipitated at PEG-8000 concentration between 250 and 400 mg/l. However, only about 80 % purity of ProCA32 was achieved after PEG-8000 precipitation.

We then use FPLC to further purify this protein. ProCA32 precipitate by PEG-8000 was dissolved in HEPES buffer at pH 7.0. These protein solution were load to Hi-trap Q column. After binding to the column, the unbounded components were first washed out with 7 column volume (CV) of buffer A (10 mM HEPES buffer at pH 8.0). Then, buffer B (10 mM HEPES buffer, 1 M NaCl at pH 8.0) concentration were increase to 25 % within 7 CV. We further wash the column with 25% of buffer B for 2 CV and then increase to 100 % of buffer B of 1 CV to wash out every component bounded to the column. At last, the column were requilibrium with 100% buffer A

for 5 CV. As show from Fig. 9-8 ProCA32 was eluted from peak 20-24 and peak 37-33 with improved the purity. Other peaks contain unwanted protein and/or DNA.

At last, since ProCA32 is very stable at 90 ˚C, we further incubate the purified ProCA32 at 90 ˚C for 20 min and followed by a centrifugation at 6000 rpm for 30 min to remove residue from final products. As shown from Fig. 9-7, above 99% purity of ProCA32 were achieved after this step. Therefore, an efficient method for large scale purification of ProCA32 was established. We will further compare the in vitro and in vivo properties of ProCA32 purified from different purification methods.

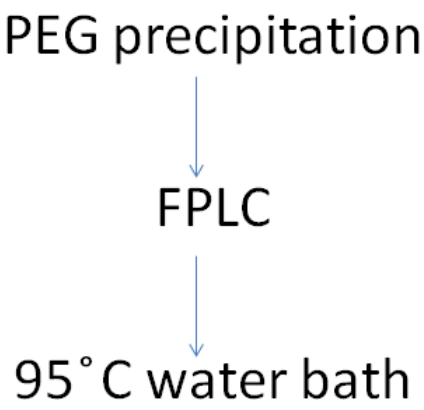

Figure 9-6. New procedure for the ProCA32 purification.

After lysate the cell, different concentration of PEG-8000 was added to the supernatant of the cell lysate. Due to the differences of the solubility and molecular weight, proteins and other bi-omolecules will be predicated at different concentration of PEG-8000. The concentration range of PEG-8000 for ProCA32 precipitation was determined by SDS-PAGE. We further use FPLC to purify ProCA32. At last, FPLC fractions with ProCA32 elution were incubated at 95˚C water bath for 10-20 min followed by centrifugation to further remove unwanted proteins.

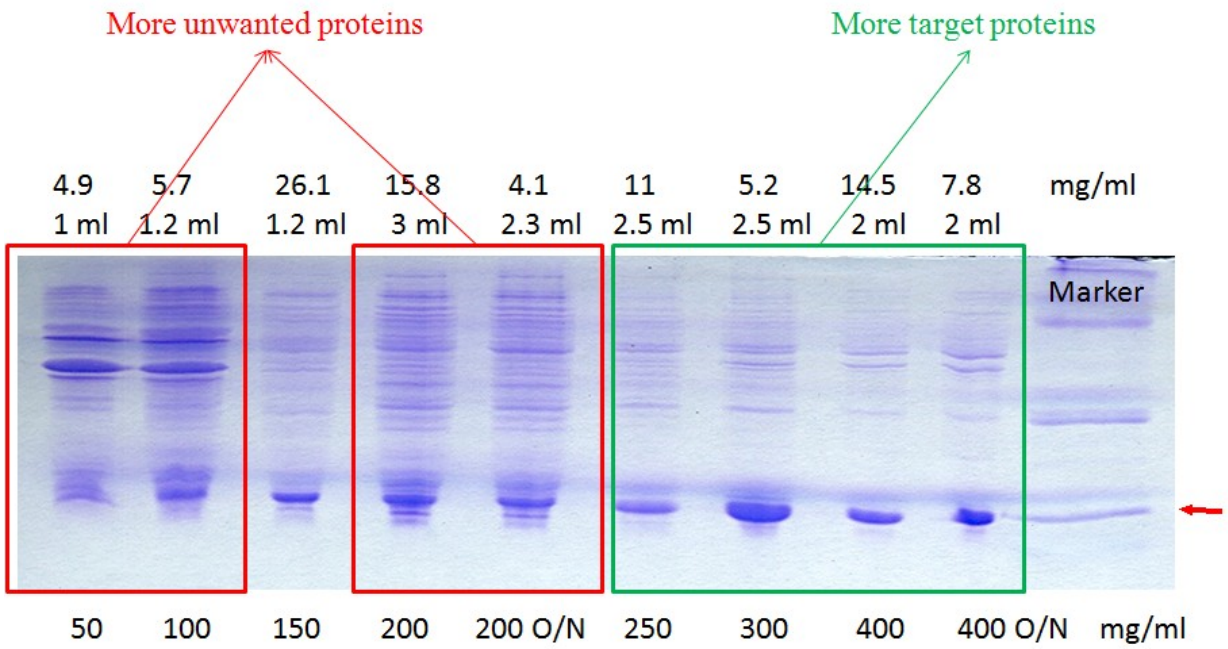

Figure 9-7. ProCA32 purification by PEG precipation.

Red arraw indicate the position of ProCA32 on SDS-PAGE. The majority of junk proteins were precipitated at PEG-8000 concentration below 250 mg/l. ProCA32 was mainly precipitated at PEG-8000 concentration between 250 and 400 mg/l. However, only about 80 % purity of ProCA32 were achieved after PEG-8000 precipitation.

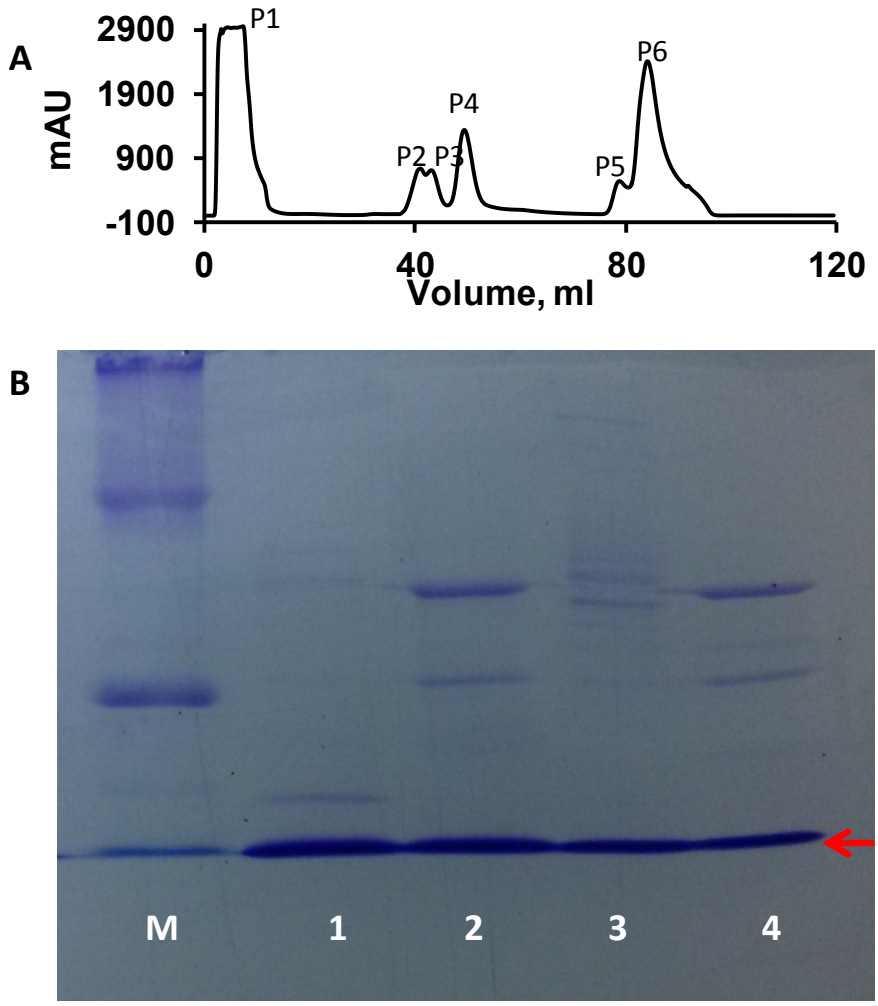

Figure 9-8. FPLC purification of ProCA32 after PEG separation.

A. After injection, 6 peaks, marked as P1, P2, P3, P4, P5 and P6 were eluted out of from HiTrap-Q colume under different concentration of buffer B (10 mM HEPES, 1 M NaCl at pH 8.0). B. SDS-PAGE analysis of each peaks eluted out from Q column. M: marker; 1. fraction P2 and heat at 95˚C for 10 min; 2. Fraction P5 and heat at 95˚C for 10 min 3. fraction P2 without heat; 4. fraction P4 without heat.

9.3 Discussion

9.3.1 PEGlytion

PEGlytion greatly improved the solubility and decrease the immunogenicity of the protein drugs. PEGlytion on ProCA1 also increase the relaxivity by optimizing water numbers and exchange rate of Gd^{3+}. Using the similar procedure, we modified the ProCA3 variants with PEG-40. To our surprise, the PEGlytated and Gd^{3+}-loaded ProCA3 can be concentrated as high as 8 mM without precipitation.

In our study, we use PEG-40-NHS ester to react with lysine residues of ProCA3. By our conjugation methods, we can conjugate 1-4 PEG-40 into ProCA3. Since the molecular weight of each PEG-40 is about 2.4 kDa, the total molecular weight of PEGlytated ProCA3 is between 13.4 - 20.6 kDa. A protein with a molecular weight less than 60 kDa can easily filtered by the xx cells in kidney. Therefore, PEGlytated ProCA3 should be excreted through kidney. We are also interested to test the changes of relaxivity in ProCA3 after PEGlytion.

ProCA3 has 16 lysine residues. Therefore, it is very hard to control the numbers of PEG being conjugated and it is also very hard conjugate PEG at specific lysine residue. An alternative way is to conjugate PEG at Cys. We added a Cys at the C terminal of ProCA3 variants. We will specifically conjugate PEG to this ProCA3 variants through the interaction between SH group and maleimide group in PEG.

The length and number of conjugated PEG are closely related with *in vitro* and *in vivo* properties of ProCA3, such as relaxivity, blood retention time, excretion, and tumor tissue penetration. We will further optimize our conjugation protocols such as the conjugation ratio, residues and size of PEG to optimize the *in vitro* and *in vivo* properties of ProCA3.

9.3.2 Humanization of ProCA3

Humanization is another important method for us to further reduce the immunognecity of ProCA3. ProCA3 is derived from rat PV with several mutations on the metal binding sites. The human PV sequence, however, has 9 amino acid differences from rat PV. Thus, to further reduce the immunogenicity, we synthesized the human ProCA3 DNA and inserted this human ProCA3 DNA in the pET22b vector for protein expression in *E. coli*.

Our next step is to express and purify the humanized ProCA3 from bacteria and test the *in vitro* and *in vivo* properties of humanized ProCA3. We will measure the metal binding affinity, metal selectivity, relaxivity, serum stability, immunogenicity of humanized ProCA3 and compare the differences between rat ProCA3 and human ProCA3. Since these is no protein sequence differences on the Gd^{3+} binding sites between human and rat ProCA3, we expect that the metal binding affinity, metal selectivity and relaxivity of human ProCA3 are the same as rat ProCA3. Due to the amino acid differences, human ProCA3 should have better *in vivo* properties.

9.3.3 Large scale expression and purification of ProCA3

The expression of ProCA32 by LB medium with constant shaking is time consuming and low efficient. Only about 5 g of bacteria pellets can be obtained from 1 liter LB media. Using fermentation methods, about 1000g bacteria pellets were expressed from 12 liter medium with continuous feeding of glucose, which is about 15 times higher yield than that of LB medium with constant shaking. SDS-PEGE results show that ProCA3 are highly expressed in this bioreactor. Thus, we could obtain 15 time higher amount of ProCA3 using fermentation within two days. Moreover, such GMP-like fermentation methods can be easily scale up to the bioreactor

with much larger the culture volume. Such unique feature made this new method easily applied for the large scale expression of ProCA3 in the factory.

The previously ProCA3 purification methods includs heating and dialysis steps. Such steps cannot be applied for ProCA3 purification when the sample volume increases. In our new purification methods, ProCA3 and different unwanted proteins were precipitated at different concentration PEG, ProCA3 and small amount of unwanted were precipitated when the PEG concentration reaches 250 mg/ml. We then dissolve the precipitated ProCA3 fraction in buffers and further purify this protein by FPLC. In principal, this new purification procedure can be applied to the large scale purification ProCA3.

9.4 Conclusion

In this chapter, the ProCA3 is optimized by PEGlytion and humanization. A protocol for PEGlyation and GMP-like expression and purification of ProCA3 was established. This expression of ProCA3 using fermentation method shows more than 20 times high yield of the protein expression.

We also successfully established GMP-like mehod for protein purification. This new established method use PEG to precipate ProCA3 and then further purified by FPLC Qcolumn. This new method does not have limitation for scale up, because all the limitation factor for large scale purification such as dialysis and high temperature incubation.Thus, we are able to produce ProCA3 with fewer costs and we could potentially also decrease the immunogenicity of ProCA3.

We further compared the *in vitro* and *in vivo* properties between humanized ProCA3 and rat ProCA3. Our preliminary data of UV, fluorescen, NMR and Tb^{3+} binding assay shows that

there are no differences in the protein structures and metal binding of proteins purified from traditional methods in Chapter 3 and new methods in Chapter 9.

In addition, we constructed the human sequence of ProCA32 by DNA synthesis. We will express, purify and test its *in vitro* and *in vivo* properties of the humanized ProCA32 in the near future.

10 MAJOR DISCOVERY AND SIGNIFICANCE

As discussed in Chapter 1, the current application of MRI with advangae of non-invasive and depth tissue penetration without using radiation are largely due to the limitations of available MRI contrast agent especially low relaxivity assocated with low sensitivity and specificity and unble to apply for molecular imaging in vivo. In the past 10 years, our lab developed a novel class of MRI contrast agents using protein as Gd^{3+} chelator. The protein-based MRI contrast agents (ProCAs) have more than 10 times higher r_1 and r_2 relaxivity than that of clinical MRI contrast agents. Such high relaxivity improves the dose efficiency *in vivo*. In addition, because of the high relaxivity and longer blood rention time, the targeted ProCA1 variants can be applied for molecular imaging of biomarker using MRI for the cancer diagnosis. However, the metal stability and metal selectivity of the first generation of ProCA needs to be improved for in vivo application. In our effort in improving metal binding affinity and addition of multiple binding sites for the first generation of contrast agent, we encoured problems associated with limited solubility and protein stability. The large scale of protein production as well as the application of ProCAs for the diagnosis has not been fully explored.

In my Ph.D. dissertation studies detailed in Chapters 2 to 9, I have developed a novel class of MRI contrast agents, ProCA3 series, by protein engineering in collaboration with collabrators and team members to address the pressing needs for better MRI contrast agents. Various techniques have been applied to answer several key questions in developing new types of contrast agents:

1). Can we develp a new generation of MRI contrast agents with multiple Gd^{3+} binding sites? 2). Can we improve the metal stablity and metal selectivity of ProCA so that we can prevent the

Gd^{3+} resease in vivo? 3). Can we tune the relaxivities of ProCAs by protein design? 4). Can we design MRI contrast agents for liver imaging? 5). How early the metastatic tumor can be detected by MRI? 6). What is the smallest size of tumors can be detected? 7). Can we improve accuracy and specificity of tumor detection by taking advantage of both r_1 and r_2 values of ProCAs?

We developed a novel class of MRI contrast agents, ProCA3 series, by protein engineering. By introducing single mutation S56D in EF-hand I of PV, the Gd^{3+} binding affinity increase more than 10^{10} fold, while the binding affinity to physiological metal ions, such as Ca^{2+} and Zn^{2+}, only has less than 10 fold increases. This is the first study shows that Gd^{3+} binding affinity can be improved 10^{10} fold by single mutation with highly desired metal selectivities. We also developed a novel method to measure Gd^{3+} binding affinity of contrast agents with controlled Tb^{3+}-DTPA buffer system. Using this metal-chelator system, the free Gd^{3+} concentration can be accurately controlled between 10^{-23} and 10^{-17} M. The Gd^{3+} binding affinity measured by this novel approach, 2.79×10^{-22} M, is the reported lowest Gd^{3+} binding affinity in the literature (Chapter 4).

By protein design, we are also able to control the relaxivity of protein contrast agents. A single mutation E60D from ProCA32 increases the per Gd r_1 relaxivity from 30 $mM^{-1}s^{-1}$ to 59 $mM^{-1}s^{-1}$. We further demonstrated that such robust increase of relaxivity is caused by introducing additional water ligand interaction to the designed MRI contrast agents (Chapter 4).

Due to high relaxivity, ProCA3 has detection limits of 2 μM, which is 15 times higher than the reported detection limit of clinical MRI contrast agents.[10] Considering such high relaxivity, we are able to imaging kidney with an injection dosage of 60 fold lower than the clinical injection dosage of Magnevist (0.1-0.2 mmol/kg) (Chapter 5).

We demonstrated that non-targeted ProCA3 can be applied for the imaging of blood vessel, liver and kidney with about 10 times lower injection dosage than that of clinical MRI contrast agents. By both T_1-weighted and T_2-weighted MRI, ProCA3 variants are able to image liver metastases of uveal melanoma with a size less than 0.25 mm, while current clinical approach can only detect tumors with high confidence with a size larger than 1 – 2 centimeters. (Chapter 5) ProCA3 variants also has a lot of advantage to be applied to the dynamic contrast enhanced MRI (Chapter 6).In addition, we developed bi-briliant dualweighted imaging methodology, which utilizes both high r_1 and r_2 properties of our contrast agents for the improvement signal differences between tumor and liver. Our work opens a new avenue for the early diagnostics of tumor metastases to liver, and has great influence for the tumor early detection and treatment. Our work also demonstrate that targeted ProCA3 variants can be applied to semi-quantitative evaluation of tumor biomarkers using MRI, and targeted ProCA3 variants have great potential to detect tumor and evaluate tumor progression and facilitate personalized medicine for tumor treatment.

We also show that ProCA3 has longer blood circulation time, which made more easy and quantitative to accurately measure AIF. In addition, we are able to calculate ProCA3 concentration in different tissues based on the DCE-MRI data and T_1 map. These features made ProCA3 as the ideal candidate for evaluate tumor vasculature, renal perfusion by DCE-MRI. (Chapter 6)

In this work, we demonstrate that ProCA3 shows excellent safety profile and pharmacokinetics for MRI imaging. ProCA3 has no toxicity to cells and mice. With the lower dose of injection, ProCA3 shows less Gd^{3+} accumulation than $GdCl_3$ and Gd-DTPA in the natural Gd^{3+} biodeposit organs, such as liver, spleen, lung and bone. Our safety and pharmacokinetics stud-

ies will facilitate the clinical application of ProCA3 for the early diagnostics of cancer. (Chapter 7)

We developed tumor specific MRI contrast agents for the molecular imaging of tumor biomarkers. These novel targeted ProCA3s variant can binds to biomarkers such as GRPR, HER-2 and integrin $\alpha_v\beta_3$ with high specificity and targeted ProCA3 has great potential to detect tumor location, tumor size, evaluate tumor progression by semi-quantitavie (Chapter 8)

We also successfully established GMP-like mehod for protein purification. This new method does not have limitation for scale up, because all the limitation factor for large scale purification such as dialysis and high temperature incubation.Thus, we are able to produce ProCA3 with fewer costs and we could potentially also decrease the immunogenicity of ProCA3. In addition, we constructed the human sequence of ProCA32 by DNA synthesis. These effects pave the way for the potential clinical application of ProCA3 variants for MRI diagnosis.

The development of designed contrast agents and *in vivo* imaging methodology is expected to significantly improve sensitivity and specificity for liver tumor imaging. It enables non-invasive early detection primary liver tumors and metastatic tumors at 0.1 mm from the current threshold of 20 mm or larger. Such improvement will greatly facilitate the development of proper treatment strategies, such as liver transplantation or locoregional treatment. It will significantly increase the accuracy of image-guided biopsies and regional treatment. Hence, This work will bring improvement to a large segment of the patients afflicted with HCC or metastatic liver malignancy. Finally, the reagents developed in this application could have far-reaching implications in the diagnosis of other malignancies, which in turn would facilitate development of targeted treatment along with effective monitoring of reduction of tumor burden.

REFERENCES

1. Meade, T.J., Taylor, A.K. & Bull, S.R. New magnetic resonance contrast agents as biochemical reporters. *Curr Opin Neurobiol* **13**, 597-602 (2003).
2. Artemov, D. Molecular magnetic resonance imaging with targeted contrast agents. *J Cell Biochem* **90**, 518-524 (2003).
3. Cheng, L.L., Chang, I.W., Louis, D.N. & Gonzalez, R.G. Correlation of high-resolution magic angle spinning proton magnetic resonance spectroscopy with histopathology of intact human brain tumor specimens. *Cancer Res* **58**, 1825-1832 (1998).
4. Jones, R.A. et al. Magnetic resonance imaging evaluation of renal structure and function related to disease: technical review of image acquisition, postprocessing, and mathematical modeling steps. *J Magn Reson Imaging* **33**, 1270-1283 (2011).
5. Gore, J.C., Manning, H.C., Quarles, C.C., Waddell, K.W. & Yankeelov, T.E. Magnetic resonance in the era of molecular imaging of cancer. *Magn Reson Imaging* **29**, 587-600 (2011).
6. Partridge, S.C. et al. Accuracy of MR imaging for revealing residual breast cancer in patients who have undergone neoadjuvant chemotherapy. *AJR Am J Roentgenol* **179**, 1193-1199 (2002).
7. Wang, Z., Su, M.Y. & Nalcioglu, O. Applications of dynamic contrast enhanced MRI in oncology: measurement of tumor oxygen tension. *Technol Cancer Res Treat* **1**, 29-38 (2002).
8. Mueller, G.C., Hussain, H.K., Carlos, R.C., Nghiem, H.V. & Francis, I.R. Effectiveness of MR imaging in characterizing small hepatic lesions: routine versus expert interpretation. *AJR Am J Roentgenol* **180**, 673-680 (2003).
9. Major, J.L. & Meade, T.J. Bioresponsive, cell-penetrating, and multimeric MR contrast agents. *Acc Chem Res* **42**, 893-903 (2009).
10. Caravan, P. Strategies for increasing the sensitivity of gadolinium based MRI contrast agents. *Chem Soc Rev* **35**, 512-523 (2006).
11. Nonat, A. et al. Gadolinium(III) complexes of 1,4,7-triazacyclononane based picolinate ligands: simultaneous optimization of water exchange kinetics and electronic relaxation. *Dalton Trans*, 8033-8046 (2009).
12. Weinmann, H.-J., Ebert, W., Misselwitz, B. & Schmitt-Willich, H. Tissue-specific MR contrast agents. *European journal of radiology* **46**, 33-44 (2003).
13. Frydrychowicz, A. et al. Hepatobiliary MR imaging with gadolinium-based contrast agents. *J Magn Reson Imaging* **35**, 492-511 (2012).
14. Robinson, P.J. Imaging liver metastases: current limitations and future prospects. *Br J Radiol* **73**, 234-241 (2000).
15. Weiss, C.R., Nour, S.G. & Lewin, J.S. MR-guided biopsy: a review of current techniques and applications. *J Magn Reson Imaging* **27**, 311-325 (2008).
16. Joffe, P., Thomsen, H.S. & Meusel, M. Pharmacokinetics of gadodiamide injection in patients with severe renal insufficiency and patients undergoing hemodialysis or continuous ambulatory peritoneal dialysis. *Acad Radiol* **5**, 491-502 (1998).
17. Clarkson, R.B. Blood-pool MRI contrast agents: Properties and characterization. *Top Curr Chem* **221**, 201-235 (2002).
18. Wedeking, P. et al. Quantitative dependence of MR signal intensity on tissue concentration of Gd(HP-DO3A) in the nephrectomized rat. *Magn Reson Imaging* **10**, 97-108 (1992).
19. Sadowski, E.A. et al. Nephrogenic systemic fibrosis: risk factors and incidence estimation. *Radiology* **243**, 148-157 (2007).
20. Swaminathan, S. & Shah, S.V. New insights into nephrogenic systemic fibrosis. *J Am Soc Nephrol* **18**, 2636-2643 (2007).

21. Gibby, W.A. & Gibby, K.A. Comparison of Gd DTPA-BMA (Omniscan) versus Gd HP-DO3A (ProHance) retention in human bone tissue by inductively coupled plasma atomic emission spectroscopy. *Invest Radiol* **39**, 138-142 (2004).
22. Prince, M.R., Zhang, H.L., Prowda, J.C., Grossman, M.E. & Silvers, D.N. Nephrogenic systemic fibrosis and its impact on abdominal imaging. *Radiographics* **29**, 1565-1574 (2009).
23. Grobner, T. Gadolinium--a specific trigger for the development of nephrogenic fibrosing dermopathy and nephrogenic systemic fibrosis? *Nephrol Dial Transplant* (2006).
24. Thomsen, H.S., Morcos, S.K. & Dawson, P. Is there a causal relation between the administration of gadolinium based contrast media and the development of nephrogenic systemic fibrosis (NSF)? *Clin Radiol* **61**, 905-906 (2006).
25. Bellin, M.F. MR contrast agents, the old and the new. *Eur J Radiol* **60**, 314-323 (2006).
26. Adzamli, K., Periasamy, M.P., Spiller, M. & Koenig, S.H. NMRD assessment of Gd-DTPA-bis(methoxyethylamide), (Gd-DTPA-BMEA), a nonionic MRI agent. *Invest Radiol* **34**, 410-414 (1999).
27. Kirchin, M.A. & Runge, V.M. Contrast agents for magnetic resonance imaging: safety update. *Top Magn Reson Imaging* **14**, 426-435 (2003).
28. Laurent, S., Elst, L.V. & Muller, R.N. Comparative study of the physicochemical properties of six clinical low molecular weight gadolinium contrast agents. *Contrast media & molecular imaging* **1**, 128-137 (2006).
29. Villaraza, A.J., Bumb, A. & Brechbiel, M.W. Macromolecules, dendrimers, and nanomaterials in magnetic resonance imaging: the interplay between size, function, and pharmacokinetics. *Chem Rev* **110**, 2921-2959 (2010).
30. Cacheris, W.P., Quay, S.C. & Rocklage, S.M. The relationship between thermodynamics and the toxicity of gadolinium complexes. *Magn Reson Imaging* **8**, 467-481 (1990).
31. Kumar, K., Tweedle, M.F., Malley, M.F. & Gougoutas, J.Z. Synthesis, Stability, and Crystal-Structure Studies of Some Ca2+, Cu2+ and Zn2+ Complexes of Macrocyclic Polyamino Carboxylates. *Inorg. Chem.* **34**, 6472-6480 (1995).
32. Lauffer, R.B. et al. MS-325: albumin-targeted contrast agent for MR angiography. *Radiology* **207**, 529-538 (1998).
33. Caravan, P. Protein-targeted gadolinium-based magnetic resonance imaging (MRI) contrast agents: design and mechanism of action. *Acc Chem Res* **42**, 851-862 (2009).
34. Choi, H.S. et al. Renal clearance of quantum dots. *Nat Biotechnol* **25**, 1165-1170 (2007).
35. Goel, A. et al. Genetically engineered tetravalent single-chain Fv of the pancarcinoma monoclonal antibody CC49: improved biodistribution and potential for therapeutic application. *Cancer Res* **60**, 6964-6971 (2000).
36. Olmsted, S.S. et al. Diffusion of macromolecules and virus-like particles in human cervical mucus. *Biophys J* **81**, 1930-1937 (2001).
37. Lund, U. et al. Glomerular filtration rate dependence of sieving of albumin and some neutral proteins in rat kidneys. *Am J Physiol Renal Physiol* **284**, F1226-1234 (2003).
38. Toth, E., Helm, L. & Merbach, A.E. in Contrast Agents I: Magnetic Resonance Imaging, Vol. 221. (ed. W. Krause) 61-102 (Springer-Verlag, New York; 2002).
39. Solomon, I. Relaxation Processes in a System of Two Spins. *Phys. Rev.* **99**, 559–565 (1955).
40. Bloembergen, N. Proton Relaxation Times in Paramagnetic Solutions. *J. Chem. Phys.* **27**, 572-573 (1957).
41. Caravan, P., Farrar, C.T., Frullano, L. & Uppal, R. Influence of molecular parameters and increasing magnetic field strength on relaxivity of gadolinium- and manganese-based T1 contrast agents. *Contrast media & molecular imaging* **4**, 89-100 (2009).

42. Bloembergen, N. & Morgan, R. Theory of proton relaxation by Mn2+ ions in solution. *The J. Chem. Phys.* **34**, 842 (1961).
43. McLachlan, A.D. Line Widths of Electron Resonance Spectra in Solution. *Proceedings of the Royal Society of London A* **280**, 271-288 (1964).
44. Helm, L. Optimization of gadolinium-based MRI contrast agents for high magnetic-field applications. *Future Med Chem* **2**, 385-396 (2010).
45. De Leon-Rodriguez, L.M. et al. Responsive MRI agents for sensing metabolism in vivo. *Acc Chem Res* **42**, 948-957 (2009).
46. Aime, S., Castelli, D.D., Crich, S.G., Gianolio, E. & Terreno, E. Pushing the sensitivity envelope of lanthanide-based magnetic resonance imaging (MRI) contrast agents for molecular imaging applications. *Acc Chem Res* **42**, 822-831 (2009).
47. Doble, D.M. et al. Optimization of the relaxivity of MRI contrast agents: effect of poly(ethylene glycol) chains on the water-exchange rates of Gd(III) complexes. *J Am Chem Soc* **123**, 10758-10759 (2001).
48. Raymond, K.N. & Pierre, V.C. Next generation, high relaxivity gadolinium MRI agents. *Bioconjug Chem* **16**, 3-8 (2005).
49. Werner, E.J., Datta, A., Jocher, C.J. & Raymond, K.N. High-relaxivity MRI contrast agents: where coordination chemistry meets medical imaging. *Angew Chem Int Ed Engl* **47**, 8568-8580 (2008).
50. Garcia-Martin, M.L. et al. High resolution pH(e) imaging of rat glioma using pH-dependent relaxivity. *Magn Reson Med* **55**, 309-315 (2006).
51. Caravan, P., Astashkin, A.V. & Raitsimring, A.M. The gadolinium(III)-water hydrogen distance in MRI contrast agents. *Inorg Chem* **42**, 3972-3974 (2003).
52. Astashkin, A.V., Raitsimring, A.M. & Caravan, P. Pulsed ENDOR study of water coordination to Gd3+ complexes in orientationally disordered systems. *J Phys Chem A* **108**, 1990-2001 (2004).
53. Lauffer, R.B. Paramagnetic metal complexes as water proton relaxation agents for NMR imaging: theory and design. *Chem. Rev.* **87**, 901–927 (1987).
54. Kowalewski, J., Kruk, D. & Parigi, G. in Advances in Inorganic Chemistry, Vol. Volume 57 41-104 (Academic Press, 2005).
55. Helm, L. Relaxivity in paramagnetic systems: Theory and mechanisms. *Progress in Nuclear Magnetic Resonance Spectroscopy* **49**, 45-64 (2006).
56. Aime, S. et al. Ternary Gd(III)L-HSA adducts: evidence for the replacement of inner-sphere water molecules by coordinating groups of the protein. Implications for the design of contrast agents for MRI. *J Biol Inorg Chem* **5**, 488-497 (2000).
57. Aime, S. et al. A paramagnetic probe to localize residues next to carboxylates on protein surfaces. *J Biol Inorg Chem* **7**, 617-622 (2002).
58. Bennett, H., Brown, R., Koenig, S. & Swartz, H. Effects of nitroxides on the magnetic field and temperature dependence of 1/T1 of solvent water protons. *Magn Reson Med.* **4**, 93-111 (1987).
59. Hwang, L. & Freed, J.H. Dynamic effects of pair correlation functions on spin relaxation by translational diffusion in liquids. *Journal of Chemical Physics* **63**, 4017-4025 (1975).
60. Freed, J.H. Dynamic effects of pair correlation functions on spin relaxation by translational diffusion in liquids II. Finite jumps and independent T1 processes. *Journal of Chemical Physics* **68**, 4034-4037 (1978).
61. Caravan, P., Greenfield, M.T., Li, X. & Sherry, A.D. The Gd(3+) complex of a fatty acid analogue of DOTP binds to multiple albumin sites with variable water relaxivities. *Inorg Chem* **40**, 6580-6587 (2001).
62. Lauffer, R.B. & Brady, T.J. Preparation and water relaxation properties of proteins labeled with paramagnetic metal chelates. *Magn Reson Imaging* **3**, 11-16 (1985).

63. Wikstrom, M.G. et al. Contrast-enhanced MRI of tumors. Comparison of Gd-DTPA and a macromolecular agent. *Invest Radiol* **24**, 609-615 (1989).
64. Brasch, R. et al. Assessing tumor angiogenesis using macromolecular MR imaging contrast media. *J Magn Reson Imaging* **7**, 68-74 (1997).
65. Karfeld-Sulzer, L.S., Waters, E.A., Davis, N.E., Meade, T.J. & Barron, A.E. Multivalent protein polymer MRI contrast agents: controlling relaxivity via modulation of amino acid sequence. *Biomacromolecules* **11**, 1429-1436 (2010).
66. Song, Y., Kohlmeir, E.K. & Meade, T.J. Synthesis of multimeric MR contrast agents for cellular imaging. *J Am Chem Soc* **130**, 6662-6663 (2008).
67. Bryant, L.H., Jr., Jordan, E.K., Bulte, J.W., Herynek, V. & Frank, J.A. Pharmacokinetics of a high-generation dendrimer-Gd-DOTA. *Acad Radiol* **9 Suppl 1**, S29-33 (2002).
68. Bryant, L.H., Jr. et al. Synthesis and relaxometry of high-generation (G = 5, 7, 9, and 10) PAMAM dendrimer-DOTA-gadolinium chelates. *J Magn Reson Imaging* **9**, 348-352 (1999).
69. Kobayashi, H. & Brechbiel, M.W. Dendrimer-based nanosized MRI contrast agents. *Curr Pharm Biotechnol* **5**, 539-549 (2004).
70. Kobayashi, H. et al. Positive effects of polyethylene glycol conjugation to generation-4 polyamidoamine dendrimers as macromolecular MR contrast agents. *Magn Reson Med* **46**, 781-788 (2001).
71. Kellar, K.E. et al. High relaxivity linear Gd(DTPA)-polymer conjugates: the role of hydrophobic interactions. *Magn Reson Med* **38**, 712-716 (1997).
72. Vander Elst, L., Chapelle, F., Laurent, S. & Muller, R.N. Stereospecific binding of MRI contrast agents to human serum albumin: the case of Gd-(S)-EOB-DTPA (Eovist) and its (R) isomer. *J Biol Inorg Chem* **6**, 196-200 (2001).
73. Behra-Miellet, J. et al. On-line HPLC-electrospray ionization mass spectrometry: a pharmacological tool for identifying and studying the stability of Gd3+ complexes used as magnetic resonance imaging contrast agents. *Biomed Chromatogr* **12**, 21-26 (1998).
74. Datta, A. et al. High relaxivity gadolinium hydroxypyridonate-viral capsid conjugates: nanosized MRI contrast agents. *J Am Chem Soc* **130**, 2546-2552 (2008).
75. Caravan, P. et al. Albumin binding, relaxivity, and water exchange kinetics of the diastereoisomers of MS-325, a gadolinium(III)-based magnetic resonance angiography contrast agent. *Inorg Chem* **46**, 6632-6639 (2007).
76. Hanaoka, K., Kikuchi, K., Terai, T., Komatsu, T. & Nagano, T. A Gd3+-based magnetic resonance imaging contrast agent sensitive to beta-galactosidase activity utilizing a receptor-induced magnetization enhancement (RIME) phenomenon. *Chemistry* **14**, 987-995 (2008).
77. Esqueda, A.C. et al. A new gadolinium-based MRI zinc sensor. *J Am Chem Soc* **131**, 11387-11391 (2009).
78. Zhang, Z. et al. Multilocus binding increases the relaxivity of protein-bound MRI contrast agents. *Angew Chem Int Ed Engl* **44**, 6766-6769 (2005).
79. Overoye-Chan, K. et al. EP-2104R: a fibrin-specific gadolinium-Based MRI contrast agent for detection of thrombus. *J Am Chem Soc* **130**, 6025-6039 (2008).
80. Caravan, P. et al. Collagen-targeted MRI contrast agent for molecular imaging of fibrosis. *Angew Chem Int Ed Engl* **46**, 8171-8173 (2007).
81. Tweedle, M.F. The ProHance story: the making of a novel MRI contrast agent. *Eur Radiol* **7 Suppl 5**, 225-230 (1997).
82. White, G.W., Gibby, W.A. & Tweedle, M.F. Comparison of Gd(DTPA-BMA) (Omniscan) versus Gd(HP-DO3A) (ProHance) relative to gadolinium retention in human bone tissue by inductively coupled plasma mass spectroscopy. *Invest Radiol* **41**, 272-278 (2006).

83. Datta, A. & Raymond, K.N. Gd-hydroxypyridinone (HOPO)-based high-relaxivity magnetic resonance imaging (MRI) contrast agents. *Acc Chem Res* **42**, 938-947 (2009).
84. Thompson, M.K. et al. Hetero-tripodal hydroxypyridonate gadolinium complexes: syntheses, relaxometric properties, water exchange dynamics, and human serum albumin binding. *Inorg Chem* **43**, 8577-8586 (2004).
85. Werner, E.J. et al. Highly soluble tris-hydroxypyridonate Gd(III) complexes with increased hydration number, fast water exchange, slow electronic relaxation, and high relaxivity. *J Am Chem Soc* **129**, 1870-1871 (2007).
86. Veronese, F.M., Mero, A. & Pasut, G. in PEGylated Protein Drugs: Basic Science and Clinical Applications. (ed. F.M. Veronese) 11-31 (Birkhäuser Basel, 2009).
87. Yang, W., Wilkins, A.L., Li, S., Ye, Y. & Yang, J.J. The effects of Ca2+ binding on the dynamic properties of a designed Ca2+-binding protein. *Biochemistry* **44**, 8267-8273 (2005).
88. de Lussanet, Q.G. et al. Dynamic contrast-enhanced MR imaging kinetic parameters and molecular weight of dendritic contrast agents in tumor angiogenesis in mice. *Radiology* **235**, 65-72 (2005).
89. Wilkins, A.L. et al. Metal-binding studies for a de novo designed calcium-binding protein. *Protein Eng* **15**, 571-574 (2002).
90. Yang, W., Lee, H.W., Hellinga, H. & Yang, J.J. Structural analysis, identification, and design of calcium-binding sites in proteins. *Proteins* **47**, 344-356 (2002).
91. Dudev, T., Lin, Y.L., Dudev, M. & Lim, C. First-second shell interactions in metal binding sites in proteins: a PDB survey and DFT/CDM calculations. *J Am Chem Soc* **125**, 3168-3180 (2003).
92. Wang, X. et al. Analysis and prediction of calcium-binding pockets from apo-protein structures exhibiting calcium-induced localized conformational changes. *Protein Sci* **19**, 1180-1190 (2010).
93. Wang, X., Kirberger, M., Qiu, F., Chen, G. & Yang, J.J. Towards predicting Ca2+-binding sites with different coordination numbers in proteins with atomic resolution. *Proteins* **75**, 787-798 (2009).
94. Kirberger, M. & Yang, J.J. Structural differences between Pb2+- and Ca2+-binding sites in proteins: implications with respect to toxicity. *J Inorg Biochem* **102**, 1901-1909 (2008).
95. Kirberger, M. et al. Statistical analysis of structural characteristics of protein Ca2+-binding sites. *J Biol Inorg Chem* **13**, 1169-1181 (2008).
96. Deng, H., Chen, G., Yang, W. & Yang, J.J. Predicting calcium-binding sites in proteins - a graph theory and geometry approach. *Proteins* **64**, 34-42 (2006).
97. Carroll, A., Yang, W., Ye, Y., Simmons, R. & Yang, J.J. Amyloid fibril formation by a domain of rat cell adhesion molecule. *Cell Biochem Biophys* **44**, 241-249 (2006).
98. Pidcock, E. & Moore, G.R. Structural characteristics of protein binding sites for calcium and lanthanide ions. *J Biol Inorg Chem* **6**, 479-489 (2001).
99. Li, S. et al. PEGylation of protein-based MRI contrast agents improves relaxivities and biocompatibilities. *J Inorg Biochem* **107**, 111-118 (2012).
100. Yang, W. et al. Design of a calcium-binding protein with desired structure in a cell adhesion molecule. *J Am Chem Soc* **127**, 2085-2093 (2005).
101. Moats, R.A., Fraser, S.E. & Meade, T.J. A ''smart'' magnetic resonance imaging agent that reports on specific enzymatic activity. *Angew Chem Int Edit* **36**, 726-728 (1997).
102. Louie, A.Y. et al. In vivo visualization of gene expression using magnetic resonance imaging. *Nat Biotechnol* **18**, 321-325 (2000).
103. Yang, J.J. et al. Rational design of protein-based MRI contrast agents. *J Am Chem Soc* **130**, 9260-9267 (2008).
104. Weinmann, H.J., Brasch, R.C., Press, W.R. & Wesbey, G.E. Characteristics of gadolinium-DTPA complex: a potential NMR contrast agent. *AJR Am J Roentgenol* **142**, 619-624 (1984).

105. Brown, E.M. et al. Cloning and characterization of an extracellular Ca(2+)-sensing receptor from bovine parathyroid. *Nature* **366**, 575-580 (1993).
106. Ogurusu, T., Wakabayashi, S. & Shigekawa, M. Functional characterization of lanthanide binding sites in the sarcoplasmic reticulum Ca(2+)-ATPase: do lanthanide ions bind to the calcium transport site? *Biochemistry* **30**, 9966-9973 (1991).
107. Biagi, B.A. & Enyeart, J.J. Gadolinium blocks low- and high-threshold calcium currents in pituitary cells. *Am J Physiol* **259**, C515-520 (1990).
108. Caravan, P., Greenwood, J.M., Welch, J.T. & Franklin, S.J. Gadolinium-binding helix-turn-helix peptides: DNA-dependent MRI contrast agents. *Chemical communications*, 2574-2575 (2003).
109. Liepold, L. et al. Viral capsids as MRI contrast agents. *Magn Reson Med* **58**, 871-879 (2007).
110. Caravan, P., Ellison, J.J., McMurry, T.J. & Lauffer, R.B. Gadolinium (III) chelates as MRI contrast agents: structure, dynamics, and applications. *Chemical Reviews* **99**, 2293-2352 (1999).
111. Chen, Y.Y., Xue, S.H., Zhou, Y.B. & Yang, J.J. Calciomics: prediction and analysis of EF-hand calcium binding proteins by protein engineering. *SCIENCE CHINA Chemistry* **53**, 52-60 (2010).
112. Zhou, Y., Xue, S., Chen, Y. & Yang, J.J. Probing Ca(2+)-Binding Capability of Viral Proteins with the EF-Hand Motif by Grafting Approach. *Methods in molecular biology* **963**, 37-53 (2013).
113. Chen, Y. et al. Role of calcium in metalloenzymes: effects of calcium removal on the axial ligation geometry and magnetic properties of the catalytic diheme center in MauG. *Biochemistry* **51**, 1586-1597 (2012).
114. Xue, S., Chen, N., Huang, Y. & Yang, J.J. Designing Single Fluorescent Protein Based Caspase Sensor For Monitoring Apoptosis In Living Cells. *Biophysical Journal* **96**, 425 (2009).
115. Zhou, Y., Xue, S. & Yang, J.J. Calciomics: integrative studies of Ca2+-binding proteins and their interactomes in biological systems. *Metallomics : integrated biometal science* **5**, 29-42 (2013).
116. Artinian, L., Tornieri, K., Zhong, L., Baro, D. & Rehder, V. Nitric oxide acts as a volume transmitter to modulate electrical properties of spontaneously firing neurons via apamin-sensitive potassium channels. *The Journal of Neuroscience* **30**, 1699-1711 (2010).
117. Artinian, L., Zhong, L., Yang, H. & Rehder, V. Nitric oxide as intracellular modulator: internal production of NO increases neuronal excitability via modulation of several ionic conductances. *European Journal of Neuroscience* (2012).
118. Durkaya, G., Zhong, L., Rehder, V. & Dietz, N. Nano-scale Topographical Studies on the Growth Cones of Nerve Cells using AFM. *Bulletin of the American Physical Society* **54** (2009).
119. Zhong, L., Artinian, L. & Rehder, V. Dopamine suppresses neuronal activity of< i> Helisoma</i> B5 neurons via a D2-like receptor, activating PLC and K channels. *Neuroscience* (2012).
120. Zhong, L.R., Estes, S., Artinian, L. & Rehder, V. Acetylcholine elongates neuronal growth cone filopodia via activation of nicotinic acetylcholine receptors. *Developmental Neurobiology* (2013).
121. Jiang, Y. et al. Elucidation of a novel extracellular calcium-binding site on metabotropic glutamate receptor 1{alpha} (mGluR1{alpha}) that controls receptor activation. *The Journal of biological chemistry* **285**, 33463-33474 (2010).
122. Huang, Y. et al. Calmodulin regulates Ca2+-sensing receptor-mediated Ca2+ signaling and its cell surface expression. *The Journal of biological chemistry* **285**, 35919-35931 (2010).
123. Jiang, J. et al. Site-specific modification of calmodulin Ca(2)(+) affinity tunes the skeletal muscle ryanodine receptor activation profile. *Biochem J* **432**, 89-99 (2010).
124. Yamaguchi, M. Role of regucalcin in brain calcium signaling: involvement in aging. *Integrative biology : quantitative biosciences from nano to macro* **4**, 825-837 (2012).
125. Sherry, A.D., Caravan, P. & Lenkinski, R.E. Primer on gadolinium chemistry. *J Magn Reson Imaging* **30**, 1240-1248 (2009).
126. Wedeking, P., Kumar, K. & Tweedle, M.F. Dissociation of gadolinium chelates in mice: relationship to chemical characteristics. *Magn Reson Imaging* **10**, 641-648 (1992).

127. Laurent, S., Elst, L.V., Copoix, F. & Muller, R.N. Stability of MRI paramagnetic contrast media: a proton relaxometric protocol for transmetallation assessment. *Invest Radiol* **36**, 115-122 (2001).
128. Frenzel, T., Lengsfeld, P., Schirmer, H., Hutter, J. & Weinmann, H.J. Stability of gadolinium-based magnetic resonance imaging contrast agents in human serum at 37 degrees C. *Invest Radiol* **43**, 817-828 (2008).
129. Thakral, C. & Abraham, J.L. Gadolinium-induced nephrogenic systemic fibrosis is associated with insoluble Gd deposits in tissues: in vivo transmetallation confirmed by microanalysis. *J Cutan Pathol* **36**, 1244-1254 (2009).
130. Kok, M.B., Strijkers, G.J. & Nicolay, K. Dynamic changes in 1H-MR relaxometric properties of cell-internalized paramagnetic liposomes, as studied over a five-day period. *Contrast media & molecular imaging* **6**, 69-76 (2011).
131. Seth, R., Yang, S., Choi, S., Sabean, M. & Roberts, E.A. In vitro assessment of copper-induced toxicity in the human hepatoma line, Hep G2. *Toxicol In Vitro* **18**, 501-509 (2004).
132. Hamid, R., Rotshteyn, Y., Rabadi, L., Parikh, R. & Bullock, P. Comparison of alamar blue and MTT assays for high through-put screening. *Toxicol In Vitro* **18**, 703-710 (2004).
133. Barnhart, J.L., Kuhnert, N., Bakan, D.A. & Berk, R.N. Biodistribution of GdCl3 and Gd-DTPA and their influence on proton magnetic relaxation in rat tissues. *Magn Reson Imaging* **5**, 221-231 (1987).
134. Morse, D.L. & Gillies, R.J. Molecular imaging and targeted therapies. *Biochem Pharmacol* **80**, 731-738 (2010).
135. Allison, M. The HER2 testing conundrum. *Nat Biotechnol* **28**, 117-119 (2010).
136. Nunn, A.D., Linder, K.E. & Tweedle, M.F. Can receptors be imaged with MRI agents? *Q J Nucl Med* **41**, 155-162 (1997).
137. Delli Castelli, D. et al. In vivo MRI multicontrast kinetic analysis of the uptake and intracellular trafficking of paramagnetically labeled liposomes. *J Control Release* **144**, 271-279 (2010).
138. Kok, M.B. et al. Cellular compartmentalization of internalized paramagnetic liposomes strongly influences both T1 and T2 relaxivity. *Magn Reson Med* **61**, 1022-1032 (2009).
139. Kok, M.B., Strijkers, G.J. & Nicolay, K. Dynamic changes in (1) H-MR relaxometric properties of cell-internalized paramagnetic liposomes, as studied over a five-day period. *Contrast Media Mol Imaging* **6**, 69-76 (2011).
140. Artemov, D., Bhujwalla, Z.M. & Bulte, J.W. Magnetic resonance imaging of cell surface receptors using targeted contrast agents. *Curr Pharm Biotechnol* **5**, 485-494 (2004).
141. Artemov, D., Mori, N., Okollie, B. & Bhujwalla, Z.M. MR molecular imaging of the Her-2/neu receptor in breast cancer cells using targeted iron oxide nanoparticles. *Magn Reson Med* **49**, 403-408 (2003).
142. Geninatti Crich, S. et al. Magnetic resonance imaging visualization of targeted cells by the internalization of supramolecular adducts formed between avidin and biotinylated Gd3+ chelates. *J Biol Inorg Chem* **10**, 78-86 (2005).
143. Sipkins, D.A. et al. Detection of tumor angiogenesis in vivo by alphaVbeta3-targeted magnetic resonance imaging. *Nat Med* **4**, 623-626 (1998).
144. Farokhzad, O.C. et al. Nanoparticle-aptamer bioconjugates: a new approach for targeting prostate cancer cells. *Cancer Res* **64**, 7668-7672 (2004).
145. Frullano, L. et al. Towards targeted MRI: new MRI contrast agents for sialic acid detection. *Chemistry* **10**, 5205-5217 (2004).
146. Morawski, A.M. et al. Targeted nanoparticles for quantitative imaging of sparse molecular epitopes with MRI. *Magn Reson Med* **51**, 480-486 (2004).
147. Schmieder, A.H. et al. Molecular MR imaging of melanoma angiogenesis with alphanubeta3-targeted paramagnetic nanoparticles. *Magn Reson Med* **53**, 621-627 (2005).

148. Flacke, S. et al. Novel MRI contrast agent for molecular imaging of fibrin: implications for detecting vulnerable plaques. *Circulation* **104**, 1280-1285 (2001).
149. Artemov, D., Mori, N., Ravi, R. & Bhujwalla, Z.M. Magnetic resonance molecular imaging of the HER-2/neu receptor. *Cancer Res* **63**, 2723-2727 (2003).
150. Wickline, S.A., Neubauer, A.M., Winter, P.M., Caruthers, S.D. & Lanza, G.M. Molecular imaging and therapy of atherosclerosis with targeted nanoparticles. *J Magn Reson Imaging* **25**, 667-680 (2007).
151. Winter, P.M. et al. Molecular imaging of angiogenesis in nascent Vx-2 rabbit tumors using a novel alpha(nu)beta3-targeted nanoparticle and 1.5 tesla magnetic resonance imaging. *Cancer Res* **63**, 5838-5843 (2003).
152. Winter, P.M. et al. Molecular imaging of angiogenesis in early-stage atherosclerosis with alpha(v)beta3-integrin-targeted nanoparticles. *Circulation* **108**, 2270-2274 (2003).
153. Burtea, C. et al. Magnetic resonance molecular imaging of vascular cell adhesion molecule-1 expression in inflammatory lesions using a peptide-vectorized paramagnetic imaging probe. *J Med Chem* **52**, 4725-4742 (2009).
154. Akhtar, A.M. et al. In vivo quantification of VCAM-1 expression in renal ischemia reperfusion injury using non-invasive magnetic resonance molecular imaging. *PLoS One* **5**, e12800 (2010).
155. Qiao, J. et al. HER2 targeted molecular MR imaging using a de novo designed protein contrast agent. *PLoS One* **6**, e18103 (2011).
156. Pathak, A.P., Artemov, D. & Bhujwalla, Z.M. Novel system for determining contrast agent concentration in mouse blood in vivo. *Magn Reson Med* **51**, 612-615 (2004).
157. Glunde, K., Artemov, D., Penet, M.F., Jacobs, M.A. & Bhujwalla, Z.M. Magnetic resonance spectroscopy in metabolic and molecular imaging and diagnosis of cancer. *Chem Rev* **110**, 3043-3059 (2010).
158. Yoo, B. & Pagel, M.D. An overview of responsive MRI contrast agents for molecular imaging. *Front Biosci* **13**, 1733-1752 (2008).
159. Stephen, R.M. & Gillies, R.J. Promise and progress for functional and molecular imaging of response to targeted therapies. *Pharm Res* **24**, 1172-1185 (2007).
160. Zhang, X. et al. 18F-labeled bombesin analogs for targeting GRP receptor-expressing prostate cancer. *J Nucl Med* **47**, 492-501 (2006).
161. Emonds, K.M., Swinnen, J.V., Mortelmans, L. & Mottaghy, F.M. Molecular imaging of prostate cancer. *Methods* **48**, 193-199 (2009).
162. Reubi, J.C. & Maecke, H.R. Peptide-based probes for cancer imaging. *J Nucl Med* **49**, 1735-1738 (2008).
163. Jensen, R.T., Battey, J.F., Spindel, E.R. & Benya, R.V. International Union of Pharmacology. LXVIII. Mammalian bombesin receptors: nomenclature, distribution, pharmacology, signaling, and functions in normal and disease states. *Pharmacol Rev* **60**, 1-42 (2008).
164. Wei, L. et al. Protein-Based MRI Contrast Agents for Molecular Imaging of Prostate Cancer. *Mol Imaging Biol* (2010).
165. Jensen, J.A., Carroll, R.E. & Benya, R.V. The case for gastrin-releasing peptide acting as a morphogen when it and its receptor are aberrantly expressed in cancer. *Peptides* **22**, 689-699 (2001).
166. Roy, A., Kucukural, A. & Zhang, Y. I-TASSER: a unified platform for automated protein structure and function prediction. *Nat Protoc* **5**, 725-738 (2010).
167. Zhang, Y. I-TASSER: fully automated protein structure prediction in CASP8. *Proteins* **77 Suppl 9**, 100-113 (2009).
168. Zhang, Y. I-TASSER server for protein 3D structure prediction. *BMC Bioinformatics* **9**, 40 (2008).

169. Xue, S., Qiao, J., Pu, F., Cameron, M. & Yang, J.J. Design of a novel class of protein-based magnetic resonance imaging contrast agents for the molecular imaging of cancer biomarkers. *Wiley interdisciplinary reviews. Nanomedicine and nanobiotechnology* (2013).
170. Hornak, J.P. 2002).
171. Zhang, F. et al. Synergistic enhancement of iron oxide nanoparticle and gadolinium for dual-contrast MRI. *Biochemical and biophysical research communications* **425**, 886-891 (2012).
172. Henzl, M.T. & Graham, J.S. Conformational stabilities of the rat alpha- and beta-parvalbumins. *FEBS letters* **442**, 241-245 (1999).
173. Grynkiewicz, G., Poenie, M. & Tsien, R.Y. A new generation of Ca2+ indicators with greatly improved fluorescence properties. *The Journal of biological chemistry* **260**, 3440-3450 (1985).
174. Horrocks, W.D. & Sudnick, D.R. Lanthanide ion probes of structure in biology. Laser-induced luminescence decay constants provide a direct measure of the number of metal-coordinated water molecules. *Journal of the American Chemical Society* **101**, 334-340 (1979).
175. Sudnick, D.R. & Horrocks, W.D., Jr. Lanthanide ion probes of structure in biology. Environmentally sensitive fine structure in laser-induced terbium(III) luminescence. *Biochimica et biophysica acta* **578**, 135-144 (1979).
176. Henzl, M.T., Wycoff, W.G., Larson, J.D. & Likos, J.J. 15N nuclear magnetic resonance relaxation studies on rat beta-parvalbumin and the pentacarboxylate variants, S55D and G98D. *Protein Sci* **11**, 158-173 (2002).
177. Celio, M.R. & Heizmann, C.W. Calcium-binding protein parvalbumin as a neuronal marker. *Nature* **293**, 300-302 (1981).
178. Kirberger, M. et al. Integration of Diverse Research Methods to Analyze and Engineer Ca-Binding Proteins: From Prediction to Production. *Curr Bioinform* **5**, 68-80 (2010).
179. Yang, W. et al. Rational design of a calcium-binding protein. *J Am Chem Soc* **125**, 6165-6171 (2003).
180. Maniccia, A.W., Yang, W., Li, S.Y., Johnson, J.A. & Yang, J.J. Using protein design to dissect the effect of charged residues on metal binding and protein stability. *Biochemistry* **45**, 5848-5856 (2006).
181. Li, S. et al. Rational design of a conformation-switchable Ca2+- and Tb3+-binding protein without the use of multiple coupled metal-binding sites. *The FEBS journal* **275**, 5048-5061 (2008).
182. Jones, L.M. et al. Rational design of a novel calcium-binding site adjacent to the ligand-binding site on CD2 increases its CD48 affinity. *Protein Sci* **17**, 439-449 (2008).
183. Koppelman, S.J. et al. Purification of parvalbumin from carp: a protocol that avoids heat-treatment. *Journal of food science* **75**, T49-56 (2010).
184. Pauls, T.L. et al. Metal binding properties of recombinant rat parvalbumin wild-type and F102W mutant. *The Journal of biological chemistry* **268**, 20897-20903 (1993).
185. Henzl, M.T., Larson, J.D. & Agah, S. Estimation of parvalbumin Ca(2+)- and Mg(2+)-binding constants by global least-squares analysis of isothermal titration calorimetry data. *Analytical biochemistry* **319**, 216-233 (2003).
186. Henzl, M.T., Larson, J.D. & Agah, S. Influence of monovalent cation identity on parvalbumin divalent ion-binding properties. *Biochemistry* **43**, 2747-2763 (2004).
187. Lee, Y.H., Tanner, J.J., Larson, J.D. & Henzl, M.T. Crystal structure of a high-affinity variant of rat alpha-parvalbumin. *Biochemistry* **43**, 10008-10017 (2004).
188. Yanyi, C., Shenghui, X., Yubin, Z. & Jie, Y.J. Calciomics: prediction and analysis of EF-hand calcium binding proteins by protein engineering. *Science China. Chemistry* **53**, 52-60 (2010).
189. Bottoms, C.A., Schuermann, J.P., Agah, S., Henzl, M.T. & Tanner, J.J. Crystal structure of rat alpha-parvalbumin at 1.05 Angstrom resolution. *Protein Sci* **13**, 1724-1734 (2004).

190. Henzl, M.T. & Tanner, J.J. Solution structure of Ca2+-free rat alpha-parvalbumin. *Protein Sci* **17**, 431-438 (2008).
191. Henzl, M.T. Characterization of parvalbumin and polcalcin divalent ion binding by isothermal titration calorimetry. *Methods in enzymology* **455**, 259-297 (2009).
192. Laurent, S., Vander Elst, L., Henoumont, C. & Muller, R.N. How to measure the transmetallation of a gadolinium complex. *Contrast media & molecular imaging* **5**, 305-308 (2010).
193. Namasivayam, S., Martin, D.R. & Saini, S. Imaging of liver metastases: MRI. *Cancer Imaging* **7**, 2-9 (2007).
194. Sato, T. Locoregional management of hepatic metastasis from primary uveal melanoma. *Semin Oncol* **37**, 127-138 (2010).
195. Vogl, T.J. et al. Liver tumors: comparison of MR imaging with Gd-EOB-DTPA and Gd-DTPA. *Radiology* **200**, 59-67 (1996).
196. Servois, V. et al. Preoperative staging of liver metastases from uveal melanoma by magnetic resonance imaging (MRI) and fluorodeoxyglucose-positron emission tomography (FDG-PET). *Eur J Surg Oncol* **36**, 189-194 (2010).
197. Hanaoka, K., Lubag, A.J., Castillo-Muzquiz, A., Kodadek, T. & Sherry, A.D. The detection limit of a Gd3+-based T1 agent is substantially reduced when targeted to a protein microdomain. *Magn Reson Imaging* **26**, 608-617 (2008).
198. Lee, J., Platt, S., Kent, M. & Zhao, Q. An analysis of the pharmacokinetic parameter ratios in DCE-MRI using the reference region model. *Magn Reson Imaging* **30**, 26-35 (2012).
199. Heldin, C.H., Rubin, K., Pietras, K. & Ostman, A. High interstitial fluid pressure - an obstacle in cancer therapy. *Nature reviews. Cancer* **4**, 806-813 (2004).
200. Yokoyama, S., Inagaki, F. & Miyazawa, T. Advanced nuclear magnetic resonance lanthanide probe analyses of short-range conformational interrelations controlling ribonucleic acid structures. *Biochemistry* **20**, 2981-2988 (1981).
201. Mendichovszky, I.A., Cutajar, M. & Gordon, I. Reproducibility of the aortic input function (AIF) derived from dynamic contrast-enhanced magnetic resonance imaging (DCE-MRI) of the kidneys in a volunteer study. *Eur J Radiol* **71**, 576-581 (2009).
202. Saito, K. et al. Assessing liver function using dynamic Gd-EOB-DTPA-enhanced MRI with a standard 5-phase imaging protocol. *J Magn Reson Imaging* (2012).
203. Tofts, P.S. & Kermode, A.G. Measurement of the blood-brain barrier permeability and leakage space using dynamic MR imaging. 1. Fundamental concepts. *Magn Reson Med* **17**, 357-367 (1991).
204. Donahue, K.M., Burstein, D., Manning, W.J. & Gray, M.L. Studies of Gd-DTPA relaxivity and proton exchange rates in tissue. *Magn Reson Med* **32**, 66-76 (1994).
205. Lemasson, B. et al. Monitoring blood-brain barrier status in a rat model of glioma receiving therapy: dual injection of low-molecular-weight and macromolecular MR contrast media. *Radiology* **257**, 342-352 (2010).
206. Loveless, M.E. et al. A quantitative comparison of the influence of individual versus population-derived vascular input functions on dynamic contrast enhanced-MRI in small animals. *Magn Reson Med* **67**, 226-236 (2012).
207. Alonzi, R., Padhani, A.R. & Allen, C. Dynamic contrast enhanced MRI in prostate cancer. *Eur J Radiol* **63**, 335-350 (2007).
208. O'Connor, J.P., Jackson, A., Parker, G.J. & Jayson, G.C. DCE-MRI biomarkers in the clinical evaluation of antiangiogenic and vascular disrupting agents. *Br J Cancer* **96**, 189-195 (2007).
209. Kim, H. et al. DCE-MRI detects early vascular response in breast tumor xenografts following anti-DR5 therapy. *Mol Imaging Biol* **13**, 94-103 (2011).

210. Kim, H. et al. Early therapy evaluation of combined cetuximab and irinotecan in orthotopic pancreatic tumor xenografts by dynamic contrast-enhanced magnetic resonance imaging. *Molecular imaging* **10**, 153-167 (2011).
211. Kanematsu, M. et al. Imaging liver metastases: review and update. *Eur J Radiol* **58**, 217-228 (2006).
212. Lewis, M., Yanny, S. & Malcolm, P.N. Advantages of blood pool contrast agents in MR angiography: a pictorial review. *Journal of medical imaging and radiation oncology* **56**, 187-191 (2012).
213. Cai, W. & Chen, X. Multimodality molecular imaging of tumor angiogenesis. *J Nucl Med* **49 Suppl 2**, 113S-128S (2008).
214. Cai, W. et al. In vitro and in vivo characterization of 64Cu-labeled Abegrin, a humanized monoclonal antibody against integrin alpha v beta 3. *Cancer Res* **66**, 9673-9681 (2006).
215. Gonzalez, N. et al. Molecular basis for the selectivity of the mammalian bombesin peptide, neuromedin B, for its receptor. *J Pharmacol Exp Ther* **331**, 265-276 (2009).
216. Tokita, K., Hocart, S.J., Coy, D.H. & Jensen, R.T. Molecular basis of the selectivity of gastrin-releasing peptide receptor for gastrin-releasing peptide. *Mol Pharmacol* **61**, 1435-1443 (2002).
217. Ruegg, C. & Alghisi, G.C. Vascular integrins: therapeutic and imaging targets of tumor angiogenesis. *Recent Results Cancer Res* **180**, 83-101 (2010).
218. Moser, M., Legate, K.R., Zent, R. & Fassler, R. The tail of integrins, talin, and kindlins. *Science* **324**, 895-899 (2009).
219. Harburger, D.S. & Calderwood, D.A. Integrin signalling at a glance. *J Cell Sci* **122**, 159-163 (2009).
220. Desgrosellier, J.S. & Cheresh, D.A. Integrins in cancer: biological implications and therapeutic opportunities. *Nature reviews. Cancer* **10**, 9-22 (2010).
221. Lee, H.Y. et al. PET/MRI dual-modality tumor imaging using arginine-glycine-aspartic (RGD)-conjugated radiolabeled iron oxide nanoparticles. *J Nucl Med* **49**, 1371-1379 (2008).
222. Riechmann, L., Clark, M., Waldmann, H. & Winter, G. Reshaping human antibodies for therapy. *Nature* **332**, 323-327 (1988).
223. Queen, C. et al. A humanized antibody that binds to the interleukin 2 receptor. *Proceedings of the National Academy of Sciences of the United States of America* **86**, 10029-10033 (1989).
224. Glass, R.I. et al. Rotavirus vaccines: current prospects and future challenges. *Lancet* **368**, 323-332 (2006).
225. Angel, J., Franco, M.A. & Greenberg, H.B. Rotavirus vaccines: recent developments and future considerations. *Nature reviews. Microbiology* **5**, 529-539 (2007).
226. Aoki, S.T. et al. Cross-linking of rotavirus outer capsid protein VP7 by antibodies or disulfides inhibits viral entry. *Journal of virology* **85**, 10509-10517 (2011).
227. Gajardo, R., Vende, P., Poncet, D. & Cohen, J. Two proline residues are essential in the calcium-binding activity of rotavirus VP7 outer capsid protein. *Journal of virology* **71**, 2211-2216 (1997).
228. Lu, X. et al. Mechanism for coordinated RNA packaging and genome replication by rotavirus polymerase VP1. *Structure* **16**, 1678-1688 (2008).

APPENDICES

Appendix A. Identification of Ca^{2+} - binding sites in rotavirus

Appendix A.1 Introduction

Rotavirus infection is the most common cause of diarrhoea whcich causes 20 - 60 deaths in the United States and around 610,000 deaths globally eververy year. In addition, rotavirus infection cause more than 600,000 and 24 million of outpatient visit in the United States and the whole world, respectively.[224] Thus, understanding the physiological and pathological mechanism of rotavirus replication, preliferation and duplication of rotavirus is very important.

Rotavirus is a double-strend RNA virus in the family Reoviridideа. The genome of rotavirus encodes 7 viral proteins (VP) and 6 nonstructural proteins (NSP). The viral proteins of rotavirus form three layers of capsid to encapsulate RNA genome. The outer capsid of rotavirus is formed by VP4 and VP7. Timers of VP4 form the outer capsid spikes. The infectivity of rotavirus in increased when VP4 is cleaved to be VP5* and VP8*. VP7 is an outer capside glycoprotein, which also determines the type of rotaviruses. VP6 is the major protein forms the middle capsid of rotavirus and VP6 is also involved in the rotavirus transcription. VP1, VP2 and VP3 are located the inner capside of rotavirus. VP1 is a RNA-dependent RNA polymerase. It binds to single-strand RNA and forms a transcription complex with VP3. VP2 is the inner capsid protein, which regulate the replicase activity of VP1. In addtions, rotavirus also encodes 6 nonstructural proteins. Althought these nonstructureal proteins are not a component of the viral structure, nonstructural proteins plays essential roles on almost every aspect of the viral replication,

preliferation, invasion. Among these nonstructural proteins, NSP4 has been identified as a vrial enterotoxin inducing diarrhoea.[225]

Intracellular and extracellular Ca^{2+} plays important roles on the rotavirus induced diarrhea. The structural proteins of rotavirus form viral capsid in the high concentration of Ca^{2+}, while these proteins disassembled at low concentration of Ca^{2+}. Such phanomonan is closely related with physiological condition of rotavirus infection. The calcium concentration in the extracellular space is around 1 mM and rotavirus is well packed as triple-layered particle at such conditions. When the rotavirus entere the cell through endocytosis, the Ca^{2+} concentration of rotavirus decrease. As a result, the outer layer of the capsid is solubilized at low concentration of Ca^{2+} abd the double-layered particle is released into the cytosol of the cell. In addition, NSP4 can disrupt Ca^{2+} homostasis by two ways. Fisrt, NSP4 is believed to form the membrane Ca^{2+} channel which increase intracellular Ca^{2+} concentration because of Ca2+ entery from ER or extracellular space through this channel. Second, NSP4 is able to intrigue membrane receptors, such as integrin, to activate PLC-γ. The activated PLC-γ converts PIP_2 to be IP_3. IP_3 can induce ER calcium release by activating ryanondine receptors. This process can further cause secretory diarrhea because the intracellular Ca^{2+} homostasis is disrupted.

Although Ca^{2+} plays essential roles on the rotavirus replication, proliferation and infection, the Ca2+ binding sites on rotavirus is not clear. Ca^{2+} were loaded in the x-ray structure of intersubunit of VP7[226] Gajardo and coleagues[227] report two prolin redidues are essential in the calcium binding activity of VP7. However, this paper does have direct evidence to sopport that an EF-hand like motif in VP7 binds Ca^{2+}. Our lab develop a series of computational approach to predict the Ca^{2+} binding sites in proteins based on the primary sequence and x-ray or NMR

structures.[115] We also developed grafting approach and Tb^{3+}-LRET assay to identify the predicted Ca^{2+} binding sites. Here, we will report our preliminary data of the indentification of Ca^{2+} binding sites in VP1 and VP7 of rotavirus.

Appendix A.2 Meterial and Methods

The calcium binding sites of rotavirus were predicted by MUG software developed in our lab.[115] The pdb structures of rotavirus proteins were downloaded and inputed into the MUG software (http://chemistry.gsu.edu/faculty/Yang/Calciomics.htm). The MUG software then predicted calcium binding sites based on the oxygen position and distance of inputed structures. Three and one Ca^{2+} binding sites were predicted from VP1 and VP7 of rotavirsus, repectively.

The predicted calcium binding peptides were then inserted between S52 and G53 position of domain 1. pGEX2T-CD2 plasmid was used as a template for this insertion by PCR. The correct insertions were identified by DNA sequencing. The proteins were expressed by *E. coli*, BL-21-DE3-plysS cell strain and then purified by GST column.

To identify Ca^{2+} binding sites in these purified proteins, 2 μM of protein were added into 10 mM PIPS buffer at pH 6.8. Then, Tb^{3+} were titrated to the buffer with gradually increase of concentration. Fluoresecent spectrum was collected in every titration steps at excitation wavelength of 280 nm and emission wavelength between 520 – 580 nm. The dissociation constants of these grafting proteins were calculated by 1 to 1 binding Equation based on the fluorescence intensity over different concentration of Tb^{3+}.

Appendix A.3 Results and Discussion

To predice calcium binding sites in rotavirus, all the pdb structures of rotavirus were downloaded and inputed into the MUG predication software. The predicted results from MUG were further evaluated by the number of negatively charged residues, electrostatic static surface environment. Three Ca^{2+} binding sites were predicted from VP1 (pdb: 2R7O) (Fig. Appedix-1) and one Ca^{2+} binding site was predicted from VP7 (pdb: 3FMG) (Fig. Appendix-1).

The predicted site 1 (519 THR, 520 ASP, 525 ASP, 629 ASP, 631 ASP, 632 ASP) has been reported as a Mg^{2+} binding site in the x-ray structure of VP1,[228] this is understandable as Mg^{2+} and Ca^{2+} shares similar but the exact same metal binding sites and calcium binding site in nature could also binds Mg^{2+} in nature. In addition, the predicted Ca^{2+} binding sites in VP7 are consistent with the reported regions which are essential in the calcium binding activity of VP7. These results strongly indicate that our prediction method is acturate.

Interestingly, we finding additional two predicted Ca^{2+} binding sites is the VP1 structure. The reseasions why these Ca^{2+} binding sites are not visualized in the x-ray stucture are probably due to weak Ca^{2+} bindig or conditions for growing crystals.

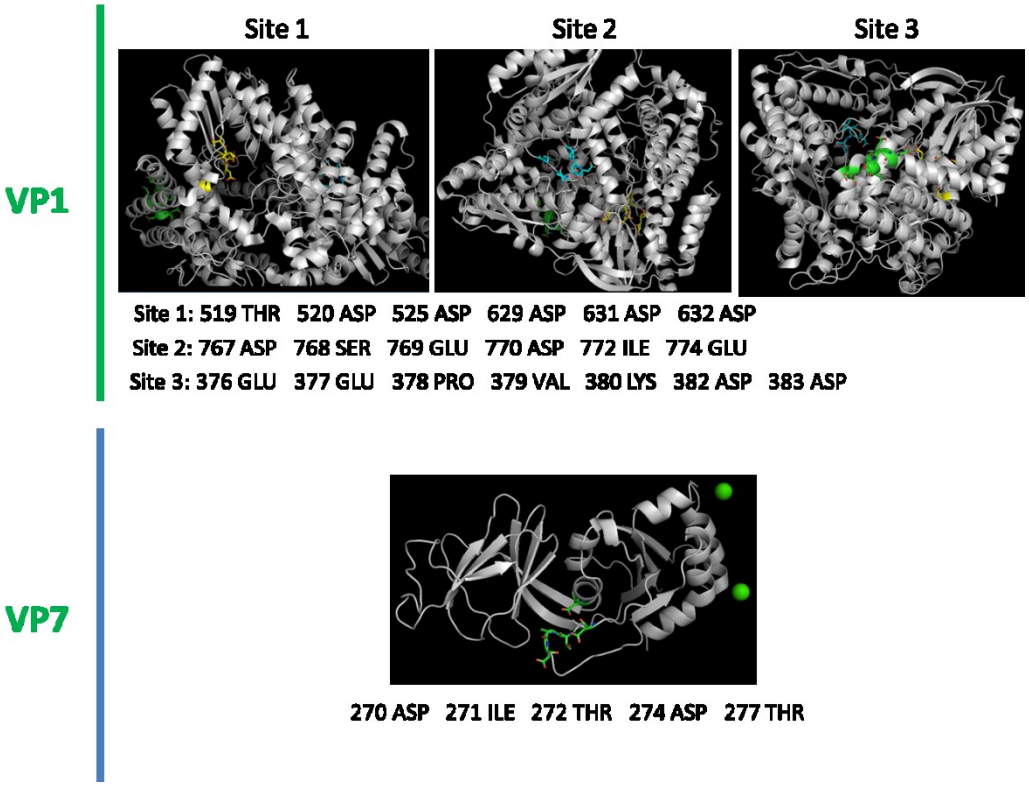

Figure Appendix-1. The predicted Ca^{2+} binding sites in rotavirus VP1 (top) and VP7.

Three Ca^{2+} binding sites were predicted from VP1 (pdb: 2R7O) and one Ca^{2+} binding site was predicted from VP7 (pdb: 3FMG) by MUG based the geometry information of oxygen. The MUG predicted results were further analyzed and identified based on the residue type and electro-static environment.

Grating approached coupled with Tb^{3+}-LRET assay were applied to further identify the predicted Ca^{2+} binding sites in VP1 and VP7. 2 μM CD2 grafted with predicted Ca^{2+} binding site in VP1 (site 3) an VP7 shows much dramtic fluoresecence increase compared with CD2 without any insertion (Fig. Appendix-2). Both of VP1 and VP7 insertion peptide shows Tb^{3+} binding with K_d of 13.8 μM and 42.5 μM, respectively. Since the VP7 peptide has been reported to involves in the calcium binding activity of VP7, our result provide additional support that this peptide directly binds to VP7 through residue 270 ASP, 271 ILE, 272 THR, 274 ASP, and 277 THR. In addition, a novel Ca^{2+} binding site in VP1 of rotavirus (376 GLU, 377 GLU, 378 PRO, 379 VAL, 380 LYS, 382 ASP, 383 ASP) is identified by MUG prediction and Tb^{3+}-LRET assay. Since VP1 envolves in RNA synthesis, single chain RNA binding, and transcription, our identified Ca^{2+} binding sites in VP1 should involves in the regulation of these functions. However, this results are preliminary studies. More expriments, such as Ca^{2+} competitation, should be applied to further confirm that these two sites bind Ca^{2+} and have physiological functions.

Appendix A.4 Conclusion

Two Ca^{2+} binding sites in rotavirus were identified by computational approaches and fluorescence spectroscopy. The identified Ca^{2+} binding sites may involve in the rotavirus assembling, RNA synthesis, single chain RNA binding, and transcription.

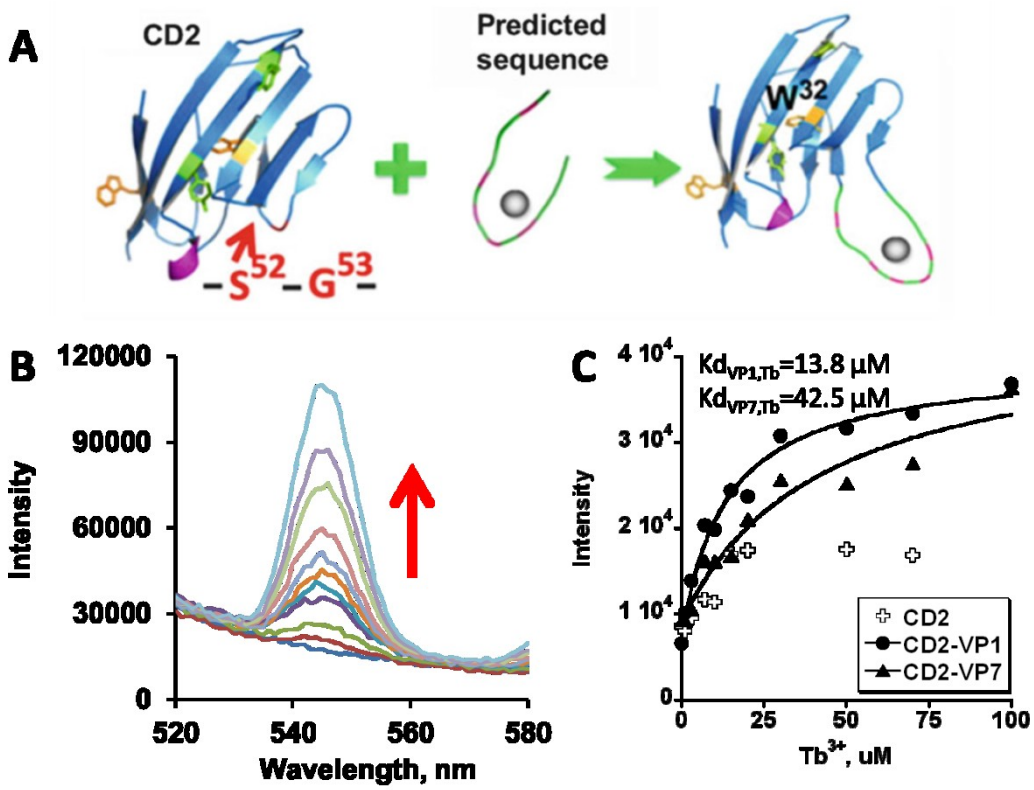

Figure Appendix-2. Identification of Ca^{2+} binding site in rotavirus by grafting approach (A) and LRET assay (B, C).

A. A carton represention of grafting approach. The predicted Ca^{2+} binding peptide is inserted into the CD2 between position S52 and G53.[112] B. Tb^{3+}-fluorescence increase with the increase of Tb^{3+} concentration. C. Calculation of dissociation constant of Tb^{3+} to VP1 peptide and VP7 peptide by fitting 1 to 1 binding Equation. As a control, wild type CD2 shows much less fluorescence increase compared with the CD2 grafted with predicted VP1 or VP7 binding peptide.

Appendix B. Prediction of Ca^{2+} binding sites in neuronal proteins

Ca^{2+} is a unique signal moelcular which regulate almost every aspect of the cellular activities including gene replication, cell perliferation, fertilization, secretion, migration, and apoptosis. The Ca^{2+} homostasis is well maintained by calcium channels, pumps, exchangers, receptors, calcium buffer proteins and Ca^{2+} proteins in different part of cellular environment. Errors in any step of Ca^{2+} signaling could cause abnormal cell activities.[112] Ca^{2+} also plays important roles on the neuron activities. Prediction and identification of Ca^{2+} binding sites in neuronal proteins is an important step to uncoding the physiological functions of these proteins.

Some Ca^{2+} responsive proteins, such as calmodulin (CaM), regulate cell functions by interacting with other proteins in a Ca^{2+} dependent manner.CaM is reported to interact with more than 100 hundred proteins to regulate the function of these proteins. CaM binding motifs are divided into five classes: 1–10 class, 1–14 class, 1–16 class, IQ class and others. Among them, the first three classes have been found to interact with CaM almost exclusively in a Ca^{2+}-dependent way while, IQ motif binds to CaM in a Ca^{2+} independent manner. A web-based served named calmodulin targeting data base has been developed to predict the possible CaM binding sites in proteins.[115]

In the past ten years, our lab developed serveral computational methods to predict Ca^{2+} binding proteins in the different type of biological system. We also developed *in vitro* and *in vivo* experimental methods to identify these predicted Ca^{2+} and CaM binding sites. In this appendix, we will show some predicted Ca^{2+} and CaM binding proteins involves in neuron system.

The Ca^{2+} binding sites can be predicted based on the primary amino acid sequences and x-ray structures. Based on the pattern search using online server, CaPS

(http://chemistry.gsu.edu/faculty/Yang/Calciomics.htm), three proteins (Dicer: NRNQDNYVSWSD; lrrk2: DLNTEGYTSEEVAD; Cdk5: DDDDEGVPSSALRE) are predicted to have putitive Ca^{2+} binding sites. In addition, we predicted calcium binding sites in CDK5 and exportin-5/ranGTP/pre-miRNA complex by MUG software based on the reported x-ray structure of these two proteins. The key residues predicted to binds Ca^{2+} are shown in Fig. Appendix-3, and 4. The predicted Ca^{2+} binding sites were analyzed electrostatic surface map. Both of these two predicted Ca^{2+} binding sits are located in the negative charge area of protein, this analysis further support that the predicted Ca^{2+} binding sites could be the real Ca^{2+} binding sites in these two proteins. We predicted another Ca^{2+} binding sites in x-ray structure of MEF2 using MUG. However, this predicted Ca^{2+} binding site is less likely to be true, because the electrostatic surface analysis shows that this predicted Ca^{2+} binding site is located in the positive charged region of protein (Fig. Appdendix-5).

Since CaM is an important Ca^{2+} responsive protein regulating cell activities. We also tried to predict CaM binding proteins using CaM target database (http://calcium.uhnres.utoronto.ca/ctdb/ctdb/). The prediction is based on the following criteria: hydropathy, alpha-helical propensity, residue weight, residue charge, hydrophobic residue content, helical class and occurrence of particular residues. Three proteins (dicer, Clc7 and exprotin 5) with 6 putative CaM binding sites were predicted with a maxium score of 13 – 14. Thus, Ca^{2+} could regulate the function of these three proteins through CaM interaction.

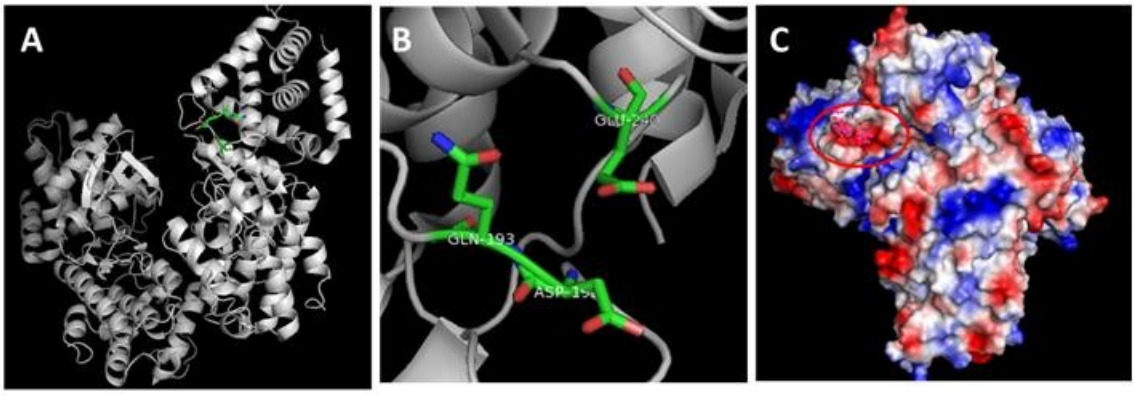

1h4l.pdb

6061 OD2	192 ASP	29.744	11.213	27.507
6069 OE1	193 GLN	29.744	11.213	29.744
6436 OE1	240 GLU	29.744	11.213	29.744
6437 OE2	240 GLU	29.744	11.213	29.744

Figure Appendix-3. The predicted Ca^{2+} binding site in CDK5 by MUG.

A. X-ray structure of CDK5 with the Ca^{2+} binding sites highlighted in green. B. The predicted Ca^{2+} binding pocket in CDK5. C. Electrostatic map of CDK5. The Ca^{2+} binding site (red cycle) is located in the negative charged ragion of CDK5.

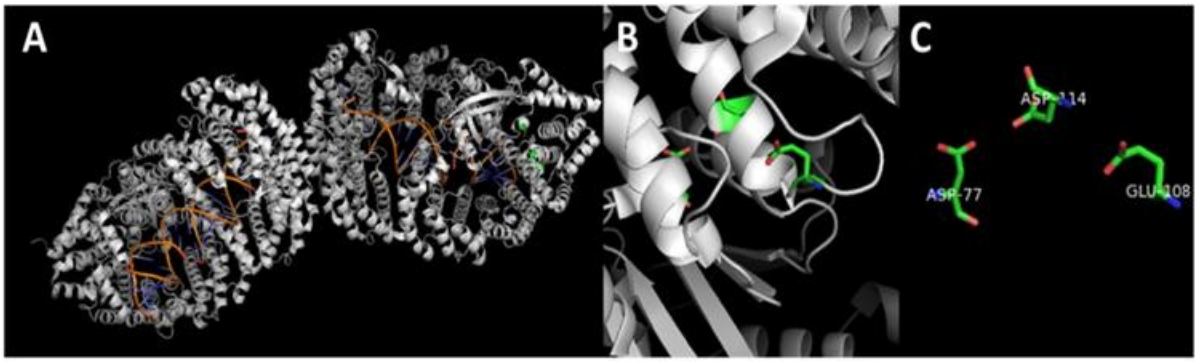

3a6p.pdb

908	OD1	114	ASP	32.860	136.812	7.828
909	OD2	114	ASP	32.860	136.812	32.860
9198	OD2	77	ASP	32.860	136.812	32.860
9446	O	107	ASP	32.860	136.812	32.860

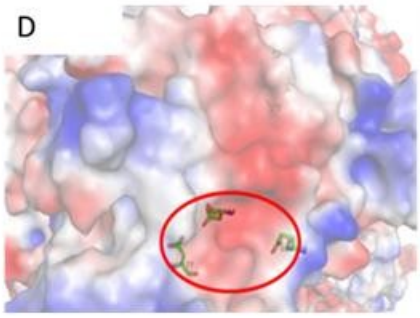

Figure Appendix-4. The predicted Ca^{2+} binding site in exportin-5/ranGTP/pre-miRNA complex by MUG.

A. X-ray structure of exportin-5/ranGTP/pre-miRNA complex with the Ca^{2+} binding sites highlighted in green. B. C. The predicted Ca^{2+} binding pocket in exportin-5/ranGTP/pre-miRNA complex. D. Electrostatic map of CDK5. The Ca^{2+} binding site (red cycle) is located in the negative charged ragion of exportin-5/ranGTP/pre-miRNA complex.

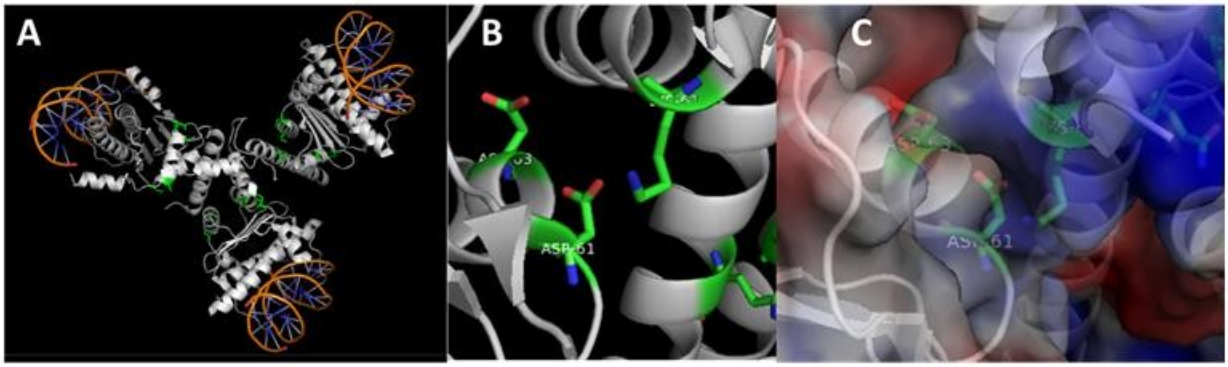

3p57. pdb

4212 OD1	61 ASP	5.826	-4.081	34.307
4213 OD2	61 ASP	5.826	-4.081	5.826
4229 OD2	63 ASP	5.826	-4.081	5.826
6655 O	61 LYS	5.826	-4.081	5.826

Figure Appendix-5. The predicted Ca^{2+} binding site in MEF2 complex by MUG.

A. X-ray structure of MEF2 with the Ca^{2+} binding sites highlighted in green. B. C. The predicted Ca^{2+} binding pocket in MEF2. D. Electrostatic map of CDK5. The Ca2+ binding site (red cycle) is located in the negative charged ragion of MEF2. Based on the election potential map, the predicted Ca^{2+} binding site is less likely to be true.

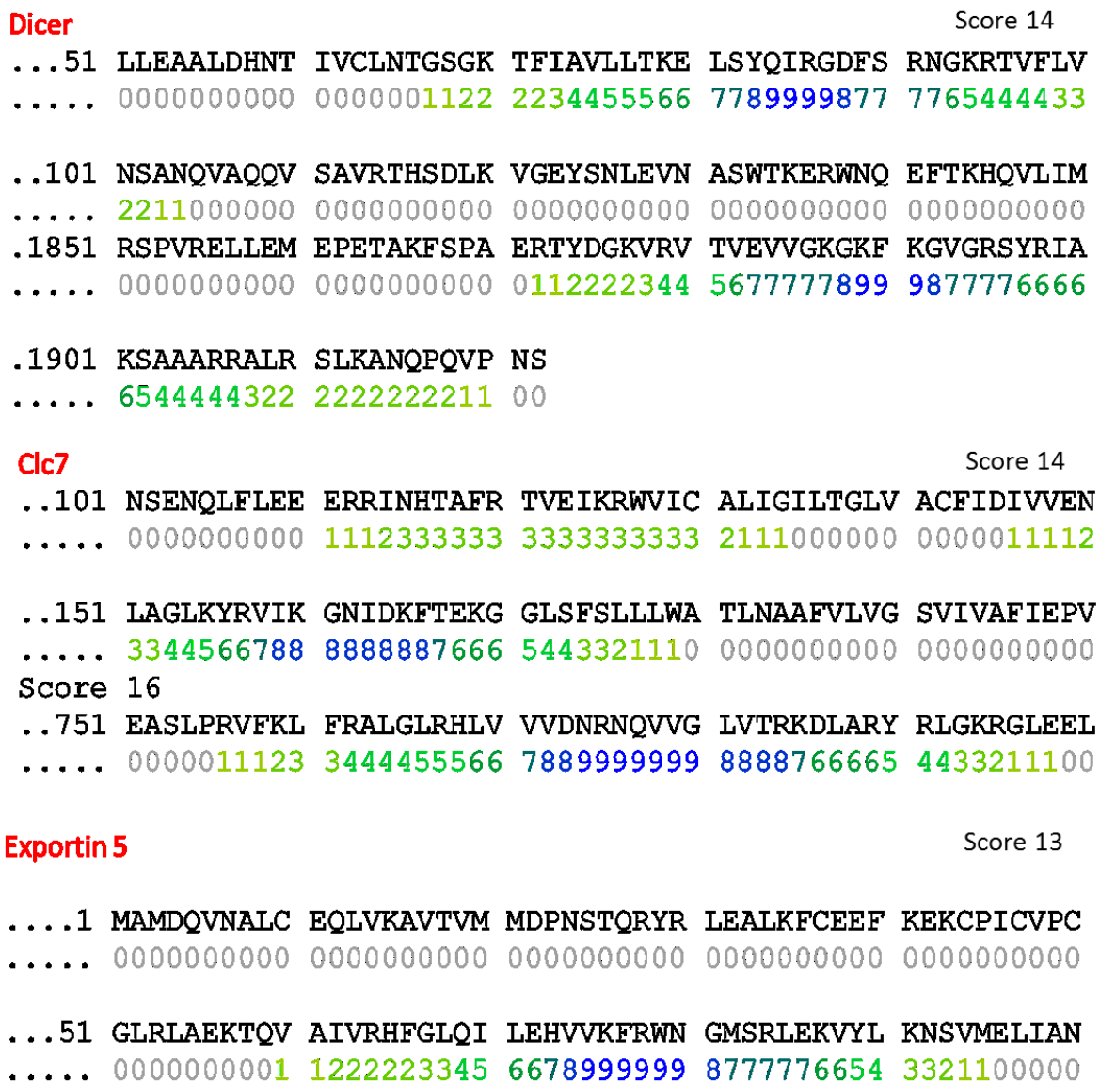

Figure Appendix-6. The predicted calmodulin binding sites in neuronal proteins.

The calmodulin binding sites were predicted by calmodulin targeting database. The normalized scores are shown below the amino acid to indicate the key residues involves in the CaM binding.

Appendix C. Relaxivity simulator

As shown in chapter 1, the relaxivities of MRI contrast agents are determined by many parameters, such as correlation time, Gd-H distance, water cooridination number, water exchange rate. The factors can be described by SMB equation. For details, please see chapter 1. In principle, the influence of relaxivities by these factors can be simulated by SMB Equation. The current difficulty is SMB Equation contains more than 8 separate Equations and currently there is not published software to simulate the relaxivity changes influenced by these factors. Therefore, it is very help to develop a relaxivity simulator based the SMB Equation.[38-40, 42, 44]

Fig. Appendix-7 shows a relaxivity simulator generated by excel based on the SMB Equation. To simulate relaxivity values, the value of each factor is required to input into the row 4 of this work sheet. For example, Gd-DTPA has a τ_R of 100 ps, while ProCA1 has a τ_R of 10 ns. After input these values, the relaxivity under different magnetic field strength can be calculated automatically.

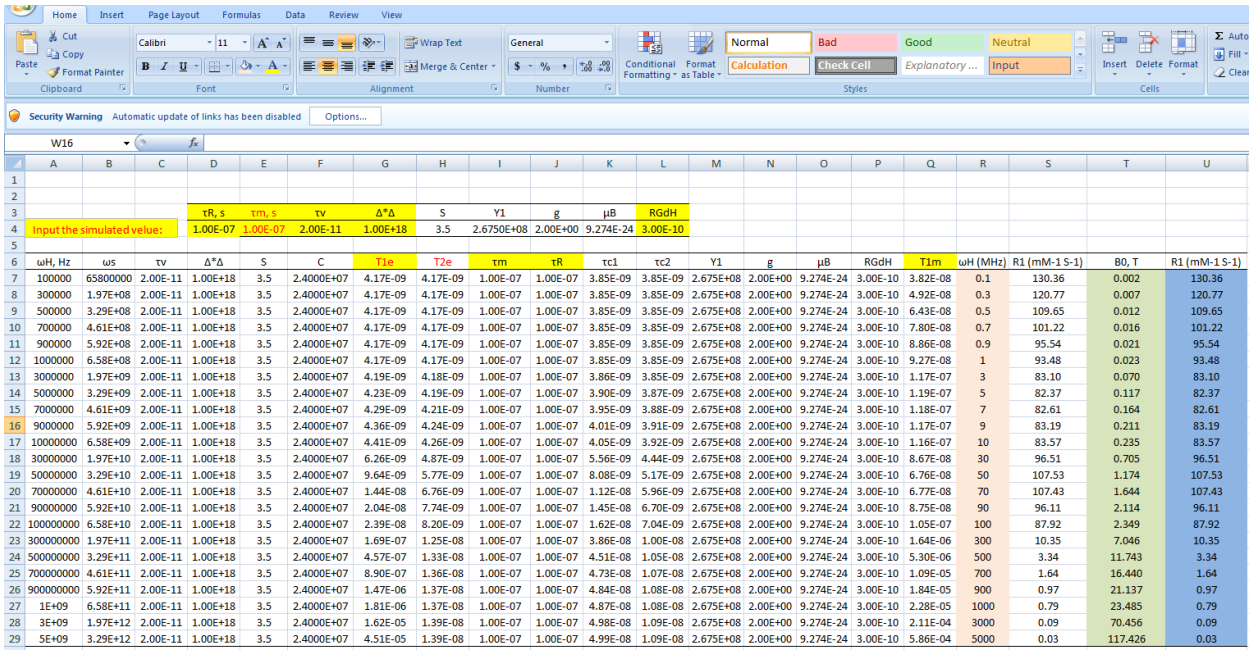

	τR, s	τm, s	τv	Δ²Δ	S	Y1	g	μB	RGdH
Input the simulated velue:	1.00E-07	1.00E-07	2.00E-11	1.00E+18	3.5	2.6750E+08	2.00E+00	9.274E-24	3.00E-10

ωH, Hz	ωs	τv	Δ²Δ	S	C	T1e	T2e	τm	τR	τc1	τc2	Y1	g	μB	RGdH	T1m	ωH (MHz)	R1 (mM-1 S-1)	B0, T	R1 (mM-1 S-1)
100000	65800000	2.00E-11	1.00E+18	3.5	2.4000E+07	4.17E-09	4.17E-09	1.00E-07	1.00E-07	3.85E-09	3.85E-09	2.675E+08	2.00E+00	9.274E-24	3.00E-10	3.82E-08	0.1	130.36	0.002	130.36
300000	1.97E+08	2.00E-11	1.00E+18	3.5	2.4000E+07	4.17E-09	4.17E-09	1.00E-07	1.00E-07	3.85E-09	3.85E-09	2.675E+08	2.00E+00	9.274E-24	3.00E-10	4.92E-08	0.3	120.77	0.007	120.77
500000	3.29E+08	2.00E-11	1.00E+18	3.5	2.4000E+07	4.17E-09	4.17E-09	1.00E-07	1.00E-07	3.85E-09	3.85E-09	2.675E+08	2.00E+00	9.274E-24	3.00E-10	6.43E-08	0.5	109.65	0.012	109.65
700000	4.61E+08	2.00E-11	1.00E+18	3.5	2.4000E+07	4.17E-09	4.17E-09	1.00E-07	1.00E-07	3.85E-09	3.85E-09	2.675E+08	2.00E+00	9.274E-24	3.00E-10	7.80E-08	0.7	101.22	0.016	101.22
900000	5.92E+08	2.00E-11	1.00E+18	3.5	2.4000E+07	4.17E-09	4.17E-09	1.00E-07	1.00E-07	3.85E-09	3.85E-09	2.675E+08	2.00E+00	9.274E-24	3.00E-10	8.86E-08	0.9	95.54	0.021	95.54
1000000	6.58E+08	2.00E-11	1.00E+18	3.5	2.4000E+07	4.17E-09	4.17E-09	1.00E-07	1.00E-07	3.85E-09	3.85E-09	2.675E+08	2.00E+00	9.274E-24	3.00E-10	9.27E-08	1	93.48	0.023	93.48
3000000	1.97E+09	2.00E-11	1.00E+18	3.5	2.4000E+07	4.19E-09	4.18E-09	1.00E-07	1.00E-07	3.86E-09	3.85E-09	2.675E+08	2.00E+00	9.274E-24	3.00E-10	1.17E-07	3	83.10	0.070	83.10
5000000	3.29E+09	2.00E-11	1.00E+18	3.5	2.4000E+07	4.23E-09	4.19E-09	1.00E-07	1.00E-07	3.90E-09	3.87E-09	2.675E+08	2.00E+00	9.274E-24	3.00E-10	1.19E-07	5	82.37	0.117	82.37
7000000	4.61E+09	2.00E-11	1.00E+18	3.5	2.4000E+07	4.29E-09	4.21E-09	1.00E-07	1.00E-07	3.95E-09	3.88E-09	2.675E+08	2.00E+00	9.274E-24	3.00E-10	1.18E-07	7	82.61	0.164	82.61
9000000	5.92E+09	2.00E-11	1.00E+18	3.5	2.4000E+07	4.36E-09	4.24E-09	1.00E-07	1.00E-07	4.01E-09	3.91E-09	2.675E+08	2.00E+00	9.274E-24	3.00E-10	1.17E-07	9	83.19	0.211	83.19
10000000	6.58E+09	2.00E-11	1.00E+18	3.5	2.4000E+07	4.41E-09	4.26E-09	1.00E-07	1.00E-07	4.05E-09	3.92E-09	2.675E+08	2.00E+00	9.274E-24	3.00E-10	1.16E-07	10	83.57	0.235	83.57
30000000	1.97E+10	2.00E-11	1.00E+18	3.5	2.4000E+07	6.26E-09	4.87E-09	1.00E-07	1.00E-07	5.56E-09	4.44E-09	2.675E+08	2.00E+00	9.274E-24	3.00E-10	8.67E-08	30	96.51	0.705	96.51
50000000	3.29E+10	2.00E-11	1.00E+18	3.5	2.4000E+07	9.64E-09	5.77E-09	1.00E-07	1.00E-07	8.08E-09	5.17E-09	2.675E+08	2.00E+00	9.274E-24	3.00E-10	6.76E-08	50	107.53	1.174	107.53
70000000	4.61E+10	2.00E-11	1.00E+18	3.5	2.4000E+07	1.44E-08	6.76E-09	1.00E-07	1.00E-07	1.12E-08	5.96E-09	2.675E+08	2.00E+00	9.274E-24	3.00E-10	6.77E-08	70	107.43	1.644	107.43
90000000	5.92E+10	2.00E-11	1.00E+18	3.5	2.4000E+07	2.04E-08	7.74E-09	1.00E-07	1.00E-07	1.45E-08	6.70E-09	2.675E+08	2.00E+00	9.274E-24	3.00E-10	8.75E-08	90	96.11	2.114	96.11
100000000	6.58E+10	2.00E-11	1.00E+18	3.5	2.4000E+07	2.39E-08	8.20E-09	1.00E-07	1.00E-07	1.62E-08	7.04E-09	2.675E+08	2.00E+00	9.274E-24	3.00E-10	1.05E-07	100	87.92	2.349	87.92
300000000	1.97E+11	2.00E-11	1.00E+18	3.5	2.4000E+07	1.69E-07	1.25E-08	1.00E-07	1.00E-07	3.86E-08	1.00E-08	2.675E+08	2.00E+00	9.274E-24	3.00E-10	1.64E-06	300	10.35	7.046	10.35
500000000	3.29E+11	2.00E-11	1.00E+18	3.5	2.4000E+07	4.57E-07	1.33E-08	1.00E-07	1.00E-07	4.51E-08	1.05E-08	2.675E+08	2.00E+00	9.274E-24	3.00E-10	5.30E-06	500	3.34	11.743	3.34
700000000	4.61E+11	2.00E-11	1.00E+18	3.5	2.4000E+07	8.90E-07	1.36E-08	1.00E-07	1.00E-07	4.73E-08	1.07E-08	2.675E+08	2.00E+00	9.274E-24	3.00E-10	1.09E-05	700	1.64	16.440	1.64
900000000	5.92E+11	2.00E-11	1.00E+18	3.5	2.4000E+07	1.47E-06	1.37E-08	1.00E-07	1.00E-07	4.84E-08	1.08E-08	2.675E+08	2.00E+00	9.274E-24	3.00E-10	1.84E-05	900	0.97	21.137	0.97
1E+09	6.58E+11	2.00E-11	1.00E+18	3.5	2.4000E+07	1.81E-06	1.37E-08	1.00E-07	1.00E-07	4.87E-08	1.08E-08	2.675E+08	2.00E+00	9.274E-24	3.00E-10	2.28E-05	1000	0.79	23.485	0.79
3E+09	1.97E+12	2.00E-11	1.00E+18	3.5	2.4000E+07	1.62E-05	1.39E-08	1.00E-07	1.00E-07	4.98E-08	1.09E-08	2.675E+08	2.00E+00	9.274E-24	3.00E-10	2.11E-04	3000	0.09	70.456	0.09
5E+09	3.29E+12	2.00E-11	1.00E+18	3.5	2.4000E+07	4.51E-05	1.39E-08	1.00E-07	1.00E-07	4.99E-08	1.09E-08	2.675E+08	2.00E+00	9.274E-24	3.00E-10	5.86E-04	5000	0.03	117.426	0.03

Figure Appendix-7. The relaxivity simulator to simulate the relaxivity of different MRI contrast agents.

To simulate the relaxivity of a specific MRI contrast agents, τ_R, τ_m, τ_v, Δ^2 and Gd-H distance (RGd-H)values required to input into this work sheet (row 4, yellow highlight). Then, the relaxivity under different magnetic field can be calculated based on the inputed values and SMB Equation.

38-40, 42, 44